UNIVERSITY OF SOUTHAMPTON

THE DEVELOPMENT OF HIGH POWER, PULSED FIBER LASER SYSTEMS AND THEIR APPLICATIONS

by Andy Piper

A thesis submitted for the degree of

DOCTOR OF PHILOSOPHY

OPTOELECTRONICS RESEARCH CENTRE

FACULTY OF ENGINEERING AND APPLIED SCIENCE

DEPARTMENT OF ELECTRONICS AND COMPUTER SCIENCE

AUGUST 2005

DECLARATION OF AUTHORSHIP

I, Andy Piper declare that the thesis entitled,

THE DEVELOPMENT OF HIGH POWER, PULSED FIBER LASER SYSTEMS AND THEIR APPLICATIONS.

and the work presented in it are my own. I confirm that:

- this work was done wholly or mainly while in candidature for a research degree at this University;
- where any part of this thesis has previously been submitted for a degree or any other qualification at this University or any other institution, this has been clearly stated;
- where I have consulted the published work of others, this is always clearly attributed;
- where I have quoted from the work of others, the source is always given. With the exception of such quotations, this thesis is entirely my own work;
- I have acknowledged all main sources of help;
- where the thesis is based on work done by myself jointly with others, I have made clear exactly what was done by others and what I have contributed myself;
- parts of this work have been published and are referenced in Appendix A5.

Signed: .....

Date: .....

Acknowledgements

I am extremely grateful to my supervisor, Professor David Richardson for his continual guidance, encouragement and especially for being patient with me throughout my research studies. I would also like to thank in particular my second supervisor, Dr Andrew Malinowski who has put in a vast amount of effort and patience to guide, encourage and teach me.

I would like to thank those who have directly helped with the work presented in this thesis. I acknowledge the contribution of all my co-workers within the pulse fiber laser group. I would like to thank Dr Jonathan Price and He Fei. I am very grateful to Dr Jonathan Price who had helped me make my very first fiber laser and for his guidance and contribution to the femtosecond pulse work. I would also like to thank Dr Johan Nilsson and members of the High Power Fiber Laser group within the ORC to allow me to use the high power diode stack pump source. In particular, I would like to thank Dr Yoonchan Jeong for his contribution that led to the success of the direct amplification work. I would also like to thank Pascal Dupriez for the numerous helpful discussions, especially the development of the high power amplification of the gain switched seed source. I would like to thank Dr Morten Ibsen for the friendly chats and for fabricating the chirped fiber Bragg gratings. I am grateful to Dr Kentaro Furusawa, who had given me advice and fabricated most of the Yb-doped fibers that were used within this thesis. I acknowledge the contribution of Dr Jayanta Sahu who fabricated the Yb-doped fiber amplifier that was used in the high power amplification of the gain switched diode. I acknowledge the contribution of Dr Benn Thomsen to the development of the directly modulated and gain switched laser diode seed sources used in this thesis. I am grateful to Dr Eleanor Tarbox for all her efforts in proof reading this thesis thoroughly and her guidance in the writing of the thesis.

I thank the other members of the ORC with whom I have had the pleasure of discussing ideas, having fun and borrowing equipment in particular: Michëal Roelens, Francesca Parmigiani, Paulo Almeida, Romeo Selvas, Periklis Petropoulos, Martin O'Connor, Christophe Codemard, Peh-Chong Teh, JuHan Lee, Anoma McCoy, Zul Yusoff, Fu Libin, Kuthan Yelen, Peter Horak and Ridzuan Mokhtar. I also thank those with whom I have shared an office in Room 2049, Physics Library and Porta Cabin A.

I thank Simon Butler, Tim McIntyre and Chris Nash for the mechanical engineering work and resources required for my experiments and for providing me with the occasional laugh. I thank David Oliver and Arthur Longhurst for their help with the many computer troubles I had. I am very grateful for the administrative staff of the ORC: Jenny Morley, Heather Spencer, Dina Smith, Eve Smith and Christine Stoner for their cheerfulness and administrative support.

I acknowledge Southampton Photonics Ltd. for their financial and resource support in providing me with the GT-Wave amplifiers, diode pump sources and laser diodes that were used in my experiments. In particular, Dr Louise Hickey, Professor Mikhail Zervas and Dr Fabio Ghiringhelli. I also acknowledge the EPSRC and ORS studentship that I had received throughout my research studies. There are many others who have contributed either directly or indirectly to the work presented in this thesis which I might have left out. I would like to thank them for their support.

I would like to thank the Southampton Chinese Church for their love, care, support and encouragement throughout my studies in Southampton University. In particular, my pastor Dr Vincent Ooi, my brothers: Tan Huai Wern, Eric Lee (a.k.a. Idiot), Daniel Lau and Simon Hon and my sisters: Karen Tan, Karen Ng, Janet Lee, Liza Lam and Erisa Ito.

I am forever grateful to my father, Mr Morris Piper, mother, Mrs Helen Piper, brother Mr Edwin Charles Piper and little sister Miss Elaine Piper for their endless love, encouragement, advise and care throughout my life.

Finally, I thank my heavenly Father, Jesus Christ for the unconditional love, guidance, encouragement and countless blessings He has poured on me throughout my life. I acknowledge that all my success and all that I have is because of Him and Him alone.

List of Contents

List of abbreviations

AOM	Accousto-Optic Modulator
AOTF	Accousto-Optic Tunable Filter
ASE	Amplified Spontaneous Emission
AWG	Arbitrary Waveform Generator
CFBG	Chirped Fiber Bragg Grating
CPA	Chirped Pulse Amplification
CW	Continuous Wave
DDL	Dispersive Delay Line
DFB	Distributed Feedback
EDFA	Erbium Doped Fiber Amplifier
EOM	Electro-Optic Modulator
ESA	Excited State Absorption
FP	Fabry-Perot
FROG	Frequency-Resolved Optical Gating
FR	Faraday Rotators
FWHM	Full Width at Half Maximum
GDD	Group Delay Dispersion
GVD	Group Velocity Dispersion
HI-BI	Highly Birefringent
HR	High Reflector
HF	Holey fiber
LMA	Large Mode Area
MOPA	Master Oscillator Power Amplifiers
MM	Multi Mode
NA	Numerical Aperture
NALM	Nonlinear amplifying loop mirrors
NLPE	Nonlinear Polarisation Evolution
NLSE	Nonlinear Schrödinger Equation
OPO	Optical Parametric Oscillator
ORC	Optoelectronics Research Centre
OSNR	Optical Signal to Noise Ratio
PBS	Polarising Beam Splitter
PC	Polarisation Controller
PPLN	Periodically Poled Lithium Niobate

RMS	Root Mean Square
RE	Rare Earth
RF	Radio Frequency
SA	Saturable absorbers
SBS	Stimulated Brillouin Scattering
SESAM	Semiconductor Saturable Absorber Mirror
SHG	Second Harmonic Generation
SNR	Signal to Noise Ratio
SPM	Self-Phase Modulation
SRS	Stimulated Raman Scattering
SM	Single Mode
SMSR	Side Mode Suppression Ratio
TEC	Temperature Controller
TOD	Third order dispersion
WDM	Wavelength Division Multiplexing
XPM	Cross Phase Modulation
YDFA	Ytterbium Doped Fiber Amplifier

Chapter 1

INTRODUCTION

1.1 Motivation

Pulsed laser systems find widespread use in present day commercial industries and in different areas of science and technology. Applications such as laser trimming, marking, welding, sensing, higher harmonic generation, sources for pumping optical parametric oscillators (OPOs), micro machining, biological imaging, laser displays and range finding make the development of pulsed laser systems an important area of research.

The traditional, and still current, workhorses for these applications are solid-state laser systems because of their proven capabilities. However, inherent problems associated with solid state based laser systems such as long-term stability, thermal management, efficiency, beam quality, compactness, cost of both manufacturing and ownership of such laser systems [1, 2] drives the search for alternative laser systems. One such alternative is rare earth (RE) doped fibre laser systems.

RE doped fibres offer high optical efficiency, high beam quality and high degrees of integration, in a compact footprint, and ready thermal management. These advantages arise for a number of physical reasons. The long lengths of active fibre provides a large surface area which ensures excellent heat dissipation and the gain medium is incorporated in a waveguide (independent of the pump power) so that maintaining diffraction limited output is possible. Due to the tight beam confinement and high doping concentrations, these fibre lasers or amplifiers offer very high single pass gain which results in low laser thresholds and high optical efficiencies. Furthermore, with the introduction of cladding pump technology, higher power but lower brightness diode pump sources can be used which enables output power scaling up to the kW levels. The research and development of fibre based laser systems is thus of great interest and potential commercial value.

Yb^{3+} based fibre laser systems are particularly attractive. This is because the Yb^{3+} rare earth laser ion offers many advantages over its counterparts. Fibres doped with Yb^{3+} exhibit very broad absorption and emission bandwidths offering wide tuning ranges and they support ultrashort optical pulses and have flexibility in terms of pump wavelength and sources. The simple, effectively two level, nature of the transition avoids many of the competing processes

like excited state absorption and concentration quenching that are seen in many other rare earth dopants (i.e. erbium), therefore providing high output powers and optical efficiencies.

In this thesis, I will present work on various Yb based pulsed fibre laser systems capable of providing high output powers and spanning a wide range of pulse durations from the femtosecond through to the nanosecond regimes.

1.2 Constraints

When amplifying pulses of high output powers or high pulse energies, various limitations restrict the achievable output performance. Which limitation is dominant depends on the particular pulse duration under consideration. For all pulse durations, because of the high peak intensity involved, nonlinear effects such as self phase modulation (SPM), stimulated Raman scattering (SRS) and stimulated Brillouin scattering (SBS), can distort the amplified propagating pulse both temporally and spectrally as the output energies are increased and eventually they set the limit on the highest output pulse energy.

Hence to be able to control or avoid the nonlinear limitations we need to understand these effects better. We need to know how they are excited and to understand the respective threshold power levels in order to optimise the system such that these effects can be avoided.

In Chapter 2, I will be introducing the advantageous and disadvantageous properties of ytterbium (Yb^{3+}) fibre based sources and the ion's spectroscopic properties. This chapter will also briefly describe the various nonlinearities encountered by the propagating pulse within an amplifier chain. Though the development of seed sources producing the required pulse durations are important, the design of the fibre amplifier cascade is most crucial. The design of the all fibre amplifier cascade greatly affects the system output performance. Other than reducing limiting effects of nonlinearities, the design also impacts on aspects such as the transverse mode quality, amplifier gain, and losses and the fibre's energy storage capabilities. In this chapter, the various fibre amplifier designs with different pumping schemes are also introduced and the considerations for the fibre designs are discussed.

1.3 Femtosecond pulse laser systems

In chapters 3 and 4, I will describe the development of femtosecond pulse laser systems having either high output pulse energy or high output average power. In chapter 3, I will describe the development and optimisation of a stable, self-starting, passively modelocked,

Yb^{3+} based fibre oscillator capable of producing output pulses with femtosecond durations. The use of this oscillator to seed a fibre amplifier cascade, to amplify these pulses, is described in Chapter 4.

In Chapter 4, fibre amplifier cascades based on two different pulse amplification techniques are introduced. The first technique, known as Chirped Pulse Amplification (CPA) is implemented to amplify femtosecond seed pulses to produce output pulses with high pulse energies and ultrashort femtosecond pulse durations. In the second fibre amplifier cascade, a direct pulse amplification technique harnessing the recently discovered parabolic pulse formation mechanism is used. In this case pulses propagating in a normally dispersive medium with sufficient gain will evolve into a pulse that develops both temporally and spectrally into a parabolic shape with a linear frequency chirp across the entire pulse form. Utilising this technique, we were able to achieve a system producing femtosecond pulses with high output average power levels of up to 25W.

1.4 Nanosecond pulse laser systems

I present two different techniques in this thesis to produce high energy nanosecond duration pulses. In Chapter 5, I will describe a single transverse moded mJ nanosecond pulse oscillator based on the Q-switch technique. This presents the highest energy single transverse mode all fibre oscillator developed to date. In chapter 6, I present a flexible nanosecond pulse amplifier system.

The development of these nanosecond pulse systems formed part of an industrial sponsorship from a commercial sponsor planning to develop pulsed fibre laser systems within its product portfolio. Our group's role was to determine the feasibility of the development of mJ pulse fibre laser systems and thereafter, if possible, to further improve these systems. A directly modulated semiconductor laser operating at 1 μm was used to produce a flexible nanosecond seed source to be amplified in an all fibre amplifier cascade. This seed source allows ready adjustment of the pulse duration, power and repetition rate. I analyse the different performance of the various segments of the amplifier chain. The various effects and eventual limitations such as inelastic scattering or gain saturation effects encountered are discussed and analysed in this chapter.

1.5 Picosecond pulse laser system

In Chapter 7, I will introduce the technique of gain switching and its implementation in a semiconductor laser diode operating at 1 μm to generate picosecond pulses. This way of producing picosecond pulses is found to be simple, cheap and flexible compared to other techniques presently used for high repetition rate picosecond pulse generation (i.e. harmonic modelocking technique). Different fibre-based compression techniques are described and used to compress the output pulse to shorter pulse durations. These compressed pulses are then amplified through an all fibre amplifier cascade to produce high output powers up to hundreds of Watts. These power levels are the highest ever achieved for a fibre amplifier cascade amplifying picosecond pulses.

1.6 Conclusion

Finally I conclude this thesis by summing up the work presented and describing some possible directions and future work.

REFERENCES

1. Limpert, J., Liem, A., Schreiber, T., Zellmer, H., Tuennermann, A., *Power and energy scaling of fiber laser systems based on ytterbium- doped large-mode-area fibers*, in *Proceedings of SPIE: Advances In Fiber Lasers.* 2003. **4974**: p. 135-147.
2. Nilsson, J., Sahu, J.K., Jeong, Y., Clarkson, W.A., Selvas, R., Grudinin, A.B., Alam, S.-U. *High power fiber lasers: New developments.* in *Proceedings of SPIE: Advances in Fiber Lasers.* 2003. **4974**: p. 50-59.

Chapter 2

YTTERBIUM DOPED FIBRE TECHNOLOGY AND NONLINEAR FIBRE OPTICS

The work described in this thesis is predominantly based on Yb-doped silica fibres. Therefore in section 2.1 of this chapter, I will briefly describe the spectroscopic properties of Yb-doped silica fibre and the background to the technology. In section 2.2, I will describe basic information on the nonlinear phenomena associated with optical fibres that were either used to develop the various devices presented in this thesis, or which placed limits on their performance. Following on in section 2.3, I will discuss issues relating to the energy storage of fibre laser systems. In section 2.4, the approach to different fibre designs that was used within this thesis and both their advantages and drawbacks are discussed. The c.w. performance of a large mode area (LMA) fibre that was designed and fabricated in the ORC is also described in this section. Fibre amplifier cascades (master oscillator power amplifiers, MOPA) were often used in the experiments carried out in this thesis, therefore an introduction to the fibre amplifier cascade will be presented in section 2.5. Finally in section 2.6, a conclusion for this chapter will be made.

2.1 Fibre laser systems

Rare-Earth (RE) doped fibre lasers were first demonstrated in the 1960s by Elias Snitzer *et al.* [1-3]. However they remained relatively unknown because their poor performance at this time was far inferior to their "bulk" solid-state laser counterparts due, in no small part, to the fact that flash lamp pumping was used. It was not until the 1980s, with the invention of RE doped single-mode silica fibres with low loss, that there was renewed interest in fibre laser technology. Single mode (SM) fibres provide robust single mode operation (important for numerous applications), high gain efficiency, low lasing thresholds and wider spectral lasing transitions than their crystal-host counterparts (allowing broadband amplification and lasing using a wide range of RE ions). They can be pumped with single mode diode pumps to generate tens of milliwatts of output power. These fibre devices were first commercialised in the late 1980s. One such commercial device, which revolutionised the optical

telecommunications market, was the erbium-doped fibre amplifier (EDFA) which operates in the 1550 nm wavelength regime.

However, though these single mode fibre lasers possess attributes which are advantageous for low power applications, the requirement for SM diode pumps poses serious problems to output power scaling due to brightness limitations of diode technology. This limited the maximum achievable output power to ~ 1W. These high brightness single mode pump diodes are coupled directly into the active SM core, and this pumping method is commonly known as core pumping. However to achieve higher output powers, pump sources providing higher output powers are required. Examples of such pump sources are broad stripe semiconductor laser diode bars and stacks and are shown in figure 2.1. But these pump sources have lower brightness multimode outputs. With the introduction of cladding pump fibre technology, these high power, low cost, broad-stripe semiconductor laser diode multimode emitters can be efficiently used to produce single and multi mode output of more than 1 kW [4-6] and 10 kW [7] c.w. output with Yb^{3+} fibre lasers. Up to 1 kW [8] of output power was shown to be commercially available from a SM Yb^{3+} fibre laser.

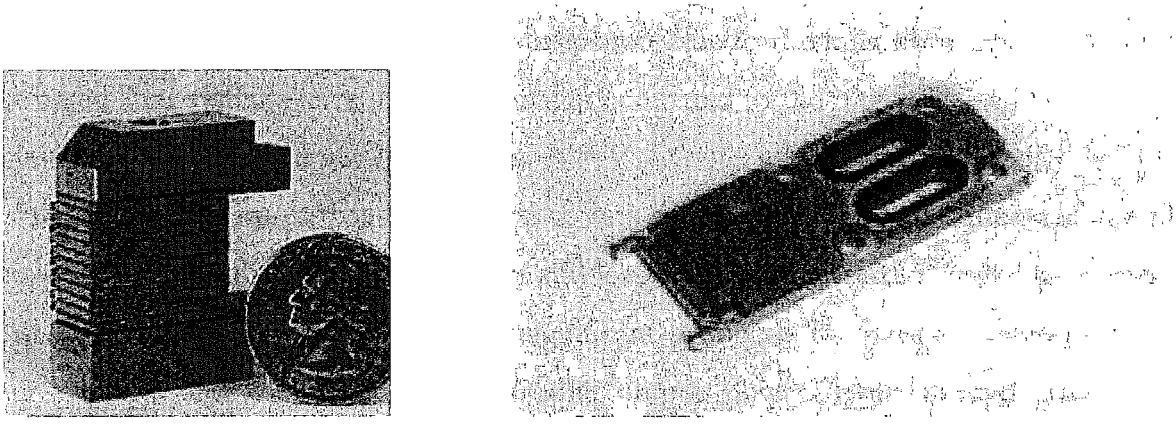

(a) (b)

Figure 2.1: An example of a semiconductor laser diode (a) stacks and (b) bar.

The difference in brightness and output power between the two groups (i.e. SM diode pump and broad-stripe diode) can be understood by looking at the differences in emitter dimensions as shown in figure 2.2. The emission from a high brightness semiconductor laser diode facet is SM and can be coupled efficiently to output fibre pigtails (having small diameters of 10 μm) which have high brightness and are generally SM. However, the semiconductor diode stacks and bars have emitter dimensions normally in lengths and/or breadths of centimetres, resulting in lower brightness multimode outputs. The output pump beams are therefore reshaped using bulk optics before being launched into optical fibres. For

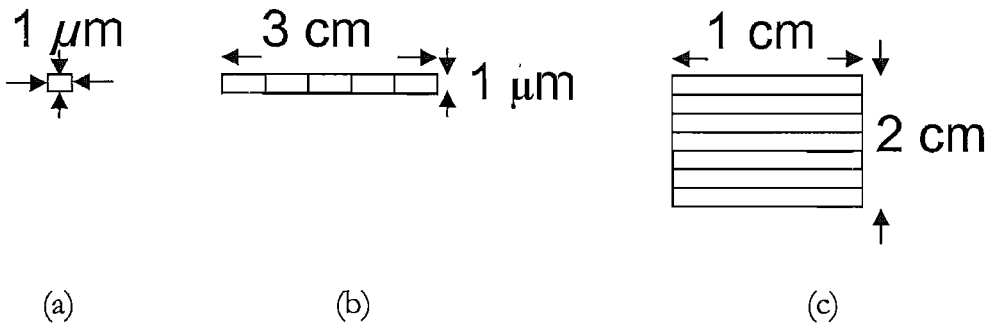

Figure 2.2: General emitter dimensions for (a) SM diode, (b) diode bar and (c) diode stacks.

available high-power diode stack pumps, neodymium (Nd) using a 808 nm pump wavelength and ytterbium (Yb^{3+}) using between 910 – 980 nm pump wavelengths are the most efficient fibre dopants

Diode-pumped, double-clad, fibre lasers can also provide broad gain bandwidths and have been demonstrated to give a bandwidth > 100 nm [9, 10]. After the pump power is launched, efficient conversion of this pump into useful signal is needed. Optical pumping efficiencies of ~ 80% are routinely attainable from Yb^{3+} doped fibre systems [11]. These properties, together with high optical gain and excellent heat dissipation, due to the long fibre lengths, mean that fibre based laser systems have many advantages compared to the presently used "bulk" crystal or glass systems in high power applications.

However, the features that come together with the wave-guiding properties within a fibre geometry, such as tight beam confinement and long length compared to "bulk" laser systems, whilst excellent for c.w. operation pose significant problems for pulsed operation, limiting energy storage and the maximum obtainable output power. Even though silica has an intrinsically low nonlinearity, the attributes above coupled with high powers makes fibre systems relatively more susceptible to well known non-linear effects such as self-phase modulation (SPM), stimulated Raman scattering (SRS) and stimulated Brillouin scattering (SBS) (for narrow-linewidth radiation). These fibre nonlinearities ultimately limit the maximum output pulse energy achievable from fibre based laser systems. But with improvements in areas of doped fibre design and the availability of high brightness high power diode pumps, fibre technology can be a serious contender and even outperform bulk-laser technology in many scientific and industrial applications, particularly those needing excellent beam quality and high average power levels (high repetition rate with moderate pulse energies).

Both Nd and Yb dopants emit at ~ 1060 nm, but Yb is a quasi-four level system at 1060 nm with high re-absorption. Thus with a smaller quantum defect, Yb can be more efficient

than Nd. Having a smaller quantum defect also means that pump absorption is more efficient for Yb^{3+} ions. Therefore optical pumping efficiencies of ~ 80% are regularly attainable [11]. Efficient pump absorption and the higher doping concentration limits of Yb (due to the solubility of Yb^{3+} ions in a silica host), allow smaller core dimensions to be designed which enhances output beam quality without compromising too much on pump efficiency. The broad gain bandwidth (50-100 nm compared to 10-30 nm) and optical pumping efficiencies (60-85 % compared to 30-40 %) also makes Yb^{3+} a preferred RE fibre dopant compared to Er^{3+} for high power applications. Therefore Yb-doped silica fibre has been used as the gain medium for all the work presented in this thesis. To give us a better understanding of its attributes, we shall describe in further detail the spectroscopic properties of Yb^{3+} in the next section.

2.1.1 Ytterbium fibre spectroscopy

The rare earths are divided into two groups of 14 elements each, the lanthanides and actinides. Lanthanides are more commonly used for rare earth doping in fibre lasers because many of the actinides have no isotopes stable enough to be useful for such devices. The lanthanides are characterised by the filling of the 4*f* shell and are most stable at the trivalent (3+) level of ionisation. Ytterbium is an element belonging to this group of rare earths having the structure $(Xe)4f^{14}5d^{0}6s^{2}$. When mixed with a host material (e.g. silica), the Yb atom becomes triply ionised. Pask H.M. *et al.* from the University of Southampton were first to study the performance of Yb^{3+} in a silica fibre [12].

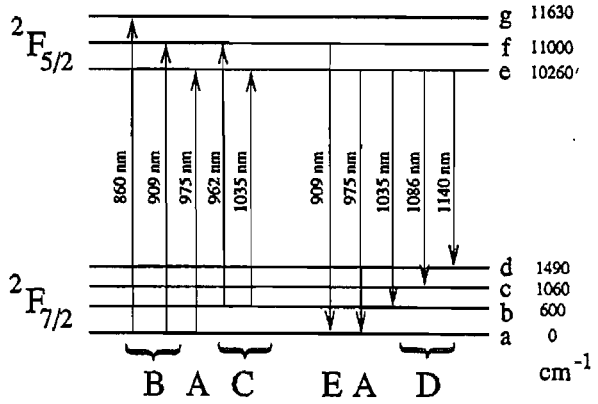

(a)

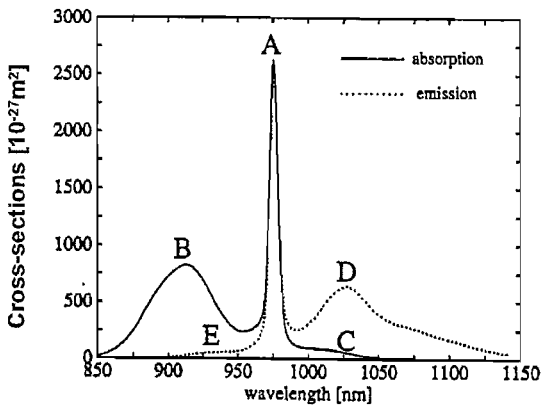

(b)

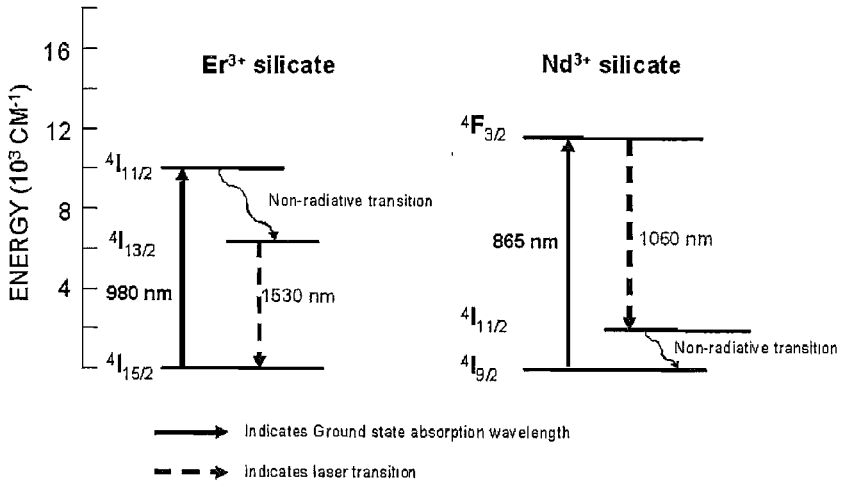

(c)

Figure 2.3: (a) The Yb^{3+} energy level structure, consisting of two manifolds, the ground manifold $^2F_{7/2}$ (with four Stark levels, labelled (a)-(d)) and the excited manifold $^2F_{5/2}$ (with three Stark levels, labelled (e)-(g)). The approximate energies above ground level in wavenumbers are indicated on the right. (b) Absorption and emission cross sections for a germanosilicate host. The prominent features of both spectra are labelled (A)-(E) for discussion. (Both figures are taken from [12]). (c) Er^{3+} and Nd^{3+} energy level structures showing commonly used and well characterised ground state absorption and laser transitions.

The Yb^{3+} energy structure is shown in figure 2.3 (a) and is relatively simple compared to other rare-earth ions. For all optical wavelengths, only two level manifolds are relevant; the $^2F_{7/2}$ ground-state manifold and the $^2F_{5/2}$ excited-state manifold [9, 12]. These manifolds split into four (shown as (a)-(d) in the figure) and three (shown as (e)-(f) in the figure) Stark sub-levels respectively via the crystal-field (Stark) interaction. The excited state manifold is well-separated ~10000 cm^{-1} (greatly exceeding the maximum phonon energy ~1100 cm^{-1} in silica) from the ground state manifold. This large energy gap without the presence of other energy levels in-between, prevents the occurrence of excited state absorption (ESA) of either the pump or laser wavelengths, concentration quenching by ion-ion energy transfer, and also precludes the nonradiative decay via multiphonon emission from $^2F_{5/2}$ which is observed in other rare-earth doped fibres (e.g. erbium Er^{3+}). It is this property that contributes to the efficient operation of Yb^{3+} and makes it such an attractive a gain medium. The corresponding transitions between sublevels are shown in figure 2.3 (a), however the transitions between the sublevels are not fully resolved for Yb^{3+} ions in glass at room temperature [12] due to strong homogeneous and some inhomogeneous broadening.

We can compare the energy level structures of the three different RE dopants (Yb^{3+}, Er^{3+} and Nd^{3+}) shown in figure 2.3 (c) so we can understand why Yb is advantageous over the other two REs. For the Er RE, although there is no excited state absorption at the $^4I_{13/2}$

manifold at the 980 nm pump wavelength and for oxide glasses there is negligible stimulated emission at the pump wavelength (because of the short lifetime at the $^4I_{11/2}$ level), the smaller separation between the lasing manifold and ground state manifold ($^4I_{13/2}$->$^4I_{15/2}$) ~ 6000 cm^{-1} and similar separation between the ground state and excited state manifold for the 980 nm absorption transition ($^4I_{15/2}$->$^4I_{11/2}$) ~10000 cm^{-1} as compared to Yb means that the Er RE would be less efficient. For Nd, other than excited state absorption (which is strong for a silica host) at the $^4F_{3/2}$ manifold which reduces the spectral region for which gain can be obtained, the Nd RE has about the same energy separation between the ground state manifold and excited state level ($^4I_{9/2}$->$^4F_{3/2}$) but again has a smaller separation between terminal state manifold $^4I_{11/2}$ and the excited state manifold, $^4F_{3/2}$ ($^4F_{3/2}$->$^4I_{11/2}$) is ~ 8000 cm^{-1}, compared to Yb, hence is less efficient. Furthermore, other than Yb^{3+} ions (in a silica host) having a larger energy gap as compared to Er^{3+} and Nd^{3+}. The absence of other energy level states between the lasing transitions for Yb^{3+} ions prevents the occurrence of ESA and concentration quenching between ions, thereby making Yb^{3+} ions more efficient.

The absorption and emission cross section of Yb in germanosilicate glass is shown in figure 2.3 (b). The absorption cross section is taken using a cut back method from the transmission measurement of a white light source. The emission cross section is obtained from a fluorescence measurement at the side of the fibre (cladding is stripped) to avoid distortion due to re-absorption. Both spectra are normalised to the peak at 975 nm which results in some discrepancy in the absorption spectrum (~5-10% higher than the emission spectrum at room temperature using McCumber analysis). It has also been found by certain authors [13, 14] that the bandwidth and peak wavelengths of the absorption and emission spectra is dependent to some extent on the host glass composition. Paschotta R. *et al.* [9] found that the emission spectra of Yb-doped germansilicate fibres varies by up to ~ 30% with differing amounts of germanium, aluminium and boron especially at wavelengths between 990-1020 nm.

The fluorescence decay times are measured to be typically ~0.8 ms and also vary between fibres by up to ~ 30%; fibres with higher germanium content in the core (introduced to increase the numerical aperture (NA)) tend to have shorter fluorescent lifetimes (leads to larger cross sections), while fibres with a pure silicate host have a longer lifetime of ~1.5 ms.

With the help of the energy structure in figure 2.3 (a), we now discuss some of the more prominent features (which are labelled (A)-(E)) shown in figure 2.3 (b) to help us understand the Yb^{3+} spectroscopy better and why certain pump and signal wavelengths are favoured in this thesis. Following from Pask *et al.* [12], the narrow peak at 975 nm (A) in both the absorption and emission spectrum corresponds to the transition between Stark levels a and e

in figure 2.1 (a). Transitions between Stark levels a to f and g correspond to the first absorption peak at (B). The weak absorption at shoulder (C) at the longer wavelength (at ~ 1035 nm) and at the foot of the narrow 975 nm peak in the shorter wavelength side (at ~ 962 nm) seen in the absorption spectrum is attributed to the smaller ion population at Stark level b.

The light radiation from a Yb-doped medium is either truly three-level in nature or quasi four-level in character. The laser operation at the 975 nm narrow peak (A) is truly three-level while the second peak (D) in the emission spectrum extending to ~ 1200 nm (corresponding to radiative transitions between level e to b,c and d) is quasi four-level in character at the longer wavelengths. This is due to transitions into the nearly empty Stark levels c and d (with radiation wavelengths around 1084 nm or 1140 nm). The emission shoulder at the shorter wavelength (E) is attributed to transitions between Stark level f and ground state a. This is however very weak due to the low thermal populations at f and laser action has not been observed.

From figure 2.3 (b), we can see that the emission and absorption spectra for Yb^{3+} are very broad. This means that there is a wide possible choice of pump wavelengths (~ 860 – 1064 nm) and a broad gain bandwidth extending from ~975 - 1200 nm. However there are limitations governing the choice of pump wavelengths, the first limitation being that we can only generate gain at a signal wavelength longer than the pump wavelength. Secondly the absorption length of the fibre required to efficiently and sufficiently absorb the pump. Thirdly, the quantum efficiency of the laser is determined mainly by the ratio of pump to signal wavelengths. Pumping close to the signal wavelength can increase the efficiency by as much as ~ 20%. For example, for signal wavelengths at 1060 nm, pumping at 975 nm theoretically gives us 6% higher lasing efficiency compared to pumping at 915 nm. Fourth, the threshold pump power is a function of the cross sections at the corresponding pump wavelength. Finally, since we are concerned about power scaling of the system, the availability of the pumps with high output powers are obviously important.

The laser systems that were developed in this thesis were designed to operate near ~ 1060 nm. The 1060 nm signal wavelength was chosen because of the high emission cross section and negligible absorption at this wavelength. Operating at this signal wavelength also dictates that we need to pump at wavelengths < 1040 nm.

As described earlier, nonlinear effects are the main limitation to the maximum output peak powers/pulse energies we can achieve from our system. Since these increase with fibre length, it would be advantageous to reduce the fibre length (if it still provides sufficient gain). It can be seen that pumping at 975 nm utilises the highest absorption cross section which means that

shorter fibre lengths can be used. However the emission cross section at this wavelength is also high and thus the effects of amplified spontaneous emission (ASE) must be considered and controlled especially with low input signal power. The availability of cheap high power 975 nm diode pumps was also limited, hence a mixture of both 915 nm and 975 nm diode pumps were used. The use of fibres with larger core dimensions and hence larger effective core areas would also reduce the limiting effects of nonlinearity. This was the main approach that was used throughout this thesis to achieve higher output power scaling.

Depending on the dimensions and design of the fibre, the type of pumping scheme is chosen. In this thesis, there are two types of pumping schemes used, core and cladding pumping.

2.1.2 Core-pump amplifiers

Core-pumped amplifiers are usually made using SM fibres where both core and pump radiation are confined within the core. They are normally found at the beginning of the amplifier cascade. This is because of their robust, stable and low-noise operation. Due to the tightly confined propagating mode, they are inherently more susceptible to non-linearity and therefore require careful nonlinearity management. Implementing them at the beginning introduces lower input peak intensities and hence avoids/reduces any nonlinear effects from occurring.

The core-pumped amplifier that was used within all our setups was made using a SM Yb-doped fibre designed and pulled within the ORC (Fibre name HD406-2). It has a core diameter of 5 μm, NA= 0.21 and doping concentration of ~2000 ppm. The pump power from SM diode pumps is introduced via 980/1060 nm wavelength de-multiplexer (WDM) couplers (their wavelength transmission characteristics are shown in figure 3.2 of section 3.2.1).

In section 4.2.2 of chapter 4, we will be describing the initial performance of this core-pump amplifier and further amplifier design refinements that could be made to enable increased gains. Both original and improved core-pumped amplifier configurations were used in this thesis.

2.1.3 *Cladding pump amplifiers*

There are two configurations of cladding pumping used within this thesis, simple end pumping and GT-Wave pumping systems. Generally end pumped systems require shorter fibre lengths compared to GT-wave pumping systems.

Cladding pump technology avoids the use of single-mode pump sources and allows the use of many high power, lower brightness, pump sources (i.e. diode bars, stacks or arrays) which could not be efficiently used before. Cladding pump fibres allow single mode laser operation without the need for single mode pump sources. This technology propels the power scaling of fibre lasers to a whole new level.

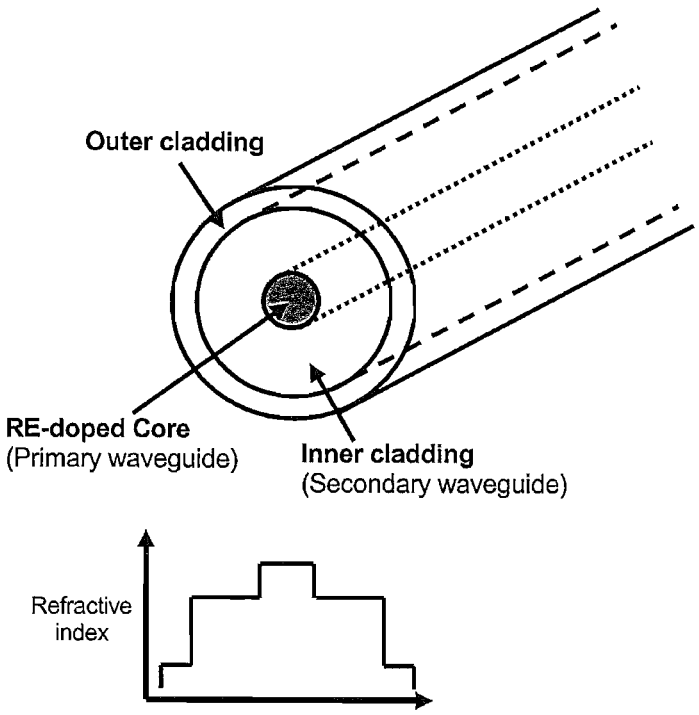

Figure 2.4: Schematic drawing of a typical double-clad fibre and refractive index profile.

A typical design of a cladding pumped fibre consists of a primary/signal waveguide (the core) which guides the signal and is normally rare-earth doped. This primary waveguide is surrounded by a secondary lower-index waveguide (inner cladding). The secondary/pump waveguide is formed by surrounding it with another coating having a lower refractive index (outer cladding). This secondary waveguide is designed to be highly multi-mode and to have larger dimensions compared to the primary waveguide to enable coupling and guiding of highly multi-moded pump sources. The primary waveguide or core is located within the secondary waveguide and forms part of the pump waveguide. This arrangement enables the

guided pump light to be coupled or absorbed within the RE doped core and to excite the active lasing ions. The material used to make the primary and secondary waveguide are typically glass whereas the outer cladding is typically made from polymer, but can also be a glass or a micro-structured region. These cladding pumped fibres with double clad structures are typically known as double clad fibre. A schematic drawing of a double-clad fibre is shown in Figure 2.4.

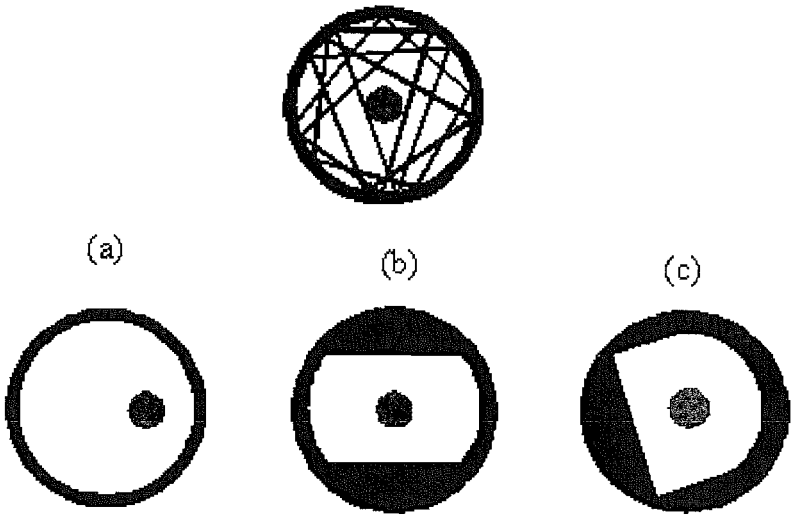

Figure 2.5: Various inner cladding geometry designs to improve pump coupling into the active core.

The most common way used to pump the double clad fibre is to launch the pump light into either one or both ends of the fibre via coupling optics. This technique is called end-pumping and is used because of its simplicity and efficiency. In practise, the output beam from the diode sources is generally much larger than the fibre (at least in one dimension and divergence in the two axes is also very different). Therefore more complicated optics (i.e. non-imaging beam shaping optics) [15] is required to couple the pump light efficiently into the fibre. However the high power pump diodes that were used in most of my experiments have fibre pigtailed outputs (~ 200 μm diameter, NA=0.2) and the need for complicated beam optics could therefore be avoided.

The launched pump light is absorbed into the core as it propagates down the inner cladding of the fibre. In double-clad fibres, the pump absorption is relatively low. Thus pump absorption (per unit length) efficiency into the core is vital for successful implementation of the cladding pump technique. For conventional cylindrical-symmetrical double clad fibre shown in figure 2.4, the pump absorption is exceptionally low (< 0.4 dB/m). This is because some of the guided pump light propagates in a helical mode (corresponding to skew rays) through the inner cladding and vanishes at the doped central core (see top picture in figure

2.5). The geometry of the inner cladding can improve the pump absorption and the maximum possible launched pump level. Significant improvements to pump absorption can be achieved by changing the geometry of the inner cladding or using an offset doped core (see figure 2.5 (a)) to break the core/cladding symmetry [16-19]. Asymmetric inner cladding shapes as shown in figure 2.5 (i.e. rectanglar shape (b), D-shape (c)) induces the propagating pump modes to cross the central doped core and have improved the pump absorption up to 10 dB/m. In this thesis, almost all (except one) the double clad fibres that have been used have a D-shape inner cladding design with a 10% chamfer (see figure 2.11 (b)).

Other parameters like core dopant concentration and cladding to core area ratio can also improve the pump absorption per unit length. A high RE concentration increases the pump absorption, but the maximum concentration is limited by factors such as quenching. Typical concentration limits depend strongly on the host materials as well as the rare-earth dopant. For example, for erbium-doped fibres the concentration limit is around 10^{18} to 10^{19} cm^{-3} ions in aluminium-silicate based fibres [20]. Typical pump absorption per unit length values for double-clad fibres lie in the range of 0.1 – 10 dB/m (for the double-clad LMA fibres used in this thesis, the pump absorption per unit length is 4 dB/m and 1.5 dB/m at 975 nm and 915 nm pump radiation respectively). The fibre length is then selected to provide sufficient pump absorption (in this thesis fibre lengths are chosen to provide ~ 10 dB absorption).

Another consideration regarding the length of double-clad fibres used in a laser system is the background losses for the signal (in the core) and the pump (in the inner cladding). This can become significant if the fibre length becomes too long. Typical values of pump background losses are 10 – 100 dB/km and for fibres with high doping concentration, the signal loss may be ~100 dB/km or even more. A degradation in fibre efficiency would be noticeable when background signal losses reaches ~1 dB, thus fibre lengths should be no more than a few tens of meters, or at most around 100 m.

Besides pump absorption, the pump launch efficiency and output modal quality of these double-clad fibres are strongly influenced by the ratio between the cross-sectional areas of the pump waveguide (core plus inner cladding) and the signal waveguide (the core). If the ratio of the areas becomes too small, the core would not significantly influence the guiding properties as it would be reduced to a small perturbation within the inner cladding. However, the ratio of the areas cannot be too large, as the pump absorption is (to a simple approximation) inversely proportional to the ratio of the areas. In practise, the fibres are design to have cross-sectional areas having a ratio of at least ten (the LMA fibres used in this thesis were designed to have a

cross-sectional area ratio of 10). This is to enable an efficient pump launch and provide significant brightness enhancement.

The NA of the inner cladding is also vital as it defines the maximum possible launched pump level. Table 2.1 shows the various NA's obtained when different material combinations are used to make the inner/outer cladding. In the next section, we will describe an alternative cladding pumped fibre that does not use the commonly used end-pumping technique.

Composition	NA
Polymer:glass	0.4
Glass: F-doped glass	0.25
Microstructured fibre	>0.8

* Cladding diameters up to 1mm are possible

Table 2.1: Various inner cladding compositions and their corresponding NA.

2.1.4 GT-wave amplifier

Despite all its simplicity and efficiency, the commonly used end-pumping technique has its disadvantages. As coupling optics and dichroic mirrors are used to launch and separate the pump and signal radiation, interruption to the signal fibre and the requirements for precise alignments can result in an increase in insertion losses and instability. Furthermore, this cavity arrangement would be less compact and thermal management of the ends of the fibre becomes necessary to avoid thermal fluctuations in alignment that could result in self pulsing or the fibre breaking.

Dr Anatoly Grudinin and Paul Turner from the ORC developed a clever and novel alternative cladding pumping scheme that avoids most of these problems, the so called GT-wave fibre [21, 22] (ORC/SPI: European patent application number Wo067350). The GT-wave cladding pumped fibre design allows pump coupling from high power multi mode diode pumps to the active signal fibre without interruption to the signal path within the cavity and any optical components. Figure 2.6 (a) shows a cross-sectional view of a standard GT-wave fibre. It consists of a signal fibre with a RE doped core and two multi-mode pump fibres. The signal fibre typically has standard SM fibre dimensions but could be scaled to larger dimensions for higher power scaling. The three fibres have similar refractive indices (see refractive index profile) and are in contact with one another. The bundle of three fibres is

surrounded within a lower index polymer coating that creates the index difference for waveguiding.

Figure 2.6 (b) shows a schematic of the GT-wave setup. Three standard passive fibre pigtails (two multi-mode pump fibre and one SM signal fibre) are broken out from the low index coating at each end. They are connected to the respective fibre within the GT-wave fibre bundle through a "trifurcating splice". Guided pump light, launched into the multi-mode pump pigtails, cross-couples between all the fibres within the GT-wave fibre. The asymmetric arrangement of the fibre bundle enhances the pump absorption into the doped core of the signal fibre (pump absorption per unit length for the GT-wave used in this thesis was ~ 1.2 dB/m with 915 nm pump radiation). Up to four multimode pump pigtails could be used simultaneously to couple pump radiation into the active fibre. Recycling of any unabsorbed pump is possible by splicing together the multi-mode pump fibres at the other end. A detailed characterisation of a GT-wave amplifier using c.w. seed sources, operating at various 1 μm wavelengths, can be found in section 6.4.1 of chapter 6.

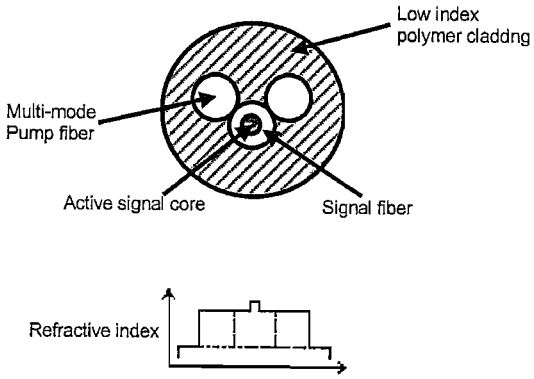

(a)

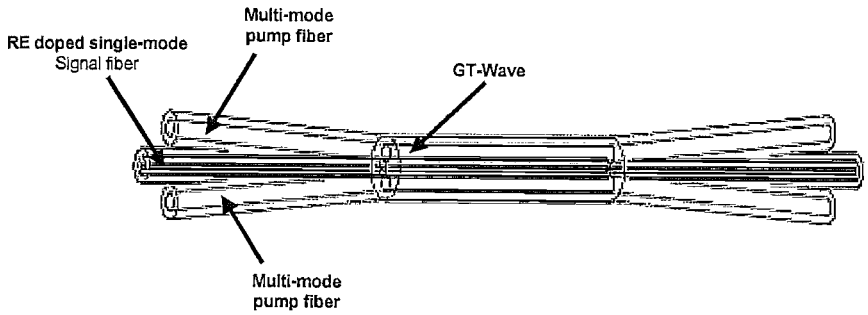

(b)

Figure 2.6 (a) Cross section and refractive index profile of GT-Wave fibre. (b) Schematic of GT-Wave fibre showing four output multi-mode pump fibre pigtails and a single mode RE-doped signal fibre. Pictures courtesy of SPI.

In most of the experiments carried out in this thesis, the pump sources that were available to pump our final stage power amplifiers were a 25 W 975 nm and a 30 W 915 nm diode combiner pump source from Boston Lasers Inc. Using different pump wavelengths (having sufficient wavelength discrimination between the two) can be advantageous when both ends of the gain fibre are pumped simultaneously in an end pumping configuration (see figure 5.3 (c) of chapter 5 or figure 5.19 of chapter 5). This is because dichroic wavelength filters can be used to prevent the unabsorbed pump radiation coming from the pump source at one end to be fed into the other (at the opposite end) causing damage to the pump source. Although the absorption cross section at 915 nm was ~ 3 times lower compared to pumping at 975 nm (which means longer fibre lengths are required) and pumping at 915 nm leads to high gains at 975 nm which can result in the build up of unwanted ASE, the lower cost and availability of high power 915 nm pumps makes them attractive. The broader absorption spectrum at 915 nm also makes the laser system less sensitive to pump wavelength drift due to temperature variations compared to 975 nm pumps. Hence requirements for the temperature cooling systems for the 915 nm pump diodes are more relaxed. The balance between the cost, availability and performance of using pump diodes at 915 and 975 nm wavelengths were carefully considered in the development of the systems described in this thesis.

2.2 Nonlinear Fibre Optics

When short pulses propagate within an optical fibre, due to their broad spectral bandwidths and high peak intensities, both dispersive and nonlinear effects influence their shape and spectrum. In this section we will describe the various principal dispersive and nonlinear phenomena that are relevant to this thesis which occur when a pulse propagates within an optical fibre. The derivation of the Nonlinear Schrödinger Equation (NLSE) governing propagation in a fibre will be discussed. The scope of this thesis, as introduced earlier in chapter 1, covers silica host Yb-doped fibre based devices producing pulses having femtosecond, picosecond and nanosecond durations.

This section is organised as follows: Section 2.2.1 introduces the wave equation that describes light propagation within an optical fibre and the idea of induced polarisation which are crucial to the understanding of nonlinearities in fibres. Section 2.2.2 will describe the effects of linear dispersion on the propagating pulse without the presence of nonlinearities.

Section 2.2.3 describes the elastic response (no energy exchange) of the bound electrons to an intense optical field resulting in the Kerr effect which gives rise to Self Phase Modulation (SPM) and Cross Phase Modulation (XPM). Finally, section 2.2.4 describes both Stimulated Raman (SRS) and Brillouin (SBS) Scattering caused by stimulated inelastic scattering that occurs in an optical fibre where part of the energy from the optical field is transferred to the nonlinear medium. Energy is transferred by the annihilation of an incident photon and creation of a lower frequency photon and phonon (with the right energy and momentum to conserve the energy).

2.2.1 Pulse Propagation in Optical fibre

In the absence of free charges in a nonmagnetic medium such as an optical fibre, the wave equation derived from Maxwell equations of the propagating light can be written as [23],

$$\nabla \times \nabla \times \vec{E} = -\frac{1}{c^2}\frac{\partial^2 \vec{E}}{\partial t^2} - \mu_0 \frac{\partial^2 \vec{P}}{\partial t^2} \qquad (2.1)$$

where $c\left(=1/\sqrt{\mu_0 \varepsilon_0}\right)$ is the speed of light in vacuum, $\vec{E}$ is the electric field and $\vec{P}$ is the total induced polarisation.

A relationship between $\vec{E}$ and $\vec{P}$ is required to obtain a solution for equation 2.1. The response of silica fibre to an intense electromagnetic field becomes nonlinear as a result of the anharmonic motion of bound electrons under the influence of the applied field. This results in a nonlinear total polarisation $\vec{P}$ being induced by the electric field $\vec{E}$ which can be described generally (since the operating wavelength range of interest between 0.5 – 2 μm is far from the medium's resonance) as,

$$\vec{P} = \varepsilon_0\left(\chi^{(1)} \cdot \vec{E} + \chi^{(2)} : \vec{E}\vec{E} + \chi^{(3)} \vdots \vec{E}\vec{E}\vec{E} + \cdots\right) \qquad (2.2)$$

where ε_0 is the vacuum permittivity and $\chi^{(j)}(j = 1,2,3,\cdots)$ is jth order susceptibility (tensor of rank j+1). This general relation assumes that the response is both instantaneous and local.

$\chi^{(1)}$ is the linear susceptibility and it is the dominant contribution to $\vec{P}$. Its effects are included through the refractive index n and the attenuation coefficient α. The second-order

susceptibility $\chi^{(2)}$ is responsible for second-harmonic generation and sum-frequency generation. However it is only nonzero for media without inversion symmetry. Since the crystalline structure of SiO_2 is symmetrical, it shows a zero value (neglecting surface effects) for $\chi^{(2)}$. Therefore second order nonlinear effects vanish for silica fibres and the lowest order nonlinear effects encountered originate from the third order susceptibility $\chi^{(3)}$ which is responsible for phenomena such as third harmonic generation, four-wave mixing and nonlinear refraction (i.e. Kerr effect). However the parametric nonlinear process that involves the generation of new frequencies (e.g. four-wave mixing and third harmonic generation) requires special efforts to achieve phase-matching, in order to obtain efficient conversion in optical fibres, which is not within the scope of this thesis and therefore not considered here.

The complexity of the following equations requires several assumptions to be made to obtain the final solution. We first assume that the nonlinear contribution to the polarisation ($\vec{P}_{NL}$) is a small perturbation to the linear contribution ($\vec{P}_L$) to the total induced polarisation. This is valid because nonlinear changes in refractive index are relatively weak in silica fibres. If we include only the third order nonlinear contribution, the total induced polarisation $\vec{P}$ consists only of two parts and is described as $\vec{P}(\vec{r},t) = \vec{P}_L(\vec{r},t) + \vec{P}_{NL}(\vec{r},t)$, where $\vec{P}_L(\vec{r},t)$ is the linear contribution govern by $\chi^{(1)}$. Assuming the medium response is local, in the electric-dipole approximation, both $\vec{P}_L(\vec{r},t)$ and $\vec{P}_{NL}(\vec{r},t)$ are related to the electric field by;

$$\vec{P}_L(\vec{r},t) = \varepsilon_0 \int_{-\infty}^{\infty} \chi^{(1)}(t-t') \cdot \vec{E}(\vec{r},t')dt', \tag{2.3}$$

$$\vec{P}_{NL}(\vec{r},t) = \varepsilon_0 \int_{-\infty}^{+\infty}\iint \chi^{(3)}(t-t_1,t-t_2,t-t_3) \vdots \vec{E}(\vec{r},t_1)\vec{E}(\vec{r},t_2)\vec{E}(\vec{r},t_3)\,dt_1 dt_2 dt_3. \tag{2.4}$$

Simplification can be made to equation 2.1 by using the mathematical relation $\nabla \times \nabla \times \vec{E} = \nabla(\nabla \cdot \vec{E}) - \nabla^2 \vec{E} = -\nabla^2 \vec{E}$, where $\nabla \cdot \vec{D} = \varepsilon \nabla \cdot \vec{E} = 0$ and ε represents the dielectric constant to give,

$$\nabla^2 \vec{E} - \frac{1}{c^2}\frac{\partial^2 \vec{E}}{\partial t^2} = -\mu_0 \frac{\partial^2 \vec{P}_L}{\partial t^2} - \mu_0 \frac{\partial^2 \vec{P}_{NL}}{\partial t^2} \quad . \tag{2.5}$$

2.2.2 *Fibre modes, linear propagation and dispersion*

The linear response of the bound electrons in silica (material dispersion) and the waveguiding (waveguide dispersion) properties of the optical fibre together define the dispersion experienced by light propagating within the optical fibre. In this section we consider the case when the nonlinear polarisation contribution is zero (i.e. $P_{NL} = 0$). Equation 2.5 is then linear in E and can be written in the frequency domain as,

$$\nabla^2 \tilde{E} + \varepsilon(\omega)\frac{\omega^2}{c^2}\tilde{E} = 0. \tag{2.6}$$

Assuming low losses (i.e. α is negligible) at the wavelength region of interest for optical fibres, the imaginary part of $\varepsilon = (n + i\alpha / 2k_0)^2$ is negligible compared to the real part and is therefore simply $\varepsilon(\omega) = n^2(\omega)$. Hence equation 2.6 can be written as,

$$\nabla^2 \tilde{E} + n^2(\omega)k^2{}_0\tilde{E} = 0 \tag{2.7}$$

where wave vector $k_0 = \frac{\omega}{c}$.

The one dimensional frequency dependent refractive index (i.e. linear response) of the material (i.e. silica) is far from material resonance to the propagating light and is well approximated by the Sellmeier equation;

$$n^2(\omega) = 1 + \sum_{j=1}^{m} \frac{B_j \omega_j^2}{\omega_j^2 - \omega^2} \tag{2.8}$$

where ω_j is the resonance frequency and B_j is the strength of the j^{th} resonance.

2.2.2.1 *Fibre modes*

At any frequency ω, optical fibres can support a finite number of guided modes whose spatial distribution $\tilde{E}(r, \omega)$ are a solution to equation 2.7 and which satisfy all appropriate

boundary conditions. The transverse propagating modes within a fibre are dependent on its design parameters. We shall now briefly describe the transverse propagating fibre modes within an optical fibre.

The cylindrical symmetry of fibres allows their cross sectional geometry to be expressed in cylindrical coordinates ρ, ϕ, z . As the electric field E and magnetic field H satisfy Maxwell equations, there are six components but only two are independent. It is common that we use $\tilde{E}_z$ and $\tilde{H}_z$ as the two independent components. Using the method of separation of variables, a general form can be written $\tilde{E}_z(r,\omega) = A(\omega)F(\rho)\exp(\pm im\phi)\exp(i\beta z)$ where A is a normalisation constant, β is the propagation constant, m is an integer and $F(\rho)$ is the transverse modal profile. A similar relation exists for the magnetic field component $\tilde{H}_z$ and the four other components $\tilde{E}_\rho, \tilde{E}_\phi, \tilde{H}_\rho, \tilde{H}_\phi$ that are not independent variables can be solved using Maxwell equations. Taking the boundary condition that the tangential components of $\tilde{E}_z$ be continuous across the core:cladding interface (i.e. $\rho = a$, where a is the radius of the core) and matching the appropriate Bessel function solutions (Bessel function for $\rho \le a$ and modified Bessel function for $\rho \ge a$) for $F(\rho)$, an eigenvalue equation (or characteristic equation) can be found. Using numerical analysis, the solutions to this eigenvalue equation will give us the propagation constants $\beta_{mn}(\omega)$ for the various propagating fibre modes. Obtaining the propagation constant for a given core mode will give us its transverse mode profile $F_m(\kappa_{mn}\rho)$ for a given frequency, where $\kappa_{mn} = (n_{co}{}^2 k_0{}^2 - \beta_{mn}{}^2)^{1/2}$ and n_{co} is the refractive index of the core. Again a similar procedure can be carried out $\tilde{H}_z$ to obtain the magnetic field components. In this thesis, both conventional and unconventional optical fibres were used. Gloge [24] showed that for weakly guiding fibres, the propagation constant can be calculated by the expression, $\beta(\omega) = \sqrt{k_0{}^2 n_{co}{}^2(\omega) - \frac{u^2(\omega)}{a^2}}$ where $u(\omega) = \left[\left(1-\sqrt{2}\right)V(\omega)\right] / \left[1+\left(4+V^4(\omega)\right)^{1/4}\right]$ and $V(\omega)$ is expressed as a frequency dependent normalised frequency (or V number) of the fibre. The index difference between the core n_{co} and cladding n_{cl}, $\Delta n = n_{co} - n_{cl}$ is related to the propagation constant through the V number. This index difference is vital to the behaviour of the guided light within the fibre and defines the numerical aperture (NA$= (n_{co}^2 - n_{cl}^2)^{1/2}$) of the core.

The number of guided modes in a conventional single mode (SM) step index fibre can be well approximated by the normalised frequency V. The V number is defined as $V = k_0 \cdot a \cdot (n_{co}^2 - n_{cl}^2)^{1/2} = k_0 \cdot a \cdot NA$ where n_{cl} is the refractive index of the cladding and a and n_{co} are defined as before [23]. The condition for single mode operation occurs when $V < 2.405$. In practise, a single mode fibre can actually support two modes of orthogonal polarisations. Ideally, the two orthogonal polarisation modes are actually degenerate (i.e. have the same propagation constant). However due to random irregularities in the cylindrical symmetry that occur along the length of the fibre from imperfect fibre fabrication, the degeneracy is broken slightly. This can result in periodic power coupling between the two polarisation modes as light propagates down the fibre. The birefringence 'beat length' of a fibre describes the mode splitting of the fibre and is described by the expression, $L_B = 2\pi / \left(\left| \beta_x - \beta_y \right| \right) = \lambda / \left(\left| n_x - n_y \right| \right)$ where λ is the central wavelength, β_x and n_x are the propagation constant of the propagating mode along the orthogonal x-axis of the fibre and the corresponding effective refractive index along that axis and vice versa.

2.2.2.2 *Linear propagation and dispersion*

After obtaining the mode profile, in this section we will derive the basic propagation equation. We make another two assumptions; first we assume that the propagating field is launched onto one axis and that it maintains its polarisation along the fibre, and second the optical field is quasi-monochromatic (i.e. central frequency ω_0 is >> than its spectral width $\Delta\omega$) so that a slowly varying envelope approximation can be used in our derivation. The electric field under the slowly varying amplitude approximation can then be written as,

$$\vec{E}(\vec{r},t) = \frac{1}{2}\hat{x}[E(\vec{r},t)\exp(-i\omega_0 t) + c.c.] \tag{2.9}$$

where $c.c.$ stands for complex conjugate, $\hat{x}$ is the polarisation unit vector and amplitude $E(r,t)$ is a slowly varying function of time.

Using the method of separation, we try to solve equation 2.7. Assuming it has a solution of the form $\widetilde{E}_z(r, \omega - \omega_0) = F(x,y)\widetilde{A}(z, \omega - \omega_0)\exp(i\beta_0 z)$ where $\widetilde{A}(z, \omega - \omega_0)$ is a slowly

varying function of z and β_0 is the propagation constant to be determined, equation 2.7 gives us two equations for $F(x,y)$ and $\tilde{A}(z,\omega)$. Using a similar procedure described in section 2.1.2.1, the equation for $F(x,y)$ can be used to obtain an eigenvalue equation that can be solved to give us the propagation constant and subsequently the mode profile. The slowly varying envelope equation obtained for $\tilde{A}(z,\omega)$ is,

$$2\,i\,\beta_0\,\frac{\partial\tilde{A}}{\partial z}+\left(\tilde{\beta}^2-\beta_0^2\right)\tilde{A}=0. \tag{2.10}$$

Subsequently, we introduce a loss as a small perturbation where Δn is a small perturbation which is given by $\Delta n=\dfrac{i\alpha}{2k_0}$ (α is a loss term). The dielectric constant is then approximated by $\varepsilon=\left(n+\Delta n\right)^2\approx n^2+2n\Delta n$. We write also $\tilde{\beta}=\beta(\omega)+\Delta\beta$ where in the first order perturbation theory, $\Delta\beta$ is evaluated and approximated so that $\tilde{\beta}^2-\beta_0^2=2\beta_0(\tilde{\beta}-\beta_0)$ to obtain,

$$\frac{\partial\tilde{A}}{\partial z}=i\left[\beta(\omega)+\Delta\beta-\beta_0\right]\tilde{A}. \tag{2.11}$$

By taking the inverse Fourier transform of equation 2.11 we can revert to the time domain but we need to expand $\beta(\omega)$ in a Taylor series about the carrier frequency ω_0 giving,

$$\beta(\omega)=\beta_0+\beta_1\,(\omega-\omega_0)+\tfrac{1}{2}\,\beta_2\,(\omega-\omega_0)^2+\tfrac{1}{6}\,\beta_3\,(\omega-\omega_0)^3+\ldots \tag{2.12}$$

$$\text{where } \beta_m=\left(\frac{d^m\beta}{d\,\omega^m}\right)_{\omega=\omega_0}\quad(m=0,1,2\ldots). \tag{2.13}$$

Substituting equation (2.13) into (2.11) and replacing $(\omega-\omega_0)$ with the differential operator $i\left(\partial/\partial T\right)$ where $T=\left(t-\dfrac{z}{v_g}\right)=\left(t-\beta_1 z\right)$ is a co-moving frame of reference to the group velocity v_g, we get a one dimensional linear propagation equation given by,

$$\frac{\partial A}{\partial z} = -\frac{i}{2}\beta_2 \frac{\partial^2 A}{\partial T^2} + \frac{1}{6}\beta_3 \frac{\partial^3 A}{\partial T^3} - \frac{\alpha}{2} A. \tag{2.14}$$

From equation 2.14, we can understand the dispersive behaviour of the light within the fibre. In most cases the frequency dependent component β_2, also known as the group velocity dispersion (GVD) parameter is the dominant term. Only when the wavelength of the propagating light is at the zero dispersion wavelength of fibre (i.e. $\beta_2 = 0$) do higher order effects dominate. To understand the effects of dispersion from β_2 and β_3, in the general case equation 2.13 can be solved numerically however, for pulses with Gaussian profiles, this equation can be solved analytically. When an input pulse of arbitrary shape starts to propagate within an optical fibre over a sufficient length, the 2nd order dispersion term (β_2) broadens the pulse symmetrically, resulting in a linear frequency chirp across the pulse, whereas the 3rd order dispersion term (β_3) causes the pulse to broaden asymmetrically and creates a quadratic frequency chirp across the pulse. It is useful to express the extent of broadening in terms of dispersion length of the fibre, $L_D = \frac{T_0^{\,2}}{|\beta_2|}$ where T_0 is the half-width at $1/e$ intensity point. The dispersion length is defined as the length of fibre required to broaden an initially unchirped pulse to twice its original pulse duration.

There are two different possible dispersion regimes in which the pulse propagates within the fibre. This is dependent on the sign of the frequency dependent GVD parameter $\beta_2(\omega_0)$. When $\beta_2 > 0$, the pulse is propagating within the normal dispersion regime and the red wavelength components of the pulse travels faster than the blue wavelength components generating a positive linear frequency chirp. However when $\beta_2 < 0$, it is in the anomalous dispersive regime where the opposite occurs. The GVD parameter is sufficient to describe the amount the entire pulse broadens per unit length of the medium and per unit bandwidth of the pulse.

It is useful for the purpose of this thesis to introduce the group delay dispersion (GDD) parameter. It describes the absolute time delay accumulated per unit frequency difference within the pulse, and is given by GDD = $\beta_2(\omega_0) \times$ length of medium. For ultrashort broad bandwidth pulses, the GDD parameter facilitates the calculation of the dispersion accumulated for each spectral component and can be summed together to obtain the total relative time

delay. This information will be used to design both the stretcher and compressor gratings in chapter 4.

In fibre optics literature, the dispersion parameter D is sometimes used instead of the GVD parameter β_2 and they are related by $D = \frac{d\beta_1}{d\lambda} = -\frac{2\pi c}{\lambda^2}\beta_2$, where c is the speed of light and β_1 and β_2 are defined as before. It is noteworthy to mention that both parameters have opposite signs. For pulsed light centred at a wavelength of 1.06 μm, it starts to disperse or broaden whilst propagating within a standard silica fibre (i.e. Corning Flexcore HI 1060nm fibre) and the dispersion parameter, D is ~-42 ps/km.nm (negative sign indicates normal dispersion where red shifted wavelength light travels faster than blue shifted wavelength) ractable energy is approximately ten t;mes the saturation energy !! ADDIN EN.CITE dwidth of 1 nm, it will broaden by 42 ps after propagating along a 1 km length of fibre. And the dispersion length L_D for a pulse with initial FWHM pulse width τ_0 = 1 ps at 1060 nm propagating in the same Corning Flexcore HI 1060nm fibre would be ~ 110 m. The dispersion is primarily due to material dispersion.

2.2.3 Non-linear polarisation effects

In section 2.1.1, we described that the total induced polarisation on a pulse propagating within an optical fibre consists of both linear and nonlinear contributions. We have introduced in section 2.1.2 a one dimensional propagation equation governing the linear dispersive effects on the pulse. However understanding the nonlinear effects on the pulses is equally important. In this section, we will further describe the nonlinear contribution to the propagating pulse within an optical fibre and introduce a fundamental propagation equation which consists of both linear and nonlinear contributions.

Nonlinear contributions are normally manifest as a small perturbation to the refractive index of the medium (Kerr nonlinearity) induced by the significant peak intensities of the propagating pulse. Polarisation components $\vec{P}_L$ and $\vec{P}_{NL}$, described in section 2.1.1, can be written in a similar form as equation 2.9 giving,

$$\vec{P}_L(\vec{r},t) = \frac{1}{2}\hat{x}\left[P_L(\vec{r},t)\exp(-i\omega_0 t) + c.c.\right] \tag{2.15}$$

$$\vec{P}_{NL}(\vec{r},t) = \frac{1}{2}\hat{x}\,[P_{NL}(\vec{r},t)\exp(-i\omega_0 t) + c.c.] \tag{2.16}$$

We then assume that the nonlinear response is instantaneous (neglecting contributions of molecular vibrations from the Raman effect) and their relationship with the electric field, defined in equations (2.3) and (2.4), can then be written as,

$$\vec{P}_L(\vec{r},t) = \varepsilon_0 \chi^{(1)}.\vec{E}(\vec{r},t'), \tag{2.17}$$

$$\vec{P}_{NL}(\vec{r},t) = \varepsilon_0 \chi^{(3)}.\vdots\vec{E}(\vec{r},t_1)\vec{E}(\vec{r},t_2)\vec{E}(\vec{r},t_3). \tag{2.18}$$

The nonlinear component $\vec{P}_{NL}$ can then be obtained by substituting equation 2.16 into 2.18. We find that $\vec{P}_{NL}(\vec{r},t)$ gives us a term oscillating at ω_0 and another at the third harmonic frequency $3\omega_0$. However unless special phase matching conditions are obtained, else the $3\omega_0$ term remains negligible in optical fibres and is not considered further. We then express $\vec{P}_{NL}(\vec{r},t)$ as,

$$P_{NL}(\vec{r},t) = \varepsilon_0 \varepsilon_{NL} E(\vec{r},t), \tag{2.19}$$

where ε_{NL} is the nonlinear part of the dielectric constant defined as,

$$\varepsilon_{NL} = \frac{3}{4}\chi^{(3)}_{xxxx}\left|E(\vec{r},t)\right|^2. \tag{2.20}$$

Using the definition $\varepsilon = (n + i\alpha/2k_0)^2$, the total dielectric constant $\varepsilon = \varepsilon_L + \varepsilon_{NL}$ can be used to define the refractive index $n(\omega)$ and the absorption coefficient $\alpha(\omega)$. Since $n(\omega)$ is found to be intensity dependent because of ε_{NL}, $n = n_0 + n_2\left|E\right|^2 = n_0 + n_2\frac{p}{A_{eff}}$ where the frequency dependent linear refractive index n_0 ~1.46 at 1 μm wavelength for silica, the Kerr nonlinearity coefficient n_2 is ~ $2.6\times10^{-20} m^2/W$ for silica [25], P represents the peak power of the pulse and A_{eff} is the effective area of the core. A_{eff} depends on fibre parameters such as the core radius and core-cladding index difference and can be describe by

$A_{eff} = \frac{\left(\iint_{-\infty}^{\infty} |F(x,y)|^2 dxdy\right)^2}{\iint_{-\infty}^{\infty} |F(x,y)|^4 dxdy}$ where $F(x,y)$ is the modal distribution of the fundamental mode. A_{eff} is the critical parameter used in defining the nonlinear properties of a fibre and we shall see its effects later. The nonlinear absorption coefficient α_2, governing two-photon absorption, is weak in silica and therefore not considered herein.

Again we introduce Δn as a small perturbation given by $\Delta n = n_2 |E|^2 + \frac{i\alpha}{2k_0}$. Using a similar procedure, as in 2.1.2.2, to describe the linear propagation equation 2.14, we obtain the nonlinear propagation equation for the pulse envelope in the time domain,

$$\frac{\partial A}{\partial z} = -\frac{i}{2}\beta_2 \frac{\partial^2 A}{\partial T^2} + \frac{1}{6}\beta_3 \frac{\partial^3 A}{\partial T^3} - \frac{\alpha}{2}A + i\gamma |A|^2 A \qquad (2.21)$$

where the nonlinearity parameter γ is defined as $\gamma = n_2\omega_0/(cA_{eff})$.

This basic equation is often used in the study of the nonlinear evolution of pulses within an optical fibre and is also called the Nonlinear Schrödinger Equation (NLSE).

2.2.3.1 Self Phase Modulation (SPM)

As the intensity across the pulse envelope changes, the nonlinear response changes across the pulse envelope. This in turn induces an intensity dependent phase change across the pulse which can be written as,

$$\phi_{NL}(z = L, t) = \frac{2\pi L_{eff} n_2 |E(z=0,t)|^2}{\lambda} = \frac{2\pi L_{eff} n_2 P(t)}{\lambda . A_{eff}} \qquad (2.22)$$

where λ is the signal wavelength, $|E|^2$ is the signal intensity, $P(t)$ is the instantaneous peak output power, L_{eff} is the effective length of a passive fibre given by $L_{eff} = 1/\alpha(1 - \exp(-\alpha L))$ and L is the actual physical length of the fibre. Generally L_{eff} is shorter than L because, practically, fibre loss, α is >0. For a fibre amplifier, the effective length can be written as

$L_{eff} = (1/g)[1-\exp(-gL)]$ defined by [26], where g is defined as the signal gain and is assumed to be uniform across the fibre. This time dependent phase change is known as self phase modulation (SPM) and leads to a modification of the pulse spectrum. This modification can be described as an instantaneous optical frequency change $\delta\omega(t) = -\frac{d}{dt}\phi_{NL}(t)$ across the pulse from its central value ω_0 which is often referred to as a frequency chirp. From equation 2.22, we see that SPM is inversely proportional to A_{eff}. The larger the A_{eff}, the higher the output power required to induce a nonlinear phase shift. Using an LMA Yb^{3+} doped fibre amplifier, operating at a central wavelength of 1060 nm, with an effective core area A_{eff} of 400 μm^2 and effective length of 2 m, the output power level required to obtain a phase shift of 2π is ~ 7.1 kW.

Taking an unchirped Gaussian pulse with an intensity envelope defined by $I(T) = I_0 \exp\left(-\frac{T^2}{T_0^2}\right)$, we obtain, from equation 2.22, the nonlinear phase shift, $\phi_{NL}(z = L, T) = \frac{2\pi L_{eff} n_2}{\lambda} . I_0 \exp\left(-\frac{T}{T_0}\right)^2$. The subsequent frequency chirp induced by a Gaussian pulse (i.e. in a passive fibre where $L_{eff} = 1/\alpha(1-\exp(-\alpha L))$) would then be,

$$\delta\omega(T) = -\frac{d}{dT}\left(\frac{2\pi L_{eff} n_2}{\lambda} . I_0 \exp\left(-\frac{T}{T_0}\right)^2\right) = 2L_{eff}\left(\frac{T}{T_0^2}\right).\left(\frac{n_2 \omega_0 I_0}{c}\right)\exp\left(-\frac{T}{T_0}\right)^2 \qquad (2.23)$$

Using equation 2.23 and assuming that n_2 is positive (i.e. $n_2 > 0$), we find with reference to the central frequency ω_0, the leading edge of the pulse is shifted to lower frequencies and the trailing edge is shifted to higher frequencies. Therefore the SPM induces spectral broadening, with new red-shifted wavelength components being generated at the leading edge, and blue-shifted wavelengths at the trailing edge, of the high intensity pulse. Coupled with normal dispersion in a fibre, the pulse broadens temporally more rapidly compared to the situation without SPM. But with anomalous dispersion, pulse compression can occur. Figure 2.7 shows a plot of the variation of ϕ_{NL} and the induced frequency chirp that occurs across a Gaussian

pulse due to SPM at $L_{eff} = \left(\frac{c}{n_2 \omega_0 I_0} \right)$. As ϕ_{NL} is directly proportional to the intensity of the pulse (see equation 2.22), the temporal change in ϕ_{NL} follows the shape of the pulse intensity (as shown in the top diagram of figure 2.7). In the bottom diagram, we can see that the time dependent frequency chirp $\delta\omega(T)$ is negative (red shifted components) at the leading edge of the Gaussian pulse and becomes positive (blue shifted components) towards the trailing edge. We can also see that the chirp is linear and positive across the large central region of the Gaussian pulse.

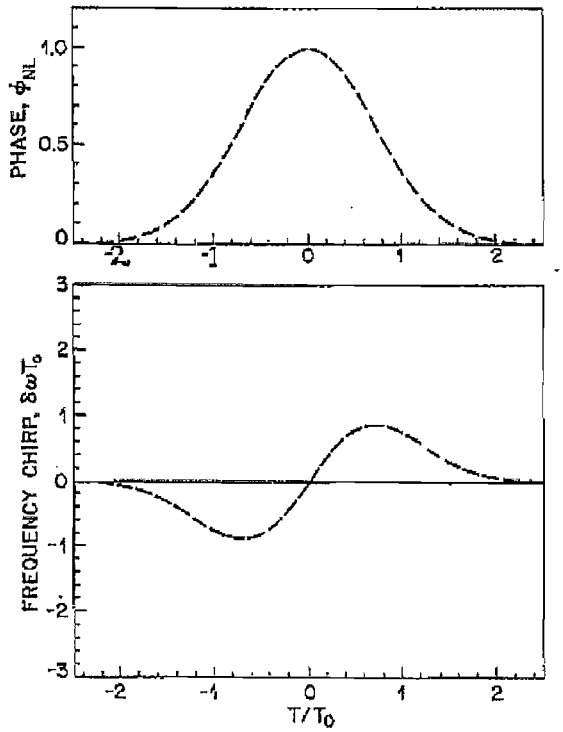

Figure 2.7: Temporal variation of the nonlinear phase shift ϕ_{NL} and frequency chirp $\delta\omega$ induced by SPM for a Gaussian pulse. Figure extracted from [23].

Here we introduce the nonlinear length, $L_{NL} = 1/\gamma P_0 = cA_{eff}/(n_2 \omega_0 I_0)$ where P_0 is the pulse peak power. It gives us an indication of the length scale when the nonlinear effects become important for pulse evolution along the fibre. In section 2.1.2.2 we have introduced the dispersion length L_D of an optical fibre. To compare the contribution from both dispersive and nonlinear effects (i.e. SPM) on the propagating pulse, we introduce another parameter $N^2 = \frac{L_D}{L_{NL}} = \frac{\gamma P_0 T_0^2}{|\beta_2|}$. When $N << 1$, the dispersive effects become dominant and when $N >> 1$, nonlinear effects become dominant. However, when $N = 1$ in an anomalously dispersive regime, the balance between the dispersive and nonlinear effects results in the

formation of optical solitons. For example, taking a pulse having a FWHM pulse width τ =1 ps at λ_0=1.06 μm propagating in an anomalously dispersive fibre (at this wavelength) having A_{eff} = 35 μm^2 (which is an approximate effective area of a SM fibre), the peak power P_0 required for optical solitons to form when $N = 1$ is ~ 2.05W.

2.2.3.2 Cross Phase Modulation (XPM)

The refractive index seen by an optical pulse propagating in an optical fibre depends not only on the intensity of itself (i.e. SPM) but also on the intensity of other co-propagating pulses [27, 28]. The interaction between two co-propagating pulses with differing wavelengths or different orthogonal states of polarisation within a fibre can generate, without any form of energy transfer, variations in the refractive index. This is known as cross phase modulation (XPM), which always occurs together with SPM. It can be shown that, for the same intensity, contribution to the non-linear phase shift by XPM is twice stronger than SPM. The difference between XPM and SPM induced spectral broadening is that XPM induced broadening is dependent on group velocity, υ_g, mismatch and the extent of shift either in the 'red' or 'blue' end of the pulse spectrum depends on the overlapping position of the two pulses.

Effects from interacting pulses of differing polarisation states or central wavelengths are also relevant to this thesis. This is because the effects of the former are relevant to the modelocking operation of the oscillator, developed in chapter 3, and the latter was relevant in both chapter 4 and 6 when the peak intensities of the pulses within the system are high enough to generate Raman scattered pulses which co-propagate together with original signal pulses.

We shall first study the effects of two co-propagating pulses at different frequencies ω_1 and ω_2. Assuming the polarisation of the fields remains constant, a similar approach, as shown in section 2.1.3.1 to define SPM, can be used. We write the rapidly varying part of the electric field as,

$$\vec{E}(\vec{r},t) = \frac{1}{2}\hat{x}[E_1 \exp(-i\omega_1 t) + E_2 \exp(-i\omega_2 t)] + c.c., \tag{2.24}$$

where amplitudes E_1 and E_2 are assumed to be slowly varying functions of time compared to the optical field.

Using equation 2.24 in equation 2.18 we have,

$$\vec{P}_{NL}(\vec{r},t)=\frac{1}{2}\hat{x}[P_{NL}(\omega_1)\exp(-i\omega_1 t)+P_{NL}(\omega_2)\exp(-i\omega_2 t)$$
$$+P_{NL}(2\omega_1-\omega_2)\exp[-i(2\omega_1-\omega_2)t]$$
$$+P_{NL}(2\omega_2-\omega_1)\exp[-i(2\omega_2-\omega_1)t]+c.c., \quad (2.25)$$

where

$$P_{NL}(\omega_1)=\chi_{eff}\left(|E_1|^2+2|E_2|^2\right)E_1, \quad (2.26)$$

$$P_{NL}(\omega_2)=\chi_{eff}\left(|E_2|^2+2|E_1|^2\right)E_2, \quad (2.27)$$

$$P_{NL}(2\omega_1-\omega_2)=\chi_{eff}E_1^{\,2}E_2^{\,*}, \quad (2.28)$$

$$P_{NL}(2\omega_2-\omega_1)=\chi_{eff}E_2^{\,2}E_1^{\,*}, \quad (2.29)$$

with effective nonlinear parameter $\chi_{eff}=\left(\frac{3\varepsilon_0}{4}\right)\chi^{(3)}$ when the three independent components of $\chi^{(3)}$ are assumed to be identical.

It can be seen in equation 2.25, that there are new frequency components oscillating in the induced nonlinear polarisation. These new frequency components are analogous to four-wave mixing. But again, unless phase matching conditions are attained, they are negligible and hence not further considered. We then write $P_{NL}(\omega_j)=\varepsilon_0\varepsilon_j^{NL}E_j$ and subsequently the total induced polarisation,

$$P(\omega_j)=\varepsilon_0\varepsilon_j E_j \quad (2.30)$$

where $\varepsilon_j=\varepsilon_j^L+\varepsilon_j^{NL}=\left(n_j^L+\Delta n_j\right)^2$, (2.31)

where n_j^L is the linear part of the refractive index and Δn_j is the changed index induced by third order nonlinear effects.

Approximating that $n_j^L >> \Delta n_j$ and assuming $n_1^L \approx n_2^L = n$, the nonlinear contribution to the refractive index is then,

$$\Delta n_j \approx \varepsilon_j^{NL} / 2n_j \approx n_2 \left(|E_j|^2 + 2|E_{3-j}|^2 \right), \tag{2.32}$$

where j=1 or 2 and n_2 is the nonlinear parameter given in section 2.1.3.

Modifying equation 2.22, the intensity-dependent nonlinear phase shift induced by two co-propagating optical fields is then written as,

$$\phi_{NL}(z = L, t) = \frac{2\pi L_{eff} n_2}{\lambda} \left(|E_j|^2 + 2|E_{3-j}|^2 \right), \qquad \text{where j=1 or 2.} \tag{2.33}$$

The first term on the right hand side (R.H.S) is attributed to SPM effects and the second term results from the interaction of another co-propagating pulse and is responsible for XPM. The factor of 2 shows that the effect of XPM is twice as strong as SPM.

We shall now describe the next situation where XPM effects are encountered when the two co-propagating fields have a similar central frequency but are propagating on a different orthogonal polarisation axis (i.e. x and y). Re-writing equation 2.24 for two different polarisation axes we have,

$$\vec{E}(\vec{r}, t) = \frac{1}{2}[\hat{x}E_x + \hat{y}E_y]\exp(-i\omega_0 t) + c.c., \tag{2.34}$$

where $\hat{x}$ and $\hat{y}$ are the polarisation unit vector for light propagating on the x and y axes respectively and E_x and E_y are their corresponding two slowly varying functions of time.

Ignoring again the third harmonic components, the nonlinear part of the induced polarisation can then be re-written as $\vec{P}_{NL}(\vec{r}, t) = \frac{1}{2}[\hat{x}\,P_x + \hat{y}\,P_y]\exp(-i\omega_0 t) + c.c.$. Making the same assumptions as before, that the three independent components of $\chi^{(3)}$ are assumed to be identical, and using equation 2.24, we obtain

$$P_x = \frac{3\varepsilon_0}{4}\chi^{(3)}_{xxxx}\left[\left(|E_x|^2 + \frac{2}{3}|E_y|^2 \right)E_x + \frac{1}{3}\left(E_x^* E_y\right)E_y \right], \tag{2.35}$$

$$P_y = \frac{3\varepsilon_0}{4}\chi^{(3)}_{xxxx}\left[\left(\left|E_y\right|^2 + \frac{2}{3}\left|E_x\right|^2\right)E_y + \frac{1}{3}\left(E_y^* E_x\right)E_x\right]. \tag{2.36}$$

Assuming a fibre with strong birefringence (i.e. $L>>L_B$) then, due to the large phase mismatch, the third term on the R.H.S is considered negligible. Using equation 2.30 and approximating that equation 2.31, $\varepsilon_j = \varepsilon_j^L + \varepsilon_j^{NL} = \left(n_j^L + \Delta n_j\right)^2 \approx \left(n_j^L\right)^2 + 2n_j^L \Delta n_j$, we obtain

$$\Delta n_x = n_2\left[\,|E_x|^2 + \frac{2}{3}|E_y|^2\,\right], \tag{2.37}$$

$$\Delta n_y = n_2\left[\,|E_y|^2 + \frac{2}{3}|E_x|^2\,\right]. \tag{2.38}$$

again assuming $n_1^L \approx n_2^L = n$ and representing $n_2 = \frac{1}{2n}\mathrm{Re}\left\{\varepsilon^{NL}\right\} \approx \frac{3}{8n}\mathrm{Re}\left\{\chi^{(3)}_{xxxx}\right\}$, where we have neglected the nonlinear loss term.

In equations 2.37 and 2.38, the first term on the R.H.S is responsible for SPM while the second term is responsible for XPM but their effects, with a factor of $\frac{2}{3}$, are somewhat lower compared to the earlier described XPM effects from co-propagating pulses with differing central frequencies.

Equations 2.32, 2.37 and 2.38 reveal that the refractive index, seen by light propagating within an optical fibre, depends not only on its intensity, but also on the intensity of other co-propagating fields. Nonlinear effects that arise due to XPM induced coupling between optical beams can be used in a number of applications. They can be used for pulse compression, optical switching applications [29] and even as fast saturable absorbers for modelocking [30] which was used for our oscillator as presented in chapter 3.

2.2.3.3 Stimulated Raman Scattering (SRS)

The effects of stimulated inelastic scattering are important for this thesis. Optimal performances of some of the systems in this thesis were mainly limited by such effects. For example, the highest pulse energies achievable from the CPA system, described in chapter 4,

and the amplifier cascade with a directly modulated diode seed source, described in chapter 6, were limited by the onset of one such effect; Stimulated Raman Scattering (SRS).

The Raman Effect was discovered by C.V. Raman [31]. In general, spontaneous Raman scattering occurs when a fraction of a beam of light, in any molecular medium (solid, liquid or gas), is scattered to new frequencies upon reaching threshold. Scattered light having lower frequencies is called the Stokes wave and light having higher frequencies is called anti-Stokes wave. The scattering is a result of the interaction between light and molecular vibrations within the material. The magnitude of the frequency shift depends on the frequency of the molecular vibrations of the medium. Hence the Raman effect can be regarded as scattering from optical phonons. When the intensity of the incident beam of light (i.e. pump light) is high enough, the spontaneous Raman scattering process becomes highly efficient and the Stokes wave grows rapidly such that most of the pump light is transferred to it. This scattering process is called Stimulated Raman Scattering (SRS). The SRS process results in a Stokes wave generated at the longer wavelengths.

An important quantity for describing SRS is the Raman gain spectrum $g_R(\Omega)$, where Ω represents the frequency difference between the Stokes wave and the pump light. The measured Raman gain spectrum for fused silica at a pump light wavelength of 1.0 μm is shown in figure 2.8 (a) [32]. It has a bandwidth of $\sim 30\,\mathrm{THz}$ which is quite broad compared to Stimulated Brillouin Scattering (discussed in the next section). Though $g_R(\Omega)$ depends on the composition of the fibre core and can vary significantly with dopants, figure 2.8 (a) presents a reasonable estimate for the fibres used in this thesis. The peak of the Raman gain from figure 2.8 (a) is found to be $g_R \sim 1\times10^{-13}\,m/W$ and occurs at a Stokes shift of Ω_{peak} ~13.2 THz which corresponds to a wavelength shift of ~ 50 nm at the pump wavelength of 1.06 μm.

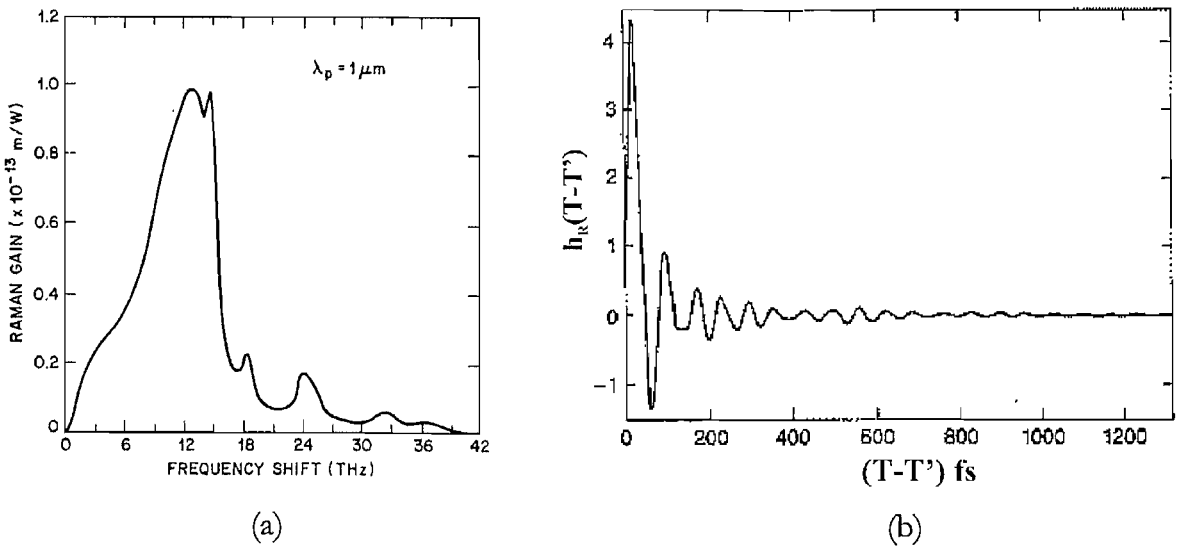

Figure 2.8: (a) Measured Raman gain spectrum for fused silica with pump light at 1.0 μm and (b) delayed time response $h_R(T)$ for silica (Figures extracted from [32]).

The understanding and calculation of the threshold power for the onset of SRS is vital for the work presented in this thesis as it gives us an estimate of the capability of our system to reach the maximum output pulse energies. In [23], Agrawal presented calculations for the critical threshold power to reach SRS for a medium without gain (passive fibre). However the systems presented in this thesis consist mainly of media having gain (actively doped fibres), therefore it is more useful to describe the calculation for the critical power to reach SRS in the presence of gain. These calculations have been adapted from both [23] and Dr Price's (from our group) thesis [33]. The nonlinear interaction between the pump and Stokes waves, in the presence of gain, can be written as,

$$\frac{dI_S}{dz} = g_R I_P I_S + g_S I_S, \tag{2.39}$$

$$\frac{dI_p}{dz} = -\frac{\omega_p}{\omega_s} g_R I_P I_S + g_p I_p, \tag{2.40}$$

where g_S and g_p are the amplifier gain for the Stokes signal and the pump (or input seed) wavelength, g_R is the Raman gain coefficient and I_S and I_P represent the intensities of the Stokes wave and pump respectively. Assuming the fibre is fully bleached, we can neglect the term representing pump depletion due to the Stokes wave in equation 2.40, we get an equation which is readily solvable,

$$\frac{dI_p}{dz} = g_p I_p, \tag{2.41}$$

A solution for the propagating seed pulse can then be written as,

$$I_P(z) = I_P(L)\exp\big(-g_P(L-z)\big), \tag{2.42}$$

where $I_P(L)$ is the output intensity of the seed pulse after propagating through a fibre of length L. Substituting equation 2.42 into 2.39, we obtain

$$\frac{dI_S}{dz} = g_R I_P(L)\exp\big(-g_P(L-z)\big)I_S + g_S I_S, \tag{2.43}$$

We then assume that the gain medium has a broad uniform gain over the seed signal and Stokes wavelengths, $g_S \approx g_p = g$, to obtain a solution for $I_S(z)$ from equation 2.43,

$$I_S(z) = I_S(0)\exp\big(g_R I_P(L)\ z_{eff} + gz\big), \tag{2.44}$$

where $z_{eff} = (1/g)[1-\exp(-gz)]$ defined by [26]. In practise the SRS builds up from quantum noise through spontaneous Raman scattering throughout the fibre length. Smith [34] has shown that this process is equivalent to injecting one fictitious photon per mode at the fibre input. Therefore the Stokes power can be calculated by integrating over the wavelength range of the Raman gain spectrum,

$$P_S(z) = \int_{-\infty}^{\infty} \hbar\omega \exp\big(g_R(\Omega) I_P(L)\ z_{eff} + g\ z\big) d\omega. \tag{2.45}$$

where $\hbar\omega$ is the energy of the photon at frequency ω and $\Omega = \omega_p - \omega$ is the frequency difference between the seed pulse and Stokes wave within the Raman gain spectrum.

Assuming that, to a good approximation, the Raman gain spectrum takes on a Lorentzian shape, the critical or threshold pump power P_0^{cr} (we normally take the peak power of the

pulse) for the Stokes power to become equal to the amplified seed power at the fibre output [34] is given by,

$$\left(g_R P_0^{cr} z_{eff}\right)/A_{eff} \approx 16. \tag{2.46}$$

where A_{eff} is the effective area of the fibre mode.

We can see from equation 2.46 that SRS is proportional to effective fibre length and inversely proportional to the mode field or effective area of the light propagating in the fibre. Hence larger mode field diameter and reduced fibre length reduces non-linearity.

Core diameter (μm)	**Example 1 τ =813 ps and L= 9 m Max. Pulse energy (μJ)**	**Example 2 τ =40 ns and L= 6 m Max. Pulse energy (μJ)**
5	1.3	97
20	21	1559
30	47.5	3057
40	84.5	6235

Table 2.2: Examples for SRS threshold pulse energy using output pulse parameters from real experiments in this thesis.

Let me now describe two real examples from experiments carried out in this thesis to understand the limits imposed by SRS on their maximum performance. To simplify this example, we assume that we require a gain of 20 dB from the active fibre. Two different experiments were chosen. The first will be the work described in chapter 4, which is the chirped pulse amplification (CPA) work where 813 ps pulses were amplified in a final amplifier length of 9 m. The second example is the work presented in chapter 5 where a seed pulse width of 40 ns was amplified in a amplifier length of 6 m. Table 2.2 will illustrate the maximum achievable pulse energy before the onset of SRS for these two examples. Final amplifier core dimensions of 5, 20, 30 and 40 μm are evaluated. Results from this example will help us understand the limits imposed by SRS for these two experiments for different final amplifier core sizes. The SRS threshold pulse energies shown in table 2.2 present the best possible scenario for output pulse energy that the two different systems could achieve. For our CPA

system (see chapter 4), the information presented in table 2.2 was a fair reflection on the maximum pulse energy achievable before SRS. However lower maximum output pulse energies before SRS were obtained from the 40 ns amplification system (see chapter 5) due to a few other reasons which I discuss in detail later.

The differing central wavelengths of the pump and Stokes pulse means that they travel at different group velocities. Therefore after propagating over a certain fibre length, the two pulses may walk off from each other and interact no more. This may affect the calculation of the Raman threshold power defined in equation 2.46. To estimate the length scales required for this to occur, we introduce the walk off length which is given by [35], to be $L_W = T/\left| v_{g\_P}^{-1} - v_{g\_S}^{-1} \right| = T/\left| \beta_{1\_p} - \beta_{1\_s} \right| = T/\left| (\omega_p - \omega_s) \times \beta_2 \right|$ where T is the duration of the pump pulse, β_2 is the dispersion parameter for silica fibres at ~ 1.0 μm and $\left|\omega_p - \omega_s\right| = 2\pi \times 13.2$ THz at the Raman gain peak. The estimated length scale over which both pulses continue to interact, given by [35], is ~ $3L_W$. Taking the amplifier cascade amplifying the pulses from a directly modulated laser diode in chapter 9 as an example, the amplified pulses were ~ 1 ns (after gain saturation effects). This corresponds to an interaction length of $3L_W$ ~ 1.4 km which is much longer than the ~ 6m length scales used in our experiments. Even in the ultrashort pulse amplification experiments carried out in chapter 4, the propagating pulses within the system are ~ 4 ps long. This corresponds to an estimated interaction length of ~ 6 m. But the amplifier lengths used in the final amplification stage are less than 6 m (i.e. ~4 m). Therefore walk off between the two pulses does not occur.

Before the onset of SRS, we will have already encountered the effects of SPM. The effects of SPM will generate additional spectral components at the shorter and longer wavelengths. This is normally not detrimental to applications where pulse compression is not carried out at the end (with the exception of self similar pulse amplification described in chapter 4). However, the additional spectral components generated due to non-linear frequency chirping in the pulse will result in a broader compressed pulse (however the opposite is true in special cases i.e. Parabolic pulse regime (see section 4.3)) and reduced peak to pedestal contrast ratio when the stretched pulses in a CPA system are linearly re-compressed at the end [36]. Although this pedestal can be suppressed, and non-linear distortion filtered off by spectral gain windowing [37], to obtain near Gaussian re-compressed pulses, the complexity involved can be avoided by operating the amplifier fibre far from saturation to prevent significant SPM from occurring. This can be achieved by using amplifier fibres with larger core dimensions (i.e. 20 -

40 μm core diameters). In Chapter 4, we will demonstrate power amplification with a 30 μm core diameter fibre to achieve high energy re-compressed sub-picosecond pulses.

2.2.3.4 Stimulated Brillouin Scattering (SBS)

Unlike SRS, acoustic phonons rather than optical phonons participate in SBS. SBS can be described as a nonlinear interaction between an incident wave (the pump), a scattered wave (Stokes field) and a phonon (an acoustic wave). An explanation of SBS is shown in figure 2.9 (a). As shown in this figure, the pump field generates an acoustic wave through the process of electrostriction. Electrostriction is the compression of a material in the presence of an electric field. This acoustic wave in turn modulates the refractive index of the medium and creates an index grating which scatters the pump light through Bragg diffraction. As shown graphically in figure 2.9 (b), because of the Doppler shift associated with the grating moving at velocity v_A, this scattered light is downshifted in frequency (longer wavelength Stokes wave). By conservation of both energy and momentum in each scattering event, the relationship between the frequencies and the wave vectors can be written as,

$$\Omega = \omega_p - \omega_s, \tag{2.47}$$

$$\vec{\kappa}_A = \vec{\kappa}_p - \vec{\kappa}_s, \tag{2.48}$$

where Ω is the downshifted frequency difference between the Stokes wave ω_s and pump light ω_p and $\vec{\kappa}_A$, $\vec{\kappa}_p$ and $\vec{\kappa}_s$ are the wave vectors for the acoustic phonon, pump and Stokes wave respectively. Assuming that the frequency shift is small (which is reasonable because acoustic phonons participate in SBS), we obtain $|\kappa_p| \approx |\kappa_s|$ and, by observing figure 2.9 (a), we can write the standard dispersion relation between the frequency difference Ω and the wave vector of the acoustic phonon,

$$\Omega = v_A|\kappa_A| \approx 2v_A|\kappa_p|\sin(\theta/2), \tag{2.49}$$

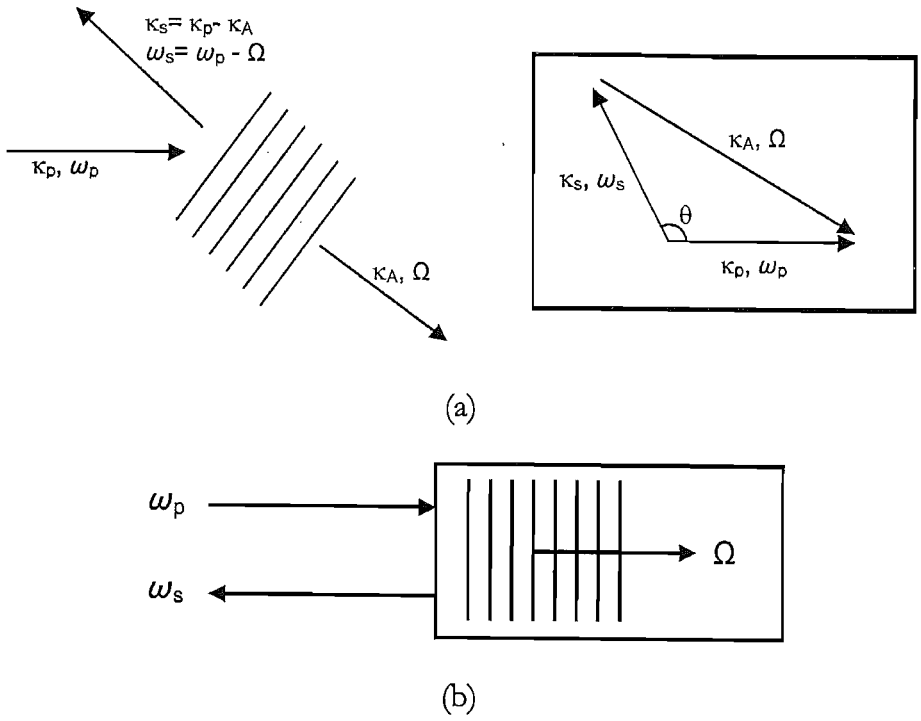

Figure 2.9: (a) Conservation of momentum for Stokes Brillouin scattering with $|\kappa_p| \approx |\kappa_s|$ and (b) Graphic representation of SBS (taken from [38]).

From equation 2.49, we find that in SBS the frequency shift depends on the scattering angle θ. In optical fibres, the scattered Stokes wave can propagate in two directions, forward and backwards. However we find that Ω is maximum in the backward scattered direction ($\theta = \pi$) and disappears in the forward direction ($\theta = 0$). Using $\nu = \Omega / 2\pi$, the maximum Brillouin shift in equation 2.49 becomes $\nu_B = \Omega_B / 2\pi = 2n\nu_A / \lambda_p$ where, to be precise, n is normally used as the modal index. It can be seen that for a given wavelength, the Brillouin frequency shift is a function of only the acoustic velocity and fibre modal index. Therefore at pump wavelength λ_p = 1.07 μm, $\nu_A = 5.96\ km/s$ and $n = 1.45$, the calculated Stokes shift ν_B is ~ 11.15 GHz. Because of the guided nature of the acoustic wave, sometimes spontaneous Brillouin scattering can occur in the forward direction but this is generally weak and is not further considered.

Similar to SRS, SBS can be characterised by the Brillouin gain spectrum $g_B(\Omega)$. But, compared to SRS, the spectral width $\Delta\nu_B$ of the Brillouin gain spectrum is very small, ~10 MHz, peaking at $\Omega = \Omega_B$. This is because it is related to the damping time of the acoustic wave or the phonon lifetime T_B. If we assume that the acoustic wave decays exponentially as $\exp(-\Gamma_B t)$, the Brillouin gain would have a Lorentzian profile given by,

$$g_B(\Omega) = g_B(\Omega_B)\frac{(\Gamma_B/2)^2}{(\Omega-\Omega_B)^2+(\Gamma_B/2)^2}, \tag{2.50}$$

where the peak Brillouin-gain coefficient is given by,

$$g_B(\Omega_B) = \frac{2\pi^2 n^7 p_{12}^2}{c\lambda_p^2 \rho_0 \nu_A \Gamma_B}, \tag{2.51}$$

where p_{12} is the longitudinal elasto-optic coefficient, ρ_0 is the material density, c is the speed of light and $\Gamma_B = 2\pi.\Delta\nu_B = 1/T_B$ where $\Delta\nu_B$ is the 3 dB bandwidth of the Brillouin gain spectrum and $T_B \sim 10$ ns. The typical peak value of $g_B(\Omega_B)$ for fused silica is ~ 5×10^{-11} m/W. However, since the spectral width of Brillouin gain is very narrow (i.e. $\Delta\nu_B$ ~ 10 MHz), this requires that the linewidth $\Delta\nu_p$ of the pump light be narrow. The peak gain is shown [39] to decrease by a factor of $\Delta\nu_B/\Delta\nu_p$. Therefore for efficient SBS to occur, the entire Stokes shift between the pump and Stokes wave should lie within the Brillouin gain spectrum. Therefore for most of the pulses, described within this thesis where their linewidths $\Delta\nu_p > 0.8$ THz (i.e. $\Delta\lambda_p > 3$ nm), the peak Brillouin gain coefficient decreases by a factor ~10^5.

We can use a similar procedure, to that we used to define the threshold power for SRS, to describe the critical threshold power P_0^{cr} for SBS to occur. The critical threshold power for SBS is defined as the power which, when exceeded, results in more than half of the power from the pump light transferring to the Stokes wave. We first define two coupled equations similar to equations 2.39 and 2.40. The differences are that the sign of dI_s/dz is changed to account for the counter propagating Stokes wave, with respect to the pump wave, and also instead of having gain for the pump and Stokes wave, we account for losses (since passive fibres are used in this example) α_p and α_s respectively. One other assumption is made to simplify matters. Since the Brillouin shift is relatively small, we assume that $\omega_p \approx \omega_s$ and therefore we assume a loss $\alpha_p \approx \alpha_s \approx \alpha$. We then write the two equations for Brilluoin scattering as,

$$\frac{dI_S}{dz} = -g_B I_P I_S + \alpha I_S, \tag{2.52}$$

$$\frac{dI_p}{dz} = -g_B I_P I_S - \alpha I_p, \tag{2.53}$$

The first terms on the R.H.S of equation 2.52 and 2.53 represent the Brillouin gain and pump depletion respectively. The second term in both equations represents the corresponding propagation losses for the pump and Stokes wave. Equation 2.52 and 2.53 assume also that linear polarisation on the same orthogonal axis, for both the counter-propagating pump and Stokes wave, is maintained along the fibre. As before, we neglect the pump depletion term in equation 2.53. Using the solution $I_P(z) = I_P(0)\exp(-\alpha z)$, where $I_P(0)$ is the intensity of the input pump light in equation 2.52, and integrating it over the entire fibre length, L, shows that the Brillouin scattered Stokes intensity grows exponentially in the backward direction:

$$I_s(0) = I_s(L)\exp\left[\left(g_B P_0 z_{eff} / A_{eff}\right) - \alpha L\right], \tag{2.54}$$

where the effective interaction length, $z_{eff} = [1 - \exp(-\alpha L)]/\alpha$, input pump power, $P_0 = I_p(0)A_{eff}$ and A_{eff} is the effective mode area of the fibre. Equation 2.54 demonstrates how a Stokes wave at z=L can grow from noise in a backward direction because of Brillouin amplification due to SBS. Using the same approach that we had for SRS in the previous section, we obtained the definition of the critical threshold power for SBS to be,

$$g_B P_0^{cr} z_{eff} / A_{eff} \approx 21. \tag{2.55}$$

This threshold power described by equation 2.55 is only an approximation as it is dependent on many other parameters. For example, the threshold can increase by 50% if the state of polarisation of the pump field is scrambled along the fibre. Variations in fibre dopants and inhomogeneties along the fibre also affect the effective Brillouin gain in optical fibres. Changes in the doping level along the radial direction of the fibre can lead to slight changes in the acoustic velocity v_A. Therefore the SBS threshold is, to some extent, dependent on the various dopants used in the fibre. The SBS threshold can also increase due to longitudinal variations in the Brillouin shift Ω_B along the fibre length due to structural variations. This feature is advantageous as it can be used to intentionally suppress SBS by varying the core sizes along the fibre.

For efficient SBS to occur, the linewidth of the pump light needs to be narrower than $\Delta\nu_B \sim$ 10 MHz and this is usually not so. However it sets a limiting factor for narrow linewidth fibre laser systems especially those designed to have single polarisation. Most of the

systems presented in this thesis do not have such narrow seed signal linewidths and therefore SBS is not likely to occur. However I have included the SBS section within the nonlinear section for the sake of completeness. In Chapter 6, when pulses having high peak intensities and relatively narrow ~ 3 nm linewidths were produced, the onset of SBS was checked by taking the backward propagating spectra with respect to the input signal direction.

2.2.3.5 Higher order nonlinear effects on propagation

Although the propagation NLSE, defined in equation 2.21, is sufficient to explain many nonlinear effects occurring to the pulse, it is still incomplete. For example, it does not include the effects of stimulated inelastic scattering such as SRS and SBS. As we have described in the earlier sections, at sufficient peak intensities above threshold, SRS and SBS can result in a new pulse shifted at a longer wavelength propagating either in the same or opposite direction. The interaction between the two pulses through Raman or Brillouin gain and XPM can modify the properties of the propagating pulse. In this section, we will modify equation 2.21 so that it includes the contributions from these higher order nonlinear effects.

The most important limitation turns out to be the neglection of SRS. Here we consider two cases with different pulse properties. We first consider the case for ultrashort pulses with durations < 1 ps and broad spectral bandwidths > 0.5 THz, besides the excitation of another longer wavelength Stokes pulse through the effects of SRS, the Raman gain can amplify the low-frequency components (red shifted wavelength) of a pulse by transferring energy from the high frequency (blue shifted wavelength) components of the same pulse. The result is that the pulse spectrum shifts toward the red wavelength side as it continues to propagate down the fibre. This phenomenon is called intra-pulse Raman scattering and is attributed to the delayed nature of the Raman (vibrational) response shown in figure 2.1 (b). The NLSE then needs to be modified to include this temporal Raman response and is given in [23],

$$\frac{\partial A}{\partial z} = -\frac{\alpha}{2}A - \frac{i}{2}\beta_2\frac{\partial^2 A}{\partial T^2} + \frac{1}{6}\beta_3\frac{\partial^3 A}{\partial T^3} + i\gamma\left(1+\frac{i}{\omega_0}\frac{\partial}{\partial T}\right) \times\left[A(z,T)\int_{-\infty}^{+T} R(T')\left|A(z,T-T')\right|^2 dT'\right]. \tag{2.56}$$

where γ is the nonlinearity parameter described in equation 2.21. The time derivative (denoted by T') on the R.H.S of equation 2.56 is the result of the remaining first order time derivative

from the slowly varying envelope of nonlinear polarisation $\vec{P}_{NL}$ when equation 2.16 is used in equation 2.5. It is responsible for self-steepening and shock formation at the pulse edge and also includes the nonlinear energy loss due to intra-pulse SRS. The response function $R(T) = (1 - f_R)\delta(T) + f_R h_R(T)$ includes both the instantaneous electronic and delayed vibrational (Raman) contributions. $f_R = 0.18$ represents the fractional contribution of the delayed Raman response to $\vec{P}_{NL}$ and $h_R(T)$ (see figure 2.8 (b)), is the normalised Raman response function for silica which was obtained from the experimentally measured Raman gain spectrum (see figure 2.8(a)). It is normalised such that $\int_{-\infty}^{+\infty} h_R(T')\,dT' = 1$. Equation 2.56 together with $R(T)$ predicts the evolution of these ultrashort pulses (τ_p <1ps) in silica optical fibre and has been verified by the conservation of photon number during pulse evolution assuming that fibre losses α are ignored.

However when the duration of the pulses are $\tau_p >$ 1 ps and their spectral widths are narrow or moderately wide (i.e. $\Delta\nu_{3dB} < 0.5$ THz), the nonlinear response can still be assumed to be instantaneous. This is because when we observe the time scale of the Raman response function, $h_R(T)$ in figure 2.8 (b), the > 1 ps duration of these pulses is comparatively much longer. Hence $R(T)$ for such pulses can be replaced by the delta function $\delta(T)$ and the NLSE, defined in equation 2.21, can still be applicable with slight modification due to the effects of SRS. An intensity dependent loss term needs to be added to the NLSE, defined in equation 2.21, to account for the transfer of power from the pump pulse to the Raman generated Stokes pulse shifted to a longer wavelength defined by the Raman peak gain (i.e. Ω_R ~13.2 THz). Another term may also be included to account for the contribution of XPM due to the interaction between the pump pulse and Stokes pulse.

2.2.4 Other nonlinear effects in fibres

In the last few sections, we have been describing the nonlinear effects of SPM and XPM which resulted in an intensity dependent phase change within the propagating pulse. We have also described the effects of stimulated inelastic scattering i.e. SRS and SBS which give rise to the exchange of energy between the pump pulse and the nonlinear medium, generating new frequencies (i.e. Stokes or anti-Stokes wave).

In this section, I will briefly describe some of the other nonlinear effects associated with the third-order susceptibility $\chi^{(3)}$. Nonlinear effects such as self-focussing and parametric processes such as third-harmonic generation and four-wave mixing are described.

2.2.4.1 Self-focusing

Earlier in section 2.2.3, we describe that there is an intensity dependent change in the refractive index that the propagating light experiences in the medium and it was defined as $n = n_0 + n_2|E|^2 = n_0 + n_2 \frac{P}{A_{eff}}$. This is known as the Kerr effect. The Kerr effect can be also written as $n = n_0 + n_2 I(r,t)$ where I is the intensity of the light with its spatial and temporal coordinates r and t respectively. The temporal part I(t) gives rise to SPM and it is the spatial part I(r) which gives rise to self-focussing.

In self-focusing, due to a Kerr lens, the beam diameter of the intense optical pulse propagating in a nonlinear medium is decreased compared to that of a weak pulse. This decrease in beam diameter increases the power per unit area which further increases the strength of the Kerr lens and leads to very high optical intensities being formed. This may result in optical damage to the medium. However, the reduction in beam size for high intensities can be used for Kerr lens mode-locking of a laser. This is a spatial process where, for example, mechanical apertures are used within the cavity to promote lower losses through the aperture when the beam diameter is reduced for higher intensity light.

2.2.4.2 Third-harmonic generation and, four-wave mixing (FWM)

Unlike stimulated inelastic scattering effects, for nonlinear parametric processes, optical fibres play a passive role except for mediating interaction between several optical waves. These parametric processes are so called because in these processes, modulation of the medium parameters (i.e. refractive index) is involved. These parametric processes can be classified into second or third order processes depending on whether the second-order $\chi^{(2)}$ or third-order $\chi^{(3)}$ susceptibility is responsible for them. However, as we have mentioned in section 2.2.1, the second-order susceptibility vanishes for silica optical fibres. Thus second-order parametric processes such as second-harmonic generation and sum-frequency generation should not

manifest. But due to quadrupole and magnetic-dipole effects, these processes do occur but generally have very low conversion efficiency.

The third-order parametric processes such as third-harmonic generation and FWM involve nonlinear interaction between four optical waves. FWM can be understood better by considering the third-order polarisation term in equation 2.2 which is given by,

$$P_{NL} = \varepsilon_0 \chi^{(3)} \vdots EEE \tag{2.57}$$

where E is the electric field, P_{NL} is the induced nonlinear polarisation and ε_0 is the vacuum permittivity.

Let us consider four optical waves oscillating at frequencies ω_1, ω_2, ω_3 and ω_4 and linearly polarised along the same axis x. Therefore the total electric field can be written as,

$$E = \frac{1}{2}\hat{x}\sum_{j=1}^{4} E_j \exp\left[i\left(k_j z - \omega_j t\right)\right] + c.c. \tag{2.58}$$

where the propagation constant $k_j = n_j \omega_j / c$, n_j is the refractive index and all four waves are propagating in the same direction.

Substituting equation 2.58 into 2.57 and expressing P_{NL} in a similar form to equation 2.58, we find that P_j (j= 1 to 4) has many terms involving the products of the three electric fields. Let us express P_4 in equation 2.59 below,

$$P_4 = \frac{3\varepsilon_0}{4}\chi^{(3)}_{xxxx}\left[\left|E_4\right|^2 E_4 + 2\left(\left|E_1\right|^2 + \left|E_2\right|^2 + \left|E_3\right|^2\right)E_4 + 2E_1E_2E_3\exp\left(i\theta_+\right) + \right.$$
$$\left. 2E_1E_2E_3^*\exp\left(i\theta_-\right) + \ldots\right] \tag{2.59}$$

where θ_+ and θ_- are,

$\theta_+ = \left(k_1 + k_2 + k_3 - k_4\right)z - \left(\omega_1 + \omega_2 + \omega_3 - \omega_4\right)t$ and

$\theta_- = \left(k_1 + k_2 - k_3 - k_4\right)z - \left(\omega_1 + \omega_2 - \omega_3 - \omega_4\right)t$

The first four terms containing E_4 in equation 2.59 are responsible for SPM and XPM effects and the rest of the remaining terms result from FWM. The effectiveness of these terms producing a parametric coupling depends on the phase mismatch between E_4 and P_4 which is governed by θ_+, θ_- or a similar quantity. Therefore efficient FWM occurs only if the phase mismatch nearly disappears. For this to happen, matching of the frequencies and the wave vectors are required. The requirement for wave vectors to be matched is known as phase matching.

FWM occurs when photons from one or more waves are annihilated and new photons are created at different frequencies such that the net energy and momentum are conserved during the parametric interaction. The θ_+ term in equation 2.59 corresponds to the case when energy is transferred from three photons to a single photon with a frequency of $\omega_4 = \omega_1 + \omega_2 + \omega_3$. This term is responsible for third harmonic generation when $\omega_1 = \omega_2 = \omega_3$ or frequency conversion when $\omega_1 = \omega_2 \neq \omega_3$. However the phase matching conditions for such processes to occur with high efficiencies are difficult to satisfy within optical fibres.

The θ_- term in equation 2.59 corresponds to the case when two photons ω_3 and ω_4 are simultaneously created when another two photons ω_1 and ω_2 are annihilated and the frequencies are related as $\omega_3 + \omega_4 = \omega_1 + \omega_2$. The phase matching condition required to satisfy this phenomenon is,

$$\Delta k = k_3 + k_4 - k_1 - k_2 = \left(n_3\omega_3 + n_4\omega_4 - n_1\omega_1 - n_2\omega_2\right)/c = 0 \tag{2.60}$$

In the partially degenerate case where $\omega_1 = \omega_2$, which is very relevant for optical fibres, it is relatively easy to satisfy $\Delta k = 0$. Here a strong pump wave with a frequency of ω_1 produces two sidebands which are symmetrical at frequencies ω_3 and ω_4 with a frequency shift of

$$\Omega_s = \omega_1 - \omega_3 = \omega_4 - \omega_1 \tag{2.61}$$

where we assume $\omega_3 < \omega_4$. The low frequency sideband ω_3 is referred to as the Stokes band and the high frequency sideband ω_4 is referred to as the anti-Stokes band in direct analogy to SRS.

2.3 Energy storage constraints

Having considered nonlinear effects in fibre, we now turn our attention to aspects of fibre performance that relate to the range of A_{eff} that can be used in fibre and how this impacts on energy storage and damage.

Previously, conventional single mode doped fibre were designed for tight mode confinement to achieve high gain efficiency for relatively small energy storage within the fibre [40] which is required for telecoms. This design leads to high gains resulting in stored energy being rapidly lost as ASE or even resulting in spurious lasing with increasing pump power. Therefore Q-switched output pulse energies were limited to 10 μJ [41] and 100 μJ [42, 43] for Er^{3+} and Yb^{3+} doped fibres respectively. Similarly, the amplification of pulses in fibres is limited by the maximum extractable energy. The maximum extractable energy from a fibre is determined by the saturation energy E_{sat} of the fibre which is given by $E_{sat} = \frac{A.h\upsilon_s}{(\sigma_e + \sigma_a).\Gamma_s}$ where A is the doped area, $h\upsilon_s$ is the energy of the signal photon, σ_e and σ_a is the emission and absorption cross sectional area at the emission wavelength and Γ_s is the signal overlap with the doped area [43]. Consequently, the maximum extractable energy is given by $E_{ext} = E_{sat}.\ln(G_s)$ where G_s is the small signal gain of the fibre [44, 45]. However as an estimate, and general rule of thumb, the maximum extractable energy is approximately ten times the saturation energy [43]. Using a step index fibre with an NA ~ 0.06 and assuming that the entire core is uniformly doped with a signal mode overlap factor Γ_s=0.75 [43], the maximum extractable energy for different core diameters are calculated and shown in figure 2.10. Experimental fluorescence measurements of an aluminium silicate Yb^{3+} doped fibre was later carried out by D.B.S. Soh from the ORC and the respective emission and absorption cross sectional areas, σ_e and σ_a, were found to be 4.52 x 10^{-25} m^2 and 4.97 x 10^{-27} m^2. We calculate, for a 30 μm core diameter fibre (assuming $A_{eff} = 706\mu m^2$) and Γ_s~0.75, the saturation energy, E_{sat}, for a 1080 nm signal would be ~ 0.38 mJ. The corresponding approximate extractable energy would be $10 \times E_{sat}$ ~ 3.8 mJ (see figure 2.10).

Another limiting factor on the maximum pulse energy extractable for a particular pulse duration is the damage threshold of the air/silica interface at the fibre ends, which can be extrapolated from the data presented by B.C. Stuart *et al.* [46] using the empirical formula:.

$$E_{damagethreshold} = 40(\Delta\tau_p)^{0.5} \text{ J/cm}^2 \qquad (2.62)$$

where $\Delta\tau_p$ is the FWHM pulse width in nanoseconds. The energy of 40 ns pulses required to reach damage threshold is plotted in figure 2.10 (red dashed lines). We can see that the maximum extractable energy, before the air/silica interface damage threshold is reached, is ~ 40% below the maximum extractable pulse energy possible for a given core dimension for pulses of this particular duration. A typical damaged fibre end produced by exceeding this threshold is shown in figure 2.11 (a).

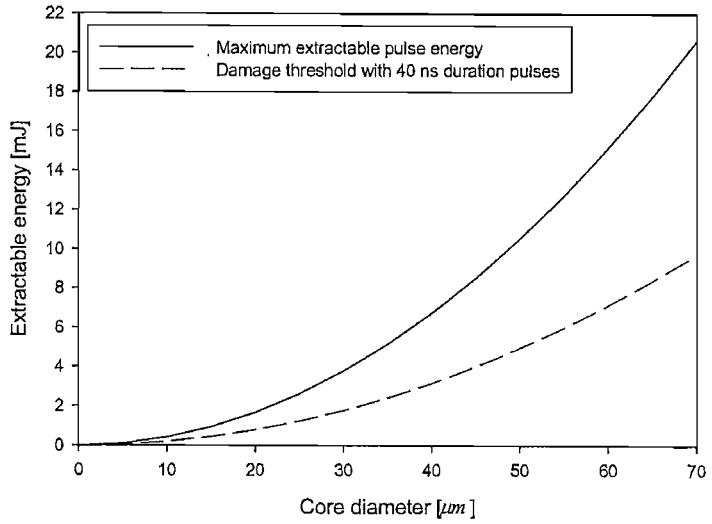

Figure 2.10: Maximum extractable pulse energy and damage threshold for the air/silica interface at fibre ends, for various core diameters.

This damage threshold constraint can be avoided by splicing angle polished core-less silica end-caps [44, 47] (or beam expanders) at the ends of the fibre. The silica endcap expands (see figure 5.8 in chapter 5) the output beam thus reducing the fluence at the silica/air interface and thus avoiding fibre facet damage. The longer the end caps, the more the beam expands thus reducing the fluence further. However, to avoid any distortions to the output beam and power loss, the diameter of the expanded beam should be smaller than the endcap. Further details and a summary of performance using endcaps can be found in section 5.3.2.4 of chapter 5.

The advent of larger core fibres has brought output power performance of fibre laser technology to a whole new era. The maximum extractable pulse energies delivered to date from larger core Yb^{3+} doped fibre amplifier and laser systems are 82 mJ at 100 Hz with a 200 μm diameter core amplifier fibre [48] and 7.7 mJ at 500 Hz [47] with 30 μm core active fibre respectively. However the active fibres used in these systems are heavily multimoded with quoted M^2 values of 6.5 and 10 respectively. The highest pulse energy from Er^{3+} doped fibre

amplifier systems is 1 mJ, achieved by C. Codemard from the ORC. He achieved this pulse energy with a 90 μm core diameter fibre and the M^2 was estimated to be ~5 [49]. Hence, presently achievable output pulse energies from large core fibres are in fact a 1000 times or more higher than energies achieved with conventional small core fibre systems, without unusable degradation to beam quality.

2.4 Fibre design and bend losses

To address the non-linearity and energy storage issues mentioned earlier, we use a larger core dimension to enlarge the modal field area (MFA), or effective mode area (A_{eff}), guided by the fibre and a shorter length of fibre to reduce the interaction length [40]. However, scaling of the MFA is ultimately restricted by two factors; obtaining acceptable mode quality and/or bend losses. First the core/cladding index difference of the fibre will influence the maximum core-size for acceptable output modal quality. Secondly, with increasing MFA, the bending losses of the guided modes experienced by the fibre will rise rapidly. The length of the active fibre used is determined mainly by the efficiency of the pump absorption and the operating wavelength.

In the past, multimode fibres have been used to scale output pulse energy up to 0.5 mJ with Er-doped Fibre Amplifiers EDFA [50] without the concern of obtaining single mode operation. Another approach was to use precise launch alignment of the input beam to excite only the fundamental mode of a multimode fibre to achieve single mode operation and yet benefit from the advantage of the higher powers obtainable with larger core multimoded fibres [51]. However, this approach is less robust due to alignment drifts over time as compared to strictly single mode fibres.

In this section, we will describe the design of the core of a power amplifier fibre that allows further extension of the core size and yet maintains single mode operation. This fibre is also designed to reduce bending losses. Both of these attributes are essential for further increase in power scaling. The optimisation of the pump coupling efficiency into the active core to reduce the required length of the fibre will also be discussed.

The fibre design concept that was pursued was a low NA large mode area (LMA) fibre with strategic Yb^{3-} doping of the core to give preferential gain to the fundamental mode [52]. The significant gain differential between the fundamental mode and the higher order modes will favour fundamental mode operation. The low NA structure reduces the total number of

guided modes for a given core diameter, which helps to achieve robust single mode operation and increase the maximum energy that can be stored. However the minimum NA that can be achieved is limited by the reliability of fabricating a small core/cladding index difference.

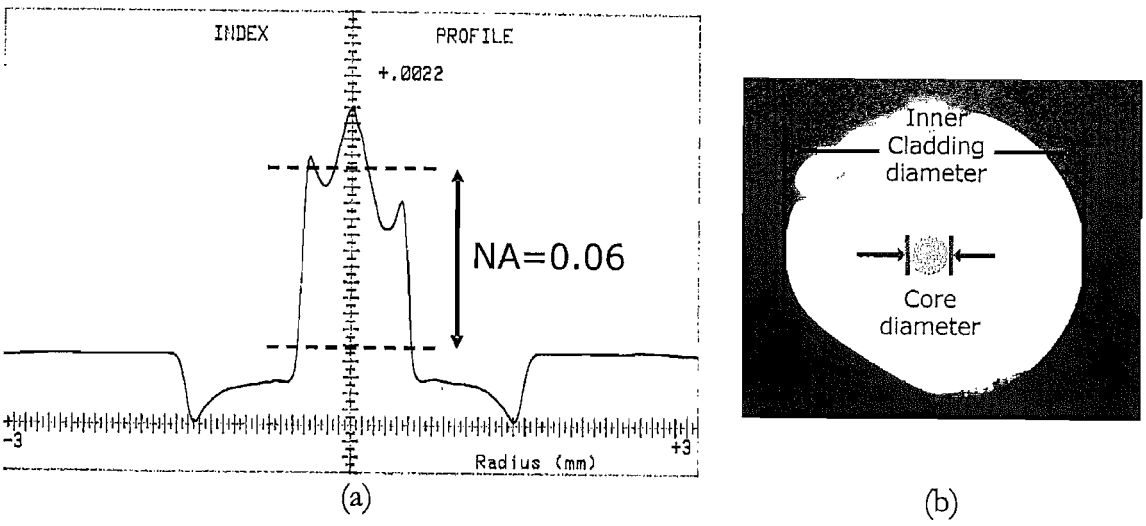

Figure 2.11: (a) Refractive index profile of LF128 preform and its (b) cross section.

The higher the signal (active core) to pump (inner cladding + active core) waveguide cross-sectional area ratio, the higher the pump absorption and the shorter the fibre length required. I will now describe a LMA fibre, designed with this approach, that was used either as a laser or an amplifier, or both, in all the experimental projects described in this thesis.

The refractive index profile of the LF128 LMA fibre is shown in Figure 2.11 (a). We can see that the fibre has a step index profile with a modulated top peaked in the middle. The fibre was pulled into core dimensions of 20, 30 and 40 μm with a core/inner cladding ratio of 10 (i.e. 400 μm diameter inner cladding for a 40 μm core). The NA of the fibre core was 0.06. As a result of selective doping at the inner region of the active core, where the fundamental mode propagates, the overlap of the doped region is greater for the fundamental mode than any other guided modes within the fibre. In addition, the outer dip within the LMA fibre core also provides higher index difference to help improve guidance of the fundamental mode and reduce bending losses.

Some theoretical modelling on the LF128 LMA fibre was carried out by Dr Fabio Ghiringhelli from SPI. The number of guided modes was estimated to be 2, 4 and 7 for the 20, 30 and 40 μm cores respectively. Figure 2.12 shows the calculated bending losses of the 40 μm core diameter LMA fibre (calculated A_{eff} of 370 μm^2) with an NA of 0.06 for six of the guided modes. As an example, with a fibre bending radius of ~75 mm, a reasonable size for use in

practical devices, the calculated bending loss for the first higher order LP_{11} mode is ~ 60 dB/m higher than for the fundamental LP_{01} mode. This provides a very significant discrimination between the fundamental and higher order transverse modes.

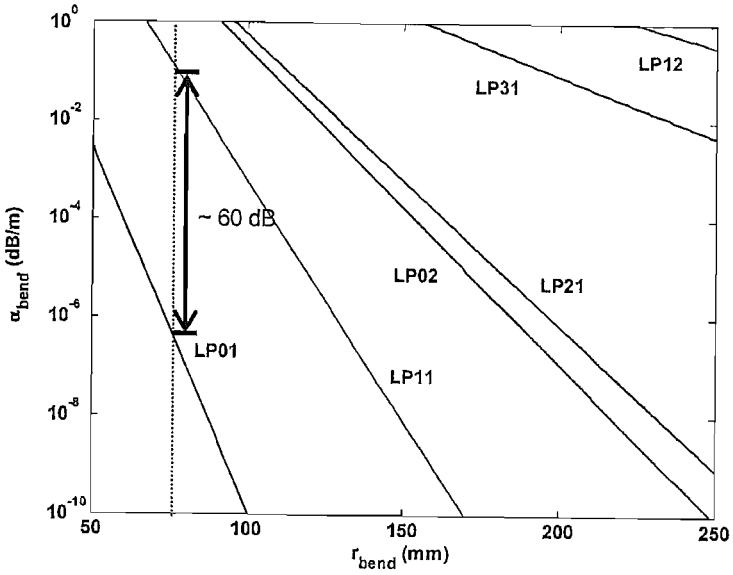

Figure 2.12: Bending loss calculations for 40 μm LF128 LMA fibre with an NA=0.06.

We can see from figure 2.11 (b) that one side of the inner cladding was milled flat to produce a D-shape inner cladding geometry. As mentioned in section 2.1.3, the asymmetrical inner cladding shape of the LMA fibre helps to improve the pump absorption into the active core by avoiding helical pump modes that do not cross the doped central core whilst propagating through the fibre.

Typical Yb^{3+} doping concentrations of doped fibres are ~ 1000 - 2000 ppm (parts per million), but here a high concentration of Yb^{3+} doping was used (~ 8000 ppm) to increase the pump absorption of the doped core. The increase in pump absorption helps to keep the required fibre length as short as possible. With a high NA of 0.4 and large dimension design of the inner cladding, a larger variety of lower brightness high power diode pumps can be used to pump the fibre.

2.4.1 Performance and characterisation of a Large Mode Area (LMA) fibre.

We now describe the c.w. performance of a LMA fibre that was designed and fabricated in the ORC. The experimental setup and pumping scheme used for the power amplifier is shown in figure 2.13. Two diode laser pumps lasing at 915 nm and 976 nm from Boston Laser Inc. were used to pump the power amplifier. Both diode pumps consist of 8 smaller semi-conductor laser diodes. The output from the laser diodes were combined (via a beam

combiner) and the final output was delivered through a 200 μm core fibre pigtail having NA ~ 0.2. The total 915 and 976 nm pump radiation, that the two diode pumps were specified to provide was 30 W and 25 W respectively. The output pump radiation from both pigtail diode pumps was free-space coupled into LF128 LMA fibres having inner cladding diameters of 200, 300 and 400 μm with NA ~ 0.4. The maximum pump coupling efficiency was experimentally found to be ~80% except for the 200 μm LMA which was ~ 65%. The 915 and 976 nm pump absorption of the LF128 LMA was ~1.46 dB/m and 4.1 dB/m respectively. Dichroic mirrors were used to separate the pump and signal beams and also to protect the diode laser pumps from the signal wavelength and any unabsorbed pump at the other pump wavelength.

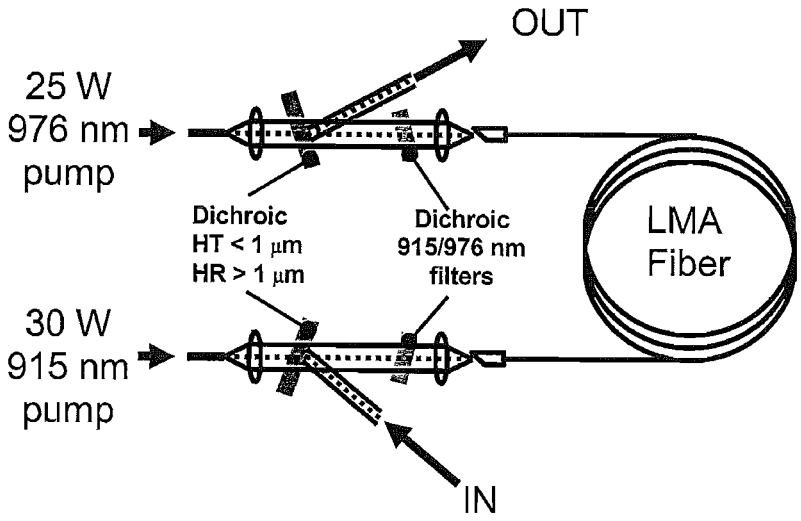

Figure 2.13: Schematic diagram of pumping scheme used for LMA as an amplifier.

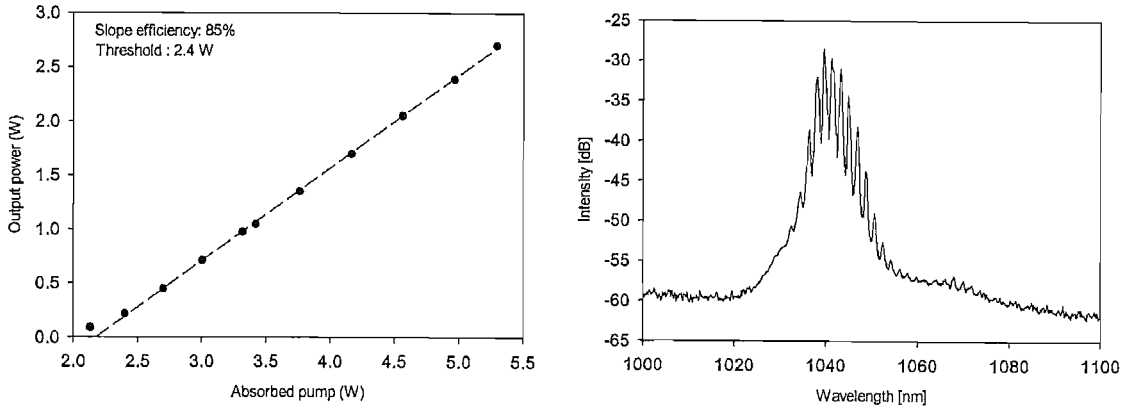

Figure 2.14: Laser power performance characteristics and the laser spectrum of a 3m length of the 40 μm core LMA. 976 nm pump radiation was used and the fibre was flat cleaved at both ends.

The absorption coefficient measured for each pump wavelength leads to the design of the pump arrangement within the cavity. Since the absorption is higher at 976 nm (see section

2.1.1: Yb spectroscopy), pumping with this wavelength from the output fibre end allows the maximum inversion to be concentrated over a shorter doped fibre length at the output (compared to using the 915 nm pump wavelength), providing higher signal gain. Therefore the chosen approach was to counter pump with the 976 nm and co-propagate pump with the 915 nm.

The efficiency of this fibre as a c.w. laser was measured and the results are shown in figure 2.14. A 3 m length of 40 μm core LMA fibre (having 4% end cleaves at both ends) was characterised using the 976 nm diode pump. The slope efficiency of the laser was found to be excellent at ~ 85% (slightly lower than the calculated quantum efficiency = 976 nm/1040 nm = 94%) and the pump lasing threshold was ~2.4 W. The c.w. M^2 of this fibre was measured to be 1.1. The amplifier and Q-switched laser performance of the LMA fibre will be discussed in detail in chapters 4-7.

2.5 Fibre amplifier cascade

Yb-doped fibre amplifiers and lasers were used throughout all the projects that we have presented in this thesis. The fibre amplifiers used in the chirped pulse amplification (CPA), direct amplification, Q-switch MOPA, direct modulation MOPA and gain switched MOPA systems will be described in this chapter. The block diagram of a typical MOPA cascade is shown in figure 2.15 below.

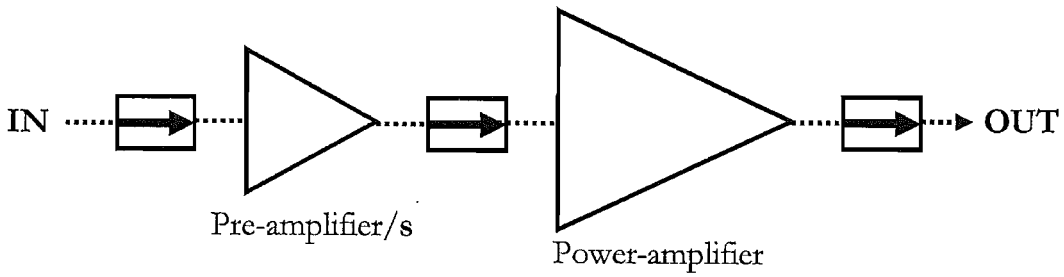

Figure 2.15: Block diagram of a typical fibre amplifier cascade.

A typical MOPA amplifier cascade consists of a seed source, one or more pre-amplifier sections and a final power amplification stage. Seed sources can range from fully and partly fibreised Yb-doped laser systems to semiconductor laser diodes or even bulk laser systems. For example, our CPA system is seeded by our in-house, passively mode-locked, all fibre oscillator producing pulses compressible to 100 fs at 50 and 62 MHz repetition rate with milliwatt

output average powers. Alternatively, our direct modulation and gain switched systems utilised a modulated high speed semiconductor laser diode operating at 1 μm as a seed source.

The pre-amplification stage normally provides signal gains between 20-35 dB and would consist of one or more of the following: a core-pumped single mode fibre amplifier (see section 4.2 of chapter 4); a cladding pumped fibre amplifier either in the usual end-pump configuration (see figure 5.3 (c) of chapter 5, or figure 6.19 of chapter 6) or using a GT-Wave technology (see section 6.4.1 of chapter 6) based amplifier. Core-pumped amplifiers offer the advantage of ease of implementation and robust operation however they provide limited scope in power scaling due to the lack of availability of appropriate high power SM semiconductor diode pumps. Cladding pumping avoids the requirement of high brightness diode pumps and enables the use of higher power, medium brightness, semiconductor diode pumps for power scaling. Clever fibre designs modifying the waveguiding properties and reduction of the NA of cladding pumped fibres offers SM output operation. The disadvantages of using the typical end cladding pump technique, with coupling optics and dichroics, would be thermal management of the fibre ends and air/silica interface damage for the end facets, as the active fibres have to be interrupted to allow pump coupling. The heating of the fibre ends causes it to drift away from alignment.

The final power amplification stage usually consists of a cladding pumped (utilising end-pumped set up) fibre, large core amplifier, providing between 20-30 dB signal gain. Both pumping schemes were implemented in all our setups. Depending on the gain required to meet the specification, the number of pre-amplification stages and one power amplifier stage are chosen. Normally, a multistage system is required to reach mJ pulse energy as the gain of the amplifiers are limited to ~ 35 dB due to the build up of ASE [53]. For example for a seed source providing 0.1μJ pulse energy, to reach 1 mJ, ~40 dB (excluding losses i.e. insertion loss within the amplifier cascade) of gain is required. Therefore if the pre-amplification stage can provide up to 25 dB gain, we would only need a single pre-amplification stage and a power amplifier stage that can provide ~25 dB gain, leaving a 10 dB excess to accommodate for cascaded losses like splice, alignment, insertion, etc.

Between each amplification stage, either a free space 1060 nm isolator or a fibreised 1060 nm isolator (depending on the input pulse energy) is used to prevent backward ASE, produced from the next amplifier, saturating the gain of the preceding amplifier by reducing the inversion near the output, and to suppress the chance of formation of a backward giant pulse (via self q-switching) which may damage the amplifiers within the chain or cause instability in the output pulse.

2.5.1 *Isolators*

2.5.1.1 *Free-space isolators*

The free-space isolators that we were using were 1054 nm Faraday isolators (made from two Polarisation Beam Splitter (PBS) cubes and one TGG crystal) from Electro-Optics technology (EOT) (model no. 4I1054). These devices have a 4 mm aperture and provide ~ 25 dB isolation over a 25 nm bandwidth centred at 1054 nm. The insertion loss of these isolators is ~ 0.5 dB and the damage threshold is specified at 5 J/cm^2.

2.5.1.2 *Fibreised isolator*

Low power 1060 nm fibreised isolators were bought from Advance Fibre Resources Holdings (AFR). The fibreised pigtails at both ends were Corning SM HI1060 fibres with cutoff wavelength at 920 nm. Insertion losses (excluding splice losses) were found to be ~ 1.45 dB. White light characterisation was carried out to determine experimentally its spectral isolation over a broad bandwidth between 900 nm to 1200 nm. The result is shown in figure 2.16, isolation between 1050 - 1085 nm was found to be ~ 35 dB.

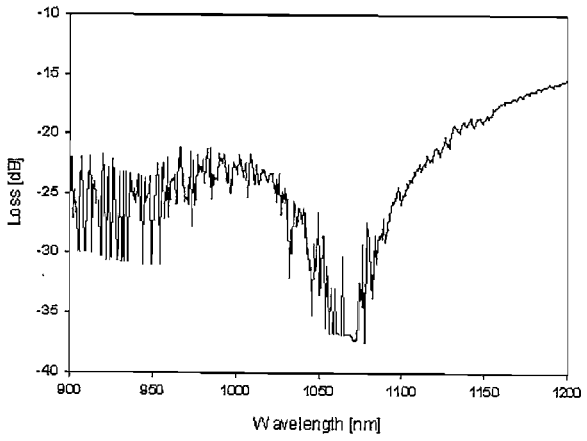

Figure 2.16: White light characterisation of AFR 1060nm isolator.

2.6 Conclusion

In this chapter, a brief background to Yb-doped fibre technology and its spectroscopic properties has been discussed. This section is written to help the reader understand the current

status of this technology, its attractiveness and several of the laser system topologies used in this thesis. In summary, besides the high optical efficiency, high gain efficiency and broad gain bandwidths of the Yb-doped fibres, the large energy gap and absence of other energy level states which prevents the occurrence of excited state absorption, of either the pump or laser wavelengths and concentration quenching by ion-ion energy transfer, which is observed in other REs, makes the Yb^{3+} RE so attractive. It has been demonstrated by several authors using cladding pump fibre technology, that Yb^{3+} fibre lasers with single and multi mode c.w. output of more than 1 kW and 10 kW are realisable.

Two different pumping strategies were introduced, core-pumping and cladding pumping. Both of these pumping methods were utilised throughout this thesis. Generally, core-pumping which produces relatively low output powers is normally used at the beginning of the amplifier cascade. This is because of their robust, stable and low-noise operation. Cladding pumping is normally used at the end stages of an amplifier cascade as pump sources providing higher pump powers are used to produce high output powers but are typically noiser. Two different cladding pump techniques were used. The commonly used end-pumping and the GT-wave pumping tehnique.

Issues pertaining to the nonlinear effects occurring within optical fibres have been described in this chapter. The understanding of these nonlinear effects helps to determine the approaches that were used to achieve the output performances of the laser systems demonstrated in this thesis. For example, the understanding of the linear and nonlinear evolution (i.e. dispersion and SPM) of a pulse propagating within a fibre was used to develop the CPA and direct amplification system to produce high output power femtosecond pulses described in chapters 3 and 4. The understanding of stimulated inelastic scattering mechanisms are important for all the laser systems developed. In particular, the onset of SRS is the main factor limiting the highest possible pulse energy achievable in all our laser systems, with the exception of the Q-switched fibre laser described in chapter 5. The main strategy that was used to avoid SRS from occurring prematurely (increase SRS threshold power) was to increase the effective areas A_{eff} of the amplifier fibres used within our systems (see table 2.2). The increase in A_{eff} also increases the amount of stored/extractable energy achievable in the fibre (see section 2.3).

Other fibre design parameters such as core/cladding area ratio, core/cladding index differences and doping concentrations and strategy is also crucial for the development and success of the laser systems built in this thesis. These parameters affect the performance of the fibre, performances such as the output modal quality, pump absorption and bending losses.

The LMA amplifier fibre (i.e. double-clad fibre) that was mainly used in this thesis has a core/cladding area ratio of 10, core dimensions of 20, 30 and 40 μm diameters, NA of ~0.06-7 (which provides preferential guidance to the fundamental LP_{01} mode) and is doped preferentially at the centre of the core. The latter two properties allow this fibre to achieve transverse SM output operation. This fibre also has 915 and 975 nm pump absorption per unit length of 1.46 dB/m and 4.1 dB/m respectively.

Finally, a block diagram of the amplifier cascade that was used in chapters 4-7 was illustrated in section 2.5. The various components that were necessary within the amplifier cascade were described and the typical gains required at each stage were discussed.

REFERENCES

1. Koester, C.J. and Snitzer, E., *Amplification in a fiber laser.* Applied Optics, 1964. **3**: p. 1182-1186.
2. Snitzer, E., *Optical master action of Nd3+ in a barium crown glass.* Physical Review Letters, 1961. **7**: p. 444-446.
3. Snitzer, E., *Neodymium glass laser.* Proc. 3rd Int. Conference Quantum Electronics, 1963: p. 999-1019.
4. Dominic, V., MacCormack, S., Waarts, R., Sanders, S., Bicknese, S., Dohle, R., Wolak, E., Yeh, P. S., Zucker, E., *110W fibre laser.* Electronics Letters, 1999. **35**(14): p. 1158-1160.
5. Limpert, J., Liem, A., Hofer, S., Zellmer, H., Limpert, J., Tunnermann, A., *150 W Nd/Yb codoped fiber laser at 1.1 micron. Conference on Lasers and Electro-Optics, CLEO.* 2002. Washington D.C. 2002: OSA Technical Digest (Optical Society of America). **73**: p.590-591.
6. Platonov, N.S., Gaponsev, D.V., Gaponsev, V.P. and Shurmilin, V. *135 W cw fiber laser with perfect single mode output. Conference on Lasers and Electro-Optics, CLEO.* 2002. Long Beach, USA. *CPDC3.* **2**(2): p. 1-4. *(postdeadline paper).*
7. Jeong, Y., Sahu, J.K., Payne, D.N. and Nilsson, J., *Ytterbium-doped large-core fiber laser with 1.36 kW continuous- wave output power.* Optics Express, 2004. **12**(25): p. 6088-6092.
8. *SPI Optics press release.* Jan 27 2004 (http://www.spioptics.com).
9. Paschotta, R., Nilsson, J., Tropper, A.C. and Hanna, D.C., *Ytterbium-doped fiber amplifiers.* IEEE Journal of Quantum Electronics, 1997. **33**(7): p. 1049-1056.
10. Sahu, J.K., Renaud, C.C., Furusawa, K., Selvas, R., Alvarez-Chavez, J. A., Richardson, D. J., Nilsson, J., *Jacketed air-clad cladding pumped ytterbium-doped fibre laser with wide tuning range.* Electronics Letters, 2001. **37**(18): p. 1116-1117.
11. Nilsson, J., Sahu, J.K., Jeong, Y., Clarkson, W.A., Selvas, R., Grudinin, A. B., Alam, S. U., *High power fiber lasers: New developments.* in *Proceedings of SPIE: Advances in Fiber Lasers.* 2003. **4974** p. 50-59.
12. Pask, H.M., Carman, R.J., Hanna, D.C., Tropper, A.C., Mackechnie, C. J., Barber, P. R., Dawes, J. M., *Ytterbium-Doped Silica Fiber Lasers - Versatile Sources for the 1-1.2 um Region.* IEEE Journal of Selected Topics in Quantum Electronics, 1995. **1**(1): p. 2-13.
13. Takebe, H., Murata, T., Nishida, H., Hewak, D.W., Morinaga, K., *Compositional dependence of optical properties of Nd3+ in gallate glasses.* Journal Of The Ceramic Society Of Japan, 1996. **104**(3): p. 243-246.
14. Weber, M.J., Lynch, J.E., Blackburn, D.H. and Cronin, D.J., *Dependence Of The Stimulated-Emission Cross-Section Of Yb-3+ On Host Glass Composition.* IEEE Journal Of Quantum Electronics, 1983. **19**(10): p. 1600-1608.
15. Clarkson, W.A. and Hanna, D.C., *Two-mirror beam-shaping technique for high power diode bars.* Optics Letters, 1996. **21**: p. 375-377.
16. Kouznetsov, D. and Moloney, J.V., *Efficiency of pump absorption in double-clad fiber amplifiers. II. Broken circular symmetry.* Journal Of The Optical Society Of America B-Optical Physics, 2002. **19**(6): p. 1259-1263.
17. Kouznetsov, D. and Moloney, J.V., *Efficiency of pump absorption in double-clad fiber amplifiers. III. Calculation of modes.* Journal Of The Optical Society Of America B-Optical Physics, 2002. **19**(6): p. 1304-1309.
18. Kouznetsov, D., Moloney, J.V. and Wright, E.M., *Efficiency of pump absorption in double-clad fiber amplifiers. I. Fiber with circular symmetry.* Journal Of The Optical Society Of America B-Optical Physics, 2001. **18**(6): p. 743-749.

19. Xu, J., Lu, J., Lu, L. and Ueda, K.-I. *Influence of cross-sectional shape on absorption characterisitcs of double clad fiber lasers. Proc. Conference on lasers and Electro-Optics, CLEO.* 2002. Long Beach, USA. **1**: p.520-521.
20. Miniscalco, W.J., *Optical and electronic properties of rare earth ions in glasses.* Second ed. Rare Earth Doped Fiber Lasers and Amplifiers, ed. M.J.F. Digonnet. 2001: Marcel Dekker. p. 17-112.
21. Yla-Jarkko, K.H., Alam, S.-U., Turner, P.W., Moore, J., Nilsson, J., Selvas, R., Soh, D.B.S., Codemard, C., Sahu, J.K.. *Cladding pumping technology for next generation of fiber amplifiers and lasers.* in *OAA. 6-9 Jul 2003.* 2003. Otaru. *TuC1 (Invited).*
22. Yla-Jarkko, K.H., Codemard, C., Singleton, J., Turner, P.W., Godfrey, I., Alam, S. U., Nilsson, J., Sahu, J. K., Grudinin, A. B., *Low-noise intelligent cladding-pumped L-band EDFA.* IEEE Photonics Technology Letters, 2003. **15**(7): p. 909-911.
23. Agrawal, G.P., *Nonlinear Fiber Optics.* 3rd Edition ed. 2001, San Diego: Academic Press.
24. Gloge, D., *Weakly guiding fibers.* Applied Optics, 1971. **10**(10): p. 2252-2258.
25. Stolen, R.H. and Lin, C., *Self-phase-modulation in silica optical fibers.* Physics Review A, 1978. **17**(4): p. 1448-1453.
26. Galvanauskas, A., *Mode-scalable fiber-based chirped pulse amplification systems.* IEEE Journal Of Selected Topics In Quantum Electronics, 2001. **7**(4): p. 504-517.
27. Alfano, R.R., Li, Q.X., Jimbo, T., Manassah, J.T., Ho, P. P., *Induced Spectral Broadening of a Weak Picosecond Pulse in Glass Produced by an Intense Picosecond Pulse.* Optics Letters, 1986. **11**(10): p. 626-628.
28. Chraplyvy, A.R. and Stone, J., *Measurement of Crossphase Modulation in Coherent Wavelength-Division Multiplexing Using Injection-Lasers.* Electronics Letters, 1984. **20**(24): p. 996-997.
29. Doran, N.J. and Wood, D., *Nonlinear-Optical Loop Mirror.* Optics Letters, 1988. **13**(1): p. 56-58.
30. Fermann, M.E., *Ultrashort-Pulse Sources Based on Single-Mode Rare-Earth-Doped Fibers.* Applied Physics B-Lasers and Optics, 1994. **58**(3): p. 197-209.
31. Raman, C.V. and Krishnan, K.S., *A new type of secondary radiation.* Nature, 1928. **121**.
32. Stolen, R.H., Gordon, J.P., Tomlinson, W.J. and Haus, H.A., *Raman Response Function Of Silica-Core Fibers.* Journal Of The Optical Society Of America B-Optical Physics, 1989. **6**(6): p. 1159-1166.
33. Price, J.H.V., *The development of high power, pulsed fiber laser systems and their applications.*, in *PhD thesis. Optoelectronics Research Centre.* 2003, University of Southampton. p. 22-24.
34. Smith, R.G., *Optical power handling capacity of low loss optical fibes as determined by stimulated Raman and Brillouin scattering.* Applied Optics, 1972. **11**: p. 2489-2494.
35. Stolen, R.H. and Johnson, A.M., *The Effect Of Pulse Walkoff On Stimulated Raman-Scattering In Fibers.* IEEE Journal Of Quantum Electronics, 1986. **22**(11): p. 2154-2160.
36. Chuang, Y.H., Meyerhofer, D.D., Augst, S., Chen, H., Peatross, J., Uchida, S., *Suppression Of The Pedestal In A Chirped-Pulse-Amplification Laser.* Journal Of The Optical Society Of America B-Optical Physics, 1991. **8**(6): p. 1226-1235.
37. Perry, M.D., Patterson, F.G. and Weston, J., *Spectral Shaping In Chirped-Pulse Amplification.* Optics Letters, 1990. **15**(7): p. 381-383.
38. Boyd, R.W., *Nonlinear Optics.* 1st ed. 1992: Academic Press Limited. 439.
39. Lichtman, E., Friesem, A.A., Waarts, R.G. and Yaffe, H.H., *Stimulated Brillouin-Scattering Excited By 2 Pump Waves In Single-Mode Fibers.* Journal Of The Optical Society Of America B-Optical Physics, 1987. **4**(9): p. 1397-1403.
40. Desurvire, E., *Erbium-Doped Fiber Amplifiers.* Wiley, New York 1994.
41. Richardson, D.J., Britton, P. and Taverner, D., *Diode-pumped, high-energy, single transverse mode Q-switch fibre laser.* Electronics Letters, 1997. **33**(23): p. 1955-1956.
42. Renaud, C.C., Offerhaus, H. L., Alvarez-Chavez, J.A., Nilsson J., Turner, P.W., Richardson, D.J., Clarkson, W.A., Grudinin, A. B., *Designs for efficient high-energy high*

brightness Q-switched cladding-pumped ytterbium-doped fibre lasers. In *Tech. Dig. Pacific Rim Conference on lasers and Electro-Optics, CLEO.* 2000. San Francisco 7-12 May. CMP1. p. 75-6.

43. Renaud, C.C., Offerhaus, H.L., Alvarez-Chavez, J.A., Nilsson, J., Clarkson, W. A., Turner, P. W., Richardson, D. J., Grudinin, A. B., *Characteristics of Q-switched cladding-pumped ytterbium-doped fiber lasers with different high-energy fiber designs.* IEEE Journal Of Quantum Electronics, 2001. **37**(2): p. 199-206.
44. Limpert, J., Hoffer, S., Liem, A., Zellmer, H., Tunnermann, A., Knoke, S., Voelckel, H., *100-W averagepowerg high-energy nanosecond fiber amplifier.* Applied Physics B-Lasers And Optics, 2002. **75**(4-5): p. 477-479.
45. Limpert, J., Liem, A., Schreiber, T., Zellmer, H., Tunnermann, A., *Power and energy scaling of fiber laser systems based on ytterbium- doped large-mode-area fibers*, in *Proceedings of SPIE: Advances In Fiber Lasers.* 2003. **4974**: p. 135-147.
46. Stuart, B.C., Feit, M.D., Rubenchik, A.M., Shore, B.W., Perry, M. D., *Laser-Induced Damage In Dielectrics With Nanosecond To Subpicosecond Pulses.* Physical Review Letters, 1995. **74**(12): p. 2248-2251.
47. Renaud, C.C., Alvarez-Chavez, J.A., Sahu, J.K., Nilsson, J., Richardson, D. J., Clarkson, W. A., *7.7mJ pulses from a large core Yb-doped cladding pumped Q-switched fibre laser.* in *Tech. Dig. Conference on Lasers and Electro-Optics, CLEO.* 2001. Baltimore, CTuQ5. p.219.
48. Cheng, M.Y., Chang, Y.C., Galvanauskas, A., Mamidipudi, P., Changkakoti, R. Gatchell, P., *High-energy and high-peak-power nanosecond pulse generation with beam quality control in 200-mu m core highly multimode Yb- doped fiber amplifiers.* Optics Letters, 2005. **30**(4): p. 358-360.
49. Codemard, C., Farrell, C., Philippov, V., Dupriez, P., Sahu, J. K., Nilsson, J., *1 mJ narrow-linewidth pulsed fiber MOPA source at 1535 nm. Conference on lasers and Electro-Optics, CLEO Europe 12-17 June.* 2005. Munich.
50. Desthieux, B., Laming, R.I. and Payne, D.N., *111 kW (0.5 mj) Pulse Amplification At 1.5-Mu-M Using A Gated Cascade Of 3 Erbium-Doped Fiber Amplifiers.* Applied Physics Letters, 1993. **63**(5): p. 586-588.
51. Fermann, M.E., *Single-mode excitation of multimode fibers with ultrashort pulses.* Optics Letters, 1998. **23**(1): p. 52-54.
52. Broderick, N.G.R., Offerhaus, H.L., Richardson, D.J., Sammut, R.A., Caplen, J., Dong, L., *Large mode area fibers for high power applications.* Optical Fiber Technology, 1999. **5**(2): p. 185-196.
53. Desthieux, B., Laming, R.I. and Payne, D.N., *111 kW (0.5 mJ) Pulse Amplification at 1.5-microns Using a Gated Cascade of 3 Erbium-Doped Fiber Amplifiers.* Applied Physics Letters, 1993. **63**(5): p. 586-588.

Chapter 3

PRACTICAL LOW-NOISE STRETCHED-PULSE YB^{3+} DOPED FIBER OSCILLATOR

3.1 Introduction

Present day technologies have realised ultrafast pulse generation with both solid state and fibre based cavity designs. Producing ultrafast pulses requires the use of either an ultrafast switch, or an environment which naturally maintains and promotes the generation of ultrafast pulses (i.e. saturable absorbers, optical Kerr gates, etc.). The proliferation of industrial applications requiring ultrafast lasers creates a strong motivation to produce mode-locked lasers which are compact, cheap and robust.

Passive mode-locking of solid-state lasers has been achieved with either additive-pulse modelocking (APM) [1, 2] or Kerr lens modelocking (KLM) [3-5]. Using a prism pair for intracavity dispersion compensation, Spence *et al.* [4] demonstrated a mode-locked Ti:sapphire laser producing 60 fs near transform limited Gaussian pulses having 90 kW peak powers operating at 850 nm. However, such lasers are bulky, costly and difficult to maintain. The fabrication of rare-earth doped fibres [6] that provide a high quality wide bandwidth fibre gain medium and the demonstration of soliton pulse propagation in optical fibres paved the way for the development of ultrafast fibre lasers which are compact, relatively cheap, simple to implement and require low pump power [7].

Ultrashort soliton pulses may be formed and supported in the presence of both anomalous group velocity dispersion (GVD) and self-phase modulation (SPM) effects in glass optical fibres. Figure 3.1 (a) shows a commonly used modelocking strategy which relies on pulses evolving into self supporting soliton pulses whilst propagating in a dominantly anomalously dispersive cavity. Pulses can be initiated by either active optical modulation techniques [8, 9] or passive modelocking schemes which utilise the noise that occurs in the continuous wave (c.w.) radiation to initiate pulsing. This soliton phenomenon, plus the availability and maturity of technology already used in the telecommunications industry, has led to the initial development of ultrafast fibre based oscillators at 1.5 μm wavelength using fibre doped with Er^{3+} rare earth (RE) ions [8].

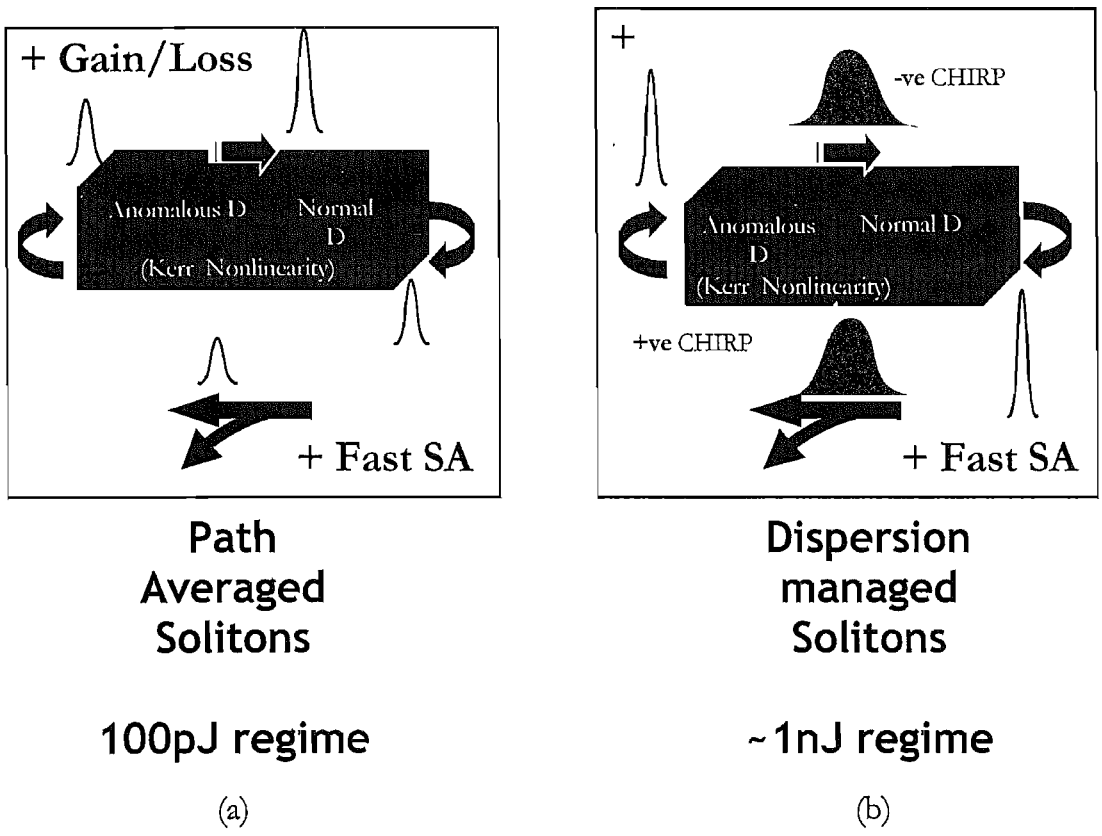

Figure 3.1: Different modelocking strategies, (a) traditional soliton modelocking (b) Stretched-pulse modelocking.

However on their own, soliton effects are not enough to achieve stable modelocked operation. This is because the large non-linearity in the long cavity lengths, and amplification upon every round trip, causes periodic perturbations to generate a background spectral continuum which destabilises the circulating soliton pulse [10]. Therefore ultrafast switches or amplitude modulation (AM) are required to filter out this low level background to maintain modelocking stability.

Early passively mode-locked, short pulse, fibre oscillators had relatively complicated cavities utilising nonlinear amplifying loop mirrors (NALMs) [11, 12], in a figure-of-eight configuration, as an all-optical switch [13, 14]. This evolved to simpler cavity designs using nonlinear polarisation evolution (NLPE) [15-19], or semiconductor saturable absorbers (SA) [20, 21], in a ring or Fabry-Perot (FP) cavity geometry. NLPE works through the combined action of SPM and cross phase modulation (XPM). The differential excitation experienced by the two polarisation eigenmodes of a standard single mode RE-doped fibre (at high pulse intensity) creates an intensity dependent phase shift between them via the optical Kerr effect. By adding polarisers and by appropriate control of the polarisation state within the optical fibre, an all-optical switch promoting pulse operation and shaping is obtained via an optical Kerr gate. This switching action is similar to the additive pulse modelocking mechanism [22].

Since propagating modelocked soliton pulses follow a kind of area theorem [23], the approach of ultrashort pulse generation, shown in figure 3.1 (a), using solitons within an overall negative GVD cavity (anomalously dispersive) environment restricts the maximum pulse energy to low values (~ 100 pJ). Consequently, the magnitude of the soliton energy is proportional to the net dispersion within the cavity [24].

An alternate modelocking strategy, as shown in figure 3.1 (b), has been demonstrated by Tamura *et al.* [25]. He demonstrated a cavity that consisted of lumped sections of large anomalous (negative) dispersion and large normal (positive) dispersion (obtaining nearly net zero cavity dispersion) that can support quasi-soliton operation. This cavity design that stretches and compresses the propagating pulse within the cavity, is called a stretched pulse cavity design. It lowers the overall peak intensity of the circulating pulse (due to the higher chirping of the pulse whilst propagating within the cavity as shown in figure 3.1(b)) and confines the minimum pulse duration to only a fraction of the cavity length (see figure 3.1 (b)). This results in a lower overall cavity non-linearity [10] which allows stable, spectrally cleaner, higher energy (~ 1nJ) and shorter duration pulses to be produced [26] (a small amount of net normal dispersion produces the shortest pulse).

The stretched pulse configuration can also be applied to operating wavelengths < 1.3 μm where standard fibres are normally dispersive by the use of bulk optics or even specially designed fibres (i.e. holey fibres, photonic bandgap fibre) for the anomalous dispersion section [27]. Recently a team from Cornell used both holey fibre (HF) [28] and photonic bandgap fibre (PBF) [29] for anomalous dispersion compensation in a Yb^{3+} ring cavity to generate 1nJ pulses with durations compressible to 100 fs and 160 fs respectively. Holey fibre [30] is a silica fibre with an ordered array of air holes along its length, surrounding a solid core, and PBF fibre [31] is also a microstructured fibre but with a hollow-core. The HFs achieve anomalous dispersion at wavelengths < 1.3 μm due to the strong waveguide dispersion property arising from their small core dimensions. Therefore the anomalous GVD wavelengths between 0.7 and 1.3 μm are determined mainly by the air filling fraction and effective core diameter. However in PBF, light is confined in the hollow core due to a photonic bandgap that arises from a regular 2-dimensional array of air holes in the cladding. The anomalous dispersion property does not come from the property of the material but from the photonic bandgap and is anomalous at the longer wavelengths of the bandgap. Due to the small core sizes (hence large effective non-linearity) of the HF, the maximum pulse energy that can be generated is approximated to be around 1 nJ [29] but, using PBF, higher pulse energies are possible. The problems associated with using PBF are the high propagation losses (lowest

demonstrated ~ 1.7 dB/km with a bandgap between 1510-1640 nm [32]), wavelength dependent birefringence and unstable single mode operation.

The first Yb^{3+} based modelocked fibre oscillator was demonstrated at the Optoelectronics Research Centre (ORC) [33]. They obtained clean, chirp free, < 100 fs pulses from a unidirectional stretched pulse ring cavity design achieved with an optical circulator arrangement and a prism-based dispersive delay line (DDL). The self-starting modelocked Yb^{3+} fibre oscillator incorporated NLPE as an ultrafast switch. However the cavity setup was complex, bulky and expensive as it was pumped with a Ti:sapphire laser. The environmentally stable low noise self-starting Yb^{3+} oscillator described in this thesis also utilises NLPE to provide fast optical switching. It operates under stretched pulse conditions incorporating a bulk dispersive grating for anomalous dispersion compensation. A FP cavity was preferred to a complex ring cavity to make commercial production more viable with a simpler and more compact cavity design. However, a FP cavity generally does not self-start at low intra-cavity powers (i.e. increased threshold power) because of spurious cavity reflections and standing wave effects [34]. Therefore to reduce the self-start threshold power, a Semiconductor Saturable Absorber Mirror (SESAM) [34, 35] is required to initiate pulse formation or self-starting mode locking. To obtain low noise operation, a grating stabilised, telecommunications qualified, 976 nm semiconductor diode laser was used to pump the oscillator. The pigtail diode pump output was coupled into the gain fibre via a Wavelength Division Multiplexer (WDM) to make the gain medium compact and all fibre.

In this chapter I describe building a clone of the oscillator previously built by Dr Jonathan Price from our group [27]. This clone oscillator was ultimately used as a seed source for many later experiments carried out (see chapter 4) in our group. Therefore it was essential that it was reliable and well understood. This clone version, through an empirical study, was modified to improve its overall reliability (i.e. self starting, environmental and noise) and characterised to understand the pulse duration limits within this cavity.

In section 3.2, I will describe the various components within the oscillator cavity and their properties. In section 3.3, I will present the development of the clone and results of its original performance. Later, in section 3.4, I will describe the improvements made to the oscillator and evaluate results from its improved performance. Finally, in section 3.5, I will conclude my work done on the development and improvement of the clone oscillator and discuss various future work that can be carried out.

3.2 Components of the oscillator cavity.

The oscillator cavity I built (shown in figure 3.2) is an almost exact replica of the oscillator cavity built by Dr Jonathan Price except for the absence of a short length of high birefringence fibre (this will be described in detail in section 3.4.1.1).

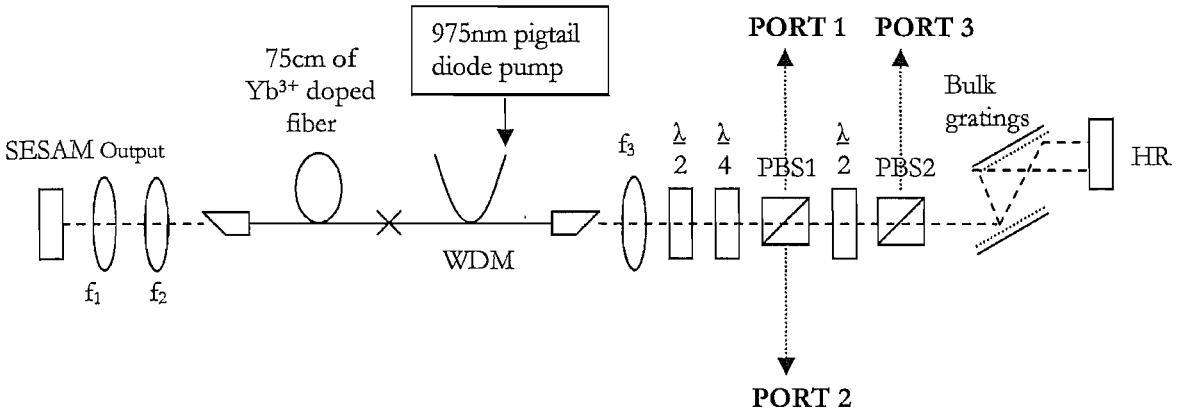

f_1 = 8mm (Thorlabs C240TM-C)
f_2 = 11mm (Thorlabs C220TM-C)
f_3 = 4.5mm (Thorlabs C330TM-C)

Port 1 = rejected (non-switched) output
Port 2 = negative chirp pulse output
Port 3 = positive chirp pulse output

Figure 3.2: Diagram of the oscillator cavity.

The cavity of the oscillator consists of a length of 75cm moderately birefringent highly-doped (2300 ppm) Yb^{3+} fibre (see chapter 3 section 3.3), a 980/1060 nm wavelength division multiplexer (WDM), polarising beam splitter cubes (PBS), half and quarter waveplates for polarisation control, an optimised SESAM device at 1 μm to facilitate reliable self-starting, bulk dispersive gratings with sinusoidal grooves (600 grooves/mm) and a telecommunications qualified, grating stabilised, 976 nm pigtailed semiconductor pump diode. To reduce spurious reflections, optical components within the cavity are anti-reflection coated and the fibre ends are angle polished. The setup of the oscillator cavity is shown in Figure 3.2. The output pulses extracted from Port 1 and 3 are pulses that have just propagated through the normally dispersive active and passive fibres thus these pulses are positively chirped (red shifted wavelength components are at the leading edge of the pulse). Output pulses extracted from Port 2 are pulses that have just been reflected back from the HR mirror via the bulk dispersive gratings which induce a negative chirp (blue shifted wavelength components are at the leading edge of the pulse) on the pulses. Positively chirped pulses from port 3 were used as the seed

pulses for the chirped pulse amplification (CPA) system described in chapter 4. This was because, in the CPA system, the seed pulses will initially be stretched using a normally dispersive pulse stretcher and using positively chirped pulses will complement the stretching. The negatively chirped pulses from port 2 were used both in the direct amplification experiment (see chapter 4) and to characterise the minimum compressed pulse duration possible (see section 3.3.5) from this oscillator. This was because a standard SM silica fibre is normally dispersive at the 1.06 μm wavelength and this was used to compensate the inherent chirp to compress the pulses. One difference between this oscillator and the oscillator build by Dr Price is that it does not contain a length of highly birefringent fibre within the cavity. This does not appear to affect performance.

Although I was cloning Dr Price's oscillator, the components used were different and, in order to improve it, I needed to understand the characteristics of the various components I was using. The empirical characterisation results of the components are shown in the next few subsections.

3.2.1 *WDM characteristics*

There are two kinds of fibre within the cavity, the Yb^{3+} RE doped fibre and conventional 1 μm single mode (SM) WDM fibre. The overall length of fibre within the cavity is 1.75m, comprising 1m length of WDM fibre and 75cm of Yb^{3+} doped fibre. The Yb^{3+} fibre is single mode and efficiently absorbs at 976 nm (pump wavelength).

A WDM was used to couple the pump into the core of the Yb^{3+} doped fibre. A total of three 980/1060nm WDMs were used. The extra WDMs were spliced together and used to provide increased protection for the 975nm semiconductor pump diode from backward travelling amplified spontaneous emission (ASE). The WDMs should have good transmission at 1060 nm and rejection or pump coupling into the Yb^{3+} doped fibre at 976 nm. A white light source was used to characterise the transmission spectra for the WDM. The result is shown in figure 3.3 below.

Figure 3.3 shows that the FWHM transmission bandwidth of the WDM around 1060 nm is ~ 80 nm and there is also good wavelength separation centred at 980 nm. Hence this WDM meets our requirements.

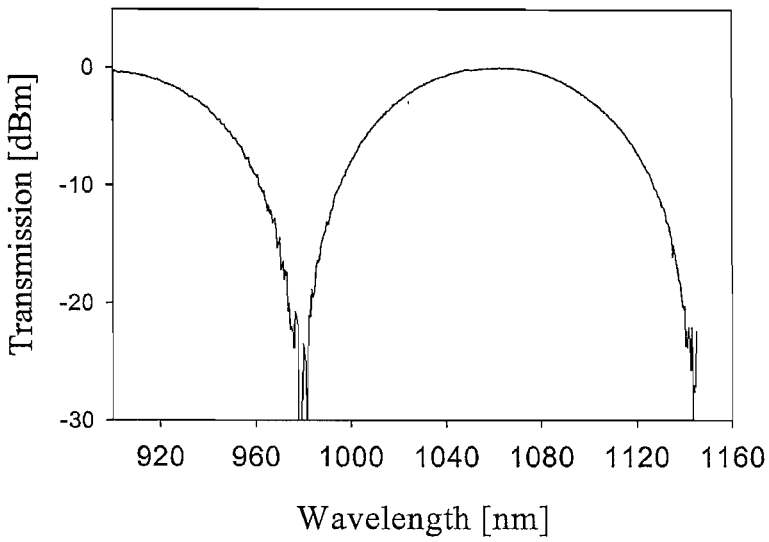

Figure 3.3: White light source characterisation for WDM

3.2.2 *SESAM*

SESAM parameters like saturation energy, modulation depths, absorption wavelength and reflectivity spectrum can be selected through choice of SESAM and/or cavity dimension so that it is suitable for a particular laser medium [36]. However, conflicting requirements like high and low finesse top mirror, low modulation depth to suppress Q-switching instabilities for stable c.w. mode-locking [37, 38] and high modulation depth to achieve shorter pulses [39-42] and provide enough perturbation for reliable self starting, makes the choice for the most suitable SESAM in our cavity difficult. We decided to adopt an empirical approach to select the most suitable SESAM from the variety of SESAMs supplied by Professor U. Keller from ETH Zurich.

We were supplied with eleven SESAMS, with different modulation depths and recovery times. These SESAMs are of the low finesse Antiresonant Fabry-Perot Saturable Absorber (A-FPSA) type [43, 44]. Low finesse A-FPSA devices use the air-InGaAs interface as the top-mirror (~30% reflection), which avoids post-growth processing. Constructing the FPSA to operate at antiresonance (achieve by adjusting SESAM dimensions) gives minimal GVD and makes the device broadband, hence suitable for use in ultrafast lasers.

The AFPSA generally has a semiconductor (III-V InGaAs) Bragg mirror at the bottom and a dielectric mirror at the top with the saturable absorber in-between. Sometimes there are transparent spacer layers between them. Modern semiconductor growth technology and improved bandgap engineering have allowed for accurate control of the device parameters

such as absorption wavelength, saturation energy, and recovery time. The reflectivity spectrum is determined by the number of layers in the bottom mirror (typically ~35 for our SESAMs), and by the dimension of the Fabry-Perot cavity. The absorber recovery time is controlled by growth temperature; a lower growth temperature produces a faster recovery time. These eleven SESAMs can be distributed into two main groups. One group consists of SESAMs having low modulation depth (1% – 4%) with fast recovery times and the other group having high modulation depth (10% - 17%) with a slow recovery time of ~3 ps and a fast recovery time of ~100 fs. They were tested using a similar oscillator cavity as a test bed, by Dr Lefort (who has now left our group) and Dr Price, and two samples from the group having high modulation depth were found to work best with the laser cavity of our oscillator.

The use of saturable absorbers for passive modelocking often results in Q-switch modelocking (QML) due to the saturable absorption losses. In QML, the output modelocked pulses are under a Q-switched envelope thereby generating output power with high unwanted amplitude fluctuations. This Q-switch instability becomes more evident when SESAMs with high modulation depths, and high gain saturation active media having smaller cross section areas (commonly found with broad bandwidth emission gain medium, i.e. Yb^{3+} used for short pulse generation), are used [37]. Honninger *et al.*, from Professor Keller's group in ETH Zurich [37, 45], found that the critical intracavity pulse energy to avoid this Q-switch instability, which impedes stable c.w. modelocking, can be estimated from the formula given in equation 3.1.

$$E_{P,c} = (F_{sat,L} A_{eff,L} F_{sat,A} A_{eff,A} \Delta R)^{1/2} \qquad (3.1)$$

where $F_{sat,L} = h\nu/[2\,(\sigma_{em} + \sigma_{abs})]$ is the gain saturation fluence, $h\nu$ is the lasing photon energy, σ_{em} is the emission and σ_{abs} absorption cross section of the lasing wavelength. $F_{sat,A}$ is the SESAM saturation fluence. $A_{eff,L}$ and $A_{eff,A}$ are the effective laser mode areas of the gain medium and on the SESAM respectively. ΔR is the modulation depth.

From equation 3.1, we can see that the critical energy increases proportionally to the effective mode areas and modulation depth but inversely with the cross sectional area of the gain medium. Since the saturation fluences are fixed by the gain medium and SESAM, one possibility of improving c.w. mode-locking stability is to reduce the effective pump mode area (spot focus) incident on the SESAM, hence reducing the critical pulse energy, as described in

section 3.3.1 below. For my cavity the radius of the spot size incident on the SESAM was ~ 3.4 μm. This corresponds to an incident spot size area of ~36.3 μm^2 on the SESAM. Using σ_{em} and σ_{abs} values estimated in section 2.3, the effective mode area of the laser to be 68 μm^2 and the SESAM parameters shown in figure 3.4 (b), we calculate the critical intracavity pulse energy to be ~ 2 nJ.

The SESAM used in my cavity has a temporal response with a slow time constant of ~3 ps and a fast time constant of ~100 fs. In the femtosecond pulse regime, the longer time response (slow time constant) is considered, which provides more reliable self-starting and stable mode-locking. It has a modulation in reflectivity of ~16 %. The reflectivity vs wavelength and saturation fluence required for bleaching are shown in figure 3.4 (a) and (b).

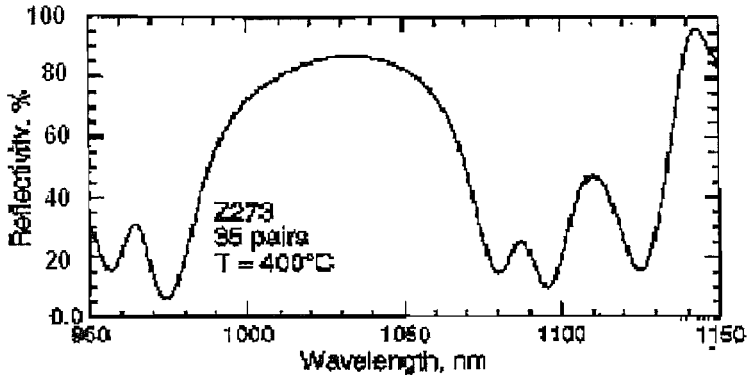

(a)

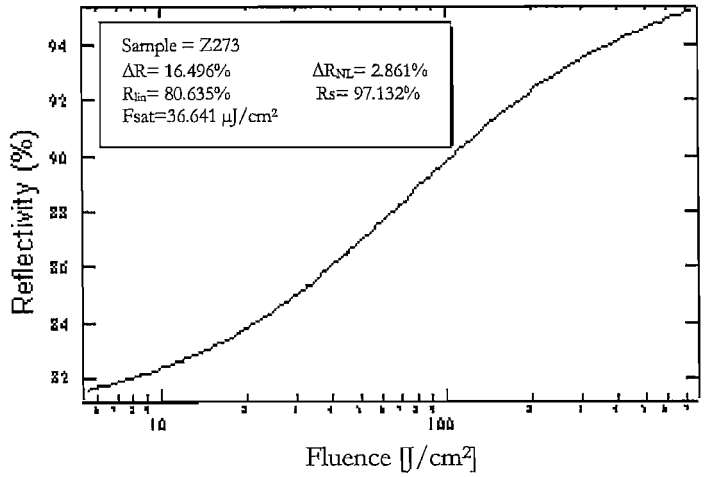

(b)

Figure 3.4: SESAM reflectivity against (a) wavelength and (b) incident pulse fluence

To optimise the performance of the selected SESAM within my cavity, an empirical approach was again adopted. Observing equation 3.1, I realised that the most convenient approach was through fluence control. In section 3.3.1, I will describe the experimental

process that was used to vary the fluence and obtain the optimum performance from the chosen SESAM for my cavity.

3.3 Development and performance of oscillator

Many parameters and dimensions of the cavity need to be considered and experimentally tested to provide optimum performance. For example, the combination of lenses to give an optimum spot size on the SESAM, alignment and separation of the diffraction gratings to obtain the best reflection efficiency and suitable anomalous dispersion, the length of Yb^{3+} doped fibre used within the cavity and settings on the polarisation controllers to achieve mode-locking and best output power coupling from port 3 (see figure 3.2).

3.3.1 *Telescope lens combination pair.*

In section 3.2.2, I mentioned that the incident intensity on the SESAM plays a crucial role in the performance of the cavity's c.w. modelocking stability and self-starting reliability. The incident intensity plays a part in optimising the modulation depth (see figure 3.4(b)), keeping nonsaturable absorption at a minimum, relaxes self-starting requirements, shortens the self-start time and reduces the critical energy required to avoid Q-switching instabilities (see equation 3.1 in section 3.2.2). The incident intensity on the SESAM can be adjusted by adjusting the incident mode area/spot size using the telescope lens combination. However, there is an upper limit determined by the onset of multiple pulsing [41, 42, 46] as a result of, the high saturation fluence of the beam incident on the SESAM, or SESAM burning due to Q-switching instabilities. Therefore, we had to experimentally find a lens combination that would give us the best performance for a particular SESAM. Different combinations were tested and table 3.1 below describes their performance.

A rule of thumb, suggested by Professor U Keller at ETH Zurich, was that the SESAM operated best (avoiding multipulsing or SESAM burning) with an incident pulse fluence ~ 3-5 times the SESAM saturation fluence [41, 42, 46, 47]. An experiment was conducted to determine the intensity of the beam incident on, and reflected from, the SESAM during modelocking operation. A piece of glass plate was used to pick off the beam. It was inserted, at an angle, in the path of the beam travelling towards the SESAM. The 8% (4% reflection at each surface of glass) reflection power was measured for both the forward and reflected beam

of the SESAM. It was found that we were actually operating at approximately 5-6 times the saturation fluence at ~ 4mW reflected power. There was however occasional SESAM burning occurring due to Q-switching instabilities within our cavity and also because we were operating at the fluence limit.

Lens Combination f_1:f_2	**Performance**	**SESAM burning**	**Remarks**
11:3	No mode locking. No Q-switching	Yes, often	Combination used in other oscillator.
11:6	QML	Yes, Often	
11:8	Stable c.w. mode-locking	Yes, uncommon	Present and best combination
11:11	Stable c.w. mode-locking	Yes, uncommon	

Table 3.1 Comparison of lens combination within cavity for f_1:f_2

3.3.2 *Length of Yb^{3+} fibre within cavity.*

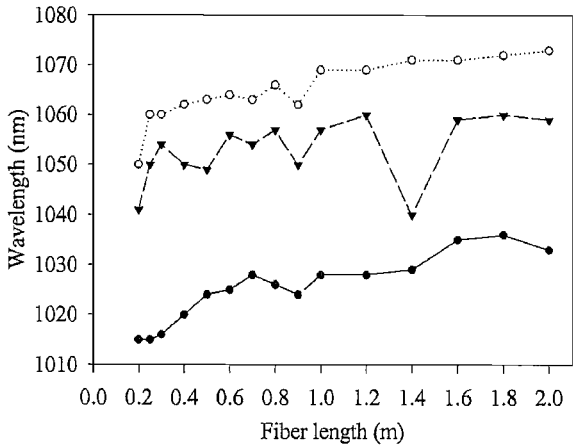

Figure 3.5: Maximum (open circles) and minimum (closed circles) lasing wavelengths with length of Yb-fibre. The centre curve (closed triangles) shows the wavelength at which the laser gave maximum output power. (Figure obtained from [48]).

As the c.w. lasing spectral tuning range varies with different lengths of Yb^{3+} doped fibre [49], I needed to determine the amount of doped fibre length that would give sufficient lasing

bandwidth for ultrashort pulse generation. A wavelength tunable, c.w., FP, laser cavity, with a bulk dispersive grating for wavelength selective feedback, was constructed by Dr Price. He varied the length of the Yb^{3+} doped fibre within the cavity and characterised the lasing bandwidth for each length. The results are shown in figure 3.5. From his results, I was able to determine that the 75 cm of doped fibre (which was used in our cavity) gave sufficient gain bandwidth between 1028 nm and 1063nm. The centre lasing wavelength changes with fibre length. With shorter lengths, the lasing peak is centred at the shorter wavelengths due to the lower re-absorption of the initial stimulated emission wavelength, at ~ 1040 nm, near the pump end (see chapter 2). At a length of 75 cm, the peak lasing wavelength was centred at ~1054 nm.

3.3.3 *Diffraction grating and optimisation of its alignment and separation distance.*

The diffraction gratings used for the anomalous dispersion segment of the cavity are from Richardson Gratings Laboratory. They have 600 grooves/mm and a blaze angle of 17.5°. Therefore to obtain maximum efficiency from the diffraction gratings, the gratings have to be aligned such that the incident angle is approximately between 30°-35° (twice the grating's blaze angle). The diffraction grating handbook [50] specified that the efficiency characteristics for this diffraction grating is >95% at 1060 nm, our operating wavelength.

The length of fibre determines the normal dispersion within the cavity and the separation distance between the grating pair determines the anomalous dispersion. This affects the performance of the oscillator. In a paper written by Tamura K *et al.* [10], the authors varied the net GVD within a stretched-pulse, mode-locked, fibre ring laser and measured the output pulse energy, and pulse width, for a given input pump power. They found that different output pulse widths and energies were obtained and the pulse parameters varied with settings of the polarisation controllers in the net positive dispersion regime. Generally, pulses of higher energy but with larger chirp were produced when there was net positive dispersion. Further, contrary to popular belief that a minimum pulse width is achieved at net zero dispersion; the shortest pulse duration was obtained by having slight net positive dispersion. These results were obtained because of the higher chirp and stretching factors achievable in the net positive regime compared to the net negative regime which is limited by soliton effects.

3.3.4 *Performance of oscillator clone with 1.75m cavity fibre length.*

The total fibre length in the clone oscillator cavity was 1.75m (75 cm was Yb-doped fibre and 1 m was passive standard SM fibre). The power from output port 3 was measured as a function of input pump power and is shown in figure 3.6 (a). We can see that the output power increases almost linearly with input power and flattens out at input powers > 235 mW. The flattening, I believe, was due to gain of the active medium being saturated at these input pump powers. However stable c.w. modelocking operation was only achievable when output power from port 3 was set to ~ 2 mW (~ 46 pJ pulse energy). The threshold pump power for mode-locking was approximately 70 mW with negligible hysteresis was observed.

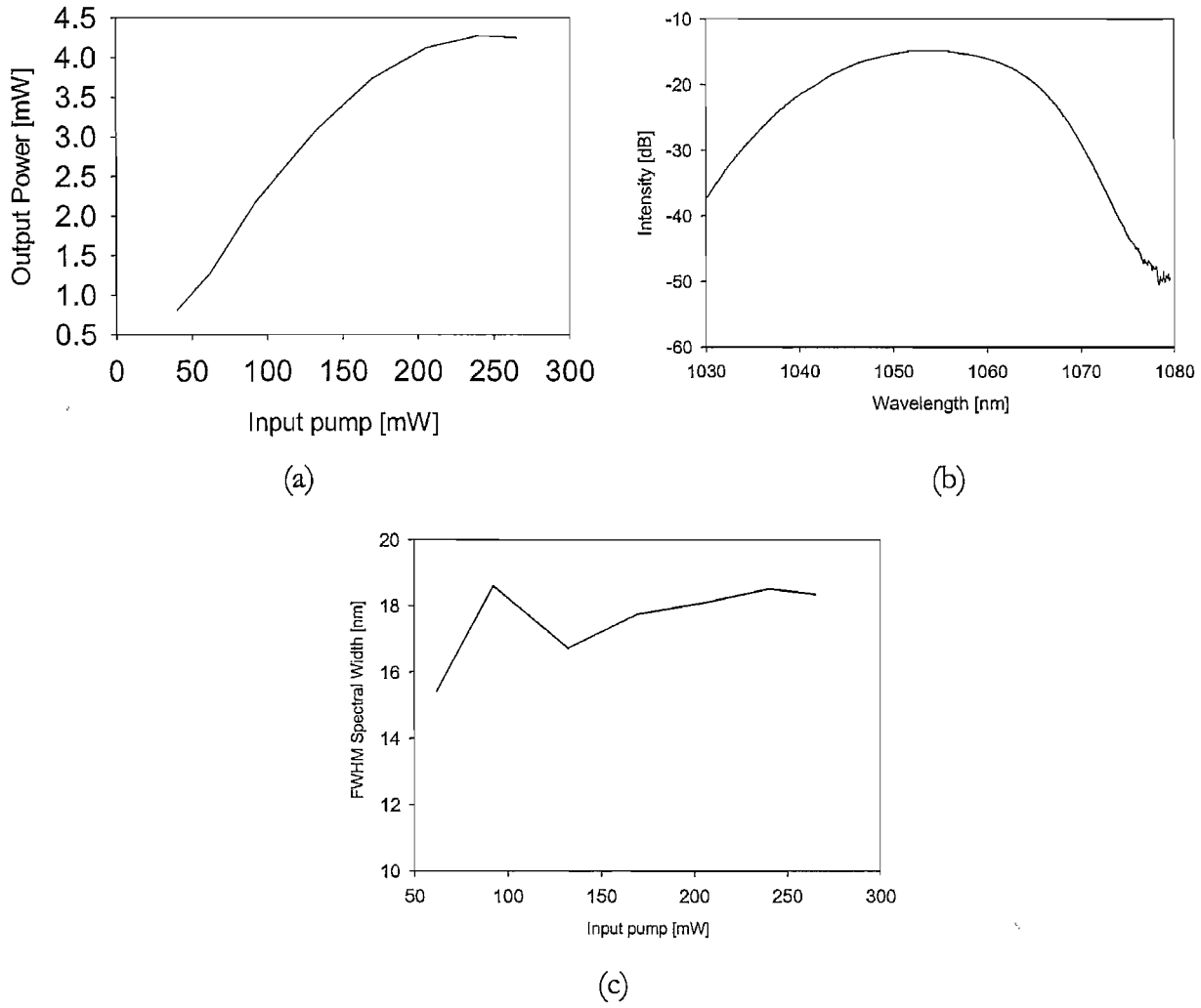

Figure 3.6: Results taken with grating separation of 6.3cm (a) Output power at port 3 against input pump power and (b) output spectrum at port 2 (FWHM=18 nm). (c) Output spectral width (FWHM) against input pump power at a grating separation of 6.3cm.

The compensating anomalous dispersion was varied by changing the grating separation. An initial grating separation was chosen to be ~6.3 cm (by taking a linear interpolation from the optimum grating separation with the fibre cavity length, found in the oscillator built by Dr Price) and it was found that this grating separation provided the most stable modelocking. The net 2nd and 3rd order dispersion generated within the cavity at this separation was 1 x 10^4 fs^2 and 2.3 x 10^5 fs^3 at 1056 nm respectively. The output spectrum from port 2 is shown in figure 3.6 (b) and the corresponding FWHM spectral width obtained with this configuration was ~ 18nm. The FWHM bandwidth of the output spectrum from port 2 was taken as a function of input pump power, at a grating separation of 6.3 cm. The results obtained are presented in figure 3.6 (c). We can see that upon reaching the mode-locking threshold pump power (~ 70 mW), it was found that the change in spectral width (FWHM) was relatively flat across a range of input pump powers but peaked at a certain input pump power.

Further characterisation of the performance of the cavity was carried out by taking the autocorrelation of the compressed output pulses and measuring the timing and amplitude jitter of the oscillator. By compensating the negatively chirped output from port 2 (see figure 3.2) with a positively dispersive standard SM fibre, the output pulse width could be compressed. Chirp compensation by the external compressor was varied by cutting back the fibre length and the output autocorrelation taken. Figure 3.7 (a) shows the pulse autocorrelation experimentally taken when the fibre was cut back from 1.4 m to 0.712 m. The minimum output pulse width of ~141 fs (assuming Gaussian profile) was obtained when the compressor was cutback to a length of ~1.1 m. Autocorrelation traces from different external compressor lengths are shown in figure 3.7 (b).

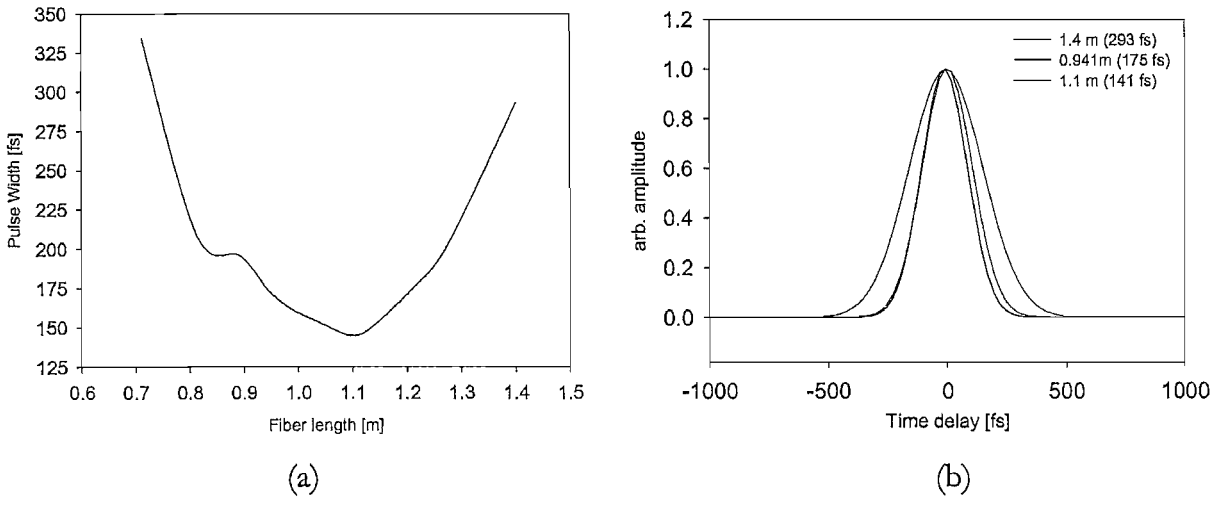

Figure 3.7: (a) Compressed pulse duration obtained when fibre compressor was cut back. (b) autocorrelation traces taken at different compressor lengths. (pulse duration in brackets).

The RF measurement of the oscillator was used to calculate the timing and amplitude jitter [51]. It also provides the actual repetition rate of the output pulses from the oscillator, which was ~ 44 MHz. Figures 3.7 (a) and (b) show the fundamental and 8th harmonic spectrum respectively obtained using an RF spectrum analyser.

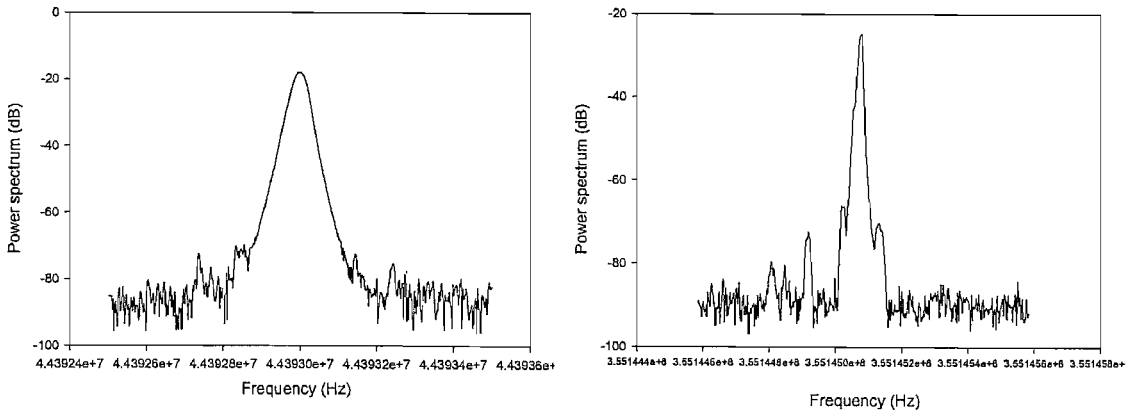

(a) (b)

Figure 3.8: RF spectrum of output (a) fundamental frequency with Δf_{res}= 30Hz (b) 8th harmonic with Δf_{res}= 10Hz.

A power spectral density sketch indicating the individual contributions from the amplitude noise and time jitter is shown in figure 3.9 below.

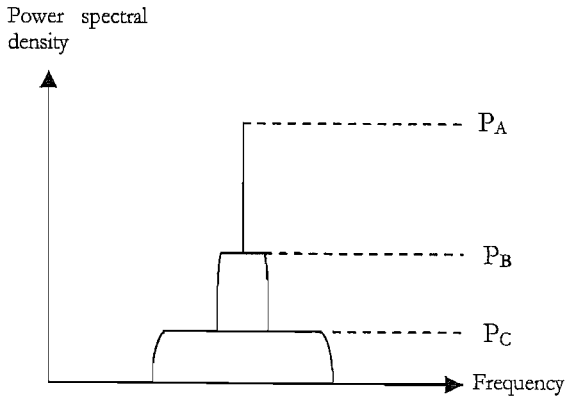

Figure 3.9: Power spectral density (PSD) sketch of various contributions of components to fluctuations.

P_A indicates the power of the pulse, P_B represents the temporal jitter and P_C indicates the amplitude fluctuations. The expression obtained for amplitude fluctuation is given by equation 3.2 [51],

$$\Delta E/E = [(P_C/P_A)_0 . \Delta f_A / \Delta f_{res}]^{1/2} \quad (3.2)$$

where E is the energy and ΔE is the variation due to amplitude noise, P_C and P_A were taken from the fundamental spectrum, and are defined above, Δf_A is the frequency width of amplitude noise and Δf_{res} the resolution bandwidth. As there is no distinct pedestal in figure 3.8 (a), we take the base of the spectrum as the frequency width for the noise fluctuation. From figure 3.8 (a), we obtained Δf_A= 250 Hz, Δf_{res} = 30 Hz and P_C/P_A = -57 dB = $10^{-5.7}$. Using equation 3.2, we get an amplitude noise ratio $\Delta E/E$ of 0.41%, which is very small.

Since the amplitude noise is very small, we can ignore it when estimating the timing jitter. The jitter noise is evaluated with the higher order noise components. Equation 3.3 below describes the calculation for the timing jitter.

$$\Delta t/T = (2\pi n)^{-1}[(P_B/P_A)_n . \Delta f_J / \Delta f_{res}]^{1/2} \quad (3.3)$$

where T is the period and Δt is the deviation due to timing jitter, n is the order of the spectrum, Δf_J is the frequency width of the timing jitter PSD. From figure 3.8 (b), we obtained n= 8, P_B/P_A = -51dB= $10^{-5.1}$, Δf_J = 100 Hz and Δf_{res} = 10 Hz. Using equation 3.3, we obtain $\Delta t/T$ = 0.018% and timing jitter= 4 ps.

Another performance criterion is the oscillator's self-starting time. Placing a chopper wheel in the cavity to block and unblock the cavity at a known rate, we measured the self-starting time for stable operation, which we found to be 10 ms.

3.4 Improvements to the oscillator.

In the earlier sections, I described the various intra-cavity components of the clone oscillator and the work carried out to characterise their performance. The performance of the oscillator was demonstrated with a total cavity fibre length of 1.75m and a stable and self-starting stretch pulse passively mode-locked oscillator with timing jitter of ~4 ps, and low amplitude noise (0.41%) was achieved. It has a FWHM spectral bandwidth of 18nm and an output pulse compressible to 141 fs. However this clone oscillator setup was found to burn the SESAM more frequently and to be less stable compared to the other oscillator built by Dr

Jonathan Price. This may be because of the different SESAM used by the two oscillators and because the intra-cavity parameters of both are slightly different. In the following sections, I will describe the investigations carried out to improve the oscillators' performance (i.e. more stable c.w. modelocking and to produce shorter duration pulses), and an alternative technique to provide pulse initiation in a FP cavity without the use of a SESAM.

3.4.1 *Altering present parameters of components within cavity.*

Our initial approach was to change the parameters of the components within the cavity to see if small changes within the present cavity could produce better performance.

3.4.1.1 Adding high birefringent Fibrecore boron doped fibre into cavity fibre.

In the previous chapter we mentioned that one of the differences between the clone oscillator and the oscillator Dr Price had built was an additional ~20 cm of boron doped fibre (highly birefringent fibre) from Fibrecore. According to Dr Laurent Lefort this enhances and assists the non-linear polarisation switching by providing better defined polarisation birefringence of the cavity, thereby improving the self-starting and mode locking stability from environmental disturbance. This was substantiated by M. Hofer *et al.* [52]. They found that adding birefringence to the cavity fibre prevents early saturation of the nonlinear reflection coefficient which causes mode-locking instability. However, they also mention that if the birefringence of the cavity fibre was too high, it would result in group velocity walkoff between the polarisation eigenmodes. Dr Price and I measured the birefringence beat length of the highly birefringent fibre to be ~ 26mm (see figure 3.10 (a)). Figure 3.10 (b) illustrates the position where this fibre was added.

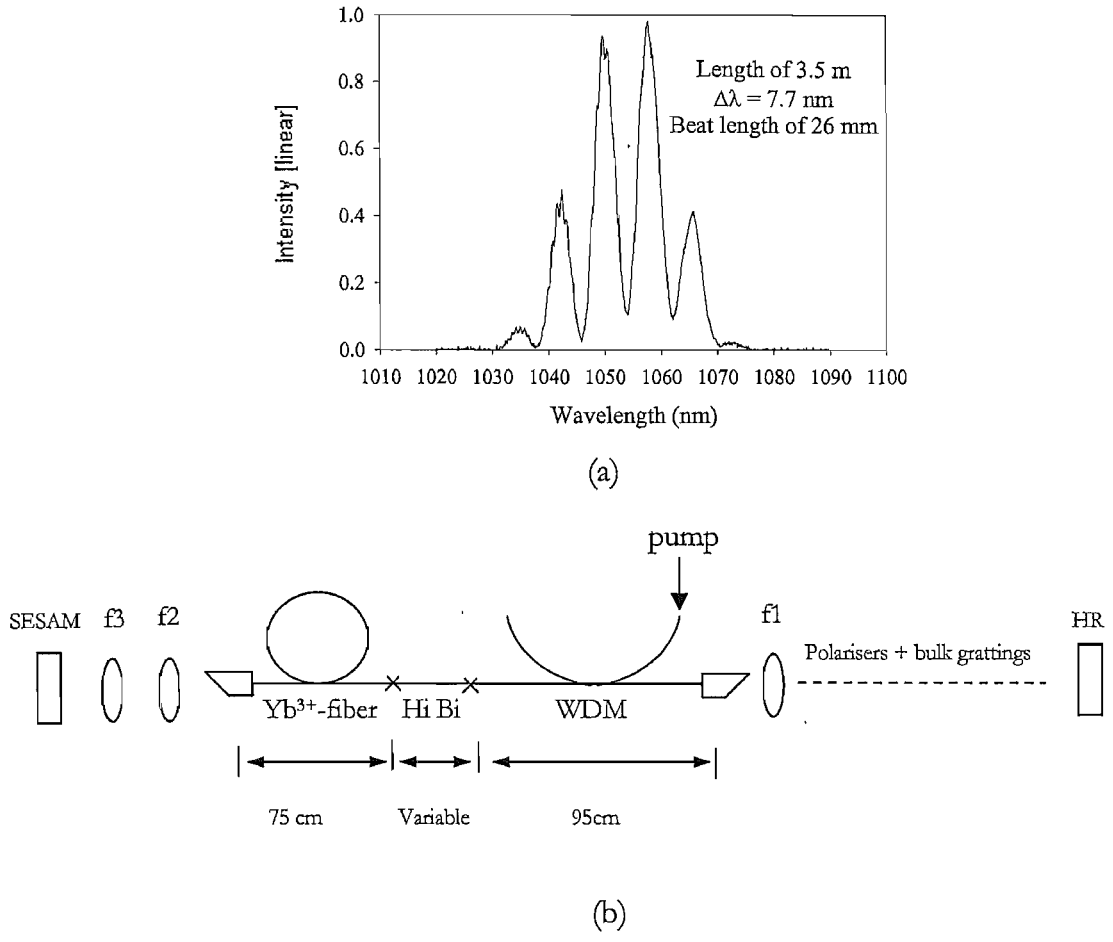

Figure 3.10: (a) Spectrum obtained at the output of the highly birefringent (Hi Bi) fibre using a broad input spectrum (10 dB bandwidth of ~ 30 nm) polarised at 45° to the two orthogonal axes of the Hi Bi fibre. (b) Schematic showing position in cavity where Hi Bi fibre was added and varied.

The performance of the oscillator, without the highly birefringent (Hi Bi) fibre and with various lengths added, is summarised in table 3.2. Initially, without the Hi Bi fibre, the oscillator was prone to SESAM damage [47] until the waveplates were correctly adjusted. The mode-locking operation was relatively more susceptible to mechanical vibration compared to Dr Price's cavity. We also had difficulty obtaining stable operation with output powers above 2 mW.

After testing with various lengths of Hi Bi fibre, the optimal length was found to be 10 cm which corresponds to ~ 4 beat lengths. At this length, the oscillator operated with rapid self starting time, robust and stable mode-locking against mechanical perturbation and higher output powers. However, if more than 10 cm of Hi Bi fibre was added, the self-starting time became slower and mode-locked operation was less robust against mechanical perturbation. In view of these findings, 10cm of Hi Bi fibre was added into the cavity which was used for later experiments. The FWHM bandwidth of the output pulses was unchanged at 18nm.

Length of Hi Bi fibre (cm)	Total fibre length (cm)	Grating separation (cm)	Lenses (f = mm)	Summary of oscillator performance
0	170	6.4	f1 = 4.5 f2 = 11 f3 = 8	Output at port 3 = 2.0 mW (low) **Characteristics:** Intermediate self-start time (~0.2s). Susceptible to Q-switching if table is knocked. **SESAM damage?** Common until correct waveplate settings established.
5	161	5.8	f1 = 4.5 f2 = 11 f3 = 8	Output at port 3 = 2.3 mW **Characteristics:** Slow (~5-10s), but reliable self-start. Susceptible to Q-switching if table is knocked. **SESAM damage?** Rare
10	171	6.15	f1 = 4.5 f2 = 11 f3 = 3.1	Output at port 3 = 3.12 mW **Characteristics:** Rapid self-start time (<10ms). Robust, stable operation. **SESAM damage?** Rare
14	172	6.4	f1 = 4.5 f2 = 11 f3 = 3.1	Output at port 3 = 1.7 mW **Characteristics:** Slow (~5-10s), but reliable self-start. Susceptible to Q-switching if table is knocked. **SESAM damage?** Rare
20	177	6.75	f1 = 4.5 f2 = 11 f3 = 3.1	Output at port 3 = 2.0 mW **Characteristics:** Poor self-start. Unstable against perturbations. **SESAM damage?** Rare

Table 3.2: Summary of oscillator's performance with varied lengths of Hi Bi fibre.

3.4.1.2 Limiting effects of the bandwidth of components within present cavity setup.

Another important limiting factor to achieving the shortest possible pulses from the oscillator is the bandwidths of the components within the cavity. Figure 3.11 below shows the bandwidth of the different components.

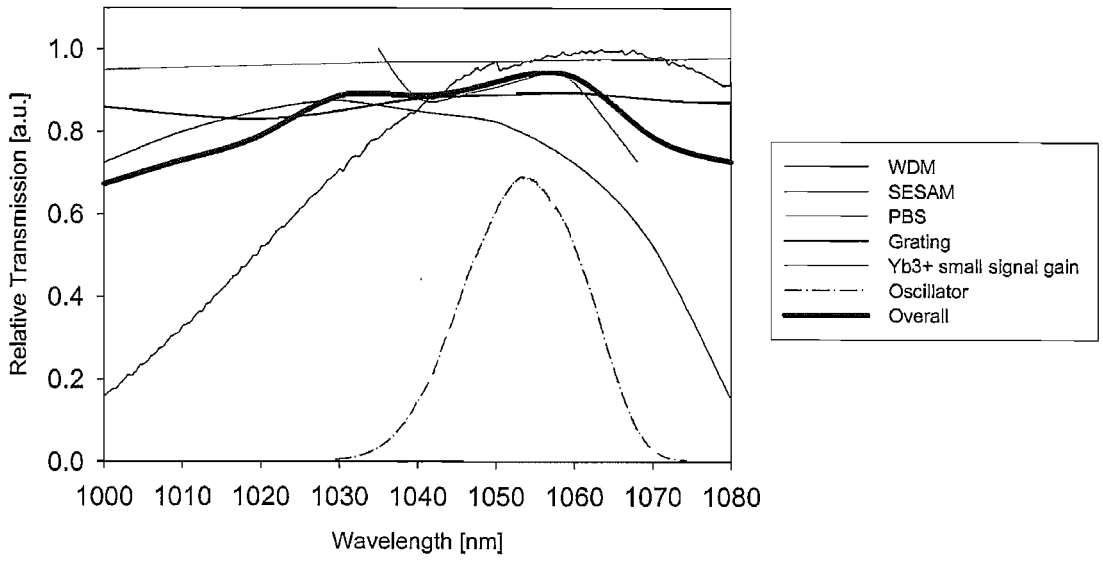

Figure 3.11: Normalised spectral bandwidth of components within the cavity.

Figure 3.11 shows the spectral reflectivity data of the SESAM (obtained from Professor U Keller of ETH), the transmission bandwidth of the WDM (taken from our white light characterisation), the reflection efficiency of the diffraction grating (given by the Diffraction Grating Handbook [50] from Richardson Labs), the small signal gain of Yb^{3+} (obtained experimentally) and the transmission bandwidth of the PBS (taken from the specification sheet of the Newport catalogue 2002).

The PBS and diffraction grating have flat transmissions between 1030 nm and 1080 nm. The gain of the Yb^{3+} fibre started to drop at 1070 nm, the WDM limits the oscillator's output at shorter wavelengths and the SESAM Z273, with a steep cut-off at 1060 nm, limits the longer wavelengths. The spectral output from the oscillator is also plotted in the diagram. If we were to improve the spectral bandwidth of the components used in the cavity (i.e. use SESAMs shifted to longer reflectivity wavelengths), we might reduce the restriction imposed on the bandwidth of the output pulses by the intracavity components and achieve shorter compressible pulse durations.

3.4.1.3 Changing intra-cavity SESAM.

In our oscillator, we used a SESAM to initiate the mode-locking process. SESAMs operate in a certain wavelength range; therefore it would be a limiting criterion in the operational bandwidth of the oscillator. From figure 3.11, it was evident that SESAM Z273 limited the longest wavelength with a sharp cut-off at ~1060nm and the shorter wavelength cut-off was determined by the WDM. Therefore in order to achieve wider bandwidth performance at the longer wavelengths, broader bandwidth SESAMs are needed. Two new SESAMs were received from Felix Brunner of ETH Zurich. They were SESAMs Z373 and C275. The reflectivity spectra of all three SESAMs are shown in figure 3.12.

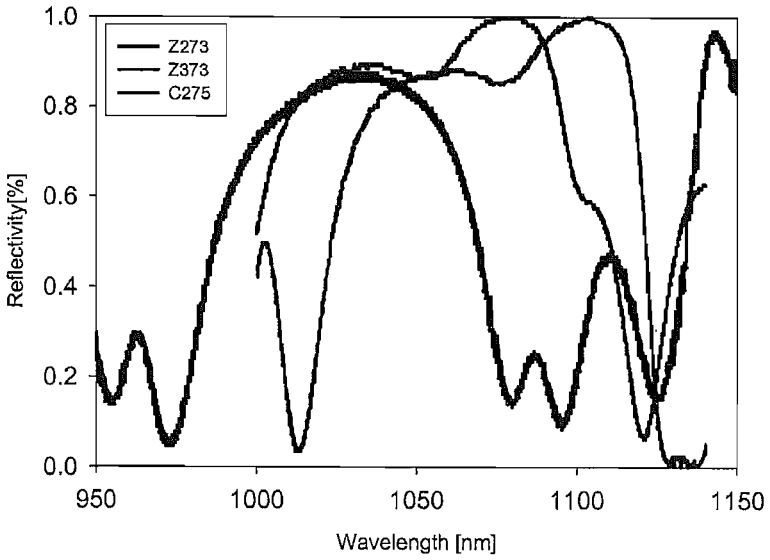

Figure 3.12: Reflectivity spectrum of SESAM Z273 (black), Z373 (blue) and C275 (red).

The C275 FWHM wavelength reflectivity range stretches between 1000 nm and 1100nm and the Z373's wavelength range stretches between 1023 nm and 1120 nm. The original SESAM Z273 has a spectral reflectivity range between 990 nm and 1070 nm. Clearly SESAM C275 and Z373 have broader reflectivity bandwidths and they operate at longer wavelengths compared to Z273. But wavelengths below 1020 nm are cut-off by the WDM (see figure 3.11), therefore taking this into consideration, the SESAM with the widest effective reflectivity bandwidth is the Z373. Furthermore, the Z373 has the flattest reflectivity spectrum across the whole bandwidth. However, as mentioned in section 3.2.2, other SESAM parameters are also important for optimal performance. Therefore the oscillator performance was analysed with all three SESAMs. Figure 3.13 presents the output pulse bandwidths obtained for all three SESAMs with the same oscillator cavity.

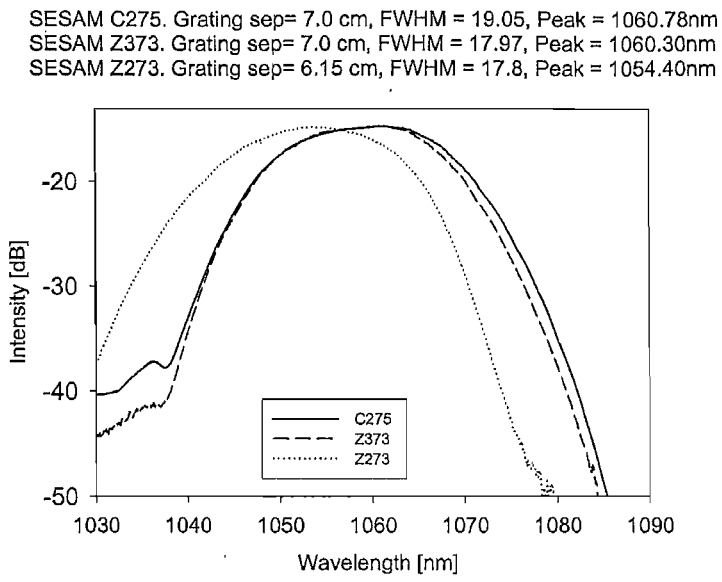

Figure 3.13: Output pulse bandwidth using different SESAM with optimal grating separation distance.

In figure 3.13, we immediately see the effects on the output spectra of using SESAMs C275 and Z373. The output spectrum is shifted to the longer wavelengths and centred on 1060 nm. However there isn't a significant improvement to the 3dB bandwidth. Compared to the Z273 SESAM, the C275 has an improved 3dB bandwidth of ~1nm and Z373 an improvement of ~0.2 nm.

Autocorrelations of the output pulses were taken using all three SESAMs and the traces obtained are shown in figure 3.14. Similar FWHM pulse durations were obtained for all three SESAMs. The Z273, Z373 and C275 produced pulses with FWHM duration of 148.14 fs, 145.7 fs and 145.1 fs respectively. Although there is not a significant reduction to the output pulse widths, overall we managed to obtain a broader output spectrum centred at longer wavelengths giving the oscillator the potential to achieve wider output pulse bandwidths. From figures 4.12 and 3.13, it might seem that C275 is a better choice than Z373. But the Z373 provided better mode-locking stability and self-starting reliability. This could be due to the other SESAM parameters of the Z373, such as modulation depth, saturation intensity and SESAM recovery times [35, 36, 38] being better suited for our cavity. Therefore the SESAM chosen for further experiments was the Z373.

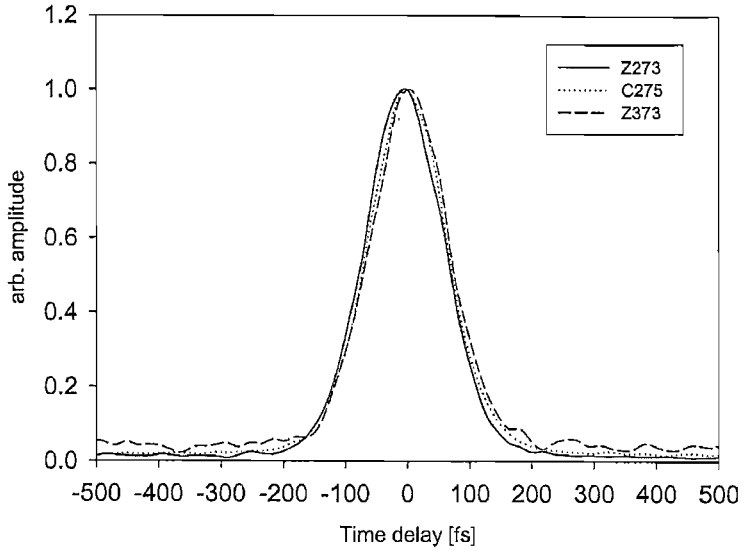

Figure 3.14: Autocorrelation traces of the output pulses using SESAMs Z273, C275 and Z373.

3.4.1.4 Reducing cavity fibre length to 1.15 m.

As the pulse propagates through the cavity fibre, it accumulates both +GVD and TOD. A pair of intra-cavity diffraction gratings was added to provide the required 2nd order dispersion (-GVD) compensation for the pulse. However, the TOD generated by both fibre and gratings are of the same sign and hence TOD accumulates as the pulse travels within the cavity. The effects of TOD are detrimental and limit the minimum pulse widths achievable from our cavity [53, 54]. TOD causes distortion to the intra-cavity pulse and inhibits the generation of transform limited Gaussian pulses [10].

Our approach to reduce the TOD effects within the cavity was to shorten the cavity fibre length. Since the amount of GVD and TOD contributed are proportional to the fibre length and separation distance of the grating, the shorter the cavity fibre length the less +GVD we need to compensate. This leads to shorter grating separation and hence lower TOD contribution. Another possible solution was to use prisms instead of diffraction gratings to compensate the +GVD. This was because using prisms as a dispersive delay line (DDL), contributes TOD of an opposite sign to the fibre providing compensation [55, 56]. In this section, we shall describe the oscillator's performance after shortening the cavity fibre.

The total cavity fibre length was shortened to 1.15m by reducing the fibre at the ends of the WDM coupler to 15 cm at each end. Effectively, the length of fibre was shortened by 1.2 m (double pass considered) which corresponds to a reduction in TOD by approximately 2.1 x 10^4 fs^3. Figure 3.15 shows the new dimensions of the different types of fibre within the cavity.

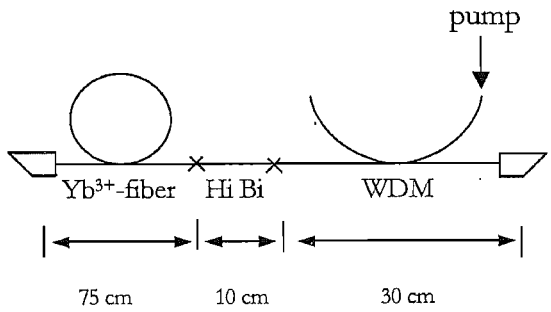

Figure 3.15: New dimensions for shortened cavity fibre lengths

The oscillator was characterised by varying the grating separation over the net negative to the net positive dispersion regimes and the shortest compressed pulse duration was obtained at a given separation distance. Output pulse FWHM bandwidth for the various separation distances was also taken and the time bandwidth product calculated. Figure 3.16 shows the results of the autocorrelation and output spectra taken from the oscillator with varying approximate net cavity dispersion.

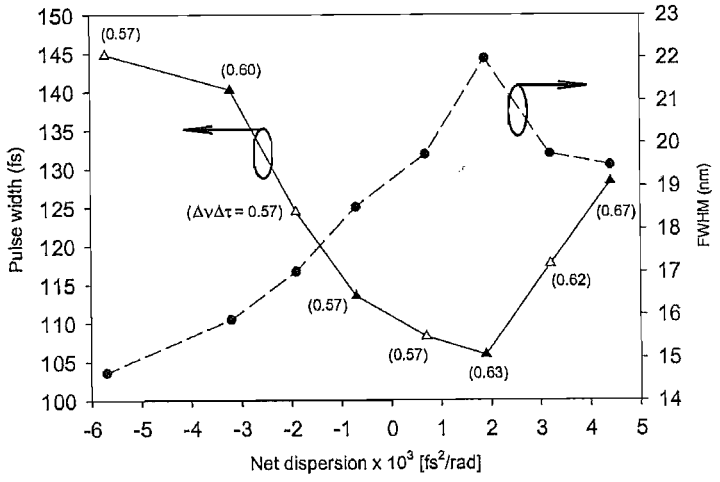

(a)

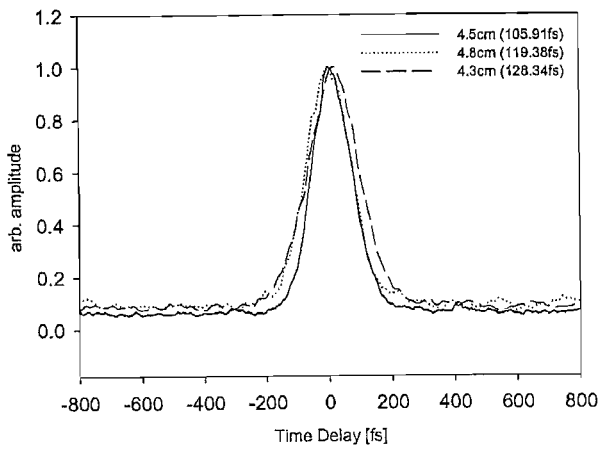

(b)

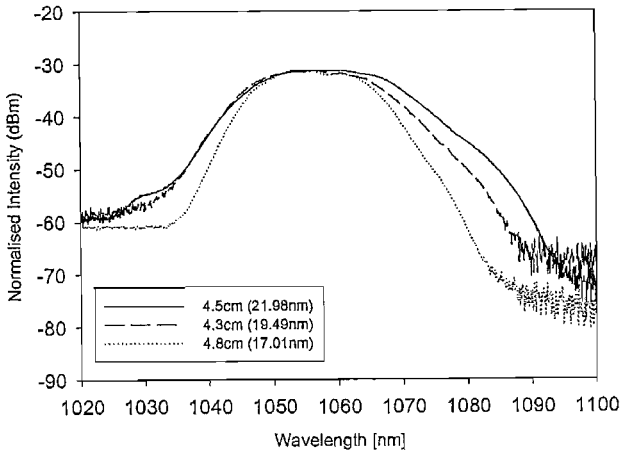

(c)

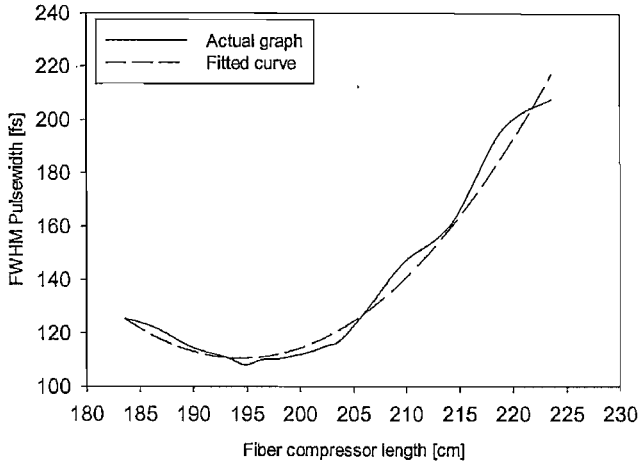

(d)

Figure 3.16: (a) Plot showing the pulse width and spectral FWHM bandwidth against the net cavity 2nd order GDD. The time bandwidth product for the corresponding pulse is labelled in brackets. (b) Autocorrelation traces for output pulse (FWHM pulse width are in brackets) and (c) spectra at grating separation 4.3 cm, 4.5 cm and 4.8. (d) Pulse duration against compressor length at optimum grating separation of 4.5 cm.

Figure 3.16 (a) shows the behaviour of the temporal and spectral width of the pulse changes as the grating separation is varied between 5.1 cm to 4.3 cm (in steps of 0.1 cm except 5.0 cm was omitted) and the net GVD of the cavity goes from net negative to net positive. The behaviour is similar to that found by Tamura K *et al.* [10]. The output soliton pulses in the net negative GVD regime were broader and narrowed as the net dispersion was brought closer to net zero GVD (which was theoretically calculated to be at a grating separation of ~4.65 cm). However, the optimum grating separation, which generates the shortest pulses with widest spectral width, was not found at net zero GVD but at slightly positive GVD. These soliton pulses also had lower chirp compared to pulses within the net positive regime. The time bandwidth products of the shortest pulses were in the range of 0.57 – 0.67, indicating some departure from the transform-limited Gaussian pulse shape. This could either be due to uncompressed TOD or the TOD introduced by the compressor fibre or both. The maximum average output power obtainable (to maintain stable mode-locking) from port 3 was found to be ~ 2 mW (~ 32 pJ) in the net negative GVD regime but was higher (indicating higher pulse energy) in the net positive GVD regime ~ 3 - 4 mW (~ 65 pJ).

Figure 3.16 (b) shows the autocorrelation trace at different net dispersion regimes (corresponding to grating separations of 4.3 cm (4.4 x 10^3 fs^2 at 1056 nm), 4.5 cm (2 x 10^3 fs^2) and 4.8 cm (-2 x 10^3 fs^2). We found that the minimum compressible pulse width achieved at

the optimum grating separation of 4.5 cm was 106 fs and that the FWHM spectral width, also widest at this point (see figure 3.16 (c)), had a bandwidth of 21.98 nm. The pulse width against compressor length at this optimum grating separation was recorded and plotted in figure 3.16 (d). The curve was fitted and the minimum point, from the fit, was estimated to be 109 fs long.

While characterising the performance of the cavity with various grating separations, we found that when the cavity was operating in the soliton regime, mode-locking was stable but prone to multi-pulse especially when the pump power was increased. Slight positive GVD gives excellent mode-locking performance but the oscillator becomes unstable and difficult to modelock if the net positive GVD becomes too large.

On the whole, reduction of the cavity fibre length has improved the performance of the oscillator. The minimum compressible output pulse width was reduced from 141 fs (see section 4.3.5) to 108 fs and the pulse bandwidth widened by ~ 4 nm. We believe the improved performance was brought about by a reduction in the amount of TOD within the cavity. Following a reduction in grating separation, the estimated TOD contribution by the gratings reduced by a third (calculated to be 2.1 x 10^4 fs^3 using Dr Chris Barty's grating dispersion calculation spreadsheet). The results from this experiment suggest that if prisms were used instead of diffraction gratings, we should achieve a much better performance as the prisms partially compensate the TOD effects from the fibre.

3.4.2 *Adding new components within cavity.*

The next approach taken to improve the oscillators' performance is to add new components into the cavity or substitute certain intra-cavity components to completely different components providing similar functions but having other beneficial properties.

3.4.2.1 Environmentally stable oscillator.

For ultrashort pulse sources to be commercially viable, it is required that they can function without the need to make frequent adjustments. Pulse sources which are very sensitive to temperature or pressure variations are not suited for commercial uses and hence not viable. Kerr-type modelocked fibre lasers are inherently sensitive to environmental changes because of the interferometric nature of the modelocking mechanism i.e. the modulo 2π nature of the

non-linear polarisation rotation switch [57]. In the same way, the two polarisation eigenmodes of the fibre can be treated as two interfering cavity arms being made to interfere at the polariser [58].

With the addition of the Hi Bi fibre and the new SESAM Z373 within our cavity, stability towards environmental changes is improved. The Hi Bi fibre aided in improving the polarisation differential between the higher and lower intensity light at the Kerr gate (see figure 4.10 (b)) and the parameters of SESAM Z373 were empirically found to be better suited for this cavity compared to the previous SESAM Z273. However, we find that our cavity is still moderately susceptible to environmental changes. For example, when the air-conditioning in our lab is turned off and the lab temperature increases by ~5 °C, the mode-locking stability deteriorates and adjustments to the polarisers have to be made to ensure stability. Mode-locking also ceases when the cavity fibre is bent, shifted or tapped as these perturbations change the birefringence of the fibre.

Previously, there have been demonstrations achieving environmental stability in Kerr-type mode-lock fibre laser. I.N Duling *et al.* [13] implemented an all polarisation maintaining figure-of-eight laser. But long lengths of several hundred metres of fibre were required to provide sufficient phase shifts to achieve mode-locking as no linear phase delay can be introduced due to the reciprocity of the cavity configuration. M.E Fermann *et al.* demonstrated two techniques to provide environmental stability. In one method, he controls reproducibly the polarisation along the whole length of fibre by using specially designed polarisation maintaining rectangular fibre with its axes aligned to the outer cladding [59]. However this technique requires the use of specially made fibres. In another experiment, he used Faraday rotators (FR) to eliminate linear phase drifts between the two polarisation eigenmodes within the cavity fibre [60] which can be caused by temperature and pressure variations. This is the technique we implemented to improve the environmental stability of our cavity.

Changes to some cavity components were made and two FRs optimised at 1054 nm, from Optics for Research (OFR), were added into the cavity. Changes to the cavity and to the positions of these FRs within the cavity are illustrated in figure 3.17.

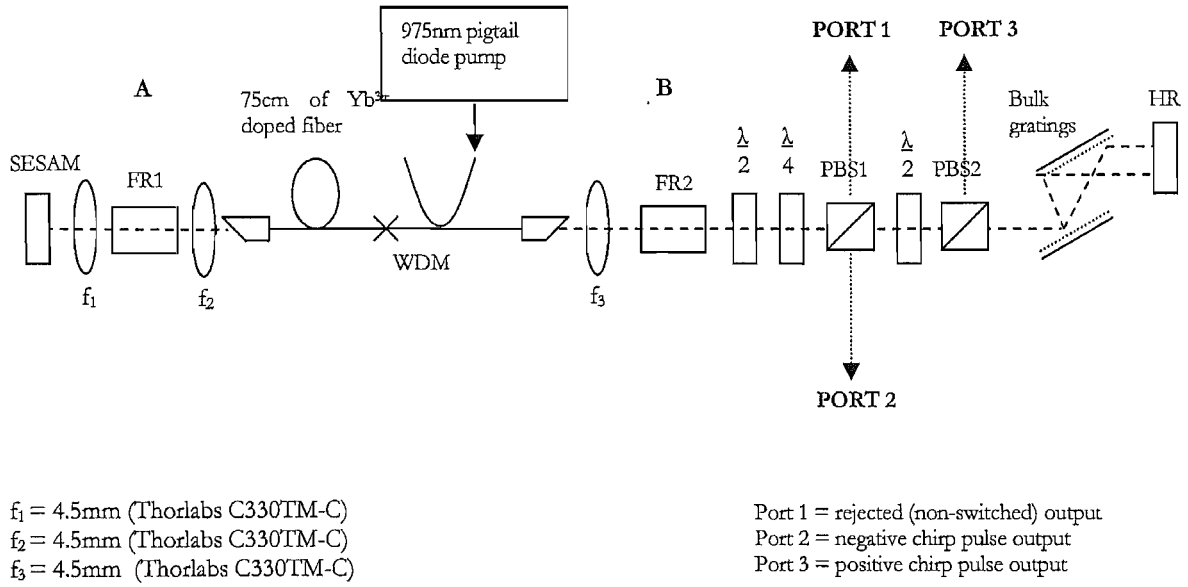

Figure 3.17: Cavity with Faraday rotators FR1 and FR2 added for environmental stability.

We shall use our cavity to explain the principle behind this method. When the elliptically polarised (via the quarter and half waveplates) light propagates down the fibre from point B to point A, linear phase drifts might occur between the polarisation eigenmodes due to environmental variations. But when the light passes through FR1 twice upon reflection from the SESAM, its polarisation gets rotated by 90° with respect to the incident light and propagates back down the fibre with polarisation exactly orthogonal to the incident polarisation state. Therefore net zero linear phase delay is obtained between the eigenmodes but the uncompensated non-linear phase shifts remains unchanged. FR2 is added to compensate for the polarisation rotation induced by FR1.

However, adding new cavity components requires compensation of the additional dispersion these add. But the dispersion value of the FR was not provided and could not be calculated because we do not have the necessary Sellmeier coefficients for the additional quartz crystal used within this FR. Therefore we had to use a practical method to estimate the dispersion of this FR. Pulses of known durations were passed through the FR and their change in durations measured. Knowing the dispersion of standard SM fibre and the change in pulse duration with respect to fibre length; we could measure the change in pulse width introduced by the FR, determine the equivalent SM fibre length and convert it to the amount of dispersion introduced by the FR.

The environmental stability of the oscillator was tested by first turning off the air-conditioning (i.e. to induce thermal fluctuations) and twisting the cavity fibres. These created linear polarisation changes in the cavity. The oscillator continued to mode-lock continuously

instead of stopping operation as before. The mode-locking stability was fully put to the test when a quarter waveplate was placed between FR1 and the fibre to scramble the polarisation. It was found that the mode-locking operation continued for almost a full rotation of the quarter waveplate. Hence we concluded that the stability of the oscillator against external disturbance was improved by the FRs.

Two stable mode-locking points, which has never previously been seen with this oscillator, were obtained during our experiment. According to Ilday F.O *et al.* [57], the interferometric and periodic nature of NLPE suggested that there should be more than one stable point even though normally the intended point of operation is at the first transmission peak. Adding the FR also reduces the spurious back reflections [23, 25, 61] from the fibre ends and the effect of this could be seen in the cleaner Q-switching signal on the scope before mode-locking. Lower threshold powers for self-starting were also observed because spatial hole burning [62] was eliminated by the FR. The threshold powers obtained for self-starting were 43mW and 47mW at the two stable points of operation. These were lower compared to the previous value of 60mW. With this modification, we have demonstrated an oscillator which is more robust against environmentally perturbation and requires lower threshold power for self-starting compared to the oscillator previously described in section 3.4.1.4.

3.5 Conclusion and further improvements.

Much has been done through empirical studies to improve and characterise the clone stretched-pulse Yb^{3+} doped fibre oscillator built. The result was the demonstration of an oscillator which produces shorter pulse duration and is environmentally more stable than the clone of the original system build by Dr Price and Dr Lefort.

The optimum length of Hi Bi fibre was obtained and this was added to improve mode-locking stability and self-starting. SESAM limitation at the longer wavelengths has been extended by changing to SESAM with a wider and flatter reflectivity spectrum. This change produced output pulses with a broader spectrum especially at the 10dB point and shifts the central wavelength to a longer 1060nm wavelength.

By reducing the cavity fibre length, we reduce the TOD contribution from both the fibre and the diffraction grating. This improved the performance of the oscillator, generating output pulses with durations as short as 106 fs and a FWHM bandwidth of 22 nm compared to previous duration of 141 fs and FWHM bandwidth of 18nm. It was demonstrated that slight

net positive dispersion would result in the pulses with the shortest duration, higher chirp and higher energy.

An environmentally more stable system was achieved by inserting FRs from OFR which compensate for any linear phase drift within the cavity fibre due to environmental variations like temperature and pressure. The stability of the oscillator against external perturbation was improved considerably such that twisting the fibre and inserting a quarter waveplate to simulate birefringence drift within the fibre does not stop the continuous mode-locking operation.

Further modifications could be made to the oscillator cavity to improve its performance. For example, in order to achieve ultrashort optical pulses, we need to minimise the phase distortions within the cavity. Treacy, Christov and Tomov [63, 64] pointed out that the pulse compression of large bandwidth signals using gratings are limited by uncompensated cubic phase distortion i.e. TOD. Thus by using prism sequences to provide the required anomalous dispersion compensation, the TOD could also be simultaneously compensated, as the prisms provide TOD with an opposite sign to the cavity fibre. Many different kinds of prism sequences have been proposed and demonstrated to optimise different factors: e.g. Kafka and Baer [65], Proctor and Wise [66], Martinez and Fork *et al.* [55, 67]. However the simplest and most effective sequence was the opposing Brewster prism pair, proposed by Fork and Martinez *et al.*, and this can be implemented in the future to produce shorter duration pulses. This prism sequence was demonstrated by Vincent Cautaerts [33] when he was at the ORC. He implemented this prism sequence to provide anomalous dispersion compensation in a stretched pulse Yb^{3+} ring cavity laser, achieving pulse durations as short as 65 fs with a spectral bandwidth of 32 nm. His results provided evidence that shorter pulses were possible using prisms.

Other improvements could be made to avoid the few limitations imposed with the use of SESAM to initiate mode-locking. Limitations by the parameters of the SESAM like recovery time, intensity saturation requirements, but most importantly, the wavelength selectivity. The Frequency Shifted Feedback (FSF) technique could be implemented to ensure robust self-starting without limitation on the wavelength of operation. This FSF technique has been demonstrated by J. Porta *et al.* [68] to develop an environmentally stable picosecond Yb^{3+} fibre laser and by L. Lefort *et al.* [69] within a similar cavity design as ours. He managed to achieve a highly stable stretched pulse 68 fs Yb^{3+} fibre laser using this technique.

In conclusion, we have demonstrated, optimised and characterised an environmentally stable Yb^{3+} modelocked oscillator capable of producing output pulses with compressible

output pulse durations as short as 106 fs and a FWHM spectral bandwidth of 22 nm at ~ 62 MHz. The average output power from this cavity is ~ 4 mW (corresponding to ~ 65 pJ) and the amplitude and timing jitter were < 0.5 % and ~ 4 ps respectively. This stable oscillator with improved output pulse performance would be suitable both as a seed source for the direct amplification system and also a similar source for the chirped pulse amplification (CPA) system that will be described in the next chapter.

REFERENCES

1. Mark, J., Liu, L.Y., Hall, K.L., Haus, H.A., Ippen, E. P., *Femtosecond Pulse Generation In A Laser With A Nonlinear External Resonator.* Optics Letters, 1989. **14**(1): p. 48-50.
2. Blow, K.J. and Nelson, B.P., *Improved Mode-Locking Of An F-Center Laser With A Nonlinear Nonsoliton External Cavity.* Optics Letters, 1988. **13**(11): p. 1026-1028.
3. Spence, D.E., Sibbett, W., *Femtosecond Pulse Generation By A Dispersion-Compensated, Coupled-Cavity, Mode-Locked Ti-Sapphire Laser.* Journal Of The Optical Society Of America B-Optical Physics, 1991. **8**(10): p. 2053-2069.
4. Spence, D.E., Kean, P. N.,Sibbett, W., *60-fs Pulse Generation From A Self-Mode-Locked Ti-Sapphire Laser.* Optics Letters, 1991. **16**(1): p. 42-44.
5. Piche, M., *Beam Reshaping And Self-Mode-Locking In Nonlinear Laser Resonators.* Optics Communications, 1991. **86**(2): p. 156-160.
6. Poole, S.B., Payne, D.N. and Fermann, M.E., *Fabrication of Low-Loss Optical Fibers Containing Rare-Earth Ions.* Electronics Letters, 1985. **21**(17): p. 737-738.
7. Duling, I.N., *Compact Sources of Ultrashort Pulses.* Cambridge 1995 ed. 1995: Cambridge University Press.
8. Kafka, J.D., Baer, T. and Hall, D.W., *Mode-Locked Erbium-Doped Fiber Laser With Soliton Pulse Shaping.* Optics Letters, 1989. **14**(22): p. 1269-1271.
9. Hofer, M., Fermann, M.E., Haberl, F. and Townsend, J.E., *Active-Mode Locking Of A Neodymium-Doped Fiber Laser Using Intracavity Pulse-Compression.* Optics Letters, 1990. **15**(24): p. 1467-1469.
10. Tamura, K., Nelson, L.E., Haus, H.A. and Ippen, E.P., *Soliton Versus Nonsoliton Operation of Fiber Ring Lasers.* Applied Physics Letters, 1994. **64**(2): p. 149-151.
11. Fermann, M.E., Haberl, F., Hofer, M. and Hochreiter, H., *Nonlinear Amplifying Loop Mirror.* Optics Letters, 1990. **15**(13): p. 752-754.
12. Doran, N.J. and Wood, D., *Nonlinear-Optical Loop Mirror.* Optics Letters, 1988. **13**(1): p. 56-58.
13. Duling, I.N., *All-Fiber Ring Soliton Laser Mode-Locked with a Nonlinear Mirror.* Optics Letters, 1991. **16**(8): p. 539-541.
14. Fermann, M.E., Hofer, M.,Haberl, F.,Schmidt, A. J.,Turi, L., *Additive-Pulse-Compression Mode-Locking of a Neodymium Fiber Laser.* Optics Letters, 1991. **16**(4): p. 244-246.
15. Hofer, M., Fermann, M. E.,Haberl, F.,Ober, M. H.,Schmidt, A. J., *Mode-Locking with Cross-Phase and Self-Phase Modulation.* Optics Letters, 1991. **16**(7): p. 502-504.
16. Tamura, K., Jacobson, J., Ippen, E.P., Haus, Fujimoto, J. G., *Unidirectional Ring Resonators for Self-Starting Passively Mode-Locked Lasers.* Optics Letters, 1993. **18**(3): p. 220-222.
17. Matsas, V.J., Newson, T.P. and Zervas, M.N., *Self-Starting Passively Mode-Locked Fiber Ring Laser Exploiting Nonlinear Polarization Switching.* Optics Communications, 1992. **92**(1-3): p. 61-66.
18. Matsas, V.J., Newson, T.P., Richardson, D.J. and Payne, D.N., *Self-Starting Passively Mode-Locked Fiber Ring Soliton Laser Exploiting Nonlinear Polarization Rotation.* Electronics Letters, 1992. **28**(15): p. 1391-1393.
19. Matsas, V.J., Loh, W.H. and Richardson, D.J., *Self-Starting, Passively Mode-Locked Fabry-Perot Fiber Soliton Laser Using Nonlinear Polarization Evolution.* IEEE Photonics Technology Letters, 1993. **5**(5): p. 492-494.
20. Desouza, E.A., Soccolich, C.E., Pleibel, W., Stolen, R.H., Simpson, J. R., Digiovanni, D. J., *Saturable Absorber Modelocked Polarization-Maintaining Erbium- Doped Fiber Laser.* Electronics Letters, 1993. **29**(5): p. 447-449.

21. Zirngibl, M., Stulz, L. W., Stone, J., Hugi, J., Digiovanni, D., Hansen, P. B., *1.2ps Pulses from Passively Mode-Locked Laser Diode Pumped Er- Doped Fiber Ring Laser.* Electronics Letters, 1991. **27**(19): p. 1734-1735.
22. Haus, H.A., Ippen, E. P.,Tamura, K., *Additive-Pulse Modelocking In Fiber Lasers.* IEEE Journal Of Quantum Electronics, 1994. **30**(1): p. 200-208.
23. Nelson, L.E., Jones, D. J., Tamura, K., Haus, H. A., Ippen, E. P., *Ultrashort-pulse fiber ring lasers.* Applied Physics B-Lasers And Optics, 1997. **65**(2): p. 277-294.
24. Namiki, S., Ippen, E.P., Haus, H.A. and Yu, C.X., *Energy rate equations for mode-locked lasers.* Journal Of The Optical Society Of America B-Optical Physics, 1997. **14**(8): p. 2099-2111.
25. Tamura, K., Ippen, E.P., Haus, H.A. and Nelson, L.E., *77-fs Pulse Generation From A Stretched-Pulse Mode-Locked All- Fiber Ring Laser.* Optics Letters, 1993. **18**(13): p. 1080-1082.
26. Haus, H.A., Tamura, K.,Nelson, L. E.,Ippen, E. P., *Stretched-Pulse Additive-Pulse Mode-Locking in Fiber Ring Lasers - Theory and Experiment.* IEEE Journal of Quantum Electronics, 1995. **31**(3): p. 591-598.
27. Lefort, L., Price, J. H. V., Richardson, D. J., Spuhler, G. J., Paschotta, R., Keller, U., Fry, A. R., Weston, J., *Practical low-noise stretched-pulse Yb3+-doped fiber laser.* Optics Letters, 2002. **27**(5): p. 291-293.
28. Lim, H., Ilday, F.O. and Wise, F.W., *Femtosecond ytterbium fiber laser with photonic crystal fiber for dispersion control.* Optics Express, 2002. **10**(25): p. 1497-1502.
29. Lim, H. and Wise, F.W., *Control of dispersion in a femtosecond ytterbium laser by use of hollow-core photonic bandgap fiber.* Optics Express, 2004. **12**(10): p. 2231-2235.
30. Knight, J.C., Birks, T.A., Russell, P.S. and Atkin, D.M., *All-silica single-mode optical fiber with photonic crystal cladding.* Optics Letters, 1996. **21**(19): p. 1547-1549.
31. Cregan, R. F., Mangan, B. J., Knight, J. C., Birks, T. A., Russell, P. S., Roberts, P. J., Allan, D. C., *Single-mode photonic band gap guidance of light in air.* Science, 1999. **285**(5433): p. 1537-1539.
32. Mangan, B. J., Farr, L., Langford, A., Roberts, P. J., Williams, D. P., Couny, F., Lawman, M., Mason, M., Coupland, S., Flea, R., Sabert, H., Birks, T. A., Knight, J. C. Russell, P. St.J., *Low loss (1.7 dB/km) hollow core photonic bandgap fiber. OFC.* 2004. Los Angeles. *PDP24.* **2**(2): p. 3. *(postdeadline paper)*
33. Cautaerts, V., Richardson, D.J., Paschotta, R. and Hanna, D.C., *Stretched pulse Yb^{3+}:silica fiber laser.* Optics Letters, 1997. **22**(5): p. 316-318.
34. Haus, H.A. and Ippen, E.P., *Self-Starting of Passively Mode-Locked Lasers.* Optics Letters, 1991. **16**(17): p. 1331-1333.
35. Guina, M., Xiang, N. and Okhotnikov, O.G., *Stretched-pulse fiber lasers based on semiconductor saturable absorbers.* Applied Physics B-Lasers and Optics, 2002. **74**: p. S193-S200.
36. Lederer, M.J., Kolev, V., Luther-Davies, B., Tan, H.H., Jagadish, C., *Ion-implanted InGaAs single quantum well semiconductor saturable absorber mirrors for passive mode-locking.* Journal of Physics D-Applied Physics, 2001. **34**(16): p. 2455-2464.
37. Honninger, C., Paschotta, R., Morier-Genoud, F., Moser, M, Keller, U., *Q-switching stability limits of continuous-wave passive mode locking.* Journal Of The Optical Society Of America B-Optical Physics, 1999. **16**(1): p. 46-56.
38. Keller, U., *Semiconductor Nonlinearities for Solid-state laser modelocking and Q-switching.* semiconductor and semimetals, 1999. **59**.
39. Haus, H.A., *Theory of modelocking with a fast saturable absorber.* Journal of Applied Physics, July 1975. **46**(7): p. 3049-3058.

40. Haus, H.A., Fujimoto, J. G.,Ippen, E. P., *Structures for Additive Pulse Mode-Locking.* Journal of the Optical Society of America B-Optical Physics, 1991. **8**(10): p. 2068-2076.
41. Kartner, F.X., Au, J. A. D.,Keller, U., *Mode-locking with slow and fast saturable absorbers - What's the difference?* IEEE Journal of Selected Topics in Quantum Electronics, 1998. **4**(2): p. 159-168.
42. Kartner, F.X., Brovelli, L.R., Kopf, D., Kamp, M., Calasso, I., Keller, U., *Control of Solid-State Laser Dynamics by Semiconductor-Devices.* Optical Engineering, 1995. **34**(7): p. 2024-2036.
43. Honninger, C., Zhang, G., Keller, U. and Giesen, A., *Femtosecond Yb-YAG Laser Using Semiconductor Saturable Absorbers.* Optics Letters, 1995. **20**(23): p. 2402-2404.
44. Keller, U., Miller, D. A. B., Boyd, G. D., Chiu, T. H., Ferguson, J. F., Asom, M. T., *Solid-State Low-Loss Intracavity Saturable Absorber for Nd-YLF Lasers - an Antiresonant Semiconductor Fabry-Perot Saturable Absorber.* Optics Letters, 1992. **17**(7): p. 505-507.
45. Honninger, C., Paschotta, R., Graf, M., Morier-Genoud, F., *et al.*, *Ultrafast ytterbium-doped bulk lasers and laser amplifiers.* Applied Physics B-Lasers And Optics, 1999. **69**(1): p. 3-17.
46. Kartner, F.X., Aus der Au, J,Keller, U., *Multiple pulse breakup in solitary laser systems.* CLEO 1998, 1998: p. 335-336.
47. U.Keller, *Semiconductor Nonlinearities for Solid-state laser modelocking and Q-switching.* semiconductor and semimetals, 1999. **59**.
48. Price, J.H.V., *The development of high power, pulsed fiber laser system and their applications*, in PhD thesis. *Optoelectronics Research Centre.* 2003, University of Southampton. p. 56.
49. Price, J.H.V., *The development of high power, pulse fiber laser systems and their applications,* in transfer thesis. *Optoelectronics Research Centre.* 2000. p. 10.
50. Palmer, C., *Diffraction Grating Handbook.* 4th Edition: Richardson Grating Laboratory. 87-93.
51. Von der Linde, D., *Characterization of the noise in continuously operating mode-locked lasers.* Applied Physics B-Photo-Physics and Laser Chemistry, 1986. **39**(4): p. 201-217.
52. Hofer, M., Ober, M.H., Haberl, F. and Fermann, M.E., *Characterization of Ultrashort Pulse Formation in Passively Mode-Locked Fiber Lasers.* IEEE Journal of Quantum Electronics, 1992. **28**(3): p. 720-728.
53. Agrawal, G.P., *Nonlinear Fiber Optics.* 3rd Edition ed. 2001, San Diego: Academic Press.
54. Spielmann, C., Curley, P.F., Brabec, T. and Krausz, F., *Ultrabroadband Femtosecond Lasers.* IEEE Journal of Quantum Electronics, 1994. **30**(4): p. 1100-1114.
55. Fork, R.L., Cruz, C.H.B., Becker, P.C. and Shank, C.V., *Compression of Optical Pulses to 6 Femtoseconds by Using Cubic Phase Compensation.* Optics Letters, 1987. **12**(7): p. 483-485.
56. Sherriff, R.E., *Analytic expressions for group-delay dispersion and cubic dispersion in arbitrary prism sequences.* Journal of the Optical Society of America B-Optical Physics, 1998. **15**(3): p. 1224-1230.
57. Ilday, F.O, Wise, F.W., *Multiple stable points of a soliton fiber laser with nonlinear polarisation evolution.* Optical Society of America NLGW 01/2000, 2000: p. 3.
58. Ippen, E.P., Haus, H.A. and Liu, L.Y., *Additive Pulse Mode-Locking.* Journal of the Optical Society of America B-Optical Physics, 1989. **6**(9): p. 1736-1745.
59. Fermann, M.E., Andrejco, M.J., Silberberg, Y. and Stock, M.L., *Passive-Mode Locking by Using Nonlinear Polarization Evolution in a Polarization-Maintaining Erbium-Doped Fiber.* Optics Letters, 1993. **18**(11): p. 894-896.
60. Fermann, M.E., Yang, L.M., Stock, M.L. and Andrejco, M.J., *Environmentally Stable Kerr-Type Mode-Locked Erbium Fiber Laser Producing 360-fs Pulses.* Optics Letters, 1994. **19**(1): p. 43-45.

61. Fermann, M.E., *Ultrashort-Pulse Sources Based on Single-Mode Rare-Earth-Doped Fibers.* Applied Physics B-Lasers and Optics, 1994. **58**(3): p. 197-209.
62. Krausz, F. and Brabec, T., *Passive-Mode Locking in Standing-Wave Laser Resonators.* Optics Letters, 1993. **18**(11): p. 888-890.
63. Christov, I.P. and Tomov, I.V., *Large bandwidth pulse compression with diffraction gratings.* Optical Communications, 1986. **58**(5): p. 338-342.
64. Treacy, E.B., *Optical pulse compression with diffraction gratings.* IEEE Journal of Quantum Electronics, 1969. **5**(9): p. 454-458.
65. Kafka, J.D. and Baer, T., *Prism-Pair Dispersive Delay-Lines in Optical Pulse-Compression.* Optics Letters, 1987. **12**(6): p. 401-403.
66. Proctor, B. and Wise, F., *Quartz Prism Sequence for Reduction of Cubic Phase in a Mode-Locked $TiAl_2O_3$ Laser.* Optics Letters, 1992. **17**(18): p. 1295-1297.
67. Fork, R.L., Martinez, O.E. and Gordon, J.P., *Negative Dispersion Using Pairs of Prisms.* Optics Letters, 1984. **9**(5): p. 150-152.
68. Porta, J., Grudinin, A.B., Chen, Z.J., Minelly, J.D., Traynor, N. J., *Environmentally stable picosecond ytterbium fiber laser with a broad tuning range.* Optics Letters, 1998. **23**(8): p. 615-617.
69. Lefort, L., Albert, A., Couderc, V. and Barthelemy, A., *Highly stable 68-fs pulse generation from a stretched-pulse Yb^{3+}-doped fiber laser with frequency shifted feedback.* IEEE Photonics Technology Letters, 2002. **14**(12): p. 1674-1676.

Chapter 4

HIGH POWER ULTRAFAST PULSED LASER SYSTEMS BASED ON LARGE CORE FIBERS

4.1 Introduction

The development of ultrafast pulse laser systems generating either high pulse energy or high average output powers have increased tremendously over the years. This is due to the diverse range of applications that require these laser systems. Applications requiring pulses with high peak intensities include supercontinuum generation, micro ablation [1], biological imaging, precision surgery, coherent and incoherent X-ray generation [2]. Also systems producing high average powers are used for laser displays, micro and nano-scale material processing, higher harmonic generation, optical parametric oscillators [3], spectroscopy, LIDAR range finding, and data acquisition applications.

Workhorses for ultrafast laser systems have traditionally been solid state laser systems because of their proven capabilities. However, inherent problems associated with solid state based laser systems led to the research and development of fiber based ultrafast laser systems which avoid these intrinsic limitations.

In chapter 1, I have described many positive attributes that fiber based systems possess and hopefully have made a convincing case to use these laser systems. However, it is also these properties (tight mode confinement, high doping concentration and long interaction lengths) that limit the potential for producing higher energy pulses from fiber based systems. Nonlinear effects in the fiber core, the most important being self phase modulation (SPM) and stimulated Raman scattering (SRS), quickly become significant due to the high peak intensities of the propagating ultrashort pulses. Therefore, the development of high power ultrafast pulsed fiber laser systems requires new amplification techniques and improvements to fiber designs (larger mode areas to reduce non-linearity).

In this chapter, we will discuss and present results from two such amplification techniques developed for short pulse amplification. We will first describe Chirped Pulse Amplification (CPA) in section 4.2 and Parabolic Pulse amplification in section 4.3. The seed source for these amplification systems was the oscillator developed in-house, presented in chapter 3. Fiber amplifiers in these systems incorporate active fibers with novel designs such as large mode area (LMA) fibers or novel amplifier configurations such as mid-pumping configuration.

4.2 Chirped pulse amplification system.

Output peak powers from laser oscillators increase as the stored energy in the gain medium is released by shorter and shorter pulse durations, from nanoseconds for Q-switched lasers to femtoseconds for modelocked oscillators. Higher output pulse energies of ultrashort pulse amplification systems have been hampered by the non-linear effects mentioned above.

The introduction of the chirped pulse amplification (CPA) technique in 1985 [4] opened the way to achieve higher pulse energies with the use of the vastly superior energy storage, and storage time, capabilities of the solid-state gain media to amplify ultrashort pulses. The approach taken in CPA, to avoid the nonlinear effects, is to ensure that the peak intensities of the propagating amplified pulses remain small. It is important to note that it is the peak intensities and not the energy or fluence of the seed pulses that results in these nonlinear effects.

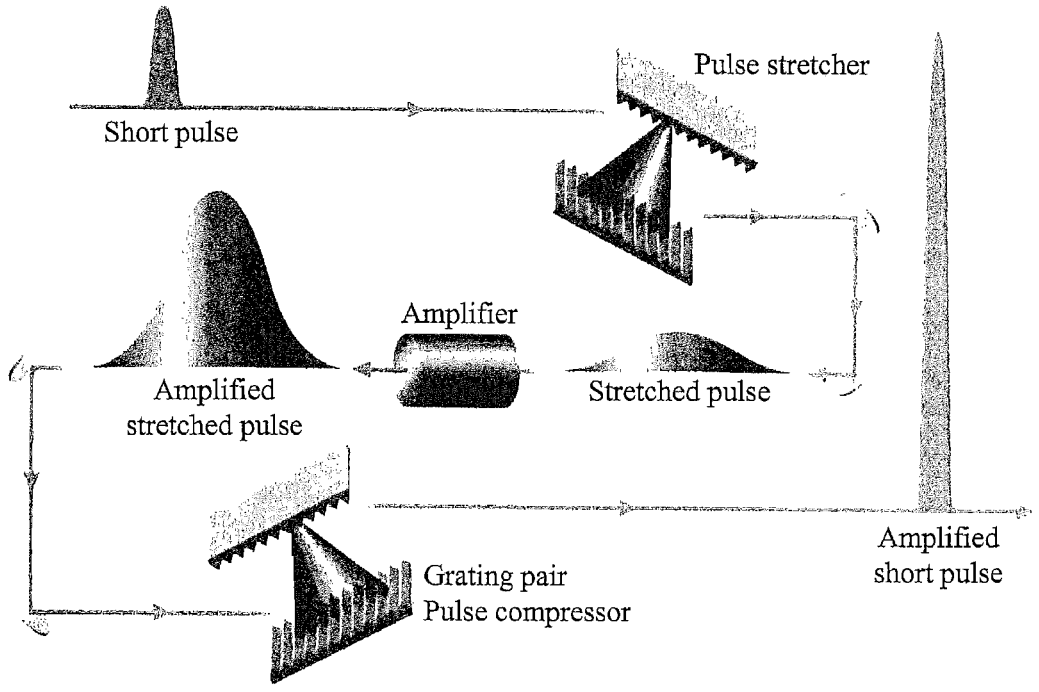

Figure 4.1: Diagram demonstrating principle of Chirped Pulse Amplification (CPA). Figure courtesy of University of Michigan Ann Arbor.

The principle of CPA systems is shown in figure 4.1. The peak intensity of the short transform limited optical seed pulses is reduced by temporally stretching these pulses using pulse stretchers (i.e. grating pair and chirped fiber Bragg gratings (CFBGs)), prior to

amplification and recompression, using pulse compressors (i.e. grating pair) close to their original duration at the output. Practically, these pulses can only be stretched by factors of 10^3 or 10^4 (typically ~ 1 ns).

Although there are a variety of RE dopants suitable for ultrashort pulse amplification, currently only Er^{3+}, Yb^{3+} and Er^{3+}/Yb^{3+} dopants are used for high-energy fiber CPA systems at the ~1 μm and ~1.55 μm regime. Again, initial development work on fiber CPA systems was carried out at 1.55 μm with Er^{3+} doped fibers because of the maturity of the telecommunications technology. Using a conventional small core Er^{3+} fiber amplifier (EDFA) cascade, Galvanauskas *et al.* demonstrated >1 μJ pulse energies from a CPA system [5]. This pulse energy level constitutes the limit achievable from conventional single mode fibers (due to their small effective mode areas, A_{eff}). It was found that even after stretching the input pulses to ~ 1 ns width, the maximum achievable output pulse energies in fiber amplifier systems, utilising standard core size fiber, are limited by nonlinear effects (namely SRS) before reaching the saturation fluence limit. Therefore fiber amplifiers having larger mode sizes (increased A_{eff}) have to be used to produce higher energy pulses, whilst trying to maintain single mode operation by clever fiber design (i.e. LMA fibers). With the introduction of LMA fibers, Taverner *et al.* demonstrated 158 μJ [6] single transverse mode pulses from an EDFA cascade having low NA LMA fibers with mode field diameters of 16 μm. This same author also presented a CPA system producing >10 μJ [7] single transverse mode pulses from their CPA system using an EDFA with 13 μm core diameter LMA fibers. Using multimode Er/Yb doped fibers, Galvanauskas *et al.* managed to obtain 100 μJ, 0.7 ps, near diffraction limited (M^2 ~ 1.5), pulses from a CPA amplifier cascade [8].

Although much of the initial work was carried out with Er^{3+}, many attributes of Yb^{3+} make it a preferred RE fiber dopant, compared to Er^{3+}, for high power applications. Attributes including a broader gain bandwidth (50-100 nm compared to 10-30 nm), higher optical pumping efficiencies (60-88 % compared to 30-40 %), and the possibility of high doping levels. These attributes prompted future work on Yb^{3+} based CPA systems.

The same industrial sponsor for our Yb^{3+} based oscillator work presented in chapter 3 negotiated a contract with Professor David Richardson to develop a compact all Yb^{3+} fiber based CPA system. The targeted specifications of the contract were to develop ~ 500 fs output pulses having between ~10-50 μJ energy and an average output power of ~10 W (this corresponds to a repetition rate of 200 kHz). When the contract was drawn up, the target system specification represented the state-of the art for existing Yb^{3+} based short pulse amplifier systems. However around the time we achieved our goals, other groups had

demonstrated Yb^{3+} fiber based CPA systems producing femtosecond pulses having pulse energy >1 mJ. In 2000, Galvanauskas A. *et al.* demonstrated the first all-fiber CPA system using Yb-doped fibers. This system produced 100 μJ pulses with durations of 220 fs and average powers of 5.5 W [9]. Later in 2001, as a result of further mode scaling, he presented the first fs Yb-fiber CPA system capable of producing millijoule pulse energies. This Yb-based CPA system produced 1.2 mJ pulses at 1667 Hz repetition rate and compressible pulse durations of 380 fs [10]. The CPA setup was similar to [8], the seed-pulse source was comprised of a stretched-pulse Er-fiber mode-locked oscillator operating at 1550 nm, followed by a length of single mode fiber used to frequency-shift the pulses to ~2.1 μm (using Soliton Self Frequency Shift). Then a chirped periodically poled lithium niobate (PPLN) frequency doubling crystal converted the wavelength to 1050 nm and finally a Yb-fiber pre-amplifier was used to increase the seed average power to 330 mW at a 50 MHz repetition rate. The linearly chirped pulses, with 2 ps duration, were centred at 1055 nm and had FWHM spectral bandwidth of 20 nm which was filtered down to 10 nm before injection into the main system. Diffraction gratings were used to implement a stretcher and a compressor. The pulses were stretched to 800 ps and amplified through 3 amplification stages with two Acousto-Optic Modulator (AOM) optical gates in between. The amplifier fiber core sizes were stepped up after every stage to enable higher power scaling. The first stage was a standard core-size SM cladding pump pre-amplifier, and the second amplifier had a 25 μm core size and the final power amplifier was 2.6 m long and had a core/cladding dimension of 50/350 μm. The large inner cladding dimension, having an NA of 0.4, allowed it to be pumped by a 20W laser diode array. Though the fiber core had a V-number of 15 (capable of supporting ~ 100 transverse modes), with careful launch alignment, robust single mode quality was achieved. M^2 of the system output was measured to be 1.16.

Although the output pulse energy from the CPA system developed by Galvanauskas A. *et al.* was much higher than the goals set out by our commercial sponsors, it should be noted that our aim was not only to produce high energy pulses but also to produce a system that is more practical, commercially attractive and has better output pulse performance. Therefore our approach was to use fiber FBG, instead of bulky grating pairs as pulse stretchers, to produce an output system that provided 10-50 μJ pulses. Another important difference between our CPA systems was the complexity of their seed pulse source. As I have described above, their seed source was far more complex compared to our Yb-oscillator (see chapter 3), making ours a far more attractive system for commercial exploitation.

Furthermore, using CFBGs, we were able to custom write the gratings such that they could be used to compensate the higher 3rd order dispersion inherently contributed to the pulse by the bulk grating compressor. Although M.E. Fermann *et al.* also demonstrated 2nd and 3rd order dispersion compensation in an Yb^{3+} based CPA system using a CFBG and 850 fs duration pulses having 40 μJ pulse energy were generated from this system [11], we believe that we achieved these results well before Fermann. However we were unable to publish our results at this time due to the commercial sensitivity of our sponsors. In the next few sections, I will be describing the development and performance characterisation of our CPA system that achieved the goals set out by our commercial sponsors.

4.2.1 *Schematic of our all Yb-fiber CPA system*

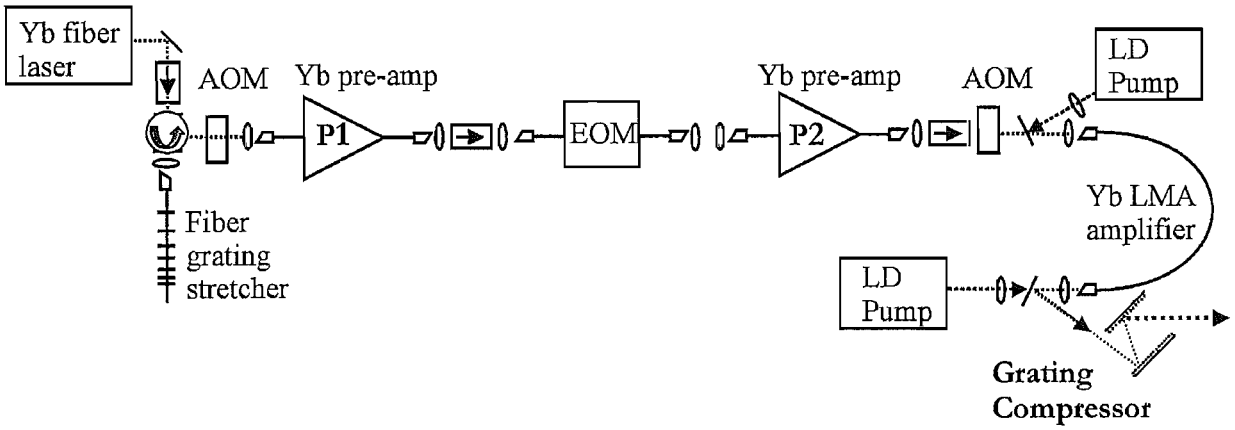

Figure 4.2: Schematic of our all Yb-fiber CPA system

Figure 4.2 shows the schematic of our CPA system. The femtosecond mode-locked Yb fiber oscillator [12] produces ~30pJ pulses with a 50 MHz repetition rate. The pulses are centered at 1055 nm with a spectral FWHM of 18.6nm. The output pulses from the oscillator are ~ 2 ps long but are compressible to a FWHM duration of ~110 fs. A very similar oscillator, that was used as a seed for our direct amplification experiment, has been described in chapter 3. The pulses were coupled to the CFBG and the reflected pulses were coupled to amplifier P1 via a free-space circulator, made by polarisation waveplates and beam splitters (PBS). This circulator arrangement, together with losses from the CFBG, introduce coupling losses of ~ 7 dB. A fiberised 3 GHz bandwidth electro-optic modulator (EOM), optimised at 1056 nm and acousto-optic modulators (AOM), optimised at 1054 nm, (from AA optics) with synchronised time gating, were used in-between amplifiers to vary the repetition rate and to

filter unwanted amplified spontaneous emission (ASE) [10, 13] between amplifier stages. The transmission losses of these AOMs are ~ 1.5 dB. The EOM (consisting of a Mach-Zender interferometer with a $LiNbO_3$ crystal in one arm) has a fast response time (> 1 GHz compared to 50 MHz for the AOMs). The EOM has an extinction ratio of ~ 50 dB, compared to ~ 30 dB provided by the AOMs. Therefore the EOM was used to select pulses from the 50 MHz pulse train. The insertion loss introduced by the EOM is ~ 4 dB. In addition to the optical modulators, free space isolators from Electro-Optic technologies (EOT) (see section 2.5.1), optimised at 1054 nm, were used to prevent backward ASE from de-stabilising the pulse train, damaging the optical components or causing early saturation of the amplifiers. These free-space isolators have transmission losses of ~ 0.5 dB.

In order to achieve 50 μJ (specified by our industrial sponsors) pulses, we require ~ 60 dB of net gain from the amplifier cascade. However ~ 20 dB loss is incurred from the insertion losses of the components within the system and from coupling losses at each amplification stage. Therefore the total gain required from the amplifier cascade is ~ 80 dB. Due to the build up ASE, maximum gain from fiber amplifiers is normally limited to ~30 -35 dB [13, 14]. Hence at least three amplification stages are required to provide sufficient gain and to keep the overall noise level acceptable.

To simplify implementation of the amplifier cascade, provide a low maintenance CPA system, and to avoid the need for careful alignment of optics (coupling losses of 1.5 dB), we generally try to avoid free space pumping schemes. Our CPA system uses two conventional single-mode (5 μm core), core-pumped, Yb doped fiber amplifiers setup in a mid-pumping configuration (see chapter 3) for pre-amplifiers P1 and P2.

Although using conventional SM core-pump amplifiers provided a cheap and simple all fiber solution; as mentioned earlier for power scaling and to obtain pulse energies > 1 μJ, larger core fibers were required. Therefore in the final amplification stage, we used a 9m length cladding pumped LMA fiber with a core/cladding diameter of 16.5/200 μm and doped with 7000 ppm Yb^{3+} ions. The core/cladding NA was ~ 0.06/0.4. The signal gain achieved at this stage was ~ 20 dB. The fiber, which was effectively single mode in operation, was pumped from both ends (via dichroics to split the signal and pump light) with 915 nm and 976 nm pump laser diodes. These 915 nm and 976 nm pump laser diodes were from Boston Lasers Inc. and they provided up to 32 W and 25 W of pump power respectively. The pump powers from both diodes are delivered through 200 μm core size pigtails with an NA of 0.2.

4.2.2 *Pre-amplifiers P1 and P2*

Core-pumped amplifiers were used for the first and second stage amplifiers. As described in chapter 1, these amplifiers are made from a SM Yb-doped fiber design and have a core diameter of 5 μm, NA= 0.21 and doping concentration of ~2000 ppm. In the next two sections, I will be describing the initial performance of this core-pumped amplifier and further amplifier design refinements that could be made to obtain a gain increment.

4.2.2.1 Initial performance

A narrow linewidth (<100 kHz) Distributed Feedback (DFB) seed laser, centred at 1059.94 nm, was used to characterised this core-pump amplifier. A pigtailed single mode MOPA pump from Newport, providing up to 280 mW of pump radiation at 976.3 nm, was used to pump in a co-propagating direction at one end of the amplifier. This pump was introduced into the active core via 980/1060 nm WDM coupler. The transmission characteristic of this WDM coupler is shown in figure 3.3 of chapter 3. The coupling efficiency of a 90/10 coupler was characterised using the same DFB seed laser and later used to couple the DFB seed signal into the amplifier. Two fiberised isolators were used at both amplifier ends to prevent any back reflections from the ends. Both isolators were characterised and were found to have an insertion loss of 1.5 dB. Launch efficiency of the WDM coupler was also characterised before splicing it onto the Yb doped fiber. A schematic diagram of the setup is shown in figure 4.3.

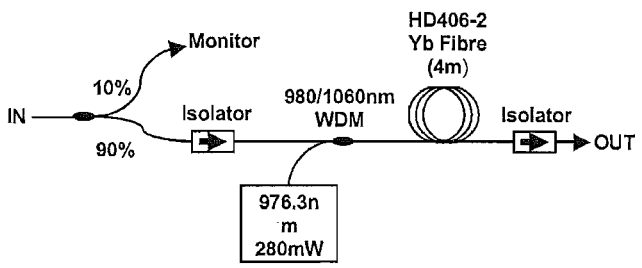

Figure 4.3: Schematic diagram of core-pump amplifier.

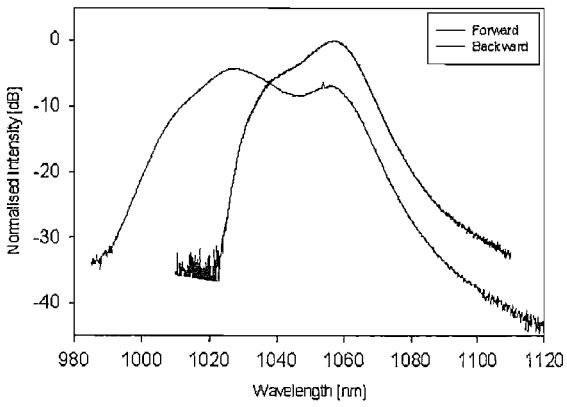

Figure 4.4: Forward and backward ASE spectra.

Assuming negligible splice losses, the gain and output of the 4m long SM Yb-doped (HD406-2) fiber amplifier (YDFA) was characterised using both the output and monitor port of the setup. This 4 m length of Yb^{3+} doped fiber was chosen such that the peak of the ASE was near our operating wavelength of 1060 nm, where it has a relatively flat gain spectrum, as shown in figure 4.4. Figure 4.5 (a) and (b) show the internal gain and output power over input signal power with 280 mW of pump power. The small-signal gain was found to be ~ 30 dB and the saturated output power was ≥ 100 mW. Figure 4.5 (c) shows the amplifier internal gain with 0.01, 0.1, 0.2 and 10 mW input powers over a range of pump powers.

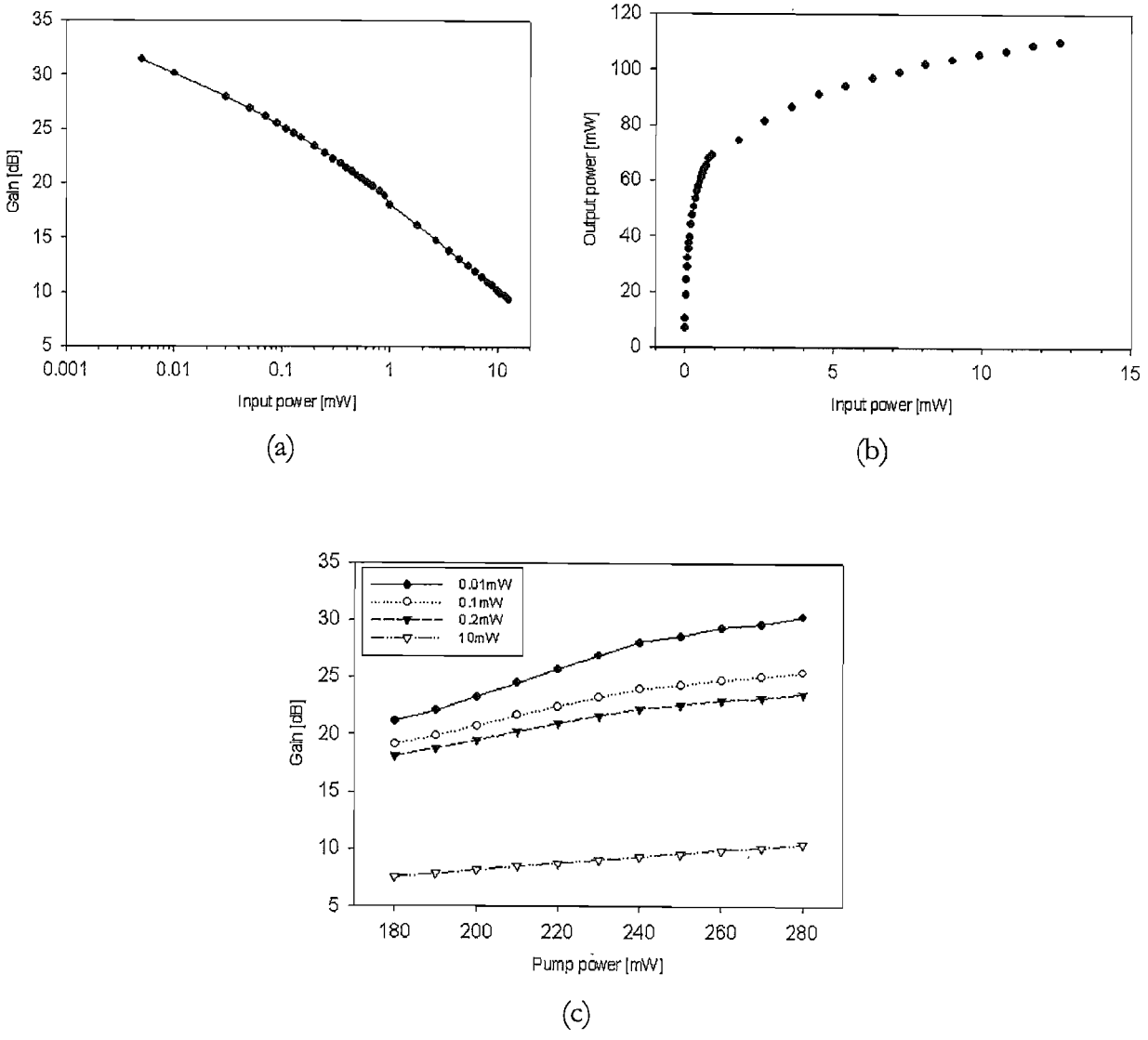

Figure 4.5: (a) Internal gain and (b) Output power characteristics of core-pumped YDFA with input power. (c) Internal gain of YDFA over a range of pump powers.

From figure 4.5 (c), we can see that even up to 280 mW of pump power at 976.3 nm, the gain does not saturate for this amplifier for small input signal powers between 0.01 – 0.2 mW. The

gain provided by the amplifier was adequate for our needs. However, it would be beneficial if we could improve the amplifiers' gain for future power scaling requirements. Research was carried out on the amplifiers' design to improve its gain.

4.2.2.2 Improve gain with mid-amplifier pump injections

A technique of recycling 'lost' shorter wavelength ASE, emitted at the pump end, to improve the amplifiers' gain was first demonstrated with Er^{3+} doped fiber amplifiers operating between 1570 – 1610 nm by J.H Lee *et al.* [15]. They found that by recycling the otherwise 'lost' 1550 nm ASE at the pump end, they could improve the amplifier gain by ~ 4 dB. It was found that this same technique, of introducing a secondary pumping scheme utilising this 'lost' ASE, could be exploited with Yb^{3+} based fiber amplifiers.

This secondary pumping scheme can be explained from the spectroscopic properties of Yb^{3+}. Observing the absorption and emission cross section of Yb^{3+} (see figure 2.3 in chapter 2), we find that the emission spectrum between 1.0 and 1.1 μm peaks at 1030 nm. The absorption cross section is also highest below 1030 nm. This high absorption below 1030 nm is reflected in the forward ASE spectrum, shown in figure 4.4. We can see that the forward ASE spectrum cuts off at < 1030 nm. Therefore, high inversion and strong pumping are required to create gain (and ASE) at 1030 nm. This means that gain at 1030 nm would only be possible near the pump end (see figure 4.3) of the amplifier. This is reflected in the backward ASE, shown in figure 4.4, where the ASE peaks close to 1030 nm. Continuing our analysis on the absorption cross section, we see that it decreases rapidly, compared to the emission cross section, at the longer wavelengths (i.e. 1060 nm). Hence the re-absorption of the emitted ASE at longer wavelengths (i.e. 1060 nm) would be low, and the emission high. This suggests that a much lower inversion level would be required to achieve gain at the longer wavelengths, which could possibly be pumped by the re-emitted 1030 nm radiation along the fiber. Hence gain at 1060 nm should be possible further away from the pump end, where there is net absorption of the 1030 nm ASE radiated from the pump end. Since we are operating at the 1060 nm wavelength, backward propagating 1030 nm ASE is considered to be 'lost' power. This same spectroscopic relationship between the absorption and emission cross section was used by J.H Lee *et al.*.

Like J. H Lee *et al.* this technique was implemented in core-pumped YDFAs by inserting an additional un-pumped length of Yb^{3+} doped fiber before the end where the pump is injected. This un-pumped length consequently absorbs the otherwise 'lost' 1030 nm ASE

(acting as a secondary pump) emitted from the pump end to generate additional gain at the longer wavelengths in this section of fiber. Theoretical modelling, employing this technique, was carried out by Dr Johan Nilsson from the High Power Fiber Laser (HPFL) group in the ORC. The result he obtained from modelling a setup similar to figure 4.3, but without the isolators and 90/10 coupler, is shown in figure 4.6. It shows that injecting the primary pump in the middle of the Yb^{3+} doped would increase the gain at 1056 nm by ~ 3 dB. The result also shows that inserting the primary pump further than 30% along the doped fiber would not make any significant changes to the peak gain achieved, thereby allowing some tolerance to the exact position where the pump is inserted. This mid point pumping scheme was implemented using the HD406-2.

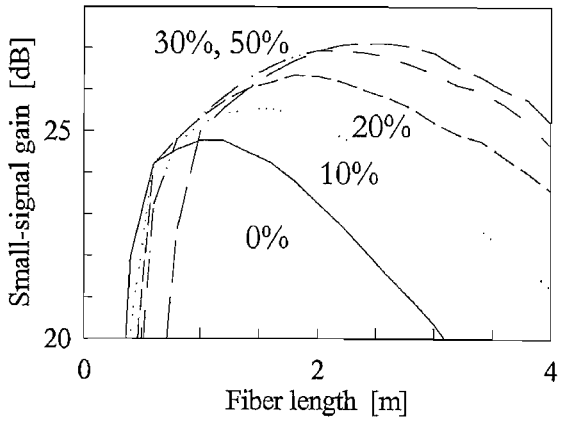

- Small-signal gain of core pumped Yb-doped fiber amplifier with midway forward pump injection.
- Pump injected at 0,10,20,30, and 50% of the YDF length.
- Signal wavelength 1056 nm

Figure 4.6: Results from Dr J. Nilsson theoretical modelling of amplifier gain; midpoint pump injection; 5 μm diameter core; 220mW pump.

Empirical results from two core-pumped YDFA setups was compared over a broad wavelength range. YDFA 1 has a conventional setup with a 2.7 m length of Yb^{3+} doped fiber in a forward pumping direction. YDFA 2 was setup to implement this new technique and has a total active fiber length of 4 m of which 1.6 m is unpumped and the rest of the 2.4 m is pumped in a forward direction (pump inserted at 40% along the total active fiber length). In this experiment, the fiberised isolators at both ends of the amplifier were removed and the ends of the amplifier were angled polished. A characterised EOT free space isolator was used in-between the seed and the amplifier to prevent backward ASE emitted from the amplifier causing instability to the seed source. The amplifiers were seeded with a broadband ASE seed source, filtered to enable wavelength tunability. The broadband ASE source was constructed using 2 m of HD406-2 fiber. Wavelength selective filtering (resolution of 1nm) was achieved using an Acousto Optic Tunable Filter (AOTF) from Gooch and Housego. The selected

wavelength was fed back into one end while the other end was angle polished. An example of the seed source is shown in figure 4.7 (a).

Maximum pump power was used for the seed source and ~ 220 mW of 976.3 nm pump light was used for both amplifiers. Small (~0.2 mW) and large (~20 mW) signal gain was characterised using a calibrated neutral density filter as an attenuator between the seed source and amplifier. Comparing the two setups, we can conclude that YDFA 2 gives us ~ 4 dB more small signal gain, predominantly at the longer wavelengths, and slightly higher large signal gain (~ 2dB). Another positive attribute of the YDFA, that was observed for both setups, was the flat gain bandwidth over a 40 nm span which is ideal for ultra fast amplification.

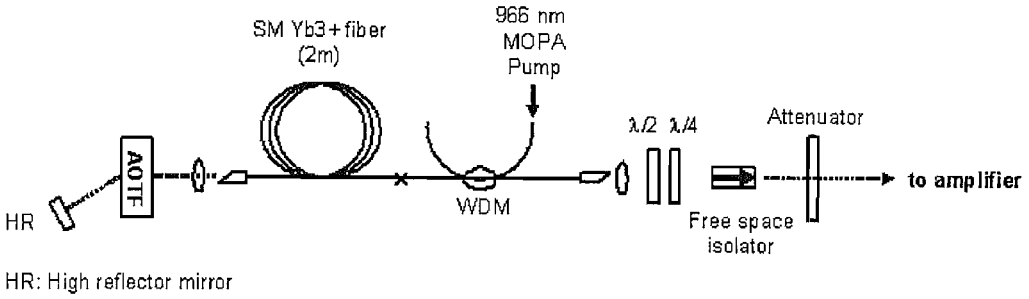

(a)

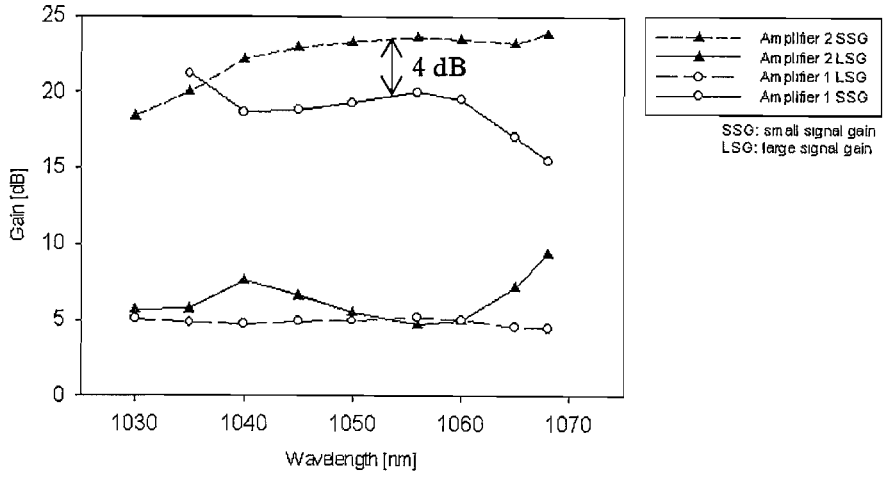

(b)

Figure 4.7 (a) Wavelength selective (resolution of 1 nm) broadband ASE source (b) Small and large signal gains between 1030 nm to 1070 nm.

Another approach to achieving higher gain, by improvements to fiber design, is to reduce the core-size of the Yb^{3+} doped fiber. The tighter mode confinement leads to higher gain for a given pump power, as the pump intensities per unit length is higher. Simulations comparing

two similar YDFA setups utilising the mid-point pumping scheme but with doped fibers having different core sizes, were carried out by Dr Johan Nilsson. The simulation results obtained with 3 and 5 μm core diameters, at 220 mW pump power, showed that the maximum gain increases by ~10 dB with the 3 μm doped fiber. However the disadvantage of using the 3 μm diameter doped fiber, in practise, is the mismatch in core sizes between the pigtails (~ 5 μm) of the WDM pump coupler and doped fiber. The mismatch in core sizes would result in pump insertion loss at the splice. Theoretically, using the mode field diameter (MFD) mismatch, the loss at each splice was calculated to be ~ 0.6 dB [16]. Therefore the net overall gain possible using these smaller core active fibers was > 8 dB. Possible solutions to this problem are to insert a fiber with intermediate core size to create a quasi-adiabatic taper, or to taper the WDM pigtail to match the doped fiber. Though these smaller core fibers provide higher gains, I did not use this smaller core fiber in the experiments presented in this thesis. However, they may be used in the future to upgrade the amplifier cascade.

The mid-pumping configuration was used for both pre-amplifiers. Both core-pumped pre-amplifiers were pumped with grating stabilised, high brightness, semiconductor laser diodes via 980/1060 nm standard SM WDM couplers to make pump coupling a simple all-fiber solution. They were built to have optimum gain at ~ 1056 nm, the centre wavelength of the Yb^{3+} doped fiber master oscillator. The choice of ~1056 nm wavelength of operation for the CPA system was determined because of the spectroscopic nature of Yb^{3+}, and is further discussed in section 2.1.1. Figure 4.8 shows the schematic of both pre-amplifiers P1 and P2.

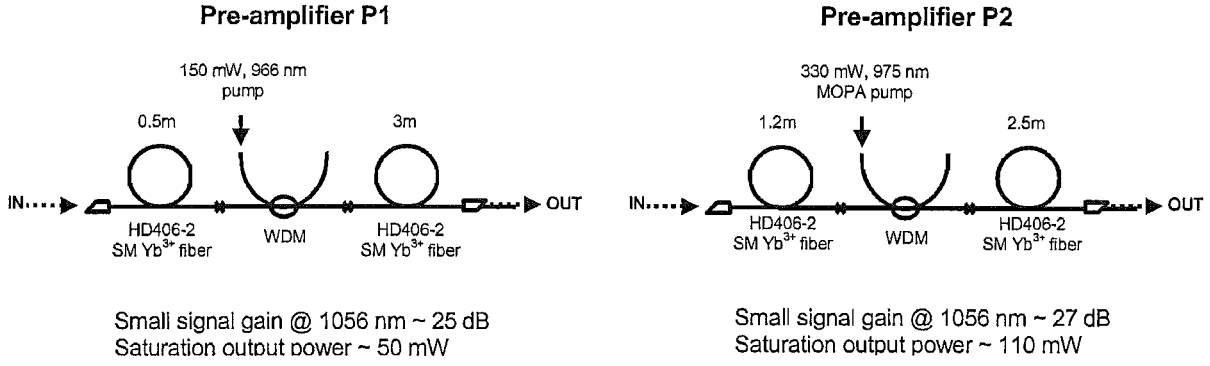

Figure 4.8: Schematic of pre-amplifiers P1 and P2

As described earlier, the mid-pumping configuration gave us ~ 4 dB higher gain by re-absorbing the 'lost' backward propagating 1030 nm ASE from the pumped end. The lengths of the active fiber in each amplifier were chosen by measuring the ASE spectrum and obtaining the peak ASE wavelength at ~ 1056 nm. The difference in lengths between the two

amplifiers was because of the differing pump wavelengths. The small signal gain at 1056 nm for P1 and P2 were 25 dB and 27 dB respectively.

4.2.3 *Pulse stretcher and compressor.*

To obtain minimum pulse duration from the output of a CPA system, the dispersion of the stretcher and amplifier must be equal and opposite to that of the compressor. Pulse stretching and compression could be performed using various dispersive devices. For example, the pulses were stretched using long lengths of fiber with positive group velocity dispersion (GVD) at 1.02 um [17], bulk optical devices such as a pair of anti-parallel bulk gratings [18, 19] or Chirped Fiber Bragg Gratings (CFBG) [20, 21]. Many authors [10], in the past, have used complementary pairs of bulk gratings for pulse stretching and compression. However, to achieve the required dispersion strength, the bulk gratings require ~ 1m separation, thus making the entire CPA system bulky and impractical for commercial products. To make CPA systems more compact, CFBG could be used for both stretching and compressing. CFBGs are highly dispersive and provide the required dispersion strength in centimetres of fiber. Broderick *et al.* demonstrated that using a 20cm long CFBG for stretching and a 10 cm long single mode large mode area (LMA) CFBG for compression in an all fiber Er-doped CPA system, 3.8 ps pulses with 500 kW peak powers could be generated [21].

However the silica based CFBGs are intrinsically non-linear and output pulse intensity and quality attainable from such CPA systems is limited by the input pulse intensity into the CFBG compressor. For our industrially sponsored CPA system, the specified 500 fs 50 μJ pulse target meant that the peak power of the pulses could reach ~ 100 MW. Thus CFBGs are unsuitable to be used for pulse compression and bulk dispersive gratings that could withstand such high intensities have to be used. However, a CFBG can still be used for pulse stretching, to keep the CPA system as compact as possible.

Using a CFBG can be advantageous to keep the CPA system compact, but a more important advantage of using a CFBG stretcher was the ability to design the CFBG to provide 3rd order dispersion compensation for that introduced by the fiber and grating compressor. This will be discussed in detail later in section 4.2.3.2.

4.2.3.1 *Bulk grating compressor*

This section will describe the characteristics of the bulk grating, the process and limitations faced in designing the CPA bulk grating compressor and its performance. In our CPA system, instead of using a grating pair, the compressor setup uses only a single grating. Figure 4.9 (a) shows a photograph of the bulk grating compressor setup used in the CPA system. The path of the beam (outward pass shown in red, return pass shown in blue) is shown in the photograph. The setup incorporates roof mirrors to shift the entire beam in the vertical and horizontal directions to utilize the entire diffraction surface of the grating, using a 4-pass configuration. One other advantage of using roof mirrors is that parallel alignment of the forward and backward propagating light between the surfaces of the grating is ensured if the roof mirrors are properly aligned.

Instead of presenting a complicated and confusing schematic having horizontal and vertical translated beams via roof mirrors, Figure 4.9 (b) shows an unfolded simplified schematic of the bulk grating compressor with two complementary surfaces. The diagram also shows two parameters under consideration, the grating separation and angle, θ_i. The top schematic shows that if the grating separation is too large for a given pulse spectral width, the dispersive beam becomes too wide and clips the surface of the grating. Hence the compressible stretched pulse duration for a given pulse spectral width and grating dispersion is limited by the maximum grating separation before clipping occurs (i.e. or grating dimension). The schematic below demonstrates that the 2nd (GDD) and 3rd (TOD) order dispersion contribution from the grating depends not only on the number of grooves/mm of the grating but also on angle of incidence. This indicates that there is still room for adjustments to the grating dispersion by changing the angle of incidence, θ_i. Figure 4.9 (c) shows the ratio between GDD and TOD with respect to the angle of incidence.

The process towards obtaining the best compressor design was both theoretical and experimental. We would like to thank Dr C. Barty for his contribution to the initial ground work in developing a suitable compressor design. To reduce their cost and ease of implementation, our sponsor specified the bulk grating to be used, as it was already used in some of their products. This added additional constraints to the design of the compressor. The bulk grating specified by our sponsor was a holographic, gold coated, bulk diffraction grating with 1500 sinusoidal grooves/mm from Richardson Gratings Laboratory. Using this grating meant that the angle to obtain optimum grating efficiency is fixed, which in turn fixed the GDD/TOD ratio. With the specified target of < 500 fs re-compressed pulses (~ 5 nm

FWHM spectral width) determining the lower limit of the spectral window required by the grating and with the fixed grating dimension (in our case 10 cm wide), the maximum possible stretched pulse duration before clipping occurs is determined. These constraints consequently set the widest grating separation. Though these additional constraints were incurred, we do have one benefit from using this grating. This grating has been theoretically modelled by Dr C. Barty and was used in the designing process.

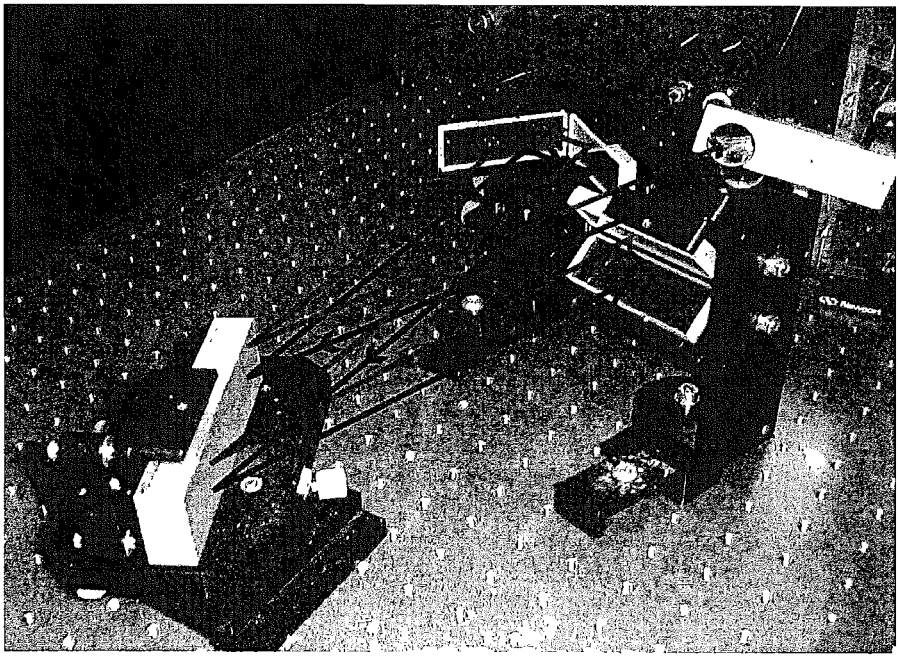

(a)

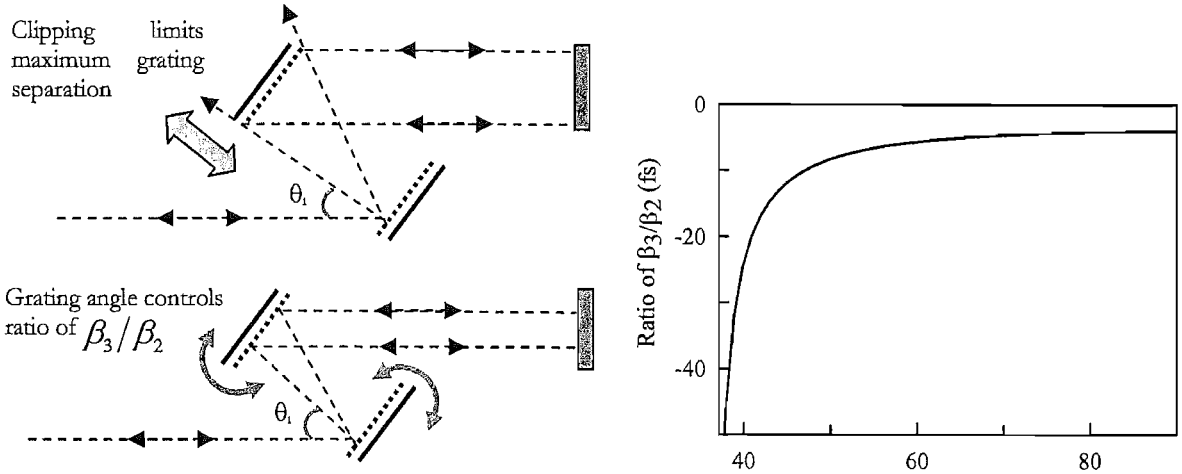

(b) (c)

Figure 4.9: (a) Photograph of the grating compressor. (b) Schematic of the grating compressor. (c) Ratio between the 3rd order dispersion and GDD against angle of incidence.

The diffraction efficiency was critical in the designing process. This was because four passes were made on the grating. This meant that if the grating efficiency was 80%, the overall transmission efficiency of the compressor would be $(0.8)^4 \sim 0.41$ or 41% and if it was 70%, the transmission efficiency would be only ~ 0.24 or 24% (3dB decrement). Therefore this would be the overriding requirement of the compressor design. We empirically measured the diffraction efficiency of the grating. We launched light polarised for optimum reflection by the grating and varied the angle of incidence. The results are shown in figure 4.10 below.

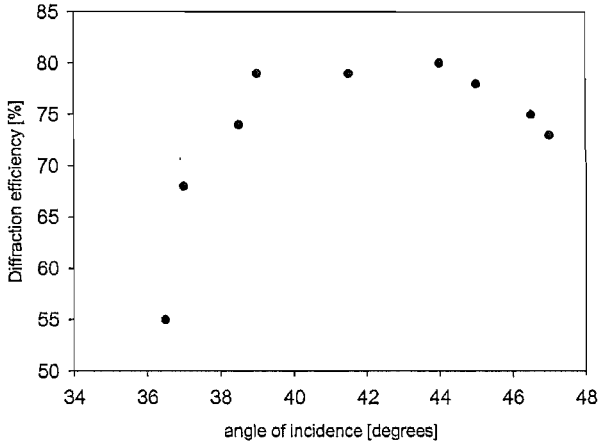

Figure 4.10: Grating diffraction efficiency with respect to angle of incidence.

From figure 4.10, we can see that maximum diffraction efficiency lies between angles 39° - 45°. The efficiency was also relatively flat across this range of angles. To give us some room for minor variations, and to adjust the grating angle of incidence without compromising too much on the diffraction efficiency, we decided to use an angle of incidence of 41°. Although the grating was specified to give a diffraction efficiency of 89% at 41°, the experimental results were slightly lower at ~ 79%.

Both GDD and TOD of a bulk-grating compressor are proportional to the grating separation [22]. Therefore, using a long stretched pulse duration that requires large GDD, also adds large TOD. For recompressed pulse durations <500 fs, uncompensated TOD would result in a significant pedestal on the recompressed pulse [23] and will lead to a large portion of the pulse energy being in the pedestal. To address this problem, there were two possible solutions. Firstly, due to the unique flexible CFBG writing technique developed at the ORC, we were able to write CFBGs that have both 2nd and 3rd order dispersion [24]. Hence, it was possible to compensate both the GDD and TOD contribution from the bulk grating with the CFBG pulse stretcher. We will describe this solution in more detail in the next section.

Secondly as we have described above, the ratio between the GDD and TOD was dependent on the angle of incidence. The ratio provided by the grating, specified by our sponsor, as a function of angle was calculated using the model develop by Dr C. Barty and is shown in figure 4.9 (c). It has a minimum magnitude ratio value of 4 fs at 89° and rapidly increases at angles < 45°. At an angle of 41°, which gave us optimum efficiency and incidentally is the angle we would operate at, the ratio is ~ 19 fs. With this flexibility, we were able to make real time adjustments (by making only slight angular changes to avoid a significant reduction in efficiency) during our experiments to obtain the cleanest and best quality compressed pulses which we were not able to do for the CFBG with fixed dispersion parameter.

To achieve our specified target of < 500 fs compressed pulses, the spectral width of the amplified pulses through the cascade should be > 5 nm. Subsequently, the measured FWHM spectral width of the amplified pulses out of the final amplifier was ~8 nm wide. Allowing a tolerance of twice the FWHM of the pulse bandwidth for the spectral window (which is the maximum allowable spectral bandwidth transmitted through the grating before clipping occurs) of the grating compressor, it was designed to have a spectral window of 16 nm. This corresponds to a maximum grating separation of 40 cm before clipping occurs. Summing together the compressor contribution to 2nd and 3rd order dispersion, at an angle of incidence of 41° and grating separation of 40 cm (calculated theoretically using Dr C.Barty spreadsheet) and the estimated dispersion contribution from the fiber amplifier cascade of D x length = -0.78 ps/nm and dD/dλ x length = 0.001 ps/nm^2; gives the total 2nd and 3rd order dispersion introduced by the CPA system after the pulse stretcher as D x length = 45.5 ps/nm ($\beta_2 = \left(\frac{\partial^2 \phi}{\partial \omega^2}\right) = 27$ ps^2/rad) and dD/dλ x length = 1.5 ps/nm^2 ($\beta_3 = \left(\frac{\partial^3 \phi}{\partial \omega^3}\right) = 530$ ps^3/rad^2), at a centre wavelength of 1056 nm, respectively. Therefore this total dispersion has to be compensated by the CFBG and the estimated maximum stretched pulse duration for a pulse having FWHM spectral width of ~ 8 nm allowed from this grating was ~ 0.3 ns (D x length x 8 nm).

With the following compressor design settings (angle of incidence of 41° and grating separation of 40 cm), we characterised the dispersion contribution of the bulk grating experimentally. The group delay response of the grating was measured by an RF phase-delay measurement technique shown in figure 4.11. A 1 GHz sinusoidal signal, generated using a HP network analyser, was used to modulate the optical signal from a tunable ASE source via an

EOM. The tunable source was a broadband ASE source centred at 1053 nm and had a resolution of 1 nm, determined by the resolution the Gooch and Housego AcoustoOptic Tunable Filter (AOTF). The delayed return signal, after passing through the grating compressor, was compared to the reference signal, using the network analyser via a fast photodetector. The phase delay measurements were converted to time delay measurements by the equation shown in the figure 4.11 (see equation at the bottom of diagram), where a phase shift of 2π corresponds to a time delay of 1 ns, determined by the frequency (i.e. 1 GHz) of the modulation signal from the network analyser. The theoretical and experimental group response results of the designed compressor are plotted together in figure 4.12 and they were found to be in excellent agreement.

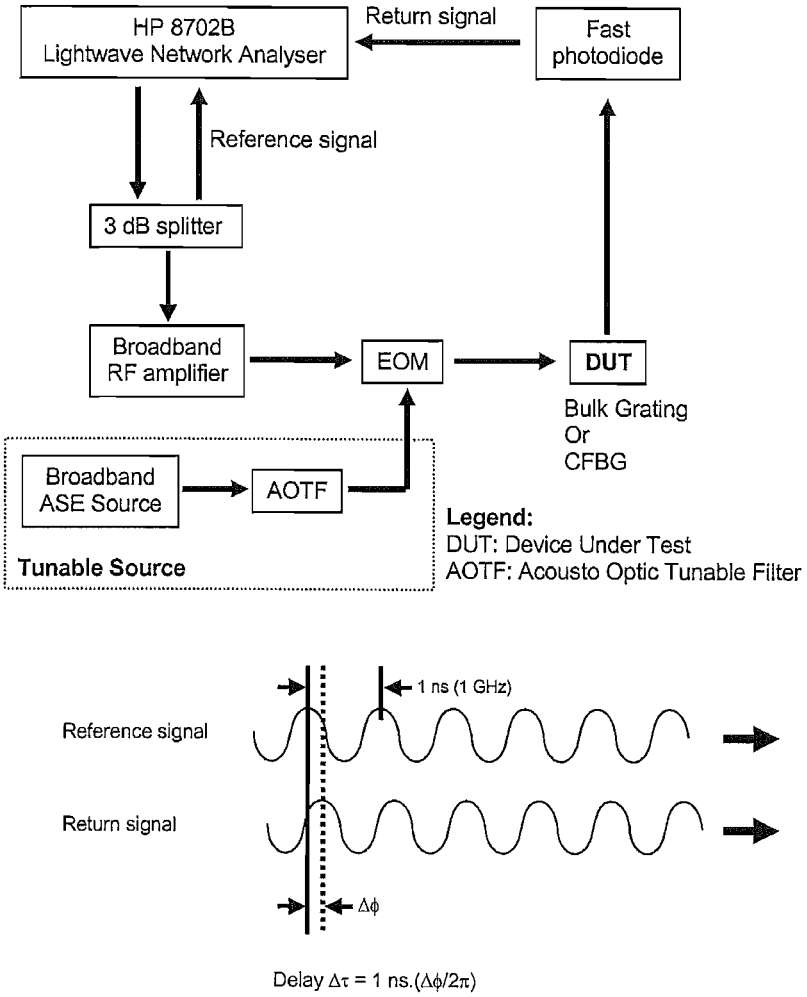

Figure 4.11: RF phase-delay measurement technique to measure dispersion of DUT.

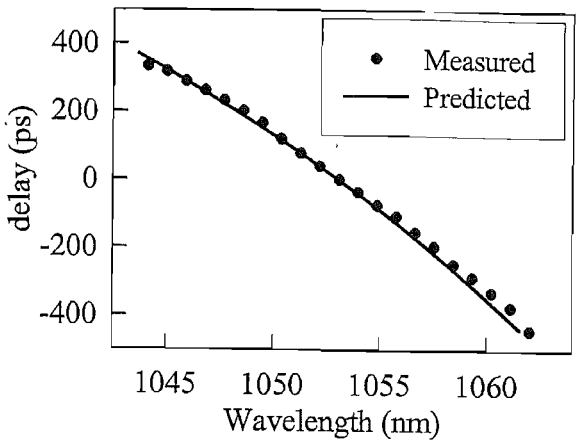

Figure 4.12: Theoretical, and empirically measured, delay response of the designed compressor.

4.2.3.2 CFBG Pulse stretcher

TOD compensation was required if we were to try to achieve clean, pedestal free, < 500 fs, compressed pulses. Uncompressed TOD will result in a distorted compressed pulse having a broad pedestal and a significant fraction of the pulse energy will lie in this pedestal. Previously, authors have used long lengths of fiber to stretch the input pulses [17]. This presents no problems for compressed pulses of duration > 1 ps, as the pulse distortion resulting from uncompensated TOD would be insignificant due to the narrow bandwidth (shown by theoretical modelling made by Dr Jonathan Price from our group using equations obtained from [23]). However for pulses < 500 fs, uncompensated TOD introduces significant distortion.

A specially designed, and written, CFBG to match both the 2nd and 3rd order dispersion values from both the fiber amplifier cascade and grating compressor was produced using a uniquely flexible scanning technique, previously used to produce precision fiber gratings for telecommunications purposes[24]. A CFBG, with 2nd and 3rd order dispersion matched to a bulk grating, has previously been demonstrated in a CPA system at 1550nm [25], but the maximum energy and minimum pulse duration will be limited using Er, compared to Yb amplifiers, because of its lower lasing efficiency and narrower gain bandwidth. Though an experiment at 1050 nm using a CFBG with matching 2nd and 3rd order dispersion to the bulk diffraction grating compressor was presented, in that experiment, no amplification was carried out and the re-compressed pulses were of poor quality [26].

Fabrication of a CFBG is performed by using a specially made phase mask to selectively expose the core of a UV sensitive germano-silicate fiber to intense light pulses from an excimer laser. This creates refractive index variations along the fiber core (typically $\Delta n \sim 10^{-3}$ –

10^{-4}). Though the reflections from these points of index discontinuity are small, thousands of these discontinuities result in an extremely strong grating with reflections up to 100%. The period between these discontinuities will determine the Bragg wavelength to be reflected [24, 27]. We are grateful to Dr Morten Ibsen, from the fiber gratings group at the ORC, for his contribution to this aspect of CPA system project. It was his research group, with input from Professor Mikhail Zervas, that developed this novel technology and related grating design algorithms to be able to fabricate CFBGs with both 2nd and 3rd order dispersion [24, 27]. Dr Ibsen advised that he could fabricate CFBGs having both broad acceptance bandwidth and high 2nd and 3rd order dispersion values. Therefore our task was to specify the required dispersion compensation values and he would fabricate a CFBG as close to our requirements as possible.

A few versions of CFBGs were fabricated; one version had a wide spectral window of ~ 30 nm but without any 3rd order dispersion compensation because, with the current technology (i.e. no suitable phase mask), it was not practically possible for a CFBG to have such a wide window and yet have 3rd order dispersion. The next version was CFBGs with both 2nd and 3rd order dispersion. Both of them had similar dispersion values but one had a 18 nm spectral window and the other had 7 nm. The 30 nm CFBG was design to have 2nd order dispersion value D x Length = 45.5 ps/nm, whereas the 7 and 18 nm CFBGs were design to have 2nd and 3rd order dispersion of D x length = 45.5 ps/nm and $dD/d\lambda$ x length = 1.5 ps/nm^2, at 1056 nm. The sign of the 2nd order dispersion, obtained from the CFBG, depends on which end of the CFBG the light enters. If it enters from the shorter wavelength end (blue light gets reflected first) then it is a minus sign and vice versa. The RF phase delay measurement described above was used to experimentally characterise the dispersion values of the 18 nm grating. The data was fitted to a quadratic polynomial and the 2nd and 3rd order dispersion values were extracted and found to be D x length = 44.7±0.4ps/nm ($\beta_2 = \left(\partial^2\phi/\partial\omega^2\right)$=-26.4 ps^2/rad), and $dD/d\lambda$ x length = 1.5±0.2ps/nm^2 ($\beta_3 = \left(\partial^3\phi/\partial\omega^3\right)$= 0.545 ps^3/rad^2) at 1056 nm respectively. This matches closely to the specified CFBG grating design.

Since 1 μm fiberised circulators were not readily available and expensive at that time, we built a circulator setup with Faraday rotators (FR) and polarisation optics (half and quarter waveplates and a polarisation beam splitter (PBS)) optimised at 1.06 μm. Figure 4.13 shows the circulator setup that was used in our experiment.

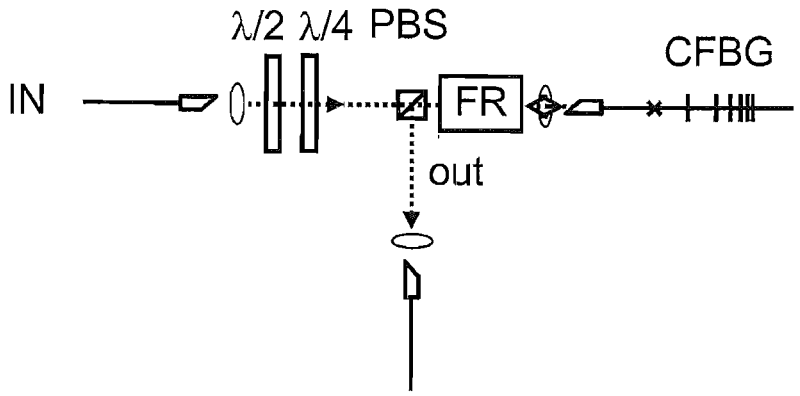

Figure 4.13: Circulator arrangement used in CPA system for CFBG.

Figure 4.14 shows the reflection spectrum with the signal entering from the longer wavelength side of the CFBG and the measured delay (centred at 1053 nm) characteristics with the fitted line.

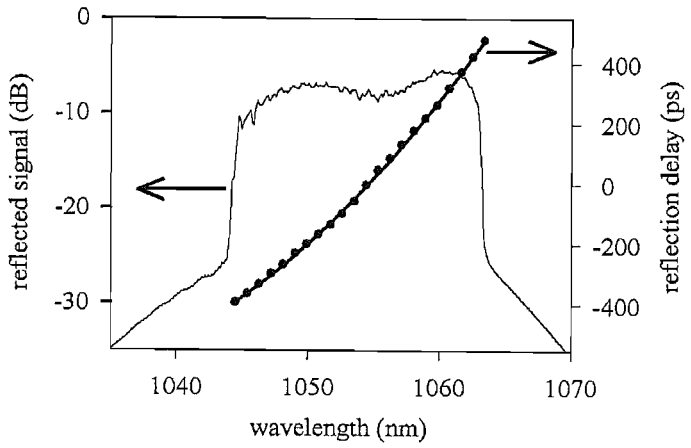

Figure 4.14: Reflected spectrum from red end of CFBG (small cladding-mode loss was observed) with measured delay data.

We can see from figure 4.14 that the reflection spectrum does not have a flat top across the spectral window. Some losses can be observed at the shorter wavelengths. These losses occur especially with broadband CFBGs and are due to cladding mode losses [28]. Ideally the CFBG would only scatter the forward and backward propagating core modes within the high index core when the core mode wave vector matched the grating wave vector. However at a given frequency, the cladding modes have longer wavelengths (shorter wave vectors) due to their lower refractive index. This causes the grating wave vector to also couple the shorter wavelength forward propagating core modes to the longer wavelength cladding modes, resulting in lost power. This occurs only when light enters from the red end of the grating because the forward propagating shorter (blue) signal wavelengths have to travel across the

whole CFBG and will be matched to the reflected cladding mode before they have propagated far enough to match to the reflected core mode.

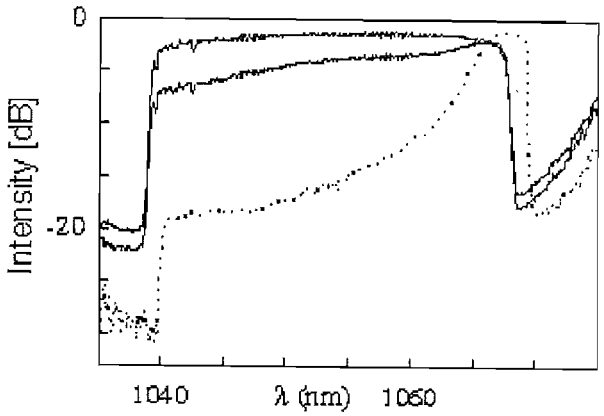

Figure 4.15: Reflected spectrum from the linearly chirp 30 nm CFBG. Signal injected from longer wavelength end of CFBG: Red dotted line (before annealing), Red line (after annealing) and signal injected at shorter wavelength end: Blue line (after annealing).

Figure 4.15 shows the corresponding reflected spectrum from the linearly chirped 30 nm CFBG. The red dotted line shows the reflection spectrum from the strong reflection (before annealing) 30 nm CFBG when the signal was injected at the longer wavelength end. The relative loss of the shorter (blue) signal wavelengths due to cladding-mode losses were > 15 dB higher compared to the peak at 1065 nm (longer (red) wavelengths). When light was injected at the blue end of the CFBG, the reflected spectrum was similar to the spectrum indicated by the blue line in figure 4.15. The strength of this un-annealed CFBG was demonstrated by its transmitted white light spectrum. Highest extinction was > 50 dB at 1055 nm and lowest at the start and end of the CFBG spectral window, at 1040 and 1070 nm respectively, with an extinction strength of > 35 dB. However, it was necessary to launch the signal from the longer wavelength end to obtain a positively chirped stretched pulse to match the sign of the dispersion of the bulk grating. The approach we took to solve this was to reduce the reflectivity of the CFBG by annealing it. By weakening the grating, it would scatter less of the shorter wavelength power to the cladding modes and hopefully thus increase reflectivity at the shorter wavelengths to flatten the reflected spectrum. This approach worked well and the effects could be observed by comparing the reflected spectrum before and after annealing. The cladding mode losses improved from > 15 dB to < 3-4 dB. We see again from the flat top reflected spectra, indicated by the blue line, that cladding mode losses do not occur when the signal is injected at the blue end of the CFBG.

In the next section, we will describe the performance of the CPA system with the CFBG stretcher and bulk grating compressor.

4.2.4 *Performance of CPA system with 2nd and 3rd order dispersion compensation.*

Positively chirped pulses from port 3 of the mode-locked oscillator (see figure 4.1) were launched into the CFBG stretcher via an optical circulator (see figure 4.15) and a 1054 nm free-space isolator (to prevent spurious reflections from de-stabilising the oscillator). The gratings of choice were the 18 nm and 7 nm gratings because they offer both 2nd and 3rd order compensation. Between the 7 and 18 nm spectral window CFBGs, we have chosen to use the 7 nm CFBG even though it has a smaller acceptance bandwidth. This was because the pre-amplifiers within the chain had a considerably smaller gain bandwidth (~ 12 nm), compared to the seed laser, and also to avoid distortions due to gain narrowing effects, we decided to stretch the pulses with the relatively narrow bandwidth 7 nm CFBG.

When we were characterising the temporal stretched pulse, the CFBG was not ready and therefore we had to use 500 m standard 1060nm SM fiber to stretch the pulse. The stretched pulses from this fiber stretcher should correspond to a similar stretch duration, provided by the 7 nm CFBG, which is ~ 318 ps ($\tau_{stretched}$=45.5 (ps/nm) x 7 (nm) = 318 ps). The stretched pulse was measured with a 20 GHz photodiode sampling oscilloscope and is shown in figure 4.16 (a). The pulse was stretched to a duration of ~ 322 ps which was close to what we had estimated to be our maximum stretched pulse duration. The stretched pulse from the 18 nm CFBG was measured to determine the accuracy between the calculated and measured stretched pulse duration. The measured pulse is shown in figure 4.16 (b). Again the calculated temporal pulse width of ($\tau_{stretched}$=45.5 (ps/nm) x 18 (nm) = 819 ps) was close to the measured duration of 800 ps.

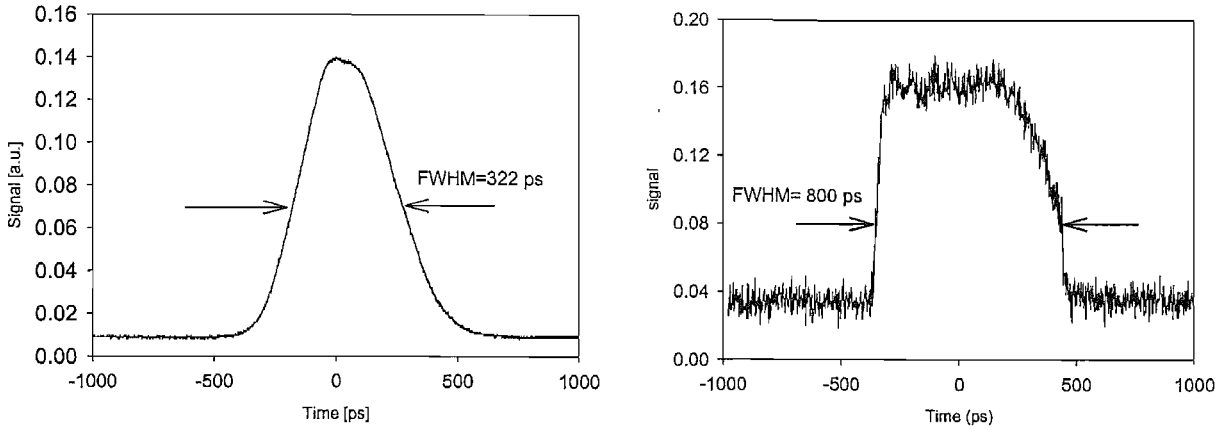

Figure 4.16: Stretched pulse duration from (a) 500 m standard SM 1060 fiber (b) 18 nm CFBG.

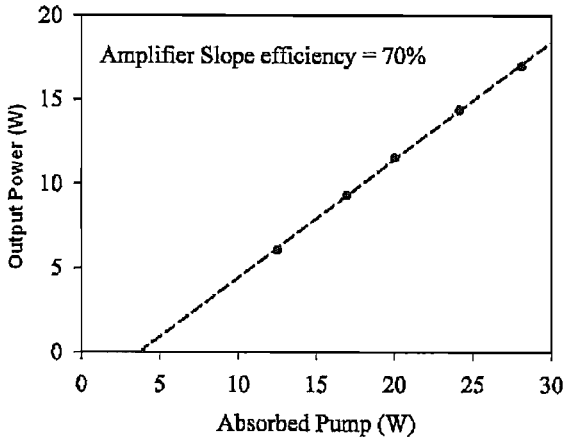

Figure 4.17: Output power vs absorbed pump power.

The stretched pulses from the 7 nm CFBG were amplified through the amplifier cascade and we achieved a maximum output power of 17 W before compression. The slope efficiency was characterised to be ~ 70%. Figure 4.17 shows the output power achieved as a function of absorbed pump power.

Figure 4.18 (a) and (b) show the autocorrelation traces of the recompressed pulses and the output spectrum respectively. The output recompressed pulses obtained using the 7 nm CFBG stretcher were ~ 500 fs long. As we can see from figure 4.18 (a), the re-compressed pulses were extremely clean and no pedestal could be seen. Figure 4.18 (a) also includes the autocorrelation trace of the re-compressed pulse obtained using the linearly chirped (without 3rd order dispersion), broadband, 30 nm CFBG. Comparing the traces, we can see the significant effect of uncompensated TOD. The re-compressed pulse has a substantially broader autocorrelation width (~ 3 ps) and a large pedestal forming at the base of the pulse, with a significant portion of the energy within the pedestal.

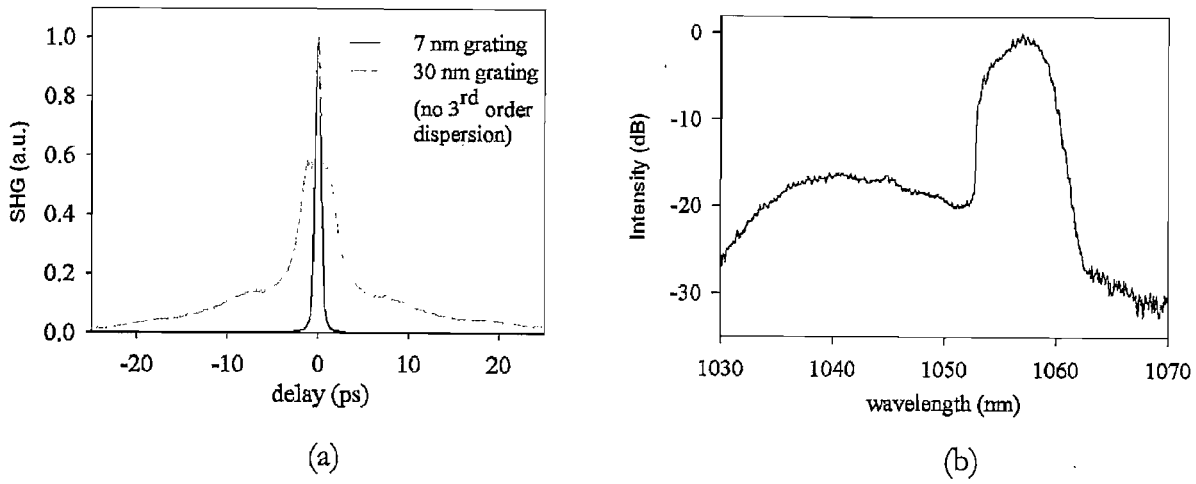

Figure 4.18: (a) Autocorrelation traces of re-compressed pulses using 7 nm CFBG with 2nd and 3rd order dispersion compensation and linearly chirped 30 nm CFBG. (b) Output spectrum of pulses using 7 nm CFBG.

The output spectrum of the 500 fs pulses is shown in figure 4.18 (b). The output spectrum was very clean with > 16 dB ASE extinction. The FWHM bandwidth of the spectrum was ~ 5 nm and the corresponding time-bandwidth product was $\Delta\tau\Delta\nu \sim 0.7$. The highest pulse energy achieved was ~ 10 μJ at a repetition rate of 1.7 MHz and was limited by the onset of SRS (approximately what we would expect, using equation 2.46 of section 2.2.3.3, that the Stimulated Raman Scattering (SRS) threshold energy for amplifying 800 ps pulses in this 16.5 μm core diameter and 9 m length LMA fiber amplifier and extracting 20 dB gain was ~ 14 μJ).

Therefore we believe that with a more optimal choice of fiber in the amplifier for maximum gain and minimum nonlinearities, the system has the potential to reach similar pulse energies to those previously achieved for CPA systems using bulk stretchers. Furthermore, the minimum recompressed pulse durations that we could achieve was limited by the bandwidth of our amplifier.

The transverse mode quality of the final amplifier fiber was characterised using a "Modemaster" beam profiler from Coherent. An output M^2 of 1.3 was the best measured for the amplified pulses from the LMA amplifier. However we found that the output beam quality has a strong dependence on the launch alignment of the input pulses into the LMA fiber amplifier. Optimisation of the fraction of output power to the fundamental mode, and hence the optimisation of the output beam quality, could be achieved by observing the autocorrelation trace. The differential propagation time of the different transverse modes will result in satellite pulses being formed on the autocorrelation trace. Therefore by optimising the

launch such that negligible satellite pulses were observed meant that almost single mode operation was achieved and most of the output energy then lies within the fundamental mode.

4.2.5 *Conclusion*

We have demonstrated an all Yb^{3+} fiber CPA system incorporating a CFBG pulse stretcher and bulk grating compressor with both 2nd and 3rd order dispersion compensation. The CPA system produced clean and stable, 500 fs, 10 μJ, pulses with a spectral FWHM bandwidth of ~ 5 nm. The maximum pulse energy was limited by the onset of SRS.

To reach the 50 μJ target, there were two main limiting factors. First, the limitations imposed by our commercial sponsor, on the type of bulk grating compressor, meant that we would encounter ~ 3 dB loss due to the efficiency throughput at the optimum compressor settings. Hence to achieve ~ 50 μJ output pulse energies, we have to obtain at least ~ 100 μJ pulses after the final amplification stage. However this limitation may be resolved by using a more efficient compressor grating with a reflective dielectric coating (e.g. >95% efficiency) as we progress to producing higher output powers, or to use silica transmission gratings that have been designed to handle >100W average power from a CPA system [29], but these are not currently commercially available. The second limitation was the onset of SRS, which limited output from our amplifier chain to ~10 μJ. This was expected, at the time of the experiment, as the SRS threshold energy for this power amplifier fiber was ~ 14 μJ.

Since the bulk grating compressor was fixed, the approach we intended to pursue to reach our target was to obtain 100 μJ pulses from the final power amplifier. There are a number of ways in which the SRS threshold can be raised. We intend to use fiber amplifiers with larger core-dimensions (to increase the effective mode area as described in section 2.2.3.3) in the final amplification stage. Since then we have fabricated LMA amplifier fibers with larger core diameters. Two examples of these fibers are 30 and 40 μm core diameter LMA fibers. Using a 6 m length for both fibers and with the requirement to obtain 20 dB of gain, the SRS threshold for each fiber was calculated to be ~ 70 μJ and ~ 125 μJ respectively, which would be sufficient to achieve 50 μJ pulses. This increase in effective core area also increases the maximum extractable energy from the power amplifier. Extracting from figure 2.10, the maximum extractable energy from a 30 μm and 40 μm core diameter fiber are 3.8 mJ and 6.7 mJ, compared to 1 mJ for a 16.5 μm diameter core. Previously, we have used both 915 and 976 nm pump diodes in the final amplification stage. Since the pump absorption length of the 915 diode was ~ three times longer than the 976 diode, by using

only 976 nm diode pumps, we would be able to use shorter fiber lengths and hence increase the SRS threshold.

Dr Ibsen has recently obtained a phase mask which could fabricate CFBGs with larger spectral windows and optimised 2nd and 3rd order dispersion values could also be implemented to achieve higher pulse energies and shorter compressed pulse durations. But this improvement must be preceded by increasing the gain bandwidths of the pre-amplifier stages at the operating wavelength so that spectrally broader pulses could be amplified. Increasing the gain bandwidth will also proportionately increase the duration of the stretched pulses for a fixed chirp rate, which will also raise the SRS threshold.

4.3 Parabolic amplifier system

As with all fiber based short pulse amplifier systems, the ultimate performance (i.e. power scaling) will always be limited by pulse distortion as a result of nonlinearities (i.e. excessive SPM or SRS) arising due to the tight modal confinement in the fiber gain media. Possible approaches to achieve higher output powers includes CPA systems described in the earlier section or by scaling up the mode areas of the fiber amplifiers in a direct amplification configuration. Since SRS critical threshold power scales proportionally with core sizes, we are able to achieve higher power scaling by increasing the fiber mode areas [23]. However, highest output energies of these short pulses, obtainable from such systems, are still lower compared to CPA systems. The high average power possible with fiber based systems allows for high repetition rates at a given pulse energy which will translate directly into higher processing speeds. With increasing applications (i.e. range finding, nano and micro machining) requiring high average, high repetition rate, output pulses, there is a real interest in the development of such systems and this is in parallel to CPA systems.

At low energies, the pulses have low peak intensities and hence avoid nonlinear evolution within the amplifier cascade. The pulses develop a linear chirp due to the GVD of the fibre, and can be re-compressed without distortions with a bulk diffraction grating pair at the output. (TOD effects are negligible because the total dispersion is very short compared to a CPA system) However, with moderate pulse energies, the higher peak intensity of the pulses will lead to significant nonlinear evolution (i.e. SPM). However, nonlinear evolution need not always lead to output pulse degradation. It has been shown theoretically that the combination of normal dispersion and SPM effects with sufficient gain in a fiber amplifier can lead to pulses

evolving towards an asymptotic solution to the nonlinear Schrödinger equation (NLSE) with a parabolic intensity profile and linearly varying chirp [30, 31]. As they propagate along the fiber amplifier cascade, these 'parabolic' pulses broaden both temporally and spectrally whilst maintaining a linear chirp (steeper compared to the linear chirp of low energy pulses) across the central region of the pulse. This enables the clean re-compression of the higher energy pulses despite significant SPM in the fiber.

Such 'parabolic' pulse amplifier systems are able to produce shorter (~100 fs) higher energy pulses than currently available CPA or direct amplification systems. These systems are also comparatively simpler than CPA systems (do not require a pulse stretcher and highly-dispersive compressor). We note that by using the CPA technique to avoid nonlinear effects, fiber-based systems producing 75 W average power have been demonstrated, albeit with substantially longer output pulses (400 fs), and requiring a more complex and less compact setup [32]. Therefore the development of such systems is of interest. In this section, I will describe the development and performance of a parabolic amplifier system.

Parabolic pulses from Yb^{3+} fiber amplifiers have previously been demonstrated with average powers up to 17 W (pulse energy ~ 230 nJ) using a bulk glass seed laser [29] and up to 13 W (pulse energy ~ 260 nJ) with a fiber based seed laser [10]. However both of these systems utilised only a single amplification stage which limits the gain to ~ 30-40 dB. This restricts the number of possible applications and suitable seed sources. For example, using Yb fiber based modelocked seed sources (i.e. the oscillator developed in chapter 3) which produce environmentally stable, low noise, and short duration pulses but with low pulse energies (~ 30 pJ), the maximum output pulse energies would be ~ 30 nJ. In this section, I will be reporting an all Yb^{3+} fiber system incorporating a two stage fiber amplifier cascade which produced average power > 25W and pulse energies of 410 nJ, which was a record for a fiberised parabolic amplification system. This system utilises a conventional bulk grating compressor to remove the chirp and obtain ~ 100 fs compressed pulses.

4.3.1 *Principles of Parabolic Pulse evolution*

The first numerical simulations of 'parabolic' pulse formation from an ultrashort pulse being amplified in a nonlinear fiber, with normal dispersion, were made by Tamura *et al.* [31]. Prior to this, Anderson D. [33] *et al.* had already made theoretical studies of asymptotic self-similar behaviour of the nonlinear propagation of ultrashort pulses having parabolic intensity profiles

in an optical fiber with normal dispersion. They found that when the pulse propagates over a substantial length of fiber, the chirp accumulated remains linear, enabling high quality compressed pulses to be produced. Results from further numerical simulations (and verified by experiment) carried out by Fermann M.E *et al.* show that these 'parabolic' pulses are in fact asymptotic solutions of the NLSE (see equation 2.21) but with gain [34] propagating in the amplifier self-similarly and obeying simple scaling laws. The modified NLSE equation with gain, described by [34], is shown in equation 4.1.

$$i\frac{\partial A}{\partial z}=\frac{1}{2}\beta_2\frac{\partial^2 A}{\partial T^2}-\gamma\left|A\right|^2A+i\frac{g}{2}A. \tag{4.1}$$

where $A(z,T)$ is the slowly varying pulse envelope in a co-moving frame, β_2 is the GVD parameter, γ is the nonlinearity parameter and g is the constant distributed gain coefficient.

Assuming an idealised optical amplifier with an infinite bandwidth, constant gain and without gain saturation, the self-similar solutions of equation 4.1 when $g \neq 0$ and $\beta_2\gamma > 0$ in the limit $z \to \infty$ are found to be [35],

$$A(z,T)=A_0\exp(gz/3)\left\{1-\left[T/T_0(z)\right]^2\right\}^{1/2}\exp\left[i\varphi(z,T)\right], \qquad |T|\le T_0(z), \tag{4.2}$$

with $A_0=0.5(gE_{IN})^{1/3}(\gamma\beta_2/2)^{-1/6}$.

$$T_0(z)=3g^{-2/3}(\gamma\beta_2/2)^{1/3}E_{IN}{}^{1/3}\exp(gz/3) \tag{4.3}$$

$$\varphi(z,T)=3\gamma A_0^2(2g)^{-1}\exp(2gz/3)-g(6\beta_2)^{-1}T^2 \tag{4.4}$$

where E_{IN} is the energy of the input pulse seeding the amplifier and $T_0(z)$ is the effective width.

Equation 4.2 shows a pulse with a parabolic intensity profile and equation 4.4 indicates a quadratic temporal phase (i.e. linear chirp). In the asymptotic regime, it propagates self-similarly, maintaining a parabolic profile subject to the exponential scaling of its amplitude and its effective width (equation 4.3). The same exponential scaling also occurs spectrally. These

solutions, described in equations 4.2 to 4.4, also imply that in the parabolic regime, it is the energy of the input pulse and the amplifier characteristics that determine the characteristics of the output pulse. The shape of the input pulse only determines the length scale required to evolve toward the parabolic pulse solution. Thus well defined linearly chirped output pulses can still be produced from parabolic amplifiers even when the input pulses are distorted.

Figure 4.19 shows a pictorial illustration of the temporal and spectral parabolic evolution of an arbitrary ultrashort input pulse being amplified in an amplifier with sufficient gain, gain bandwidth, length and normal dispersion (with respect to the pulse wavelength). SPM and dispersion cause the input pulse to evolve to an asymptotic solution with parabolic envelope in time, and wavelength, and linear chirp.

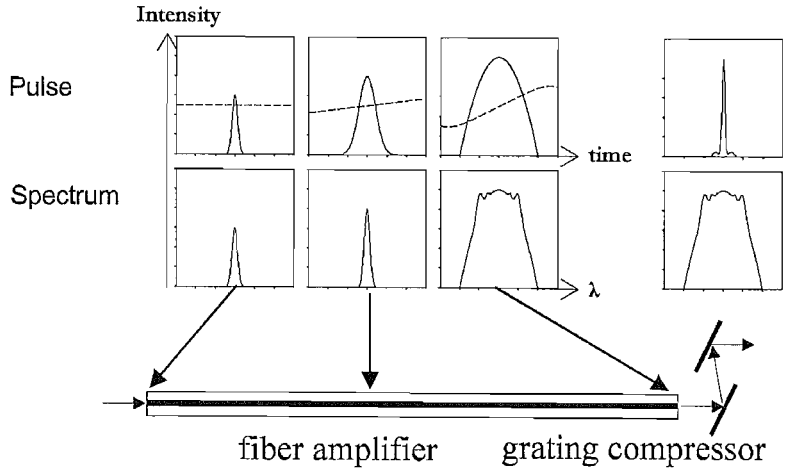

Figure 4.19: Pictorial illustration of the formation of a parabolic pulse from an arbitrary input pulse shape. The dotted lines in the pulse temporal plots represent the frequency chirp across the pulse.

4.3.2 *Experimental setup and performance*

The schematic of the parabolic amplifier cascade is shown in figure 4.20 below. A semiconductor diode pumped, modelocked, Yb^{3+} fiber seed laser (see chapter 3) followed by two Yb^{3+} fiber amplifiers, was used. The oscillator produced ~ 30 pJ pulses at 62 MHz repetition rate, centred at a wavelength of 1055 nm. The seed pulses were taken from port 3 (see figure 4.1) of the oscillator, they were positively chirped. They had a spectral bandwidth of ~ 20 nm and FWHM durations of 1.8 ps which were compressible down to ~ 110 fs FWHM durations using bulk gratings. However in these experiments, the uncompressed, positively chirped, pulses were directly input into the amplifier cascade.

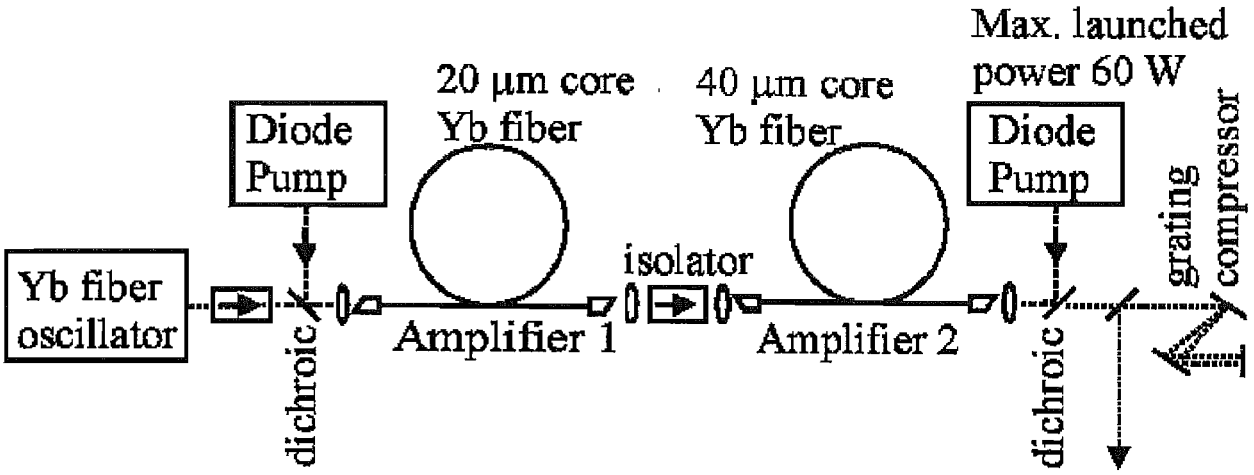

Figure 4.20: Schematic of the parabolic amplification setup.

Both fiber amplifiers were cladding pumped. Though the dimensions for both fibers were different, they were pulled from the same perform. The fibers were step index profile LMA LF128 fibers, with a NA of ~0.06, and were doped with 8000 parts per million (ppm) by weight Yb^{3+} ions. The fiber was doped on axis to provide higher overlap with the fundamental mode, so that gain is favoured in the fundamental mode. The fundamental mode area of the 40 μm core fibre was calculated to be A_{eff}~370 μm^2. Due to the low NA even the loose coiling of ~300 mm diameter we employed was sufficient to produce high bend losses for high order modes. The gain differential between fundamental and higher-order modes and lack of coupling (due to the large cladding diameter) between modes allowed us to obtain robust single transverse mode output from the fibre during laser operation by means of optimised launching into the fundamental mode (see section 2.4 of chapter 2).

Free space isolators from EOT (see section 2.5.1.1 of chapter 2) were used between each amplification stage to suppress build up of ASE through the amplifier cascade (which causes premature gain saturation) and to prevent spurious feedback from de-stabilising of the oscillator. Optical coupling of pump to active fiber cladding and of signal to fiber core was by means of bulk optics: pairs of aspheric lenses with 8 and 11 mm focal lengths. The lenses had large enough diameters to avoid clipping of the beams, and the exact focal lengths of lens pairs were selected empirically to maximize coupling.

The amplifier efficiency as a function of absorbed pump for both amplification stages was characterised to be 79%. Figure 4.21 shows the output power with respect to absorbed pump power of the final amplifier stage with an input signal launch power of ~ 60 mW. Gains of up to 28 dB were achieved.

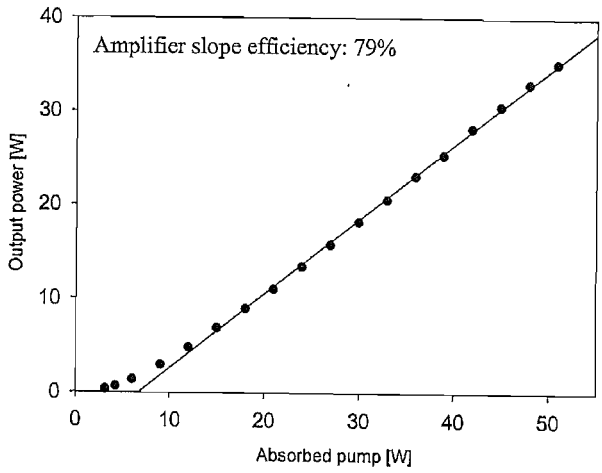

Figure 4.21: Output power vs absorbed pump power for final amplification stage.

The first amplifier fiber was forward pumped via suitable dichroics by a 3 W, 975 nm, Mylon diode source which has a 200 μm diameter, multimode, fiberised pigtail, with an NA of 0.22. The amplifier fiber has core/inner cladding diameters of 20/200 μm and a length of 1.6 m. The transverse output mode quality was strictly single moded. We noticed very little nonlinear evolution of the pulses occurring in this amplification stage at the operating pump power of ~ 1.5 W. This can be seen from figure 4.22 which shows the temporal (a) and spectral (b) output of 2.5 nJ pulses from the pre-amplifier.

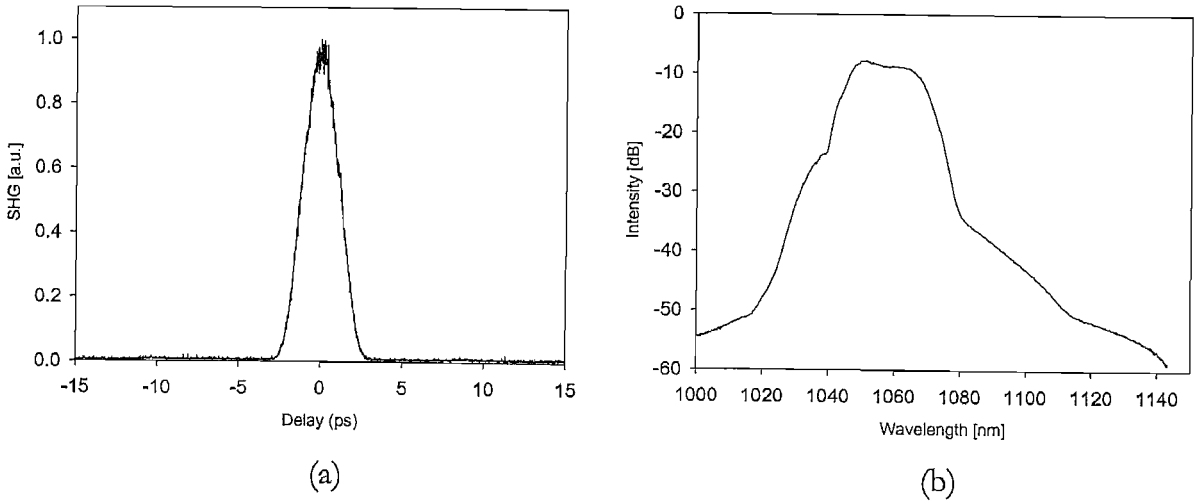

Figure 4.22: (a) Autocorrelation trace and (b) spectrum of 2.5 nJ output pulses from pre-amplifier.

The autocorrelation FWHM of the 2.5 nJ output pulses obtained was ~ 2.4 ps and the spectral width increases from the oscillator pulse width of 20 nm to 20.8 nm for the same output pulse energy. The characteristics of the output pulses over a range of pulse energies from the pre-amplifer were characterised by increasing the Mylon pump power to observe

any substantial nonlinear evolution. It was found that the autocorrelation FWHM of the output pulses remained at ~ 2.4 ps and the spectral width increases from the oscillator pulse width of 20 nm to 22 nm for output pulse energies in the range of 0.2 nJ to 4.7 nJ, which indicated that pulse evolution was essentially linear. In our experiment, output pulse energies in the range of 1-2 nJ (average power 60-120 mW) were fed into the second amplifier stage.

The second amplifier fiber was reverse pumped by a commercial 972 nm diode source capable of delivering up to 1 kW of pump power. A fraction of the free-space output from this source was coupled into a commercial multi-mode delivery fiber. The delivery fiber had a core diameter of 365mm and NA=0.26. Up to 90 W of power was transmitted by the delivery fiber in these experiments. The launch efficiency from the delivery fiber to the amplifier fiber was ~67% (~60 W). Note that suitably powerful commercial diode pump sources, which could couple efficiently directly into our amplifier fiber, exist but that we did not have such a source available to us during these experiments. The amplifier fiber had a length of 4 m and core/inner cladding diameters of 40/400 μm. The maximum launched pump power of 60 W corresponds to 50 W of absorbed pump for this pump wavelength and fiber length. By carefully launching the seed pulses so as to excite only the fundamental fiber mode, we obtained close to single mode output from the amplifier. The mode was optimised by adjusting the bulk-optic signal launch into the second amplifier whilst monitoring the autocorrelation. Since the different transverse modes of the fiber have slightly different propagation rates in the fibre, cross-correlations between different transmitted modes are manifest as extra peaks on the autocorrelation signal, with delays of several picoseconds. Therefore seed launch alignment could be optimised to achieve single mode operation by the suppression of these peaks. In c.w. operation we have measured an M^2 of 1.1 from this fiber. Concern about damage due to high peak powers in our beam analyser meant that we could not perform this measurement with the pulsed system. However, no visible change in mode profile was observable, on switching between c.w. and pulsed laser operation, leading us to conclude that there was no associated degradation in beam quality. The final stage amplifier maintained a stable transverse mode, and power output, for up to several hours after alignment. The seed source has excellent stability (see section 3.3.4) and the amplitude stability of the whole system was correspondingly good. The degree of polarisation of the output signal was not carefully monitored, but the dependence of autocorrelation measurements on waveplate alignment show that it could not be less than 95% and was probably much higher. Spectral measurements (see below) showed that output ASE power was very small (<1%) compared to the output signal power.

The output pulses were compressed using conventional bulk gratings, with 830 grooves/mm, from Richardson Gratings Laboratories. The gratings had 70% diffraction efficiency. To prevent damage to the gratings due to the high output powers, we passed only a fraction of the output power through the compressor. However, the power handling capacity and efficiency could be improved by using suitably optimised gratings, i.e. high power transmission gratings.

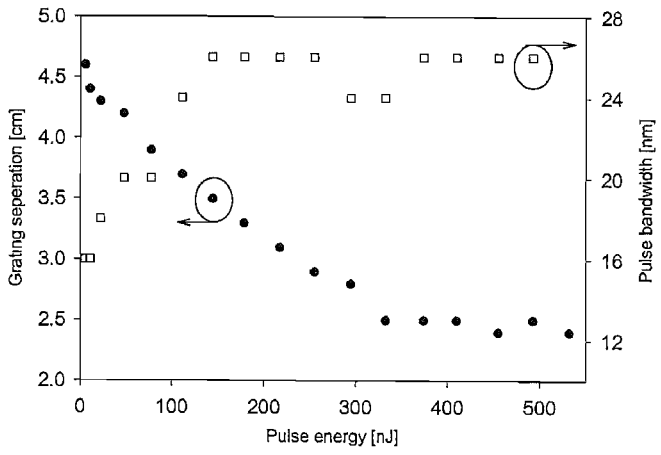

Figure 4.23: Optimum compressor grating separation and 3dB spectral width as a function of output pulse energy.

The grating separation was optimised experimentally by minimising the width of the recompressed pulse autocorrelation. Figure 4.23 shows the optimum compressor grating separation as a function of the output pulse energy. It shows that the optimum grating separation decreases with increasing output pulse energy, which incidentally corresponds to the increasing chirp of the pulse with increasing output pulse energy. Figure 4.22 also shows the increasing 3dB spectral bandwidth of the pulses with output pulse energy. The spectral bandwidth rises from 16 nm at low output energy to 26 nm at a pulse energy of ~ 200 nJ, above which it remains unchanged up to the highest output powers. The significantly lower 16 nm bandwidth, compared to the seed pulses from the pre-amplifier (~ 20.5 nm) at the low energies, we believe was due to gain narrowing near the signal launch end of the final amplifier as a result of the relatively low inversion at this end of the fiber. The increasing chirp and spectral bandwidth at the high pulse energies are indicative of strong nonlinear evolution. Ideally the fiber amplifier cascade should have unlimited spectrally flat gain bandwidth. However in a practical system, the finite gain bandwidth will limit spectral broadening and distort the pulse if the nonlinear spectral broadening (due to SPM) creates a pulse bandwidth greater than the amplifier bandwidth. It appears that we have reached the maximum bandwidth of the amplifier at 26 nm. Before compression the pulses had FWHM

durations which increased with pulse energy from ~4.6 ps at 5 nJ to a peak of ~6.0 ps at pulse energies of 300-400 nJ.

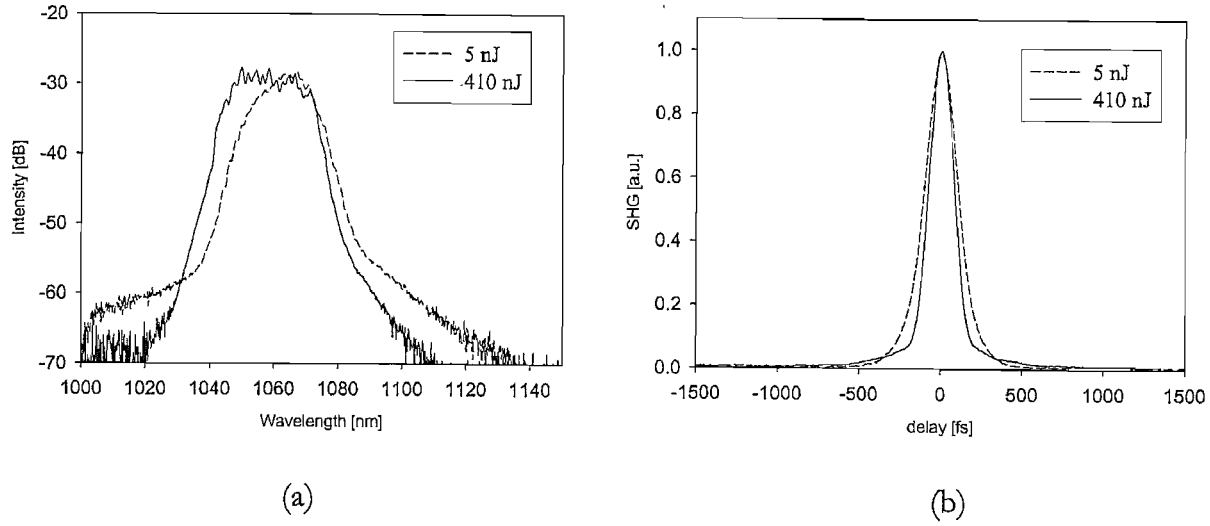

Figure 4.24: (a) Spectrum and (b) autocorrelation of compressed pulses at 5 nJ and 410 nJ pulse energies.

The spectra and autocorrelation of the compressed pulses are shown in Figure 4.24 (a) and (b) respectively. At low pump powers, we observe that the centre wavelength of the output spectrum from the final amplifier has shifted to 1062 nm and spectral clipping of the pulses occurs at the short wavelengths. It had a FWHM spectral bandwidth of 16 nm. At higher pump powers, the bandwidth is 26 nm and the spectrum has developed a flat top which is a characteristic of parabolic pulse evolution.

The system produced pulses of energy up to 560 nJ (average powers of up to 35 W) without the onset of significant Raman scattering (theoretically calculated threshold from [23] was ~ 600 nJ), although the pulse quality at these higher pulse energies was somewhat degraded. The measured autocorrelations of the compressed pulses correspond to pulse durations of ~ 150 fs and ~ 110 fs (assuming a sech^2 pulse shape) at 5 nJ and 410 nJ respectively. The time-bandwidth products of the pulses are therefore $\Delta\tau\Delta\nu \sim 0.7$ for both pulse energies, which is approximately twice transformed limited. A small pedestal was observed for recompressed pulses at 410 nJ and the pedestal grows with increasing pulse energies. The appearance of these pedestals appears to coincide with the saturation of the spectral broadening. Therefore achieving higher pulse energies (before the onset of distortion to the recompressed pulse) from this amplifier cascade was limited by the finite gain bandwidth of the final amplifier.

4.3.3 *Conclusion*

In conclusion, we have demonstrated a robust, diode pumped, all Yb^{3-} fiber direct amplification system (both seed and amplifier) based on parabolic pulse amplification, capable of producing high quality single moded ~ 400 nJ pulses with a recompressed pulse duration of 110 fs at average powers in excess of 25 W. The system could be engineered to have a compact form and represents a simple and practical, fiber based, solution for a wide range of high average power femtosecond pulse laser applications.

We believe we have achieved parabolic pulse amplification because of the spectral and chirp features obtained. The flat top and significant broadening of the spectrum with increasing pulse energies, yet without distortion to the recompressed pulses (linearly chirped), and the significant increase in the chirp slope are indicative of parabolic pulse amplification. In this experiment, pulse energies were limited (before the onset of pulse distortions) by the gain bandwidth of the final amplifier. Therefore increasing the gain bandwidth of the amplifier would enable clean, higher energy, pulses to be obtained. Although at the present output pulse energies, SRS was not encountered, eventually, with higher output pulse energy, it is likely to be the ultimate limitation. Further improvements to increase the effective mode area of the fiber amplifiers could increase the SRS threshold energy. Another practical limitation that we found whilst running this experiment was damage to the LMA fiber end facet. However this issue could be easily solved by using end caps (see chapter 5.3.2.4).

REFERENCES

1. Liu, X., Du, D. and Mourou, G., *Laser ablation and micromachining with ultrashort laser pulses.* IEEE Journal of Quantum Electronics, 1997. **33**(10): p. 1706-1716.
2. Kieffer, J.C., Matte, J. P.,Chaker, M.,Beaudoin, Y.,Chien, C. Y.,Coe, S.,Mourou, G.,Dubau, J. and Inal, M.K., *X-Ray-Line Polarization Spectroscopy in Laser-Produced Plasmas.* Physical Review E, 1993. **48**(6): p. 4648-4658.
3. O'Connor, M.V., Watson, M. A.,Shepherd, D. P.,Hanna, D. C.,Price, J. H. V.,Malinowski, A.,Nilsson, J.,Broderick, N.G. and Richardson, D.J., *Synchronously pumped optical parametric oscillator driven by a femtosecond mode-locked fiber laser.* Optics Letters, 2002. **27**(12): p. 1052-1054.
4. Strickland, D. and Mourou, G., *Compression of Amplified Chirped Optical Pulses.* Optics Communications, 1985. **55**(6): p. 447-449.
5. Galvanauskas, A., Fermann, M.E., Blixt, P., Tellefsen, J.A, Harter, D., *Hybrid Diode-Laser Fiber-Amplifier Source Of High-Energy Ultrashort Pulses.* Optics Letters, 1994. **19**(14): p. 1043-1045.
6. Taverner, D., Richardson, D. J., Dong, L., Caplen, J. E., Williams, K., Penty, R. V., *158-μJ pulses from a single-transverse-mode, large-mode-area erbium-doped fiber amplifier.* Optics Letters, 1997. **22**(6): p. 378-380.
7. Taverner, D., Galvanauskas, A., Harter, D., Richardson, D.J., Dong, L., *Generation of high-energy pulses using a large-mode-area erbium doped fiber amplifier*, in *Tech. Dig. Conference Lasers and Electro-Optics.* 1996. p. 496-497.
8. Minelly, J.D., Galvanauskas, A., Harter, D., Caplen, J.E., *et al.*, *Cladding-pumped fiber laser/ amplifier system generating 100uJ energy picosecond pulses*, in *Tech. Dig. Conference Lasers and Electro-Optics.* 1997. p. 475-476.
9. Galvanauskas, A., Cho, G.C., Hariharan, A., Fermann, M.E., *et al.*, *Generation of high-energy femtosecond pulses in multimode-core Yb-fiber chirped-pulse amplification systems.* Optics Letters, 2001. **26**(12): p. 935-937.
10. Galvanauskas, A., *Mode-scalable fiber-based chirped pulse amplification systems.* IEEE Journal Of Selected Topics In Quantum Electronics, 2001. **7**(4): p. 504-517.
11. Hartl, I., Imeshev, G. and Fermann, M.E. *In-line high energy Yb fiber laser based chirped pulse amplifier system.* in *Conference on Lasers and Electro-Optics, CLEO.* 2004. San Francisco 16-21 May 2004. **1**(1): p. 3
12. Lefort, L., Price, J.H., Richardson, D.J., Spuhler, G.J., *et al.*, *Practical Low-Noise stretched-pulse Yb-doped fiber laser.* Optics Letters, 2002. **27**(5): p. 291-293.
13. Desthieux, B., Laming, R.I. and Payne, D.N., *111 kW (0.5 mj) Pulse Amplification at 1.5 μm Using a Gated Cascade of 3 Erbium-Doped Fiber Amplifiers.* Applied Physics Letters, 1993. **63**(5): p. 586-588.
14. Renaud, C.C., Offerhaus, H.L., Alvarez-Chavez, J.A., Nilsson, J., *et al.*, *Characteristics of Q-switched cladding-pumped ytterbium-doped fiber lasers with different high-energy fiber designs.* IEEE Journal Of Quantum Electronics, 2001. **37**(2): p. 199-206.
15. Lee, J.H., Ryu, U.C., Ahn, S.J. and Park, N.K., *Enhancement of power conversion efficiency for an L-band EDFA with a secondary pumping effect in the unpumped EDF section.* IEEE Photonics Technology Letters, 1999. **11**(1): p. 42-44.
16. Cheo, P.K., *Fiber Optics and Optoelectronics.* 2nd Edition, ed. P. Hall. 1990.
17. Biswal, S., Nees, J., Nishimura, A., Takuma, H., *et al.*, *Ytterbium-doped glass regenerative chirped-pulse amplifier.* Optics Communications, 1999. **160**(1-3): p. 92-97.
18. Martinez, O.E., *Design of High-Power Ultrashort Pulse-Amplifiers by Expansion and Recompression.* IEEE Journal of Quantum Electronics, 1987. **23**(8): p. 1385-1387.

19. Pessot, M., Maine, P. and Mourou, G., *1000 Times Expansion Compression of Optical Pulses for Chirped Pulse Amplification.* Optics Communications, 1987. **62**(6): p. 419-421.
20. Boskovic, A., Guy, M.J., Chernikov, S.V., Taylor, J.R., *et al.*, *All-Fiber Diode-Pumped, Femtosecond Chirped Pulse Amplification System.* Electronics Letters, 1995. **31**(11): p. 877-879.
21. Broderick, N.G.R., Richardson, D.J., Taverner, D., Caplen, J.E., *et al.*, *High-power chirped-pulse all-fiber amplification system based on large-mode-area fiber gratings.* Optics Letters, 1999. **24**(8): p. 566-568.
22. Fork, R.L., Cruz, C.H.B., Becker, P.C. and Shank, C.V., *Compression Of Optical Pulses To 6 Femtoseconds By Using Cubic Phase Compensation.* Optics Letters, 1987. **12**(7): p. 483-485.
23. Agrawal, G.P., *Nonlinear Fiber Optics.* 3rd Edition ed. 2001, San Diego: Academic Press.
24. Ibsen, M., Durkin, M.K., Zervas, M.N., Grudinin, A.B., *et al.*, *Custom design of long chirped Bragg gratings: Application to gain-flattening filter with incorporated dispersion compensation.* IEEE Photonics Technology Letters, 2000. **12**(5): p. 498-500.
25. Imeshev, G., Hartl, I. and Fermann, M.E., *Chirped pulse amplification with a nonlinearly chirped fiber Bragg grating matched to the Treacy compressor.* Optics Letters, 2004. **29**(7): p. 679-681.
26. Olivie, G., Villate, D., Videau, L. and Salin, F. *Recompression of Short Pulses Stretched by Fiber Bragg Gratings.* in *Post-conference Dig. Conference Lasers and Electro-Optics, CLEO* 2003. Baltimore, MD. *PDA10.* p. 2110-2111. *(Postdeadline paper)*
27. Ibsen, M., Durkin, M.K., Cole, M.J., Zervas, M.N., Laming, R. I., *Recent Advances in Long Dispersion Compensating Fiber Bragg Gratings.* in *IEE Colloquium on Optical Fiber Gratings IEE.* 1999. London, U.K. p. 6/1-7.
28. Erdogan, T., *Fiber grating spectra.* Journal Of Lightwave Technology, 1997. **15**(8): p. 1277-1294.
29. Limpert, J., Schreiber, T., Clausnitzer, T., Zollner, K., Fuchs, H. J., Kley, E. B., Zellmer, H., Tünnermann, A., *High-power femtosecond Yb-doped fiber amplifier.* Optics Express, 2002. **10**(14): p. 628-638.
30. Fermann, M.E., Kruglov, V.I., Thomsen, B.C., Dudley, J.M., Harvey, J. D., *Self-similar propagation and amplification of parabolic pulses in optical fibers.* Physical Review Letters, 2000. **84**(26): p. 6010-6013.
31. Tamura, K. and Nakazawa, M., *Pulse compression by nonlinear pulse evolution with reduced optical wave breaking in erbium-doped fiber amplifiers.* Optics Letters, 1996. **21**(1): p. 68-70.
32. Limpert, J., Clausnitzer, T., Liem, A., Schreiber, T., *et al.*, *High-average-power femtosecond fiber chirped-pulse amplification system.* Optics Letters, 2003. **28**(20): p. 1984-1986.
33. Anderson, D., Desaix, M., Karlsson, M., Lisak, M., *et al.*, *Wave-Breaking-Free Pulses In Nonlinear-Optical Fibers.* Journal Of The Optical Society Of America B-Optical Physics, 1993. **10**(7): p. 1185-1190.
34. Desurvire, E., *Erbium doped fiber amplifiers: principles and applications.* 1994, NY: John Wiley & Sons, Inc.
35. Kruglov, V.I., Peacock, A.C., Dudley, J.M. and Harvey, J.D., *Self-similar propagation of high-power parabolic pulses in optical fiber amplifiers.* Optics Letters, 2000. **25**(24): p. 1753-1755.

Chapter 5

HIGH POWER, HIGH BRIGHTNESS, mJ Q-SWITCHED YTTERBIUM DOPED FIBRE LASER SYSTEM.

5.1 Introduction

High power nanosecond pulse laser systems are in widespread use in many present day industrial applications and in different areas of science and technology. The market is currently dominated by crystalline or glass solid state laser systems. Diode pumped rod, solid-state lasers are widely used in low-power applications owing to their inherent stability, robustness and efficiency.

However without the use of more complex, system architectures, thermal effects such as thermal lensing and induced birefringence limit the power scaling in these lasers. Several solid-state MOPA systems have been shown to demonstrate average output powers of up to hundreds of Watts with peak power levels in the mega to gigawatts range [1-7]. However these systems tend to have low repetition rates (because thermally induced effects worsen with increasing output average powers) and poor output beam quality, especially at higher powers. St Pierre *et al.* demonstrated average powers of up to 875 W at 100 Hz, with a peak power of 1.3 GW [4], from a laser-diode-pumped Nd:YAG slab system, but the beam quality at the highest output power was not described. This same group had also achieved an average output power of 690 W, with peak intensity of 14 MW at 2.5 kHz repetition rate, having reasonably good beam quality of 1.1 × the diffraction limit (DL) with another laser-diode-pumped Nd:YAG slab system [5], which was named Active Tracker Laser (ATLAS). Recently, Amano *et al.* showed that simultaneous high average power, high peak power and brightness could be achieved in a diode-pumped Nd:YAG MOPA system [6]. The system provided an average output power of 235 W with peak intensities of 30 MW at 320 Hz. The output beam quality was near diffraction limited having an M^2=1.5. Although the performance of these solid state systems seems adequate for current industrial demands, the rise in demand for such a laser system in today's industries also motivates the search for a compact and economical, high performance system which the solid state systems do not provide.

Compared to solid-state systems, fibre laser systems provide better quality pulses (the tighter beam confinement within their smaller core provides better output modal quality) at much higher repetition rates, higher wall-plug efficiency and excellent heat dissipation. In the

past, the limited power of single-mode diode pump sources has restricted the maximum output powers of rare-earth doped fibre lasers to ~ 1 W. But this limitation has been overcome with the development of the cladding pump technique [8, 9]. Also, the use of higher power, lower brightness, diode pump sources has led to the power scaling of fibre lasers up to the kilowatt level [10]. This in turn has led to fibre lasers being able to compete with bulk solid state lasers in the high power regime. Fibre laser systems provide other benefits, such as lower production cost and greater compactness, over bulk solid state lasers. Therefore the motivation behind the work in this chapter is to take advantage of these benefits and produce a low cost, compact, Q-switched, fibre laser system that can provide pulse energies compatible with application requirements and comparable to their solid state counterparts. The present state-of-the-art in single stage, Q-switched lasers is shown in table 5.1.

Author	C.C Renaud *et al.* [11]	Y. Jeong *et al.* [12]	Y. X. Fan *et al.* [13]
Pulse energy (mJ)	**7.7 mJ**	0.6 mJ	1.57 mJ
Pulse duration (ns)	250 ns	460 ns	**4.2 ns**
Repetition rate (KHz)	500 Hz	**200 KHz**	10 KHz
Average power (W)	3.85	120	15.7
Peak Power (kW)	30.8	1.3	373
M^2	7	>2	?
Core diameter size (μm)	60 μm	30 μm	21.2 μm

Table 5.1: Present state-of-the-art single stage Q-switched fibre lasers

The most significant result for each laser system is highlighted in bold. We can see that the current all fibre, single stage, Q-switched laser system with the highest pulse energy was demonstrated by C.C Renaud *et al.* [11]. However the beam was highly multimode with an M^2 of 7 and the pulse duration was long. This was not surprising as the active double clad fibre

had a core-diameter of 60 μm and the fibre was very long. Y. Jeong *et al.* [12] demonstrated 0.6 mJ pulse energy, at a very high repetition rate of 200 kHz, within a medium size 30 μm core LMA Yb^{3+} doped fibre. Though high repetition rates were achieved, the pulse energy did not reach the mJ regime, the beam was of medium quality, and pulses were relatively long. Y.X Fan *et al.* [13] achieved short output pulses with relatively high 1.57 mJ pulse energies through a Stimulated Brillouin Scattering Q-switched technique. However this Q-switching technique was generally a very unstable process and the beam quality was not even mentioned in this paper.

The highest pulse energy from a Q-switched, fibre laser, MOPA system was demonstrated by M.Y Chen *et al.* [14] from the University of Michigan. They demonstrated 27 mJ, 50 ns long, pulses from a MOPA chain at repetition rates of a few Hz (not mentioned in the paper, but obtained via personal communication at CLEO 2004). However, in this system, 3 amplification stages were needed which would increase the systems' complexity, size and production cost considerably. The output beam was again highly multimoded with an M^2 of 6.5.

It can be seen from the above few examples that Q-switched laser systems developed over the last few years produced pulses which were either too long, unstable and/or multi transverse moded. Our target, set by our commercial sponsor SPI, was to achieve a Q-switched system producing relatively short (~40 ns) pulses having >1 mJ pulse energy, with good mode quality. Though the Q-switching technique has been known for many years, such a system has yet to be achieved. But with the recent improvements in fibre and pump technology this target, though hard, seems achievable. In this chapter, I will describe how a 1.21 mJ, 37 ns, single stage, Q-switched system with single mode (M^2=1.1) beam quality was achieved. I will also describe dual stage, MOPA systems which were investigated so that laser systems, with customized pulse widths, could be developed whilst providing similar power scaling performance to the single stage, Q-switched laser.

5.2 Principles of Q-switching

In Q-switching, a loss modulator is introduced into the laser cavity to prevent laser radiation from building up. During this time, energy is being stored to levels comparable to the saturation energy (typically 10 × saturation energy), within the active medium, as it is being pumped. When sufficient energy is stored, the loss element switches to high transmission. This suddenly and rapidly increases the Q-factor of the cavity resulting in the formation of a giant,

high intensity, pulse that extracts the stored energy. Once the depleted gain falls below the cavity loss, the intensity of the pulse starts decreasing at a rate proportional to the cavity length and losses. This process is repeated over the repetition period determined by the loss modulation.

5.2.1 *Cavity rate equations for Q-switch lasers*

There are two rate equations that could be used to describe the evolution of the total inversion and photon population within the cavity.

$$\frac{\delta \Delta N}{\delta t} = -(1+\gamma_s)\left(\frac{c\sigma_e}{L}\right)n_p \Delta N \tag{5.1}$$

$$\frac{\delta n_p}{\delta t} = \left(\frac{c\sigma_e}{L}\right)n_p \Delta N - \frac{n_p}{\tau_c} \tag{5.2}$$

where ΔN is the population inversion integrated along the cavity, n_p is the signal photon number integrated along the cavity, σ_e is the cross-sectional area at the signal wavelength, γ_s is defined as $\gamma_s = \frac{\sigma_a}{\sigma_e}$, c is the speed of light and L is the length of the cavity.

τ_c is the photon lifetime in the cavity and is defined as $\tau_c = \left(\frac{1+R}{1-R}\right)\frac{L}{c}$ where R is the reflectivity forming the cavity at the end. The photon lifetime τ_c is thus dependent on the losses and the cavity round-trip time. However equations 5.1 and 5.2 are only valid if the laser field intensity is assumed to be uniform along the oscillator. For this condition to be met, the field should not vary too quickly relative to the cavity round-trip time and the reflectivity of the output coupler should be > 50% [15].

5.2.2 *Modulator switching time and extraction efficiency*

The required switching time for the loss modulator is determined by the build-up time of the Q-switched pulse within the cavity. For Q-switched fibre lasers, the switching times required are < 10 ns to avoid switching related loss [16].

Let us now define an initial inversion ratio $r_{in} = \frac{\Delta N_i}{\Delta N_{th}}$ where ΔN_i is the population inversion just before switching (to high Q) and ΔN_{th} is the population inversion required to reach threshold. The extraction efficiency η_{ext} of the stored energy by the Q-switched pulse can be determined by equation 5.3.

$$r_{in} = \frac{1}{\eta_{ext}/\xi} \ln\left(\frac{1}{1-(\eta_{ext}/\xi)}\right) \tag{5.3}$$

where ξ is the maximum obtainable extraction efficiency and is defined as $\xi = (1-\gamma_s)^{-1}$ for a three-level system and $\xi = 1$ for a four-level system.

Plotting equation 5.3 in figure 5.1, we can see that the extraction efficiency is dependent on the inversion ratio and increases with the inversion ratio. This increase in extraction with inversion can be understood by taking the Q-switch oscillator as a self-seeded regenerative amplifier. As the inversion increases, so does the overall gain seen by the photons. The higher gain that the photons see is either in a single pass (the Q-switch oscillator developed in this chapter obtains most of its gain in a single pass, see section 5.3.1) or over multiple passes. Figure 5.1 also shows that > 90% of the stored energy is extracted by the Q-switch pulse when the inversion ratio is 3 and above.

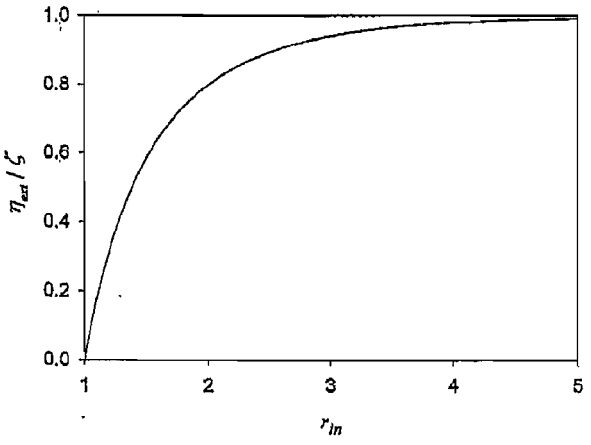

Figure 5.1: Normalised extraction efficiency in a Q-switched fibre laser as a function of the initial inversion. Efficiency is normalised to the maximum achievable extraction efficiency ξ (figure taken from [15]).

However due to internal cavity losses, only a fraction of this extracted energy is actually useful output. Therefore continual increment of the inversion by increasing the reflectivity of

the output coupler does not translate into higher output pulse energy. This is because continual increment of the output coupler reflectivity will result in a larger fraction of extracted energy being lost within the cavity. However, there is a range of reflectivity over which the output pulse energy produced is maximised which we shall describe later (this effect is illustrated experimentally in figure 5.6 (b) in section 5.3.1).

5.2.3 *Output peak power and pulse duration of Q-switch lasers*

The peak power per unit area for Q-switched lasers can be defined by equation 5.4 below.

$$I_{ext}^{peak} = \frac{\Delta N_{th} h \nu_s}{(1+\gamma_s)\tau_c}\left[r_{in} - 1 - \ln(r_{in})\right] \tag{5.4}$$

where h is the Planck's constant and ν_s is the frequency of the signal photon. From equation 5.4, we can see that the peak power is inversely proportional to the cavity photon lifetime. On the right hand side (RHS) of the equation, the expression in brackets contributes to the influence of pumping on the peak intensity of the output pulse. The parameters in front of the square bracket are contributions from the characteristics of the cavity and are independent from the pumping. Figure 5.2 shows how the expression in brackets, and hence the peak intensity, changes as a function of the inversion ratio (which is approximately proportional to the pump power).

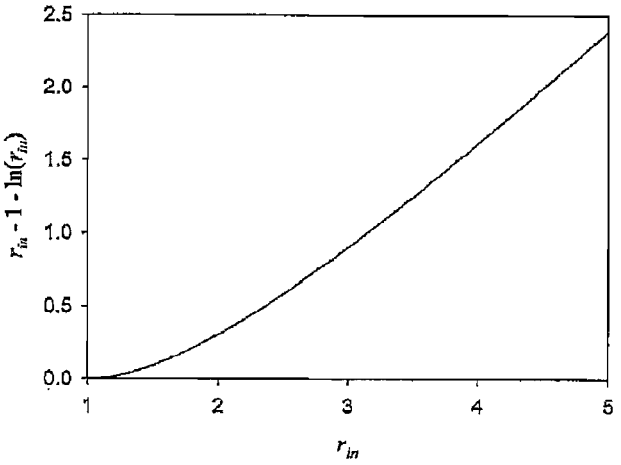

Figure 5.2: Theoretical influence on the output peak power per unit area as a function of inversion ratio (figure courtesy of [15]).

Comparing figure 5.2 and figure 5.5 (b), we can observe that the peak power versus pulse energy plot in figure 5.5 (b) (assuming pulse energy is proportional to the pump power, see figure 5.5 (a)) follows a similar trend with the curve in figure 5.2.

In the absence of gain, the solution to equation 5.2 can be written as an exponential decrease in photon count, $\exp\left(-\frac{t}{\tau_c}\right)$. This loss is attributed to the passive losses and the coupling losses in the cavity. Therefore,

$$\exp\left(-\frac{2L}{c.\tau_c}\right) = R.\exp(-\delta) = R_{eff} \tag{5.5}$$

where δ is the round–trip passive loss. The cavity lifetime can then be written as,

$$\tau_c = \frac{2L}{c[\delta + \ln(1/R)]} = \frac{2L}{c\ln(1/R_{eff})} \tag{5.6}$$

In a lossless cavity, R approaches unity, this corresponds to our earlier definition of τ_c in equation 5.2. From [17], the initial single-pass gain G_i can be written as $G_i = \exp[\sigma_e \Delta N_i]$ and the lasing threshold condition expressed as $R_{eff}\exp[2\sigma_e \Delta N_{th}] = 1$. With these definitions together with equation 5.6, equation 5.4 can then be expressed as,

$$I_{ext}^{peak} = \frac{U_{sat}}{4L/c}\ln^2(R_{eff}^{-1})\left[\frac{\ln(G_i^2)}{\ln(R_{eff}^{-1})} - 1 - \ln\left\{\frac{\ln(G_i^2)}{\ln(R_{eff}^{-1})}\right\}\right] \tag{5.7}$$

where U_{sat} is the saturation fluence (J/cm^2) and is defined as $U_{sat} = \frac{\tau_2 . I_s^{sat}}{1+\gamma_s}$ and τ_2 is the lifetime of the active ions.

Equation 5.7 tells us that the peak power per unit area is proportional to the ratio between the saturation fluence of the gain medium and the round-trip time of the cavity. Therefore if all other conditions are similar, then shorter cavities produce more intense pulses. Using equation 5.7, we can also understand the influence that the cavity effective reflectivity R_{eff} has on the

peak power of the output pulses. Using equation 5.7, the plots of output peak powers for different initial gains with varying cavity reflectivity is shown in figure 5.3 below.

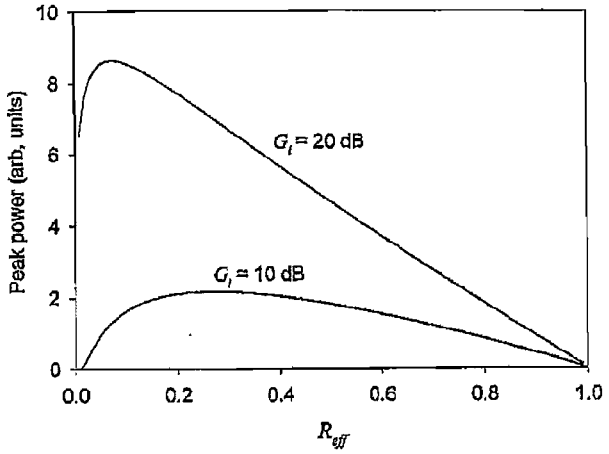

Figure 5.3: Output peak intensities for different initial gain with varying cavity reflectivity (figure taken from [15]).

We can see from the theoretical plot in figure 5.3, there is an optimum reflectivity for maximum output peak power. The reason behind this is as described. When the reflectivity is low, the inversion ratio is too small for efficient extraction. However, when the reflectivity is too high, the photons remain trapped in the cavity for a longer time and hence it takes longer time for the output power to be extracted (i.e. longer duration pulses with lower peak power). The empirical results on the influence of the output coupling reflectivity on peak power is shown indirectly in figure 5.6 (b) in section 5.3.1.

The pulse duration obtained from a Q-switched laser is approximated by equation 5.8 below.

$$\tau_s = \frac{r_{in}\eta_{ext}/\xi}{r_{in} - 1 - \ln r_{in}} \times \tau_c \tag{5.8}$$

Equation 5.8 shows that the pulse width is proportional to the cavity length and scales with the photon cavity lifetime. In the earlier sub-section, we saw the influence that the reflectivity has on the output peak power. The influence is due to the effect that the inversion ratio has on the peak intensity and we know that the changes in peak power are partially due to the result of changes in pulse duration. In short, lowering output reflectivity lowers the inversion ratio. This reduces the lifetime of the photons which has an opposite effect on the output pulse width. Figure 5.4 illustrates the influence that the inversion ratio has on the output pulse duration.

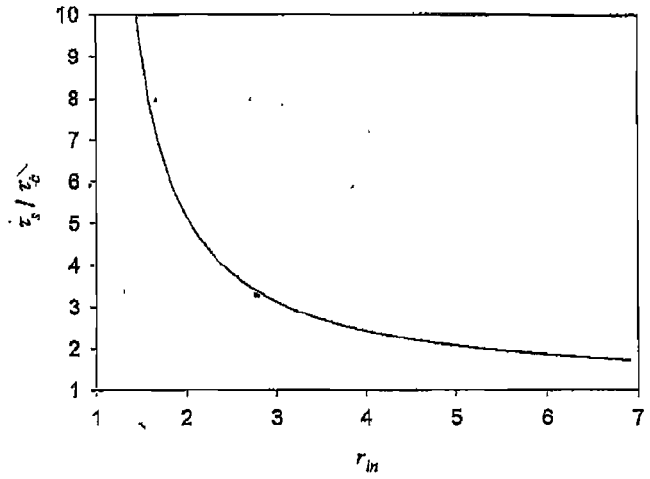

Figure 5.4: Output Q-switched pulse width normalised to the cavity photon lifetime as a function of inversion ratio (figure taken from [15]).

The pulse width decreases exponentially with inversion ratio. It decreases rapidly at the small inversion ratios and changes only slightly at the higher inversion ratios. This is demonstrated empirically in figure 5.7 (a).

5.2.4 *Repetitive operation*

When the repetition rates are low, the pump has enough time to completely re-populate the population inversion to equilibrium. Thus at low enough repetition rates, the characteristics of the individual output pulses remain the same. However with increasing repetition rates, the available gain decreases and therefore reduces the inversion ratio. As we have described in the previous sub-sections, this results in less energetic, less powerful and wider output pulses. This is empirically illustrated in figure 5.7 and 5.8 (c) where the pulse energies of the output pulses are observed to increase with reducing repetition rates and then reach a steady state at equilibrium repetition rate.

5.2.5 *Q-switching techniques*

Q-switching can be carried out using different techniques. Passive Q-switching, such as saturable absorber Q-switching, is a simple technique. However, it has a low power threshold and the laser performance depends critically on the saturation characteristics of the absorber, and active medium, which can change over time. Active Q-switching techniques such as mechanical, electro-optic and acousto-optic Q-switching can be used. However, mechanical

Q-switching is too slow, produces poor quality pulses and has serious jitter problems. Electro-optic Q-switching is too costly, bulky and requires high, and fast, driving voltages. The acousto-optic technique was used in our experiments even though small losses are incurred through the modulator. It was used because of its simplicity, low cost, low-driving voltage, high speed and high power threshold.

The amount of energy that can be stored in an active fibre is proportional to its saturation fluence. As a general rule of thumb, the maximum extractable stored energy (i.e. above the bleaching level) from an active fibre is limited to approximately ten times the saturation energy [18]. The amount of stored and extractable energy for a given fibre has been discussed in section 2.3 of chapter 2. Additional pumping above this threshold will be lost as spurious ASE between pulses, without significant improvements to output energy.

5.3 Q-switched fibre lasers

To reach our target of 1 mJ output pulse energies, we need a fibre gain medium that has sufficient energy storage before the onset of spurious lasing due to the high gain efficiency (see section 2.3). Although increasing the length of fibre can increase the overall gain, the 40ns pulse duration specified sets the limit on the maximum length of the fibre. Whereas to achieve an output power of 10W (1 mJ pulses at 10 kHz repetition rate), sufficient pump absorption is required and hence this sets the limit on the minimum fibre length. Finally the maximum core area dimensions of the fibre are limited by the requirement for single transverse mode operation.

Initial characterization of Q-switched lasers, using various active fibres, was carried out to determine the output performance from each fibre so that we would experimentally determine what was required to reach our target. The properties of the various fibres used and the effects of the different fibre characteristics on output performance are evaluated experimentally, and the results are presented in table 5.2. The lengths of the fibres used in the experiments were chosen such that a compromise was made between achieving enough gain, producing approximately 40 ns output pulses and having optimum pump absorption (~9dB).

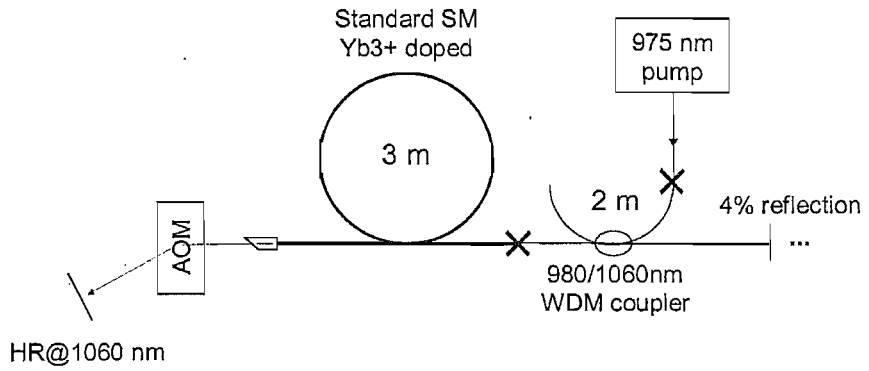

(a)

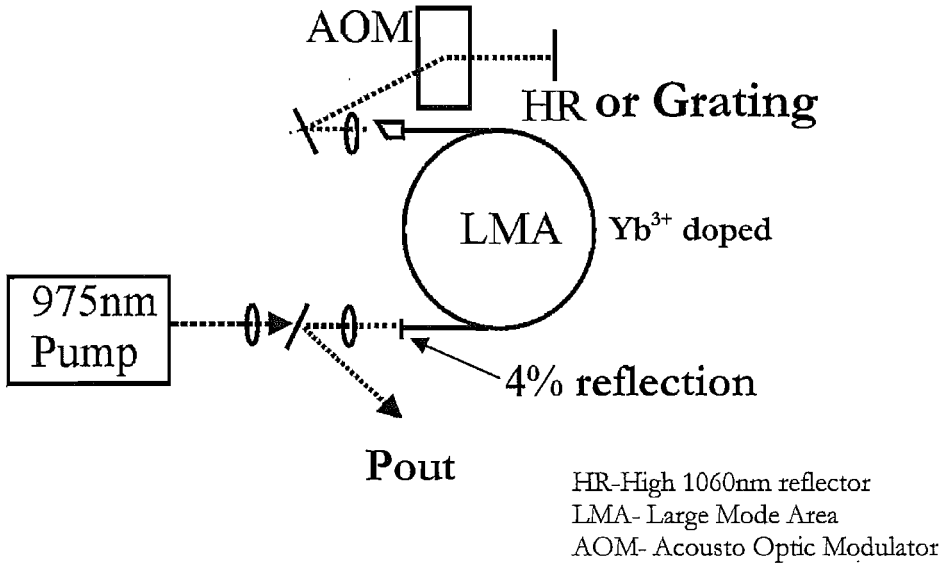

(b)

Figure 5.5: (a) Core-pumped and (b) Cladding-pumped Q-switched oscillator

Both core-pumped and cladding-pumped active fibres were investigated. The setups for the core and cladding pumping schemes are shown in figure 5.5 (a) and (b) respectively. The core-pumping configuration uses a 980/1060 nm wavelength division multiplexer (WDM) to couple the 976 nm pump radiation directly into the active fibre. The 976 nm pump source used in this configuration was a fibreised, semiconductor diode, MOPA pump providing up to 250 mW pump power with SM beam quality. In the cladding pumping configuration, wavelength selective dichroic mirrors were used to separate the signal and pump wavelengths. Multimoded outputs from the 915 nm and 975 nm pumps are free space coupled via lenses into the inner cladding of the LMA fibres. The pumps used are the same polychrome diode combiner pumps as described in section 2.4.1. Feedback is provided by either a narrow band, AR coated, 1060nm high reflector or a bulk grating (for wavelength selectivity) from the AOM end. A 4% reflective flat cleave at the end of the fibre acts as output coupler. In later sections,

we will describe the effects of varying the output coupling using either an attenuator setup or a dichroic mirror with variable output coupling. Acousto-optic Q-switching was achieved with a broadband, 1054nm, AOM from AA optics to provide loss modulation. The AOM was driven with a Stanford (model PG535) pulse generator providing 4V peak square waves having variable duty cycle and repetition rate. This repetition rate sets the output pulse frequency from the laser and the duty cycle affects the output pulse duration. However there needs to be a compromise on the length of the duty cycle. It should be set such that it is long enough to avoid clipping the output pulses and yet short enough to avoid c.w. lasing. The AOM was measured to have a c.w. diffraction efficiency of 80% whilst passing a single transverse mode beam.

There were three trials of different fibre dimensions. The first used standard core-pumped single mode fibre having 5 μm core diameter. The second used 20 -25 μm core diameter (to maintain strictly single transverse mode operation) double clad LMA fibre, and finally larger 40 μm core diameter double clad LMA fibre were characterised.

With standard Yb-doped SM fibres, the c.w. and pulse lasing efficiencies were 77% and 31% respectively. 70 ns pulses at 100 Hz, having pulse energy of 0.027 mJ, were produced. Higher pulse energy was mainly limited by the core dimension. It was expected (see section 2.3) that 1 mJ pulse energy would not be able to be extracted from a fibre having a 5 μm core. The high gain density leads to spurious lasing, with increasing pump power, and the onset of ASE gain saturation could be seen especially at repetition rates < 1 kHz. This is not surprising as the life time of Yb^{3+} ions is ~ 0.8 ms (see section 2.1.1). . However this Q-switched laser would be useful as a SM seed source for two stage MOPA systems.

20-25 μm core diameter, cladding pumped, LMA fibres were characterized next. Three different 20 μm core LMA fibres were characterized, POLO fibre, LF92 and LF128. With this core-dimension, it would be theoretically possible to achieve output pulse energies of 1 mJ and yet maintain strictly single mode output beam quality.

The POLO fibre has a core/cladding dimension of 22/125 μm. Hence this makes the pump coupling poor (48%), since the 975 nm Mylon pump has an output fibre pigtail that is 200 μm in diameter. Though the c.w. efficiency of the fibre was adequate at 67%, the efficiency when operated in the pulse regime was poor (22%). The highest output

Fibre	Absorption (dB/m)		Pump method	Core/ Cladding Diameter (μm)	NA_{core}/ $NA_{cladding}$	Length (m)	c.w. η (%)	Pulse η (%)	Rep Rate (kHz)	Pulse duration (ns)	Pulse Energy (mJ)	Peak power (kW)	Limit
	975nm	915nm											
SM Yb^{3+}	400	NA	Core pumped	5	0.22	5	77	31	0.1	70.36	0.027	0.38	975nm Pump
POLO (22μm)	3	NA	Cladding	22/125	0.1/0.4	2.875	67.1	22	1	39	0.3	7.6	ASE buildup
LF92 (25μm)	1.6	NA	Cladding (Rectangle)	25/250	0.05/0.4	5.2	80	65	0.5	54	0.25	4.6	Spurious Lasing
LF92 (25μm)	1.6	NA	Cladding (Rectangle)	25/250	0.05/0.4	3.8	80	65	10	52	0.28	5.3	Spurious Lasing
LF128 (20μm)	4.1	1.46	Cladding (D-shape)	20/200	0.06/0.4	3	81	76	10	43	0.276	6.4	Spurious Lasing
LF128 (40μm)	4.1	1.46	Cladding (D-shape)	40/400	0.06/0.4	2.5	81.6	80	10	37.4	0.52	19	975nm Pump

***NA denotes Not Avaliable**

Table 5.2: Results obtained from single stage Q-switched oscillators using different active fibres

pulse energy obtained was 0.3 mJ, at 1 kHz repetition rate. The onset of spurious lasing at higher pump powers restricts the achievement of higher pulse energies. I suspect that the spurious lasing could be the result of the ASE between pulses and the high ion density confinement (gain) within the 20 μm core [11, 19].

A 3.8m and 5.2m length of LF92 fibre were tried next. The LF92 fibre is a double clad fibre with a rectangular shaped inner cladding. It has a raised index around the core to enhance the spot size of the fundamental mode and this also decreases the bend losses, as the mode confinement of the fundamental is better [20, 21]. Its c.w. and pulse efficiencies were 80% and 65% respectively. The highest output pulse energy that was attainable with the 3.8 m and 5.2 m fibre were 0.25 mJ at 500 Hz and 0.28 mJ at 10 kHz respectively. Again, higher pulse energy was not achieved due to spurious lasing at the higher pump powers, mainly due to the high gain within the 25 μm core fibre which causes the ASE between pulses to lase. Effects of spurious lasing can be observed temporally on the oscilloscope. The output temporal pulse de-stabilises giving large amplitude jitters and blurred pulse peaks.

The next fibre that was tested was a 3 m length of LF128 20 μm core diameter, LMA fibre. This fibre has a step index doping profile with a D-shaped inner cladding. The c.w. and pulse efficiencies were found to be similar at 81% and 76% respectively. The highest pulse energy achieved with this fibre was 0.276 mJ at 10 kHz. Though the output pulse energy was lower, this fibre had better performance to reach our target, compared to the POLO or LF92 fibre. It was mentioned previously that a compromise between the fibre length and gain had to be made to achieve the 40 ns, 1 mJ target. Hence the length of the active fibre had to be approximately 4 m (pulse width $\propto$ (2*fibre length*refractive index of silica/speed of light) according to equation 5.8). Therefore the pump absorption length for 975 nm, for the LF92 fibre, was too long to be efficient at this length. The POLO fibre's inner cladding diameter was too small for our higher power pumps. The D-shape inner cladding profile of LF128 also provided better pump coupling compared to the rectangular shaped profile. The benefits of the properties of the LF128 fibre were evident as it was found to have a 10 kHz pulse slope efficiency of 76% and an output pulse duration of 43 ns which was close to the 40 ns target. However, we were still far from the mJ pulse energy target.

Although it was estimated theoretically that 1 mJ pulses could be achieved from the 20 μm core fibre, this was an ideal situation. I believe that due to cavity losses and rather low pump absorption (i.e. POLO and LF92 fibre), higher pump powers were required to reach the mJ target, which leads to spurious lasing as a result of the higher gain density. The high level of

doping concentrations and perturbations along the fibre length may also increase the fibre's susceptibility to spurious lasing, or even self-pulsing, which would be detrimental.

We decided to try a fibre with a larger core dimension. Another 40 μm core diameter fibre, pulled using the same perform as the 20 μm LF128 fibre, was used. Since the LF128 fibre had a high 975 nm pump absorption of 4.1 dB/m, a 2.5 m length of the fibre was chosen to obtain short pulses and yet achieve enough pump absorption for high gain. The c.w. and pulse efficiencies achieved with this fibre were 81.6% and 80% respectively. With this fibre, we were able to achieve promising results. 37.4 ns, 0.52 mJ pulses at 10 kHz repetition rates were generated, only to be limited by the amount of 975 nm pump power we had available. Though we have not reached the required target, the 40 μm core LF128 fibre seems to be the most promising. In the next few sections, we will describe a few approaches that were considered to obtain higher pulse energy output from this fibre. The other concern regarding the output beam quality from a fibre, with large core dimensions, will also be discussed in a later section.

5.3.1 *Oscillator feedback characterisation*

In the previous experiments with the same fibre lengths as described in table 5.2, reflections from flat end cleaves were used to provide 4% output coupling. However, the amount of feedback/output coupling from the cavity can significantly change the output pulse properties. Changing the feedback changes the inversion levels near the ends of the cavity thereby changing the amount of gain that the signal sees while propagating within the cavity. Lowering the feedback would reduce the number of photons lost via stimulated emission (excited by the feedback) at the fibre end and this might increase the inversion level, resulting in higher gain at the fibre end. Both fibre ends of the cavity were tested.

Figure 5.6 (a) shows the effects on output c.w. power at different pump power levels, when the feedback from the AOM end was changed between 1% to 75% (25% feedback insertion loss). For feedback >10%, output powers remain fairly constant. The relative insensitivity to the feedback from the AOM end indicates that most of the gain is achieved in the final/single pass through the cavity. Another indication of this can be observed from the duration of the output pulses obtained at high pump powers, shown in table 5.4. These pulse durations correspond to approximately one single cavity length. This would mean that the gain (or inversion level) at the output end could possibly have significant effects on the characteristics of the output pulse.

The variable feedback setup, shown in figure 5.6 (c), is built using waveplates and polarization beam splitters (PBS). The amount of attenuation is measured by the sum of the powers from all the output ports of the two PBS, relative to the input power Pin. The attenuator is first calibrated by using c.w. output power from the laser. The waveplates' settings are adjusted, and recorded, to obtain the respective powers from the output ports of the two PBS. This information allows us to calibrate the waveplates to the amount of attenuation required. The output end of the active fibre was angle cleaved to suppress any reflection from the end of the fibre.

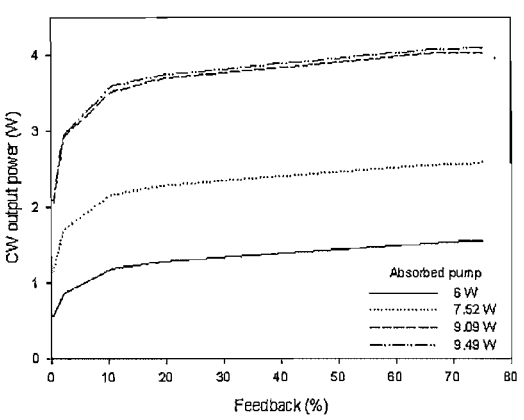

(a)

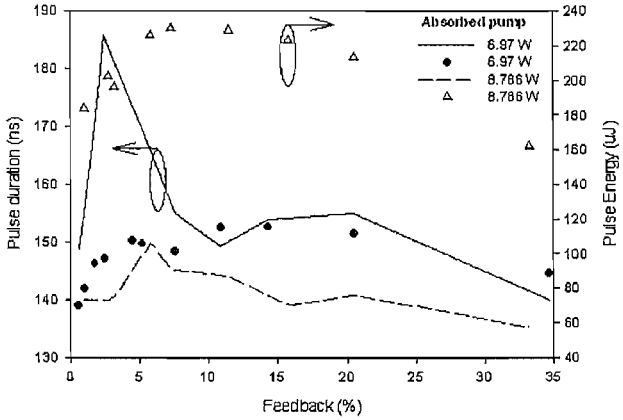

(b)

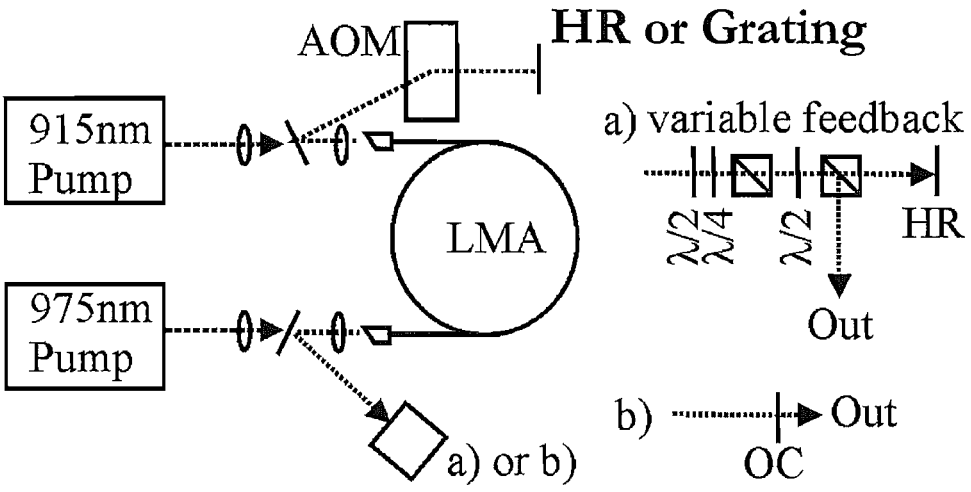

HR- 1060nm High Reflector Mirror

(c)

Figure 5.6 (a) c.w. output power with varying feedback at the AOM end. (b) Output energy and duration of 10 kHz pulses with varying feedback at the output. (c) Attenuator setup for variable output coupling/feedback.

Two pump power levels were characterized, over an attenuation range of 1% to 34%, and the results of the pulse energy and duration obtained is described in figure 5.6 (b). Optimum pulse energy and duration seems to be obtained between 7 – 10 % feedback for both cases. By increasing the 975nm pump power to its maximum, 31 ns long pulses with energy of 0.59 mJ at 10 kHz could be obtained. Comparing with the 4 % feedback that was used previously, the pulse duration decreased, and energy improved by approximately 17 % and 12 % respectively. From this graph, we can observe that either lowering the feedback below 4 %, to enhance the inversion level at the fibre end, or increasing above 15 %, to increase signal feedback, would result in performance degradation.

5.3.2 *Double end-pumping single stage configuration.*

In the experiments described above, we only utilized the high power 975 nm pump diode and the highest pulse energy that we achieved with 91% output coupling was 0.59 mJ. Obtaining higher output pulse energies was attempted by reducing the repetition rates. However, especially at rates below 4 kHz, the onset of instability which arises due to the high inversion build-up leading to spontaneous emission or fibre facet damage as a result of self-pulsing prevented us from going higher. We concluded that higher pump powers were required to reach 1 mJ at the required repetition rate.

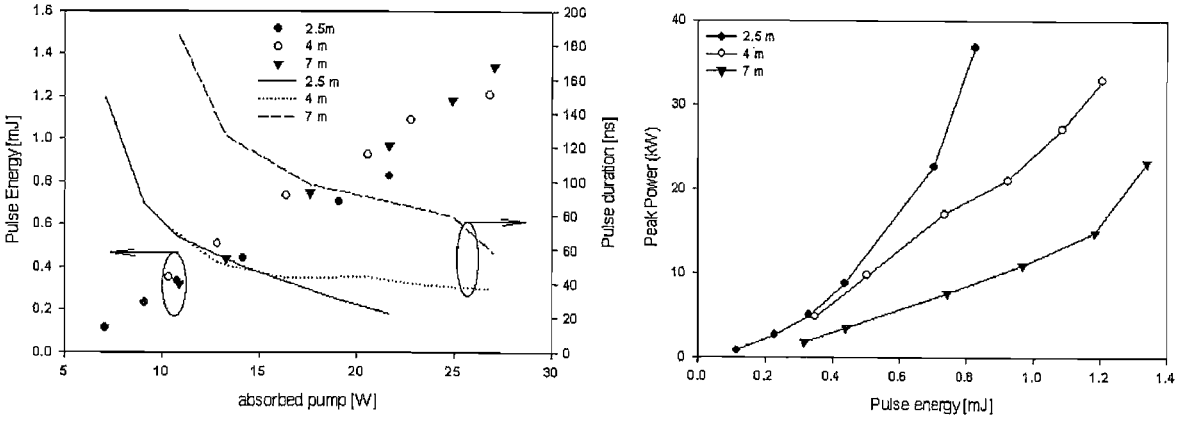

Figure 5.7: Q-switch performance of 2.5m, 4m and 7m length of 40 μm LF128 with 10% output feedback. (a) Pulse energy and duration vs absorbed pump and (b) Peak power and pulse duration vs output pulse energy

We added a multimode 200 μm, pigtailed, 32 W, 915 nm semiconductor pump source to pump the active fibre at the AOM end (See figure 5.6 (c)). Initially the same 2.5 m fibre was used in this configuration. However this length of fibre was too short to absorb the 915 nm pump radiation efficiently. The 915 nm pump absorption was measured to be 1.46 dB/m. This

corresponds to an optimum absorption length for this pump (9 dB) of 6.2 m. The performance of the laser was then investigated at 10 kHz repetition rate for 3 different active fibre lengths: 2.5m, 4m and 7m.

The pulse energies achieved were very similar, as a function of absorbed pump, at all lengths (see figure 5.7 (a)), but the maximum attainable pulse energy was reduced at 2.5m to 0.83 mJ because the fraction of launched pump absorbed by the fibre was significantly reduced. The pump power that could be absorbed at maximum pump power with the 2.5m length of fibre was 21.67 W. Higher pump absorption can be achieved using longer fibre lengths. With 4 and 7 m fibre lengths, the amount of pump power that was absorbed increased by approximately 25 %. They were 26.83 W and 27.06 W respectively. The pulse energies obtained at the highest pump power, were 1.21 mJ and 1.34 mJ for the 4 and 7 m lengths. The slope efficiencies, with respect to absorbed pump power of the 3 fibre lengths measured at 10 kHz repetition rate were 38.3%, 48% and 58.1% for the 2.5, 4 and 7 m length respectively. Comparing the output pulse energy and efficiency results obtained, indicates that using a 7 m length would be most efficient.

However, pulse duration was strongly dependent on fibre length. Pulse durations of 22 ns, 37 ns and 58 ns were obtained, at maximum pump power, for 2.5m, 4m and 7m lengths of fibre respectively. Hence, only the 4 m length would meet our 1 mJ, 40 ns pulse specification. Figure 5.7 (b) compares the peak intensities of the pulses, produced from different fibre lengths. Peak intensities of 36.86 kW, 32.95 kW and 23.2 kW were obtained with the 2.5, 4 and 7 m length respectively. No non-linear inelastic effects were observed from the output spectrum obtained with all 3 lengths. Using the well known Raman threshold equation (see equation 2.46) from Agrawal [22], empirical signal gains (obtained when the fibre was used in an amplifier configuration in another experiment) and a theoretically modeled effective mode area of 370 μm^2 for the LF128 40 μm fibre, the estimated Raman threshold peak powers are shown in table 5.3 below.

Length (m)	Gain (dB)	Pulse duration (ns)	Peak power (kW)	Raman threshold (kW)
2.5	17	22.42	36.86	94.6
4	26	36.6	32.95	88.8
7	27	58	23.2	52.7

Table 5.3: Raman threshold peak powers with different fibre lengths and actual highest peak intensities.

We can see that the output peak intensities were far lower (at least a factor of 2) than the estimated Raman threshold peak powers. No signs of SRS could be observed from the output spectra and only slight spectral broadening due to SPM.

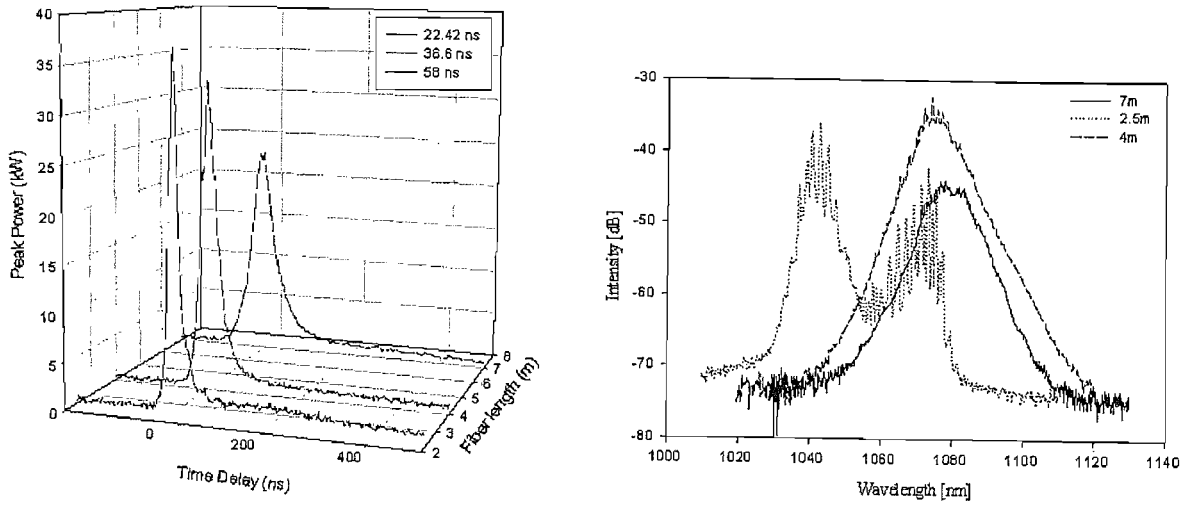

Figure 5.8: Q-switch performance of 2.5m, 4m and 7m length of 40 μm LF128 with 10% output feedback. (a) Output temporal pulses and (b) Output spectrum.

Figure 5.8 (a) and (b) show the output temporal pulses and spectra from the different lengths. All the temporal pulses were observed to have long tails, but no pedestal. These tails were estimated to contain less than 15% of the total output energy at the highest pulse energies. This indicates that ASE remained negligible. It can be seen that the pulses from the 4 and 7 m lengths were clean, with almost all of the output energy contained within the main peak of the pulses. However, the 22 ns pulses from the 2.5m fibre showed significant distortion, with a second peak (of width ~150 ns) containing about ~10% of the pulse energy, arising ~200 ns after the main peak. This seems to correspond to the two peak spectrum of the 2.5 m length, seen in figure 5.8 (b). The gain observed at two different wavelengths could be due to the three level system at shorter wavelengths (< 1040 nm) and quasi four level system at the longer wavelengths (see section 2.1.1) of Yb^{3+}. At a length of 2.5 m, lasing would be preferred at the shorter wavelengths. However due to the more efficient four level system, coupled with high pump powers, lasing at the longer 1070 nm occurred. Output pulse spectra from the 4 and 7 m lengths are very clean showing no significant ASE buildup. But the latter has a slightly broader spectrum and is peaked slightly to the longer wavelength. The FWHM bandwidths of the pulses are estimated to be 9 nm and 13 nm and the peak wavelengths are 1075 nm and 1078 nm for the 4 and 7 m lengths respectively. This would be expected since it has a longer interaction length (see section 2.1.1).

LMA length (m)	Pulse Energy (mJ)	Pulse width (ns)	Efficiency (%)	Spectral BW (nm)
2.5	0.83	22	38.3	Double peaks
4	1.21	37	48	9
7	1.34	58	58.1	13

Table 5.4: Summary of performance for 2.5,4 and 7 m lengths.

The results achieved from the 3 lengths are summarized in table 5.4. The 1 mJ output pulse energy target has been achieved by both 4 and 7 m lengths. Though the 915 nm pump absorption, with the 4 m length, was less than optimal and hence the overall efficiency was lower, it allows us to achieve the 1 mJ and 40 ns target required, which the 7 m length does not (output pulse width > 40 ns). Finally, it is important to note that even at the highest pump level; the output pulse energy continues to rise linearly, indicating that gain saturation and ASE buildup limitation were not reached. The peak powers obtained were at least 50% less than the calculated Raman thresholds. Therefore we believe that higher power scaling is achievable with higher pump power.

5.3.2.1 *Output coupling characterization*

In section 5.3.1 we characterized the output oscillator performance using the attenuator setup (a), shown in figure 5.6 (c) and identified that changing the output coupling improved its performance. In section 5.3.2, we identified the optimum length of active fibre that would give us an output that meets our specification. Implementing the attenuator setup (a) (shown in figure 5.6 (c)) would be impractical in a commercial product because of its bulkiness, its requirement for careful alignment, its polarisation sensitivity and having multiple output ports. In this section, we will describe the use of fixed dichroic output couplers (as shown in figure 5.6 (c) with attenuator option (b)) which are polarization insensitive, do not require adjustments once aligned and all output powers are provided in a single output source. The

performance for 96%, 90% and 80% output couplers using a 4 m device length are compared and the results obtained are summarized in table 5.5.

Feedback (%)	Duration (ns)	Energy (mJ)	Efficiency (%)
4	50*	1.25	61.3
10	37	1.21	58.5
20	48	0.96	53

*Indicates pulse distortion

Table 5.5: Performance summary using 96%, 90% and 80% output dichroic couplers and 4m fibre length.

The highest pulse energy was produced with 4% (flat cleaved end) coupling, although pulse energy is only slightly lower with 10% coupling. However with 4% coupling the pulse became distorted, with multiple peaks, and an increased FWHM of ~ 50 ns. With 10% coupling the laser produced 1.21 mJ, 37 ns pulses with 58.5% efficiency.

5.3.2.2 *Spectral broadening*

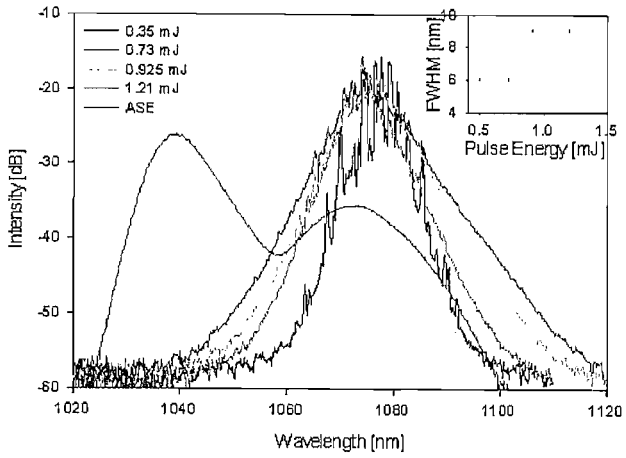

Figure 5.9: Spectra at different output pulse energies. Insert: FWHM bandwidth at various pulse energies.

The output spectrum, over a range of output pulse energy, was measured and slight spectral broadening was observed with increasing of the output pulse energy. This I believe was due to SPM. Using equation 2.22, the theoretical, intensity dependent, phase change ϕ_{NL}

with a 40 ns pulse having 1.21 mJ of pulse energy (corresponds to a peak power of 30.2 kW), effective mode area of 370 μm^2 and a gain of 15 dB, was calculated to be 4.27π. This corresponds to an 11 nm FWHM spectrum centred at 1070 nm and an initial FWHM spectral bandwidth of 6 nm. The pulse spectrum broadened from 6 nm to 9 nm at the highest pump powers. This empirical value was close to the theoretically obtained broadened pulse, spectral bandwidth. No SRS wavelength conversion effects were observed at any pulse energy.

5.3.2.3 *Repetition rate characterization (limited by end facet blowing)*

Extractable energy performance of this fibre was tested by lowering the repetition rate of the oscillator. For a given pump power, extractable energy is increased by reducing the repetition rate. The response time of the large area silicon photo-detector was slow enough (> 1 ns) to integrate across the significantly shorter pulses, so that pulse energy is proportional to the peak output signal of the photo-detector, but fast enough (<<0.1 ms) such that the signal between pulses, produced by the ASE, is not integrated. In this experiment, the pump was turned on to its maximum and 24 W of pump radiation was absorbed. A 10% feedback was used at the output. The output pulse energy obtained, against repetition rate, is shown in figure 5.10.

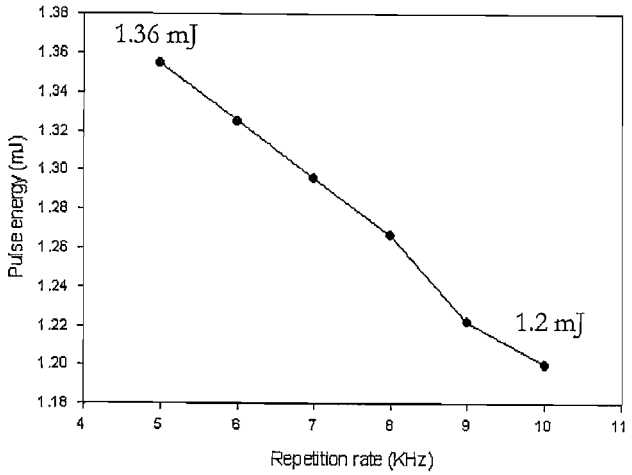

Figure 5.10: Pulse energy (mJ) vs repetition rate (kHz)

As the repetition rate was decreased to 5 kHz, there was only a 12.8 % increase in output pulse energy. This was unlikely to be due to the build up of ASE between the pulses, as the DC level on the oscilloscope remained at a constant level throughout the various repetition rates. This experiment indicates that, at 10 kHz operation, we have extracted most of the

energy that this fibre can store. At 5 kHz, the fibre end facet failed before we could reduce the repetition rate further. The failure under normal operation of the fibre facet was likely to be due to the end facet burning as the damage threshold of the silica/air interface was breached. The pulse duration was ~ 30 ns, which corresponds to a peak power of 46 kW. Observing through a 10X microscope objective, we can see that the core was crystallized. We will describe the details of the fibre end failure in the next section and the solution we used to overcome it.

5.3.2.4 *Adding End caps. (comparison of with, and without, end-caps)*

Occasionally, damage to the end-facets of the active fibre was observed whilst operating at high pump power (particularly if misalignment of the cavity occurs, leading to high inversion build-up and self-pulsing). An example of a damaged fibre end facet is shown in figure 5.11 (a). This is not a surprising result when one calculates the fluences obtained in this laser. We calculate that for our fibre (effective mode area of 370 μm^2); a 1 mJ pulse propagating in the fundamental mode has a peak fluence of ~270 J/cm^2. Extrapolating from the data in [23], we would expect the damage threshold for an air/silica interface to be ~240 J/cm^2 for a 37 ns pulse (with an uncertainty of at least 15%).

Splicing on ~3mm length angle-polished endcaps [11, 24], of 400 μm diameter, coreless silica fibre, to the ends of the active fibre eliminated this problem. Figure 5.11 (b) illustrates that the silica endcap expands the output beam, reducing the fluence at the silica/air interface, thus avoiding fibre facet damage. The longer the end caps, the more the beam diverges, reducing the fluence at the air/silica interface further. However, to avoid losses and distortions to the output beam, the diameter of the diverging beam should not exceed that of the endcap. Hence the maximum length of the endcap will be determined by d, the diameter of the end cap and NA_{silica}, the numerical aperture (to silica) of the active fibre core.

$$L_{\max} = \frac{n.d}{2NA_{silica}} \qquad (5.9)$$

where n is the refractive index of the endcap.

With endcaps of 3mm length, the diverged beam covers ~ 87% of the face of the endcap. Endcaps also function, like angle cleaving, to remove the 4% back reflection due to the end

facet of the fibre, since most of the light reflected from the air/silica interface will not couple back into the core.

Comparing the performance obtained with and without the endcaps, we found similar output pulse durations and a modest reduction (~10%) in maximum attainable pulse energy. The reduced pulse energy is due to losses associated with extra collimating optics in the laser cavity, required when using end-caps due to the fact that the pump and signal need to be focussed to different points. This loss should be avoidable in future by optimisation of launch optics. With the endcaps, we were able to reduce the repetition rate below 5 kHz with no sign of facet damage. At 2 kHz lasing efficiency reduced significantly, as the lifetime of Yb^{3+} ions is about 0.8 ms.

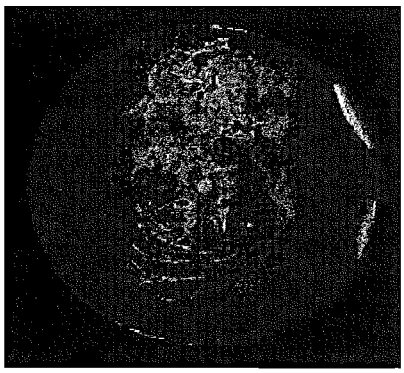

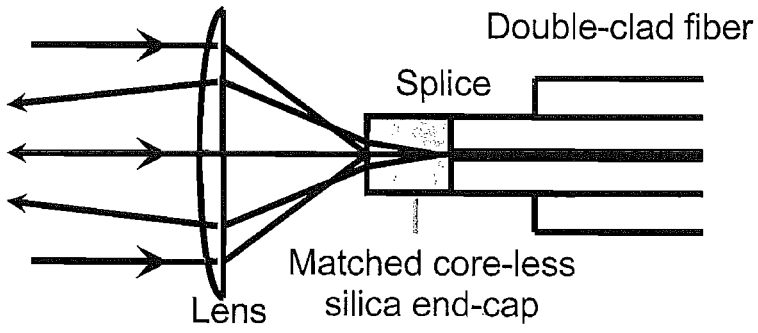

Damage threshold of bulk silica:
~2 GW/cm² (20 W/mm²)

(a) (b)

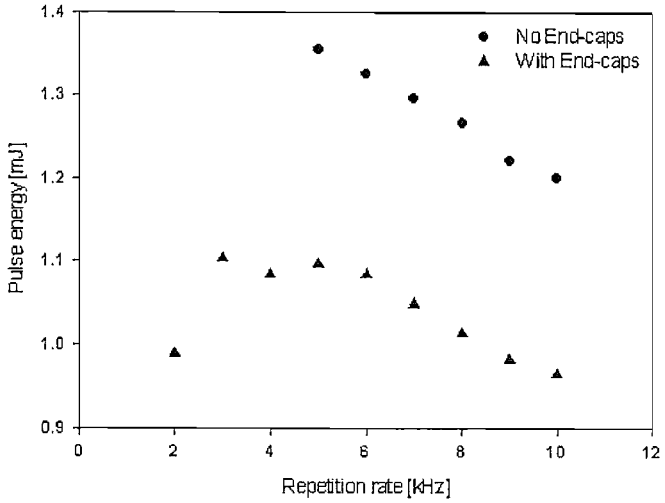

(c)

Figure 5.11 (a) Fibre facet damage example. (b) Illustration of the effect on the output beam using endcaps. (c) Comparison of pulse energy with repetition rate between a system with and without endcaps.

Observing figure 2.10, we can see that the limitation imposed, by fibre facet damage, on the maximum extractable energy from an amplifier fibre precedes the energy storage constraint. Therefore silica end caps can be used on the power amplifier fibres in future experiments to resolve this fibre facet damage constraint.

5.3.2.5 *Beam quality*

The beam quality of this fibre (40 μm core LMA fibre) was measured using a Mode Master beam profiler from Coherent. This beam profiler was checked using the standard SM Yb-doped fibre. Its measured M^2 was 1.1, which indicates that the device was calibrated correctly for this operating wavelength and the test setup was working well.

The 40 μm core diameter and 400 μm cladding LF128 LMA fibre has a step-index, refractive index profile with a low core NA of ~0.06. Due to its large core size, the fibre is theoretically capable of supporting up to ~ 7 modes (excluding degeneracies). However, the design of this fibre results in differences in overlap of the modal profiles with the Yb doped core, favouring gain in the fundamental mode. The low NA (~0.06) core property could also be used to clean the output modal quality of the fibre by using a tighter bend radius. The loose confinement of the core may help to create higher losses in the higher order modes, than the fundamental LP_{01} mode by bending the fibre [25, 26].

Modelling of this fibre had been done by Dr Fabio Ghiringhelli from Southampton Photonics Inc. (SPI) to study the effects of bending on the output mode profile. Figure 2.12 in chapter 2 shows the calculated bending losses for the 40 μm core diameter LMA fibre for six of the guided modes. It can be seen that for a bending diameter of 200 mm, the discrimination between the fundamental (LP_{01}) and first higher order mode LP_{11} is about 60 dB, which is significant. Hence at this bending diameter, we would expect near diffraction limited operation.

In c.w. laser operation (our beam analyser would not accept pulses), the output from the LMA fibre was found to be single-moded (M^2=1.1). No visible change in mode profile was observable on switching between c.w. and pulsed laser operation, leading us to conclude that there was no degradation in beam quality. Also, no change in beam quality was observed between operation with and without endcaps.

5.3.2.6 *Bend characterization*

With a low NA (~0.06) core design, this 40 μm diameter LMA fibre may be susceptible to high bending losses [20, 27]. However, as described by Dr Ghiringhelli's model, this core property can be used to clean the output modal quality of the fibre by using a tighter bend radius. Many authors have also showed that pump absorption may be altered by the bend radius, or bend shape, of the active fibre. Li Yuhua *et al.* [28] demonstrated that pump absorption could be increased by bending the fibre into a kidney shape, rather than normal circular bending. Bending characterization of this fibre was also potentially important in a commercial perspective. The tighter we can bend the fibre, without loss in performance, the more compactly a product can be packaged.

The c.w. output power performance, using 4% end cleaves, and pump transmission loss were characterised over a range of bending radius. Figure 5.12 (a) shows the variation in the output performance over a bending diameter range of 45-20cm. The reduction in output c.w. power was only 6% when the bend diameter was reduced from 45 cm to 20 cm (diameter used in commercial sponsor's system). From figure 5.12 (b), we observed only a 4.1% increase in pump absorption when the bend diameter was reduced from 45 cm to 20 cm. Also through visual observation, bending of this fibre did not change the output modal quality significantly. Hence, bending in the diameter range examined had only a small effect on laser performance.

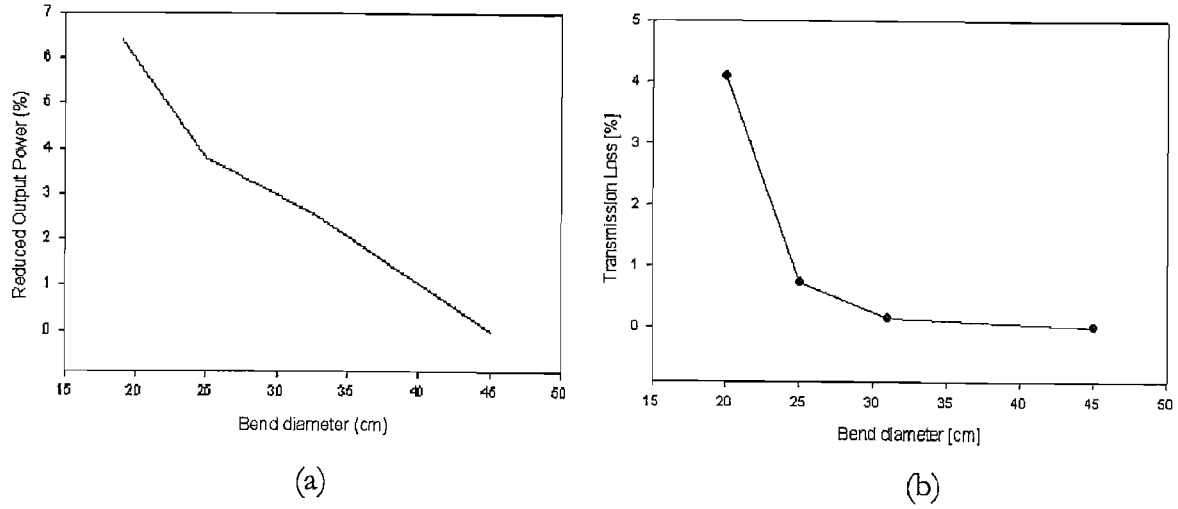

Figure 5.12: (a) Reduced output power (%) with respect to 45 cm bend diameter at maximum pump power. (b) Pump transmission loss (%) with respect to 45 cm bend diameter at 14 W launched pump power.

5.3.2.7 *Amplitude and timing jitter measurements*

Amplitude and timing stability are important for certain potential applications of the Q-switched laser, e.g. higher harmonic generation with crystals, precise material machining for depth control. Amplitude jitter characterisation was carried out by measuring the peak to peak amplitude of the noise, at the peak of the pulse, and for the entire pulse, for a series of pulses. The amplitude jitter was attributed to be the average of the relative ratios between the two values. Timing jitter characterisation was taken by measuring the standard deviation of the peak time over a series of pulses.

Figure 5.13 shows amplitude and timing jitter as a function of output pulse energy. The Q-switched oscillator had a relatively good amplitude and timing jitter performance (meeting commercial specification of < 10%), especially at the higher output pulse energies. The jitter improvements with output pulse energy, that we see in figure 5.10, are not surprising as the output pulse train from the fibre improves its stability as the gain gets saturates with pump power. The amplitude jitter is 5.9 % and timing jitter is 2 ns at the highest output pulse energy examined (1.1 mJ).

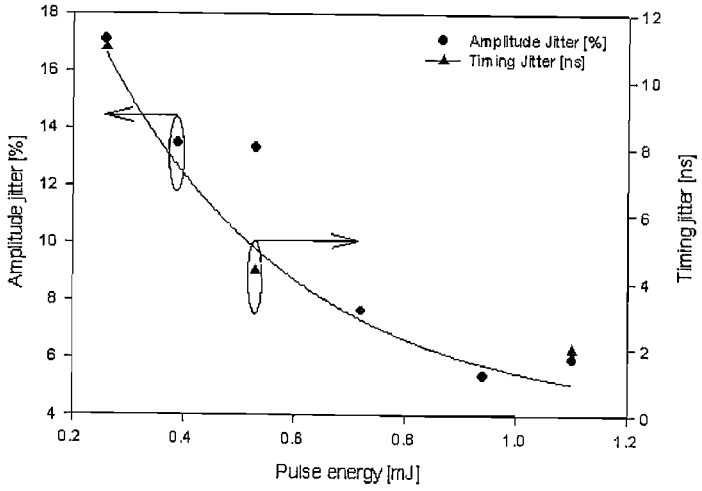

Figure 5.13: Amplitude and timing jitter performance with output pulse energy.

5.3.2.8 *Wavelength feedback characterization*

In this section we study the effects of changing the feedback wavelength at the AOM end using the same cavity as shown in figure 5.6 (c). The corresponding wavelength gain will differ

with length of the active fibre, but we decided to fix its length at 4 m. The cavity back-mirror was replaced with a bulk diffraction grating to act as a wavelength filter.

Figure 5.14 shows the output pulse duration and pulse energy as a function of wavelength, when the cavity was pumped at maximum pump power (both 915 and 975 nm polychrome diode pumps were used). Maximum output power was achieved approximately in the wavelength range 1050-1075nm. This increase in gain also reduces the generated pulse width. This is because, as the inversion level within the cavity increases, the rate at which it emits the output radiation also increases [15]. When the cavity was set to lase at 1039 nm, it can be seen on the oscilloscope that the temporal pulse has a large DC level indicating the high ASE content in the output. This was expected and can be explained from the Yb spectroscopy (found in chapter 2) where the emission cross section peaks at 1040 nm and hence this leads to unwanted ASE building up quickly. The sensitivity to changes for both output pulse energy and width, within this range, were less than 5 %.

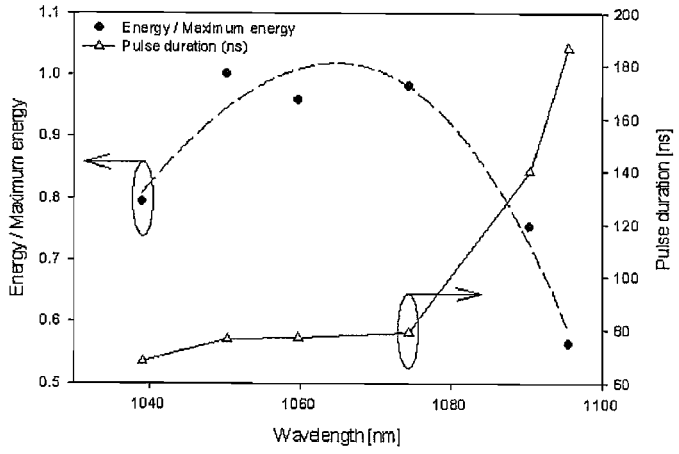

Figure 5.14: Ratio of output pulse energy with highest pulse energy achieved and pulse duration vs lasing wavelength, when absorbed pump power was 12.3 W.

5.4 Q-Switched MOPA End-pumped Fibre Laser Design

The required characteristics of the pulse sources differ depending on the intended application. Therefore the development of compact pulsed fibre lasers with good beam quality, controllable peak, and average output power, would be suitable for a wide range of applications.

A schematic of the Q-Switched MOPA, end pumped, fibre laser is shown in figure 5.15. The Q-Switched seed laser was essentially similar to the laser setup described in section 5.3, with a 2.8m long active fibre, of the 20μm version of the LF128 LMA fibre, and pumped with up to 4W of 975nm pump from a 100 μm delivery fibre. The back mirror of the cavity was a diffraction grating, allowing wavelength tuning in the range 1030-1090 nm.

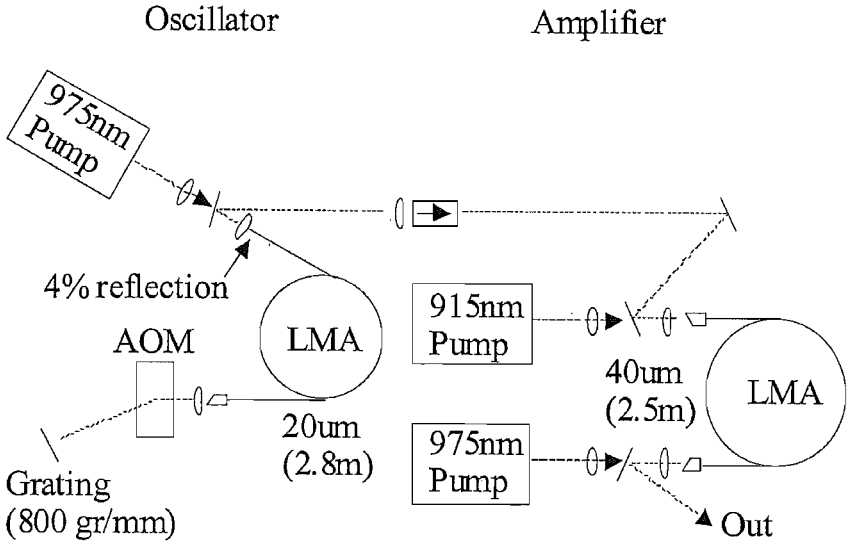

Figure 5.15 Experimental arrangement of end pumped Q-Switched MOPA fibre laser.

The amplification stage consisted of an Yb^{3+} doped (8000 ppm), 2.5 m long, 40/400 μm core/clad diameter fibre (LF128), which was angle cleaved at both ends. The amplifier fibre was pumped, through dichroic mirrors, using two fibre coupled multi-emitter laser diodes, with the 915nm source from the input end and with the 975 nm source from the output end, i.e. the same configuration as the LMA fibre laser evaluated above. A broadband, free-space, isolator was used between the Q-Switched seed laser and power amplifier, introducing ~0.7 dB loss. Signal launching efficiency into the amplifier was approximately equal to 75%. Typical pump coupling efficiency was ~ 70%, and pump absorption was ~70% of launched power. Both fibre spools were characterized and had ~80% efficiency, with respect to absorbed pump power, in c.w. operation.

5.4.1 *Performance and discussion*

For most experiments described below the seed laser was pumped with ~1.8W (1.1W

absorbed). At 10 kHz repetition rate it produced pulses of energy 33μJ, with FWHM pulse duration of ~90ns, (0.33W average power). Reducing the repetition rate to 5 kHz increased pulse energy to 65μJ (still 0.33W average power) and reduced pulse duration to 60ns. ASE was a negligible proportion of the output, at both repetition rates. The wavelength of the laser was set by the grating at 1050nm, for all experiments described below.

Figure 5.16 shows the performance of the amplifier, as a function of AOM operating frequency, in the range of 5-10 kHz. The amplifier was seeded by the Q-switched laser with the parameters as described in the previous paragraph, with coupling efficiency about 70% (0.24W average seed power launched). The amplifier was pumped with 18.7 W of absorbed pump power. Figure 5.16 (a) shows the measured pulse energy. Figure 5.16 (b) shows the corresponding peak powers and pulse durations. The pulse energy varied from 1.6 mJ to 0.8 mJ. Pulse duration varied from 53 ns to 107 ns, with pulse repetition rate and peak power varied from 18-6 kW, over this range of repetition rates.

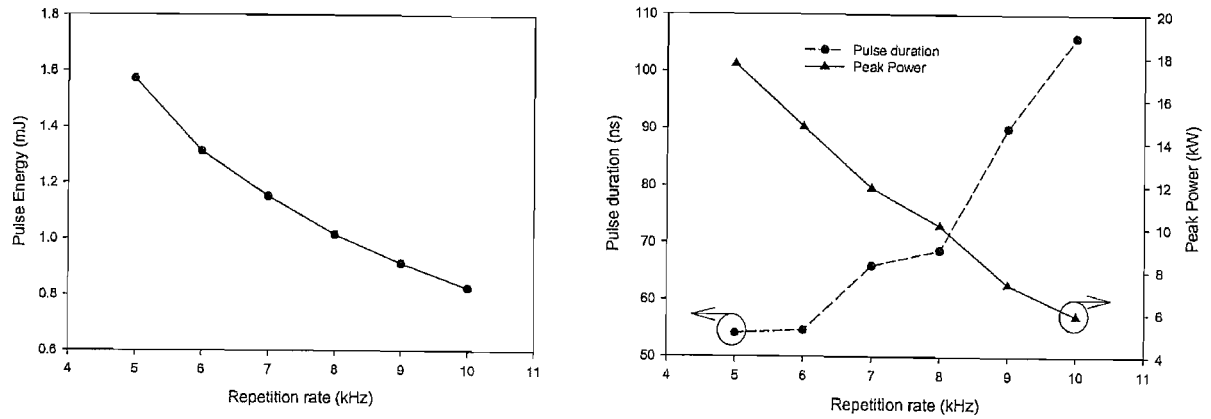

(a) (b)

Figure 5.16: Measured pulse energy, peak power and pulse duration of 40μm amplifier against pulse repetition rate

Figure 5.17 (a) shows pulse energy and pulse duration from the amplifier as a function of launched seed power (seed power was varied by increasing the pump power to the seed laser to a maximum of 4W). In this case the absorbed pump in the amplifier was 22W. Seed laser repetition rate was 10 kHz. Under these conditions we obtained ~1.0 mJ amplified pulses. It can be seen that, over a range of seed pulse energies from ~23-46μJ, output pulse energy varies by only ~4%, indicating saturation of the amplifier. However, the corresponding output peak intensities varied between 7.582-13.3 kW. The maximum pulse energy produced at 10 kHz was 1.02 mJ, with a corresponding peak power of 13.3 kW. The pulse durations decrease with increasing seed power, matching the duration of the seed pulses.

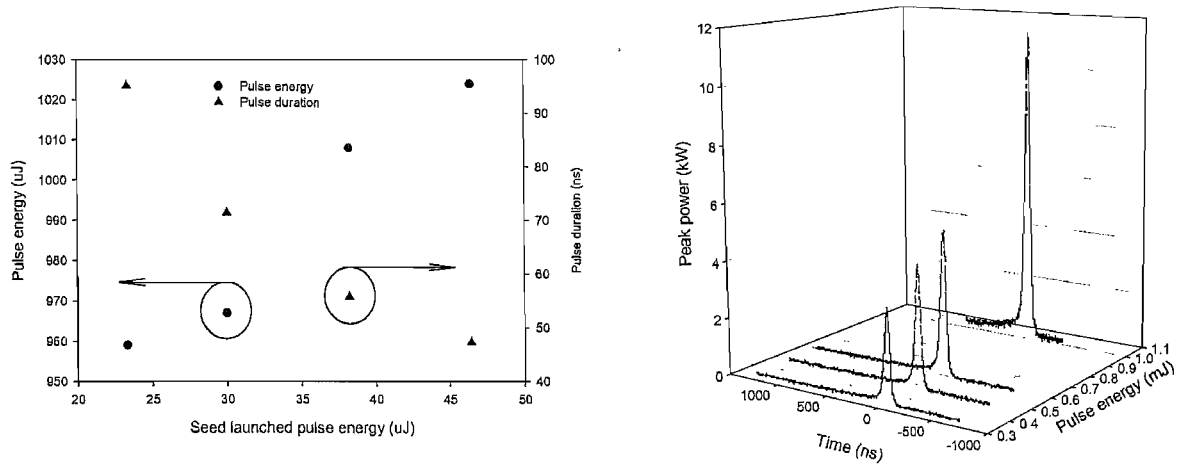

(a) (b)

Figure 5.17: (a) amplified pulse energy and duration as a function of launched seed pulse energy. (b) Temporal characteristics of pulses produced at fixed seed energy and various amplifier pump powers.

Figure 5.17 (b) shows a selection of pulses produced by varying amplifier absorbed pump power in the range 9-22W, with 38 μJ launched seed pulses and 10 kHz repetition rate. The pulses all have FWHM durations of ~55ns. Significant ASE or SRS was not observed over the range of experimental conditions described above and pulse energies were limited by available pump power.

5.5 Conclusions

We delivered a compact and cheap, pulsed, fibre laser system that meets the requirements specified by our commercial sponsors. A 1.2 mJ, Q-switched, fibre laser operating at a 10 kHz repetition rate, with single spatial mode output and sub 40 ns pulse duration, was developed. We believe this to be the first time that such a combination of output parameters has been reported for a simple, Q-switched, fibre laser system. Pulse stability of the system was also characterized and was found to be good. Amplitude and timing jitter were 5.9% and 2 ns respectively, at the highest output pulse energy. End facet failures were resolved, with slight degradation of output energy performance, by adding silica endcaps to reduce the output fluence at the air/silica interface.

We have also demonstrated a MOPA system consisiting of a Q-switched fibre laser and a fibre amplifier, with flexible pulse duration (~45-100 ns) at high power with maximum pulse energy, at 10 kHz, of 1.02 mJ.

Further improvements such as increased repetition rate/average power, and increased pulse energy, should be achievable with increased pump powers and realistic improvements in both fibre and cavity design. Our experiments show that fibre lasers have the potential to compete, in performance terms, with the established solid state solutions (e.g. Nd:YAG based pulsed lasers) for certain industrial applications.

1. Seidel, S. and Kugler, N., *Nd:YAG 200-W average-power oscillator-amplifier system with stimulated-Brillouin-scattering phase conjugation and depolarization compensation.* Journal Of The Optical Society Of America B-Optical Physics, 1997. **14**(7): p. 1885-1888.
2. Eichler, H.J., Haase, A. and Menzel, R., *100-Watt Average Output Power 1.2 Diffraction-Limited Beam From Pulsed Neodymium Single-Rod Amplifier With Sbs Phase- Conjugation.* IEEE Journal Of Quantum Electronics, 1995. **31**(7): p. 1265-1269.
3. Dane, C.B., Zapata, L.E., Neuman, W.A., Norton, M.A., Hackel, L. A., *Design And Operation Of A 150-W Near Diffraction-Limited Laser- Amplifier SBS Wave-Front Correction.* IEEE Journal Of Quantum Electronics, 1995. **31**(1): p. 148-163.
4. StPierre, R.J., Mordaunt, D.W., Injeyan, H., Berg, J.G., Hilyard, R. C., Weber, M. E., Wickham, M. G., Harpole, G. M., Senn, R., *Diode array pumped kilowatt laser.* IEEE Journal Of Selected Topics In Quantum Electronics, 1997. **3**(1): p. 53-58.
5. StPierre, R.J., Holleman, G.W., Valley, M., Injeyan, H., Berg, J. G., Harpole, G. M., Hilyard, R. C., Mitchell, M., Weber, M. E., Zamel, J., Engler, T., Hall, D., Tinti, R., Machan, J., *Active tracker laser (ATLAS).* IEEE Journal Of Selected Topics In Quantum Electronics, 1997. **3**(1): p. 64-70.
6. Amano, S. and Mochizuki, T., *High average and high peak brightness slab laser.* IEEE Journal of Quantum Electronics, 2001. **37**(2): p. 296-303.
7. Eichler, H.-J.T.U.B., Haase, A. and Mehl, O. *500-W average output power MOPA system with high beam quality by phase conjugation.* in *Tech. Dig. Conference on Lasers and Electro-Optics Europe.* 1998, *CThH2.* p. 353-354.
8. Snitzer, E., Po, H., Hakimi, F., Tumminelli, R., McCollum, B.C., *Double-Clad, offset core Nd fiber laser.* in *Optical Fiber Communication Conference.* 1988. New Orleans, PD5.
9. Nilsson, J., Sahu, J.K., Jeong, Y., Clarkson, W.A., Selvas, R, Grudinin, A. B., Alam, S. -U., *High power fiber lasers: New developments.* in *Proceedings of SPIE: Advances in Fiber Lasers.* 2003. **4974**. p. 50-59.
10. Jeong, Y., Sahu, J.K., Payne, D.N. and Nilsson, J., *Ytterbium-doped large-core fiber laser with 1.36 kW continuous- wave output power.* Optics Express, 2004. **12**(25): p. 6088-6092.
11. Renaud, C.C., Alvarez-Chavez, J.A., Sahu, J.K., Nilsson, J., Richardson, D. J., Clarkson, W. A., *7.7mJ pulses from a large core Yb-doped cladding pumped Q-switched fibre laser.* in *Tech. Dig. Conference on Lasers and Electro-Optics, CLEO.* 2001. Baltimore, CTuQ5. p.219.
12. Jeong, Y., Sahu, J.K., Laroche, M., Clarkson, W.A., Furusawa, K., Richardson, D. J., Nilsson, J., *120-W Q-switched cladding-pumped Yb-doped fibre laser.* in *CLEO/Europe-EQEC.* 2003. Munich, CL5-4-FRI.
13. Fan, Y.X., Lu, F.Y., Hu, S.L., Lu, K.C., Wang, H. J., Dong, X. Y., Zhang, G. Y., *105-kW peak-power double-clad fiber laser.* IEEE Photonics Technology Letters, 2003. **15**(5): p. 652-654.
14. Chen, M.-Y., Chang, Y.-C., Galvanauskas, A., Mamidipudi, P., Changkakoti, R., Gatchell, P., *27-mJ nanosecond pulses in M2 = 6.5 beam from a coiled highly multimode Yb-doped fiber amplifier. Conference on Lasers and Electro-Optics. CLEO.* 2004. San Francisco, CTuS4. **1**(1): p.3.
15. Morin, M., Larose, R. and Brunet, F., *Q-switched fiber lasers.* Second ed. Rare Earth Doped Fiber Lasers and Amplifiers, ed. M.J.F. Digonnet. 2001: Marcel Dekker. p. 375-388.
16. Barnes, B., Morkel, P., Reekie, L. and Payne, D. *Q-switching in fibre lasers.* in *Fibre Laser Sources and Amplifiers.* 1990: SPIE.

17. Siegman, A.E., *Lasers*. 1986, Mill Valley: University Science Books. Chapters 10, 26.
18. Renaud, C.C., Offerhaus, H.L., Alvarez-Chavez, J.A., Nilsson, J., Clarkson, W. A., Turner, P. W., Richardson, D. J., Grudinin, A. B., *Characteristics of Q-switched cladding-pumped ytterbium-doped fiber lasers with different high-energy fiber designs*. IEEE Journal Of Quantum Electronics, 2001. **37**(2): p. 199-206.
19. Alvarez-Chavez, J.A., Offerhaus, H.L., Nilsson, J., Turner, P.W., Clarkson, W. A., Richardson, D. J., *High-energy, high-power ytterbium-doped Q-switched fiber laser*. Optics Letters, 2000. **25**(1): p. 37-39.
20. Broderick, N.G.R., Offerhaus, H.L., Richardson, D.J., Sammut, R.A., Caplen, J., Dong, L., *Large mode area fibers for high power applications*. Optical Fiber Technology, 1999. **5**(2): p. 185-196.
21. Offerhaus, H.L., Broderick, N.G., Richardson, D.J., Sammut, R., Caplen, J., Dong, L., *High-energy single-transverse-mode Q-switched fiber laser based on a multimode large-mode-area erbium-doped fiber*. Optics Letters, 1998. **23**(21): p. 1683-1685.
22. Agrawal, G.P., *Nonlinear Fiber Optics*. 3rd Edition ed. 2001, San Diego: Academic Press.
23. Stuart, B.C., Feit, M.D., Herman, S., Rubenchik, A.M., *et al.*, *Nanosecond-to-femtosecond laser-induced breakdown in dielectrics*. Physical Review B, 1996. **53**(4): p. 1749-1761.
24. Limpert, J., Hoffer, S., Liem, A., Zellmer, H., Tunnermann, A., Knoke, S., Voelckel, H., *100-W average-power high-energy nanosecond fiber amplifier*. Applied Physics B-Lasers And Optics, 2002. **75**(4-5): p. 477-479.
25. Di Teodoro, F., Koplow, J.P., Moore, S.W. and Kliner, D.A.V., *Diffraction-limited, 300-kW peak-power pulses from a coiled multimode fiber amplifier*. Optics Letters, 2002. **27**(7): p. 518-520.
26. Koplow, J.P., Kliner, D.A.V. and Goldberg, L., *Single-mode operation of a coiled multimode fiber amplifier*. Optics Letters, 2000. **25**(7): p. 442-444.
27. Baggett, J.C., Monro, T.M., Furusawa, K. and Richardson, D.J., *Comparative study of large-mode holey and conventional fibers*. Optics Letters, 2001. **26**(14): p. 1045-1047.
28. Li, Y.H., Jackson, S.D. and Fleming, S., *High absorption and low splice loss properties of hexagonal double-clad fiber*. IEEE Photonics Technology Letters, 2004. **16**(11): p. 2502-2504.

Chapter 6

DIRECTLY MODULATED LASER DIODE

6.1 Overview

In this chapter, I will describe the motivation for, and the development of, a 1 μm wavelength nanosecond MOPA system using a directly modulated laser diode as a pulse seed source. Section 6.2 will introduce the current technology used in nanosecond pulse MOPA systems and the motivation for pursuing this project. Section 6.3 will describe the development and characterisation of a directly modulated laser diode which generates nanosecond pulses and that gives us a wide range of output pulse parameters. Section 6.4 will compare the output performance of a single stage, MOPA system using one of two fibre amplifiers having different pumping techniques. In sections 6.5 and 6.6, we will describe the development of a MOPA system with multiple amplification stages. Further characterisation of the chosen pre-amplification stage will be discussed in section 6.5. The performance and limitation of the entire amplifier cascade, used to amplify the nanosecond pulses over a range of pulse parameters, is discussed in section 6.6 and I will conclude the chapter in section 6.7.

6.2 Introduction

Laser systems delivering pulses with high peak intensities and durations of tens of nanoseconds are particularly useful in laser marking and material processing applications. In Chapter 5, we have demonstrated a single stage Q-switched oscillator that produces 1 mJ, 37 ns pulses at 10 kHz. Although a single stage oscillator will reduce manufacturing cost and size, it does not offer the flexibility to allow the real time adjustments to the output pulse parameters, such as pulse durations and peak powers, that MOPA systems can give.

Several nanosecond MOPA systems, based on fibre amplifiers, have been developed and commercialised over the years [1-10]. However, none of the pulse seed sources used in these MOPA systems gives us enough flexibility and control over the output pulse parameters. Currently, the most commonly used nanosecond pulse sources are Q-switched lasers because of the high peak power (e.g. for nonlinear frequency conversion), narrow linewidth (e.g., for laser spectroscopy) and large pulse energy (e.g. for LIDAR) requirements. Limpert *et al.* [5] demonstrated average powers of up to 100 W, at repetition rates between 3-50 kHz, achieving

4 mJ pulses in a diffraction limited amplifier and 8 mJ in a multimode amplifier. Recently, during CLEO (US) 2004 in San Francisco, Chen *et al.* from the University of Michigan presented a MOPA chain with a highly multimode, 200 μm core, power amplifier which delivered 27 mJ pulses but with a poor beam quality of M^2 =6.5 [10]. Although both of these MOPA systems could deliver nanosecond pulses in the mJ regime having repetition rates up to tens of thousands of Hz, the Q-switched pulse seed sources that were utilised do not readily allow real time control to their output pulse parameters. In addition, the output pulse width dependence on the cavity lifetime limits the available freedom of operation.

With the increase of the number of applications requiring high energy nanosecond pulses, having control over the output pulse parameters in a single MOPA system is commercially very advantageous. Here we will describe the development of a fibre MOPA system, utilising a directly modulated laser diode seed source, where control over its output pulse characteristic is possible in real time.

This project is a collaboration between Southampton Photonics Inc. (SPI) and our group. Funding for this project is provided by SPI. This project was part of SPI's pulsed fibre laser programme. The initial objectives were to develop a MOPA system that delivers 0.5 mJ, 40 ns pulses at a repetition rate of 10 kHz and thereafter develop a variable MOPA system that delivers pulses with durations between 10 -100 ns, at repetition rates of 10 – 200 kHz and having the highest possible pulse energies. The potential for this system is tremendous, especially in the material processing industry.

6.3 Directly modulated laser diode

6.3.1 *Semiconductor Laser Diode*

Two, high frequency response, InGaAsP FP semiconductor laser diodes, provided through a joint development project between Bookham Technologies and SPI, were available to be used in this system. The respective operating wavelengths for each were 1054.8nm and 1047.9 nm at room temperature (r.t.p). The first diode was chosen as it has a longer peak wavelength at r.t.p. which would be advantageous for later amplification stages. The threshold current for this diode at r.t.p was 26.8 mA. However, the peak lasing wavelength can be tuned by tuning the diode temperature. For example, to obtain peak lasing gain at 1070nm, we temperature tuned the diode to 61 °C (corresponding TEC resistance of 2.7 kΩ), increasing

the lasing threshold to 36 mA, which was measured empirically. Figure 6.1 (a) shows the peak lasing wavelength and threshold current with TEC resistance.

Dr. Benn Thomsen, a researcher from our group, modelled the drive circuit and laser diode in an electronic circuit modelling programme (Pspice). The modelled DC characteristic and the DC characteristics provided by the manufacturer of the laser diode, are shown in figure 6.1 (b), (c) and (d). The model and manufacturer's specification were in good agreement, indicating that the parameters used in the model were reliable and could be used for further modelling of the transient response (see figure 6.2) and design of the electronic drive circuit board. The maximum DC current that can be applied to the diode is 300 mA and the resistance of the diode is 2 Ω after reaching threshold. The laser diode is not grating stabilised and therefore the lasing spectrum, taken at r.t.p with 170 mA drive current (shown in figure 6.1 (e)), can be seen to lase at a few longitudinal modes and is erratic. The measured Fabry Perot mode spacing between the longitudinal modes is ~ 0.2 nm and the root mean square (-13 dB) bandwidth of the spectrum is 0.87 nm.

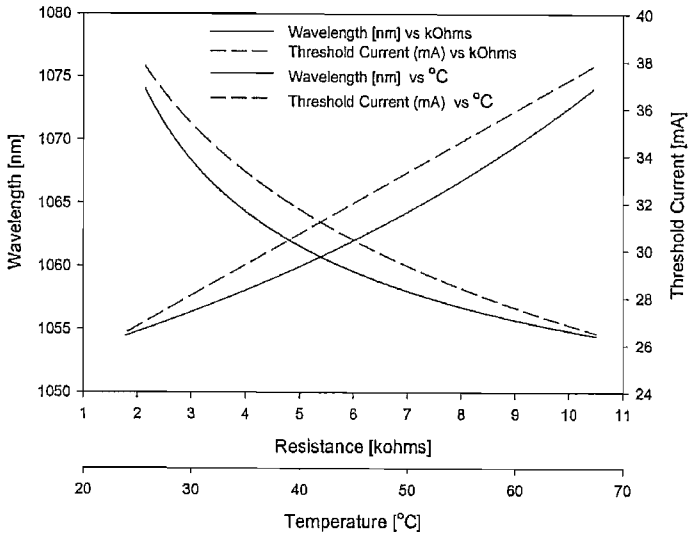

(a)

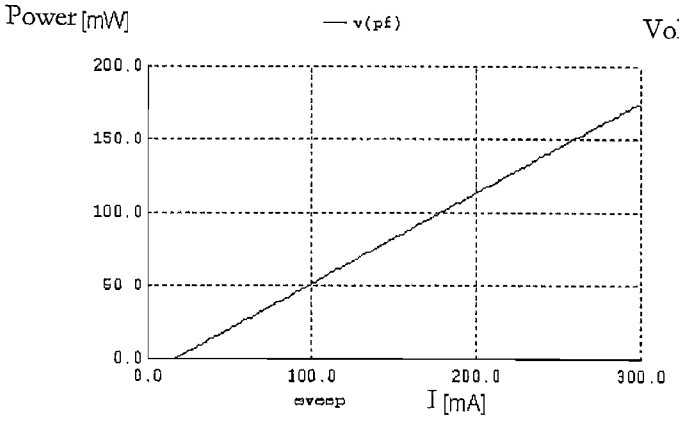

(b)

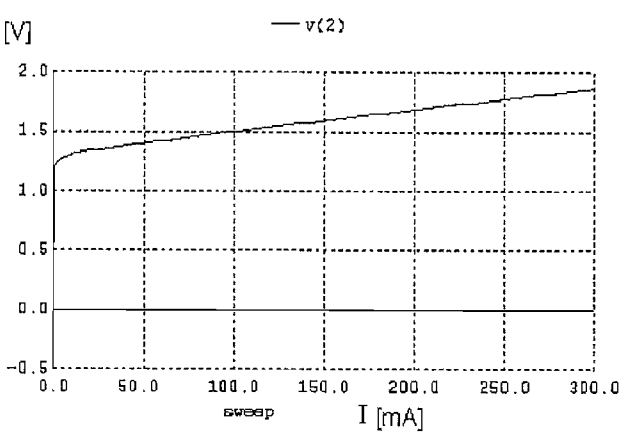

(c)

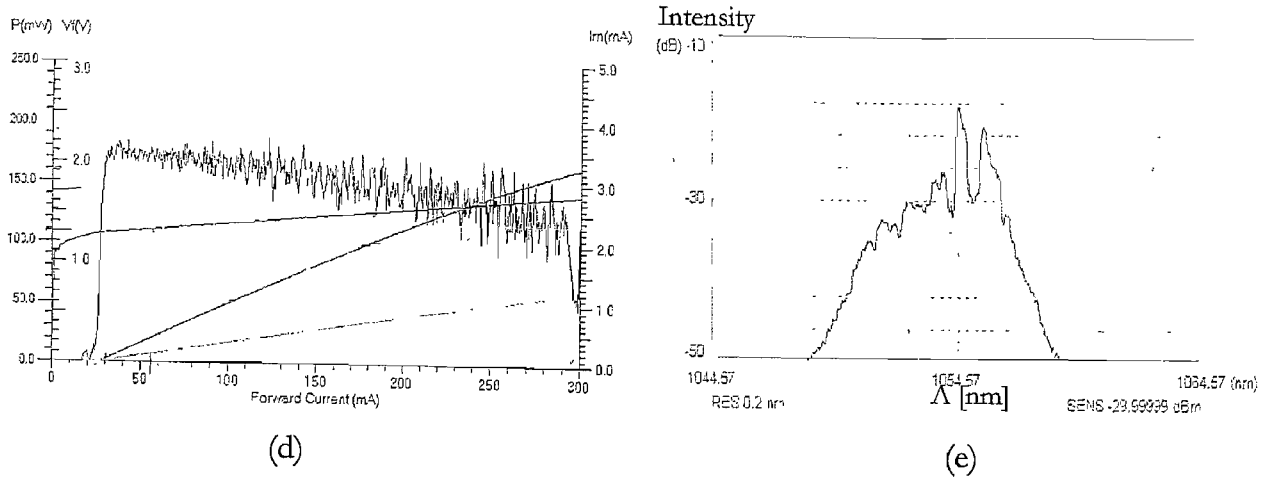

(d) (e)

Figure 6.1: (a) Wavelength tuning of laser diode with TEC resistance (temperature), Modelled (b) P vs I and (c) V vs I and (d) experimental DC characteristics of laser diode. (e) Output spectrum with 170 mA input DC current.

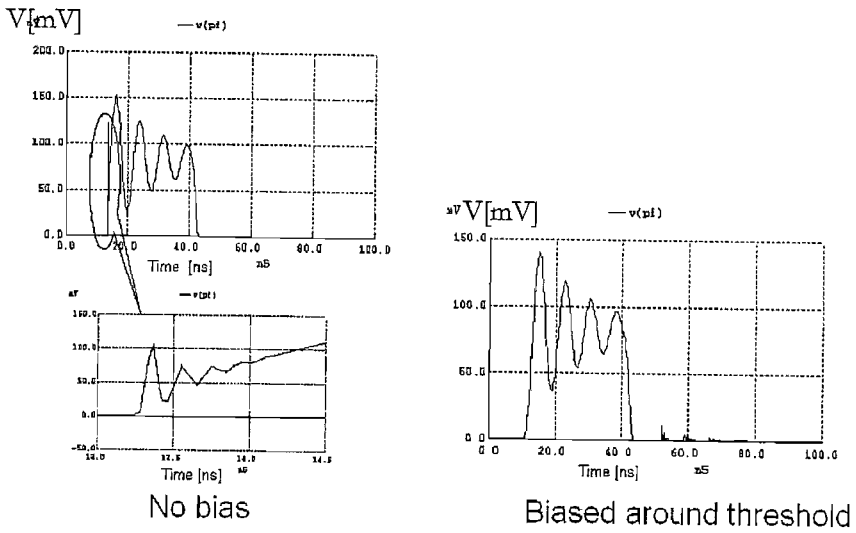

(a)

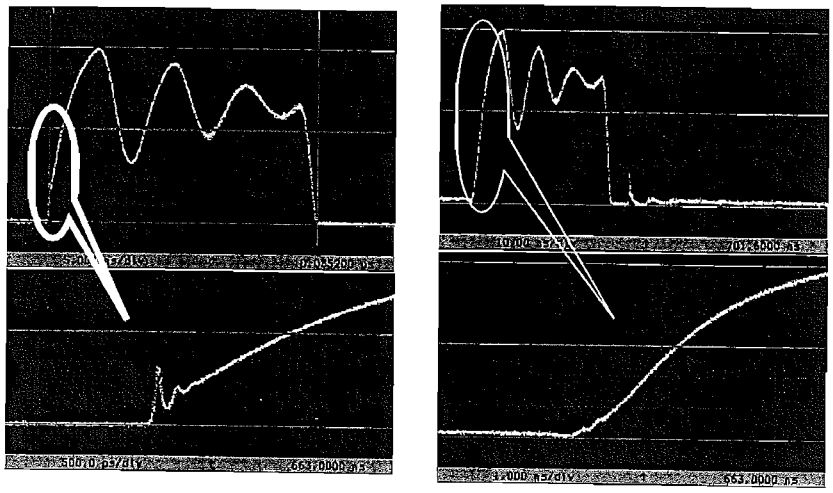

(b)

Figure 6.2: Transient response with and without input bias (a) modelled and (b) experiment.

A modulated current source with pulse duration of 28 ns and a repetition rate of 100 kHz was used to drive the laser diode. The transient response output from the laser diode is shown in figure 6.2. Figure 6.2 (a) shows the modelled transient response from Dr. Thomsen's PSpice model and figure 6.2 (b) shows the transient response from experiment.

Two dominant features can be seen from both transient response plots. Firstly, the large amplitude modulations we see on the top of the transient response are the result of electrical relaxation oscillations of the drive circuit, at the onset of the drive current, into the laser diode.

Secondly, we can see that if no initial bias is provided, a small spike is observed at the onset of the rising edge. We attribute this small spike to an initial gain switched [11] pulse due to overshoot oscillations (i.e. relaxation oscillations of the optical field generated from the laser diode) on the square modulation signal from the AWG. However no spike is observed if the diode is biased near threshold and the rising edge transition is smooth. This is because when the diode is biased near threshold, at the trough of the initial overshoot in the modulated signal, the diode gain would still be above threshold. The initial gain switched spike was treated as negligible and hence, no bias was used in the subsequent experiments. The rise time (10% to 90% of the rising edge) of the diode's output is ~ 4 ns, limited by the modulation signal from the AWG.

Since the Fabry Perot spacing between the longitudinal modes is ~ 0.2 nm, a narrowband (3 dB linewidth of 0.2 nm) fibre Bragg grating filter was needed to filter out each single longitudinal mode separately to analyse the sequence of modes that are generated from the laser diode over the duration of the driving current pulse. Figure 6.3 illustrates this filtering process.

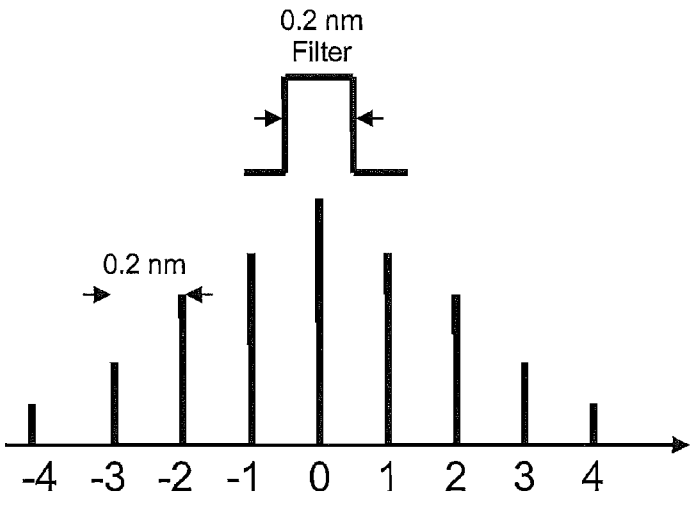

Figure 6.3: 0.2 nm Bragg grating filter tuned across the pulse spectra to separate the different longitudinal modes.

Figure 6.4 (b) shows the temporal output of the laser diode, taken over a long train of pulses, when no filter was used. The output was actually a superposition of a few longitudinal modes from the diode. This was observed when the Bragg grating filter was introduced. We can see that the pulse shown in figure 6.4 (b) was actually a superposition of 4 excited modes. The histogram function in figure 6.4 (c) shows that the amplitude variation is caused by the excitation of different modes having different gains.

This amplitude noise can be explained using figure 6.4 (a). This figure shows a sketch of the output gain profile from the laser diode. The four longitudinal modes, excited by the driving electrical pulse, are indicated in red. It can be seen that each longitudinal mode experiences different gain and thus, depending which mode was preferred at each pulse, the temporal amplitude changes, resulting in amplitude fluctuations within the train of pulses, which are reflected in the overall pulse (shown in figure 6.4 (b)) as amplitude noise.

This phenomenon can also be seen in figure 6.4 (c). At each pulse, gain in either one of the modes is preferred and the different colours you see are actually the different modes excited. The green waveform actually represents the mode (of the four longitudinal modes i.e. 0 from figure 6.4 (a)) where gain is highest (peak of gain spectra) and the yellow waveform where gain is least (i.e. -2 in figure 6.4 (a)). The histogram function shown on the left indicates the distribution of the modes averaged over a train of output pulses and it indicates that the predominant mode is depicted by the green waveform.

The excitation for the different longitudinal modes (starting from the bottom to the top) within a 28 ns optical pulse (averaged over a number of pulses), is shown in Figure 6.4 (d). We can see that the predominant modes within the pulse are the modes -2 to 1 in figure 6.4 (d). The rest of the modes (2 to 5 in figure 6.4 (d)) excited are negligible and not considered. The mode with the highest gain is indicated by mode 0 and the lowest is -2. The superposition of the different longitudinal modes excited, forms the overall temporal pulse shape, and is shown at the top-most waveform. This variation in magnitude between the different modes results in amplitude fluctuations, which are reflected as noise in the overall pulse.

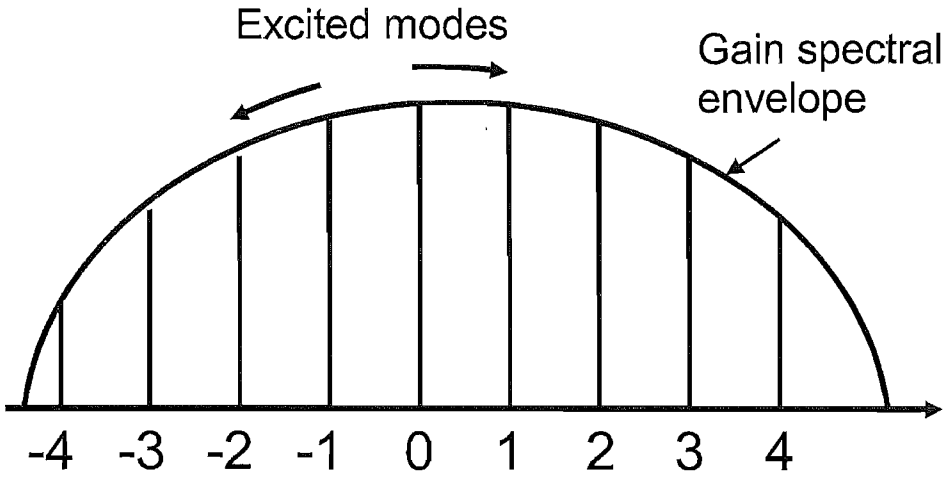

(a)

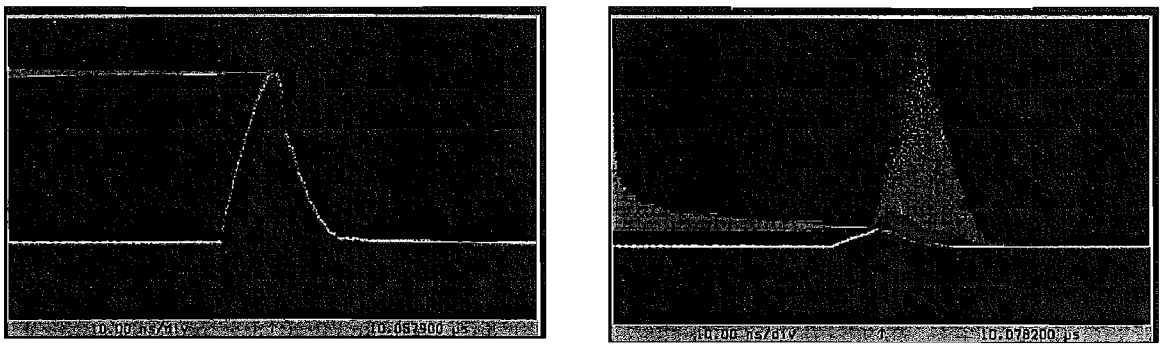

Before Filter

With Filter

(b)

(c)

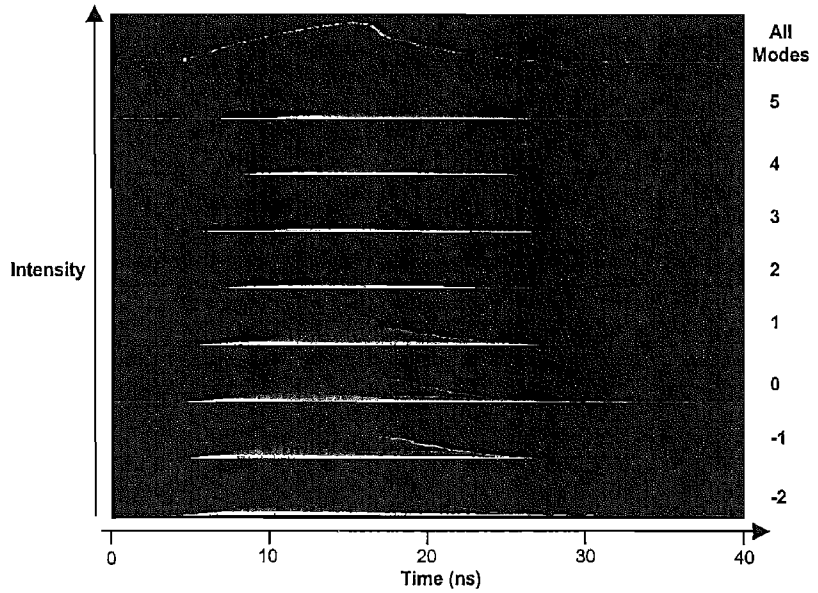

(d)

Figure 6.4: (a) Drawing of gain envelope of laser diode output. Temporal output profile of pulse (b) with and (c) without filter. (d) Illustrates the different longitudinal modes that are excited in each pulse.

Two different driver boards were used to drive the laser diode. Namely they are the EVLD02 commercial driver board from Directed Energy Inc. (DEI) and an in-house driver board. Their design, implementation and performance comparison are described in appendix A2.

6.4 Single stage amplification

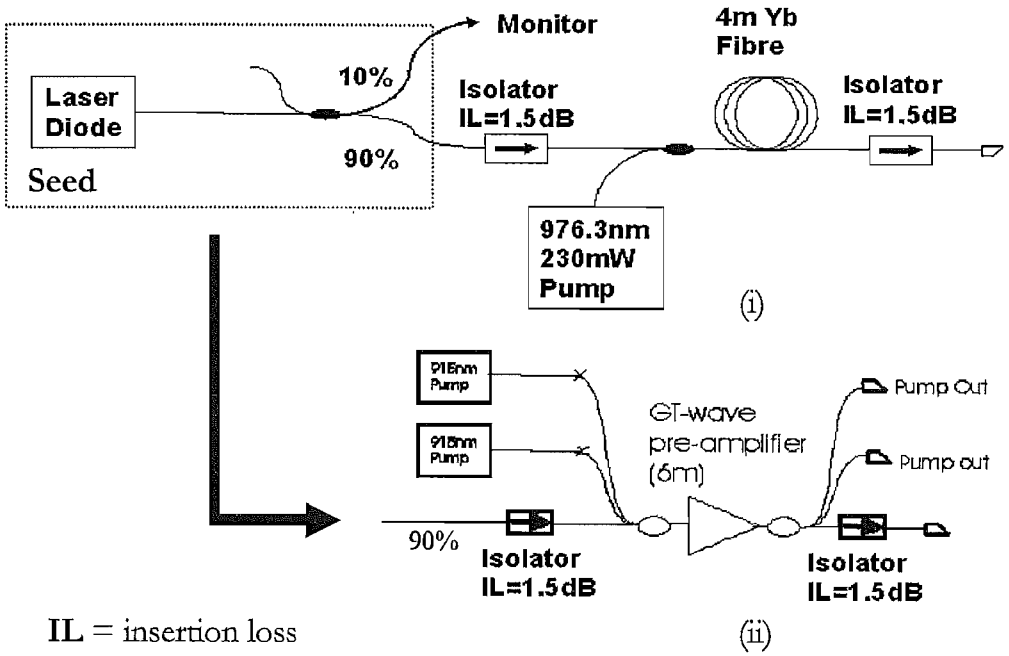

Figure 6.5: Single amplification stage setup.

The setup, in figure 6.5 above, shows two versions of the single stage MOPA system that was setup to compare two different amplification stages. The first amplifier (i) was a conventional core-pump amplifier using a 4 m piece of HD406-2 SM Yb^{3+} doped fibre. The characterisation results of this core-pumped amplifier are shown in section 4.2.2.1 of chapter 4. Pumping was achieved using a 976.3 nm MOPA pump, providing 230 mW of pump power, when driven at 1.7 A, using a Newport current driver. The pump was delivered into the amplifier via a 975/1060 nm wavelength division multiplexer (WDM) and the estimated insertion loss is less than 0.5 dB.

6.4.1 *Initial characterisation of the GT-wave amplifier*

The second amplifier (ii) was a GT-wave cladding pump amplifier [12, 13]. The GT-wave amplifier had a 6 m long doped Yb^{3+} fibre length within the GT-wave fibre bundle. The output SM signal fibre pigtail has 6/125 μm core/cladding diameters, with NA of 0.14. The

multi-mode pump pigtails have 105/125 μm core/cladding dimensions, with NA of 0.22. Initial characterisation of the GT-wave amplifier, using c.w. seed lasers at various wavelengths, was carried out to evaluate its performance before being used in the pulsed MOPA system.

The c.w. lasers centred at 1050, 1060 and 1070 nm wavelengths were built using high reflection, narrow linewidth, Fibre Bragg gratings optimised at the respective wavelengths and a 2m length of HD406-2 Yb^{3+} doped fibre. Two 915 W diode pumps, from JDS Uniphase providing up to 4.93 W of pump power, were used to pump the amplifier.

Figure 6.6 (a) shows the setup used to characterise the GT-Wave amplifier. Two fibreised isolators (1.5 dB insertion loss) were used at both ends of the amplifier to prevent any spurious lasing, or self pulsing caused by back reflections from the output end, and to prevent backward ASE from de-stabilising the input seed. A 90/10 coupler was used to determine the input signal power injected into the amplifier.

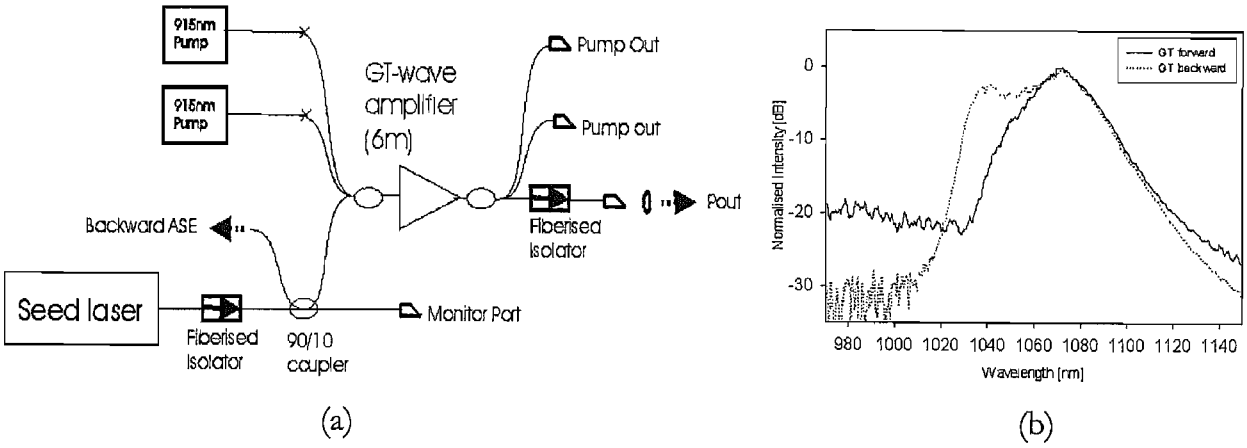

Figure 6.6: (a) GT-Wave amplifier setup. (b) Forward and backward ASE at 4.93W pump.

Figure 6.6 (b) shows the forward and backward ASE spectra of the amplifier at full pumping power from both pump diodes sources. We can see that both ASE spectra have a relatively sharp peak spectrum, centred on 1070 nm, and we would expect the gain to be optimum at that wavelength.

Figure 6.7 shows the amplifier gain and output power with respect to input power obtained at maximum pump power using the 1050, 1060 and 1070 nm c.w. seed sources. As expected, the 1070 nm c.w. laser achieved the best performance with a highest small-signal gain of ~ 36 dB. We can see from figure 6.7 (a) that the large signal gain tends towards the same asymptote for all wavelengths. The saturated output powers for all wavelengths were > 350 mW. However the total absorbed pump, subtracting coupling (total transmitted pump from the output pump fibres was ~ 2W) and negligible splice losses, was only 1.09W

(corresponding to 25% pump coupling efficiency) of pump power. Coupling losses in the GT-wave amplifier come from 2 sources, the pump coupling loss between the pump and signal fibre and coupling loss at the output splice boat (~ 3dB loss). The splice boat was made of a type of ceramic that can withstand up to 20W of dissipated power. However since the pump coupling loss at the splice boat was at the output end, the loss was not important unless recycling of the pump was carried out (by splicing the two pump output pigtails together). The pump to signal optical efficiency, with 0.2 mW input power, at 1070 nm, of this GT-Wave amplifier was found to be ~ 30 %.

SPI is the sole proprietor of the GT-Wave amplifier and has now develop both Er^{3+}/ Yb^{3+} and Yb^{3+} doped amplifiers, with power limits up to 100W, as standard products.

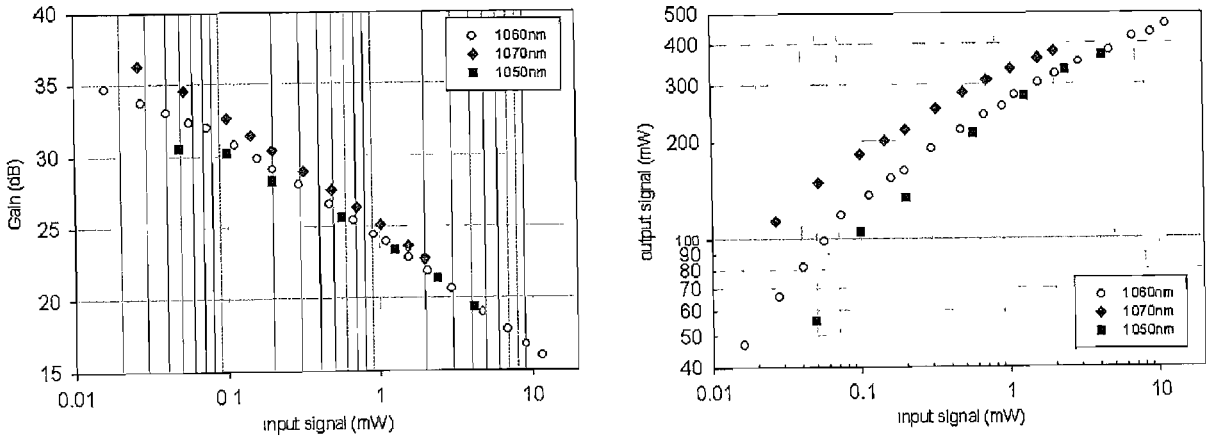

Figure 6.7: GT-Wave amplifier characterisation with 1050, 1060 and 1070 nm c.w. lasers. (a) Gain and (b) Ouput power at 4.93W pump.

6.4.1.1 Polarisation instability of the GT-wave amplifier

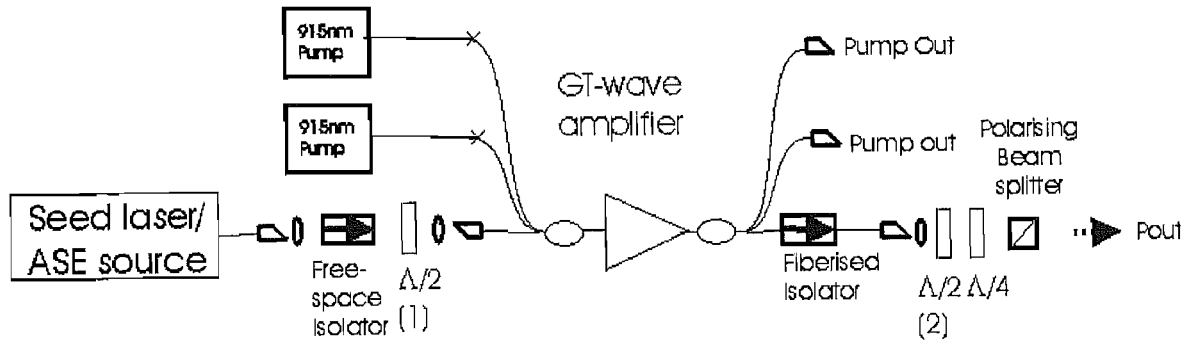

Figure 6.8: Setup to characterise polarisation stability performance of GT-wave amplifier. GT-wave amplifiers of different configurations were used.

It was also found that the GT-wave amplifier was birefringent and that the output birefringence changes over time. It was thought that this was due to the heating of the GT-wave fibres as a result of the high pump power dissipating within the amplifier.

Hence two configurations of 6 μm standard core-size GT-wave amplifiers of the same length were tested to see any change in output power, after a polariser, over time. The setup is shown in figure 6.8. One GT-wave amplifier was mounted on a heat sink while the other was mounted on a heat sink cooled with a 15V cooling fan. Two sources were used to characterise the birefringence of the amplifier. One source was a 1060 nm laser and the other was a 30 nm bandwidth ASE source, centred at 1070 nm. This un-polarised ASE source was polarised via the free space isolator.

Polarisation stability of the amplifier was characterised using the polarised input source and by measuring the change in transmitted signal, through a polarising beam splitter (PBS) cube, over time. The polariser was initially set for maximum transmission; changes in the transmitted power over time indicated changing output polarisation. The other output of the PBS was also monitored to provide a measure of the total power transmitted over time. Some pump power was also injected to see the effects on polarisation of the output with increasing pump power.

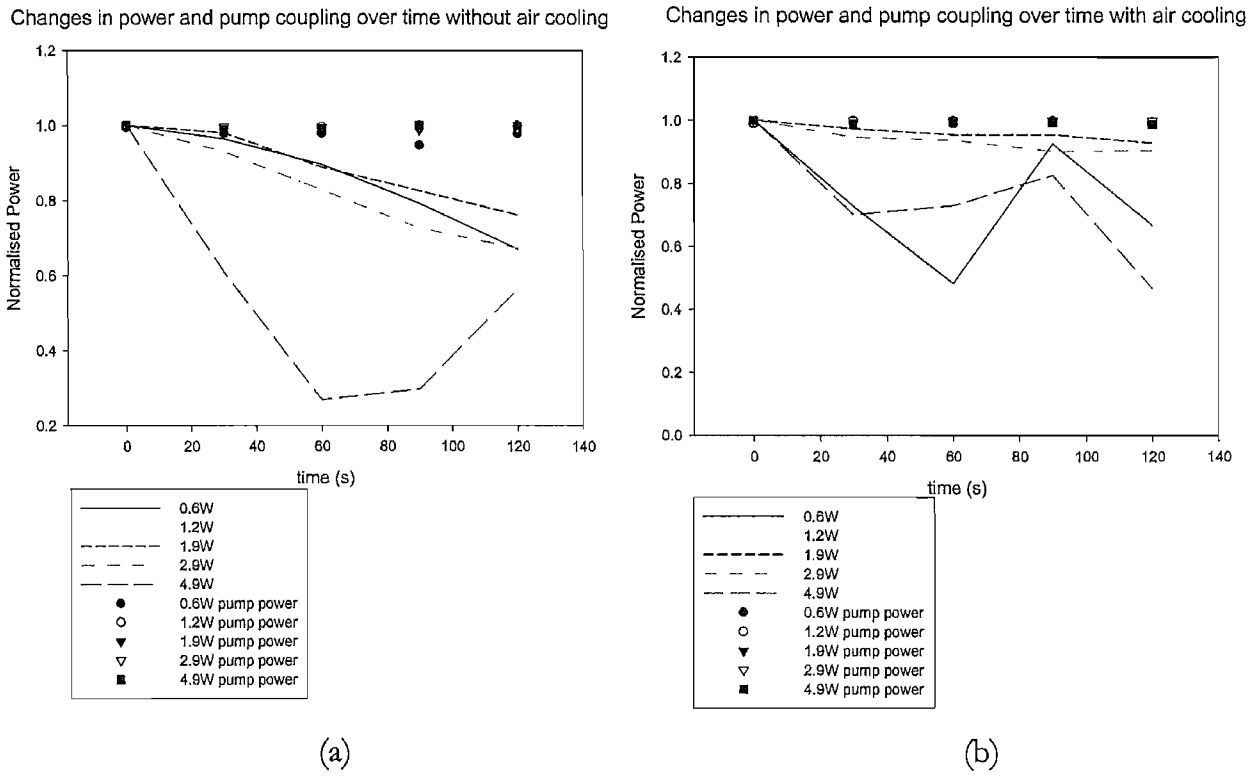

Figure 6.9: Illustrates the change in output power with different pump powers and pump coupling over time (a) without (b) with cooling fan. Line indicates changes in output power while dots indicate changes in pump transmission.

The 1060 nm laser source was first used to test the amplifier. A small amount of pump power was also injected to reduce the absorption of the 1060 nm signal by the active fibre. Figure 6.9 (a) and (b) demonstrate the change in output power with time for both configurations of the amplifier.

For both cases, the transmitted unabsorbed pump power (i.e. pump coupling) does not change over time. This indicates that the output power does not change as a result of a reduction in pump absorption, which would affect the gain. When the PBS was removed from the output of the amplifiers, the output power was found to be stable over an equivalent or longer period of time. The results observed for both experiments, indicate that the output power monitored after the PBS, was changing due to polarisation changes in the amplified signal.

In the case of the amplifier without fan cooling, it was found that the output power changes significantly at all pump powers. The magnitude of change was greatest at the highest pump power (see figure 6.9 (a)). We found that the fan does help to stabilise the polarisation changes within the amplifier. The magnitude of variation was reduced at the highest pump power and the output power stabilised at pump powers of 1.9 W and 2.9 W (see figure 6.9 (b)). Therefore I believe that polarisation changes were mainly due to heating caused by the dissipating pump power.

The birefringence beat length and polarisation stability of the 6 μm standard core-size GT-wave amplifiers was further characterised using a polarised ASE source. Figure 6.10 shows changes in output polarisation with pump power over time. The plots depict the attenuation, as a function of wavelength, through the PBS over time. Plots 6.10 (a) to (c) illustrate the effects of increasing pump power. Figure 6.10 (a) shows a plot without any pump power. In (b), we introduce 1.9 W of pump power and in (c) we inject 2.9 W of pump. We can see that the polarisation starts to change more drastically with increasing pump, indicating a pump power dependent change in polarisation.

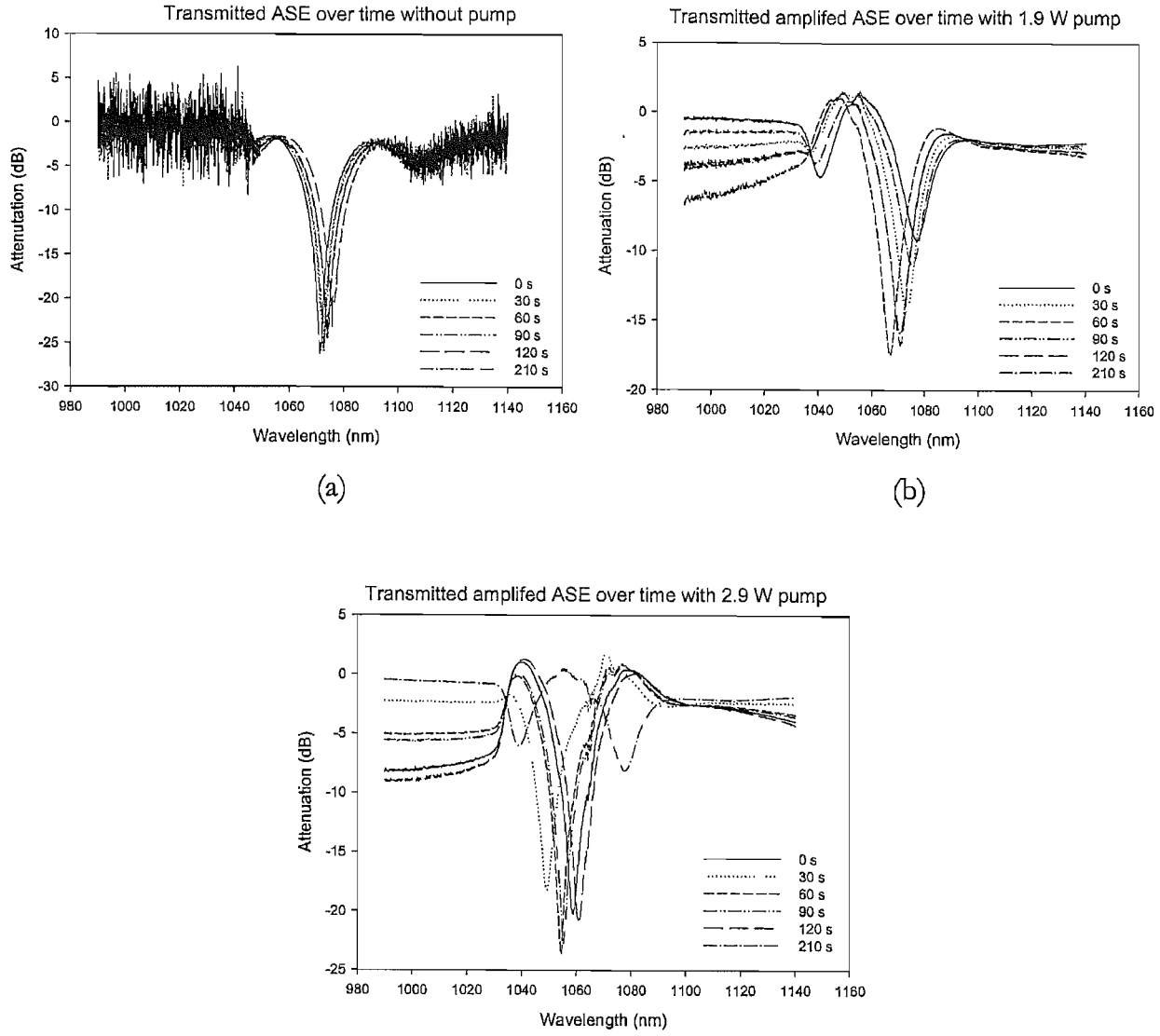

Figure 6.10: Illustrates the normalised wavelength dependent transmission after various times for several pump powers. A birefringence beat length of 20cm was obtained with two adjacent modulation peaks. (a) Without any pump, (b) with 1.9 W pump power and (c) with 2.9 W pump power.

Initially, I identified the birefringence axes of the fibre under test (FUT) by first utilising $\lambda/2_{(2)}$ and $\lambda/4$ (see figure 6.8) to maximise the throughput of one of the PBS outputs. Without making any further changes, I then maximise the output power from the same output port using $\lambda/2_{(1)}$ (see figure 6.8). This indicates that $\lambda/2_{(1)}$ is set to one of the axes. Subsequently, the beat length of the GT-wave fibre was characterised by launching light at 45° to the birefringence axes of the fibre and maximising, using $\lambda/2_{(2)}$ and $\lambda/4$, the depth of modulation superimposed on the output spectrum. The modulation that occurs on the output spectrum, is a result of the mode beating between the polarisation eigenmodes. Adjacent peaks of the modulation occur for wavelengths between which the number of polarisation beats, which occur along the length of the fibre, differs by 1. By taking enough points, the beat length could be estimated using equation 6.1.

$$L_B = \frac{L}{\lambda}.\Delta\lambda \qquad (6.1)$$

where L_B is the beat length of the fibre of wavelength λ, L is the length of fibre and $\Delta\lambda$ is the wavelength difference between the two adjacent peaks.

The beat length of the fibre was found to be 20 cm at 1060 nm. From equation 6.1, we can see that the maximum possible beat length we can measure, with this technique, depends on the length of the FUT and the bandwidth of the ASE source. In this case, the short beat length of 20 cm can be measured with this technique.

This change in output polarisation could be inconvenient in a practical device, if polarisation sensitive components were used in the later stages. One approach, to remove this polarisation sensitivity, is to depolarise the light before launching into the GT-wave amplifier. This might be done through a Lyot depolariser. In this technique, two lengths of highly birefringent (Hi Bi) fibres are spliced together with the birefringence axes of one fibre orientated at 45° to those of the other. The ratio of the two lengths is 2:1 and the length of Lyot depolariser for required level of polarisation will scale approximately inversely with bandwidth. Work on this was not carried out, during the time of the experiment because it was not necessary as polarisation sensitive components were not used. However, it was subsequently done by Dr Malinowski from our group and was shown to work.

6.4.2 *Performance comparison between core-pumped (HD406-2) and GT-wave amplifiers*

Comparisons were made between the amplifiers using 10 ns pulses at 10, 50 and 100 kHz repetition rates. The forward ASE spectra of the two amplifiers in the absence of signal are shown in figure 6.11 (a). The ASE spectra, for the core-pumped (HD406-2) and GT-Wave amplifiers, peak at 1060 nm and 1070 nm respectively. The laser diode was temperature tuned to operate at the wavelength of the ASE peak of the amplifier under test. Figure 6.11 (b) shows the output spectra when pulses were amplified with the two amplifiers. No significant spectral broadening and ASE build up can be seen from either amplifier.

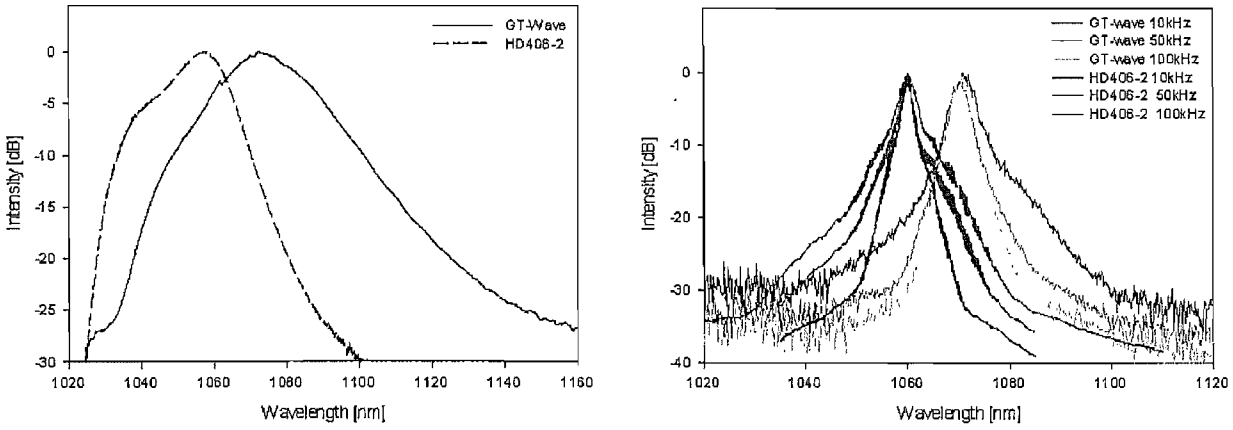

Figure 6.11: (a) Forward ASE spectra and (b) Output spectrum of 10 ns pulses at 10, 50 and 100 kHz repetition rate for both GT-Wave and HD406-2 amplifier.

Repetition rate (kHz)	HD406-2 [nm]	GT-Wave [nm]
10	3	3.6
50	1.6	3
100	1.5	3

Table 6.1: Comparisons of output 3 dB spectral width between GT-wave and HD406-2 pre-amplifier.

The 3 dB spectral bandwidth at 10, 50 and 100 kHz repetition rates, for the HD406-2 and GT-Wave amplifer, are presented in table 6.1. The output spectral bandwidths at all repetition rates, after the HD406-2 pre-amplifier, are similar to the output bandwidth obtained directly from the diode. The spectral bandwidths are slightly broader from the GT-Wave amplifier and this is due to the output pulses having higher peak powers (see figure 6.12 (d)). The higher peak powers obtained from the GT-wave amplifier are a result of gain shaping which we shall further discuss in section 6.6.3.2 of this chapter. The higher peak powers results in broader spectral broadening via SPM (see section 2.2.3.1) which is proportional to the peak power (see equation 2.22). As higher signal pulse energies (hence higher pulse peak powers) are obtained when the repetition rates are reduced, for this same reason, the output spectral bandwidth increases with decreasing repetition rate.

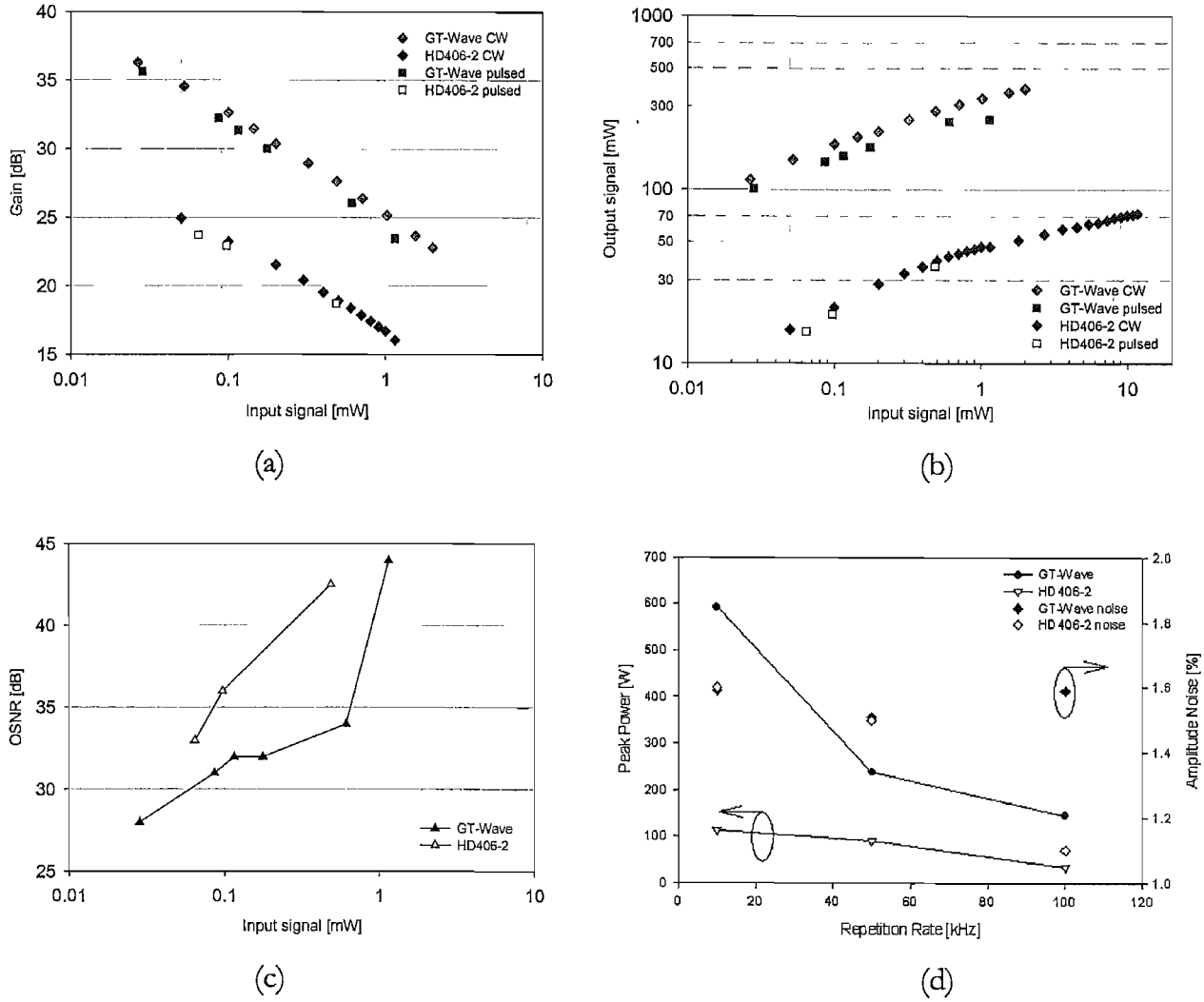

Figure 6.12: Output c.w. and pulsed performance with input signal power at highest pumping power from GT-Wave and HD406-2 amplifier. (a) Gain, (b) Output signal power and (c) OSNR. (d) Peak power and amplitude jitter obtained at different repetition rates for 10 ns input pulses.

The gain, amplified signal power and OSNR, over a range of continuous wave (c.w.) and pulsed input signal powers for both amplifiers, are shown in figure 6.12 (a), (b) and (c) respectively. The upper limit (assuming all experimental conditions are similar) on the amount of gain achievable for an amplifier is determined by its c.w. performance. The pulsed gains, achieved for both amplifiers, were no more than 1 dB lower than the c.w. gain performance over the range of conditions examined.

The greater pump power, available through utilising cladding pumping [12-15], is a clear advantage of the GT-Wave amplifier. The gain achieved by the GT-Wave amplifier is ~ 10 dB higher, for a similar input signal power, compared to the HD406-2 amplifier. For input signal powers < 0.2 mW, the signal gains that the GT-Wave amplifier could provide were > 30 dB, with the highest reaching ~ 36 dB. However, the highest possible gain from the HD406-2 amplifier was ~ 24 dB. The pulsed gain w.r.t pump power for both amplifiers were not

measured, but we can see, from figure 6.12 (a) and (b), that the amplifier's performance for both pulse and c.w. inputs do not vary greatly. Therefore the c.w. gain comparison between both amplifiers, that was presented earlier in figures 4.5 (a) (for core-pump) and 6.7 (a) (for GT-Wave), can be used as a good reference. The gain provided by the GT-wave was far superior (~ 10 dB greater with 1.1 W absorbed pump) and its pump to signal optical efficiency, with 0.2 mW of input c.w. signal, is 48% compared to the HD406-2 amplifier's efficiency of 21%.

The choice between the two amplifiers to be use as a pre-amplifier, for the development of the MOPA system in this chapter, was made by comparing their performance at an input signal power of 0.2 mW. This is because it is equivalent to the seed power of the 40 ns pulses, with 500 mW peak powers at 10 kHz, provided by the directly modulated laser diode. From figure 6.17 (a), we see that the gains obtained by the GT-Wave and HD406-2 amplifier, at an input signal power of 0.2 mW, were ~ 30 and ~ 21.5 dB respectively.

Output signal power, produced from both amplifiers, is shown in figure 6.12 (b). The output power performance from the GT-Wave was clearly superior over the range of input powers. The highest output power achieved was 250 mW. With an input power of 0.2 mW, the output signal power of the GT-Wave and HD406-2 amplifier was ~ 217 and 29 mW respectively.

The OSNR with input signal power, for both amplifiers, is shown in figure 6.12 (c). The OSNR performance was better with the HD406-2 amplifier compared to the GT-Wave. Comparing corresponding input signal powers, the OSNR demonstrated by the HD406-2 was 2 – 8 dB higher than the GT-Wave amplifier with increasing input power. Particularly, the measured OSNR for the GT-Wave amplifier, with 0.2 mW input signal power, was ~ 32 dB and the extrapolated OSNR for the HD406-2 amplifier was ~ 39 dB. However the OSNR obtained for both amplifiers for all input signal powers (lowest OSNR of 28 dB) was adequate.

Peak output intensities obtained with 10 ns input pulses at different repetition rates were also compared. The highest peak powers achieved were ~ 592 W from the GT-wave and 112 W from the HD106-2 amplifier. Slight deterioration in amplitude jitter was observed from both amplifiers with increasing repetition rate. This was due to the larger buildup of ASE between pulses at the lower repetition rates. The amplitude jitter was 1.6 % for the GT-Wave and 1.1 % for the HD406 amplifier, compared with 0.44 % directly from the diode.

With superior gain, efficiency, peak output intensities and potential for higher power scaling, the amplifier of choice was the GT-Wave amplifier. Therefore, further characterisation of the GT-Wave amplifier with nanosecond pulses was performed.

6.5 Pre-amplification stage

6.5.1 *Performance of GT-wave amplifier*

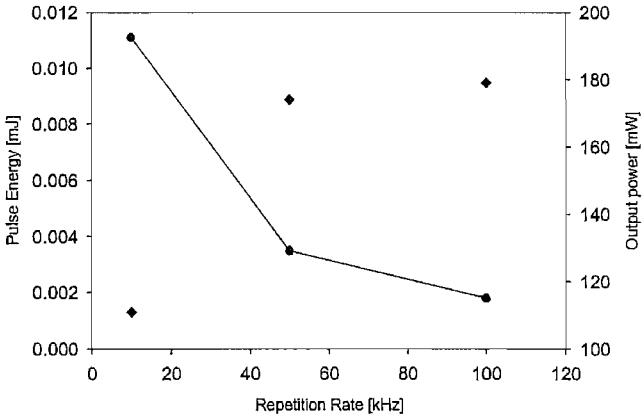

(a)

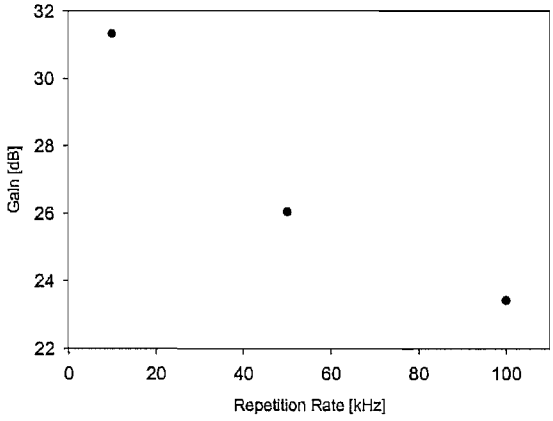

(b)

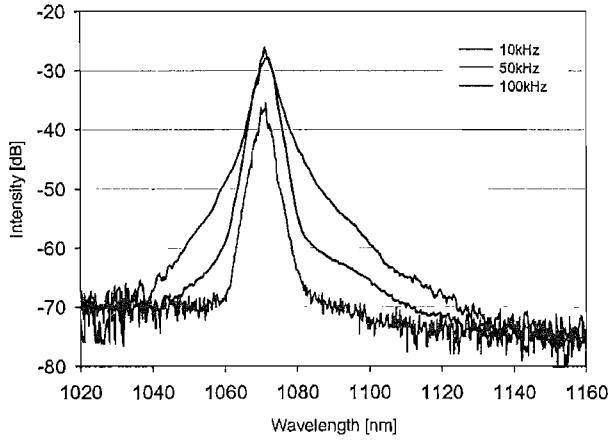

(c)

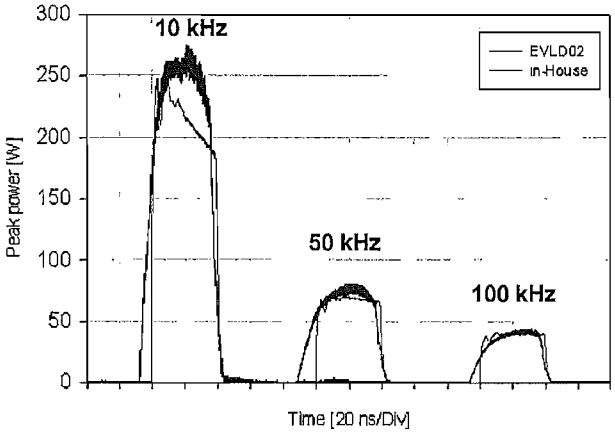

(d)

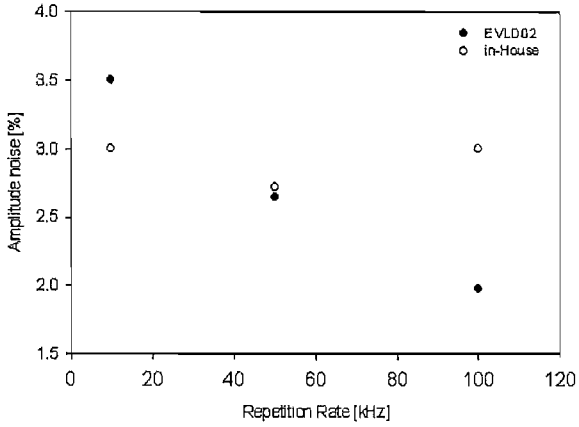

(e)

Figure 6.13: (a) Pulse energy and average power against repetition rate (b) gain against repetition rate and (c) output spectra. (d) Amplified 40 ns pulses taken from HP scope and (e) amplitude noise at 10, 50 and 100 kHz repetition frequencies for both driver boards.

In this section, the performance of the GT-Wave pre-amplifier is evaluated. 40 ns pulses at 10, 50 and 100 kHz repetition rate were seeded into the amplifier. The pump power and energy of the input seed pulses were kept constant, at 4.93 W and 16.3 nJ respectively, for all repetition rates. The output performance obtained is shown in figure 6.13.

The output pulse energy, average power and gain are all shown in figure 6.13 (a) and (b). The highest output pulse energy and gain, of 11 μJ and 31 dB respectively, was obtained at 10 kHz and the lowest was 1.8 μJ and 23 dB at 100 kHz. The output average power and gain seem to saturate at repetition rates above 50 kHz for the fixed pump power.

Figure 6.13 (c) shows that there was no sign of ASE build-up or unwanted non-linear effects The OSNR of all spectra were still high at > 30 dB. The FWHM output spectral linewidth increases with decreasing repetition rate. FWHM between 3 - 3.6 nm, with decreasing repetition rate, were obtained. The input and output spectra obtained were almost similar except for the slight spectral broadening observed at the lowest repetition rate of 10 kHz. The broader spectral width was attributed to SPM, due to the higher peak power of the propagating higher energy output pulses.

Although both driver boards gave similar output performances from the amplifier, the differences between the input pulse shapes from both boards have more significant effects on the profiles of the amplified pulses. In figure A2.5 (a) of appendix A2, we observed that pulses from the EVLD02 board were much squarer compared to the pulses generated by the in-House board. Figure 6.13 (d) shows the output pulses from the amplifier for seed pulses from both driver boards. We observed that input pulses from the EVLD02 board led to more significant pulse shaping (i.e. pulse sharpening) due to gain saturation [16] (we shall see in a later section the effect that it has on higher output pulse power scaling). The reason for this, I believe was because of the squarer leading edge pulse profiles produced by the board (this will be explained further in section 6.6.2.2). The effects of pulse shaping are most prominent at 10 kHz repetition rate. Comparing figures 6.13 (d) and A2.5 (a), at 10 kHz repetition rate for both boards, we can see that the pulse sharpening effects were more prominent with the EVLD02 board, compared to the rounder top pulses generated by the in-House board. The output temporal pulses at different repetition rates, shown in figure 6.13 (d), were normalised to their corresponding peak power.

The measured amplitude fluctuations are shown in figure 6.13 (e). Although they remain relatively constant over all repetition rates, they increased from 0.46% from the diode to ~3% and 1.1% to ~3.5 % at the worst case for the in-House and EVLD02 board respectively.

6.5.2 *Overview of GT-Wave amplifier performance*

Earlier in section 6.2, we mentioned that the targeted specification was 0.5 mJ pulses with durations of 40 ns and at repetition rates of at least 10 kHz. Table 6.3 below indicates the present pulse energies so far achieved for 40 ns pulses at different repetition rates, and determines how much gain we need from the final amplifier stage to establish the feasibility of achieving our target.

Repetition rate [kHz]	Pulse energy [mJ] after pre-amplifier	Gain required from final amplifier [dB]
10	0.011	16.6
50	0.0035	21.6
100	0.0018	24.5

Table 6.2: Gain required from final amplifier to achieved target for input pulse energies from pre-amplifier.

Generally the gain provided by LMA final stage amplifiers is approximately 20 dB. Therefore it can be seen from table 6.2 that obtaining the 0.5 mJ target for 10 kHz pulses would not be difficult. However obtaining our target pulse energy for 50 and 100 kHz pulses, especially at 100 kHz, might be more difficult. This difficulty arises mainly due to the limited pump power (see section 6.6.3.1) we had at the time of the experiment. In the next section, we shall evaluate the output performance of the final amplification stage and discuss the limitations encountered for obtaining higher pulse energies.

6.6 Final amplification stage

6.6.1 *Final amplification setup*

The complete setup used for the amplification of the ns pulses is shown in figure 6.14. The final amplification was provided by a power amplifier built using a large mode area (LMA) fibre. This fibre used the cladding pump technique (see section 2.1.3 of chapter 2) to allow pumping from multimoded pump sources. The fibre has an inner cladding diameter of 300 μm

and core size of 30 μm. The respective numerical apertures (NA) are 0.4 and 0.06 for the inner cladding and core. A 6m length, of 30 μm core LMA fibre, was nearly single moded with an M^2 quality of ~ 1.3. The pump source is provided by pigtailed 915 nm and 976 nm medium brightness, multi-emitter, diode polychrome pumps, from Boston Lasers Inc. The NA and diameter of the core is 0.22 and 200 μm for both pump fibres. The 915 nm and 976 nm pumps provide up to 30 W and 25 W pump power respectively. Isolation between the pre-amplifier and final amplification stage was provided by a fibreised isolator, from O-net communications Ltd.

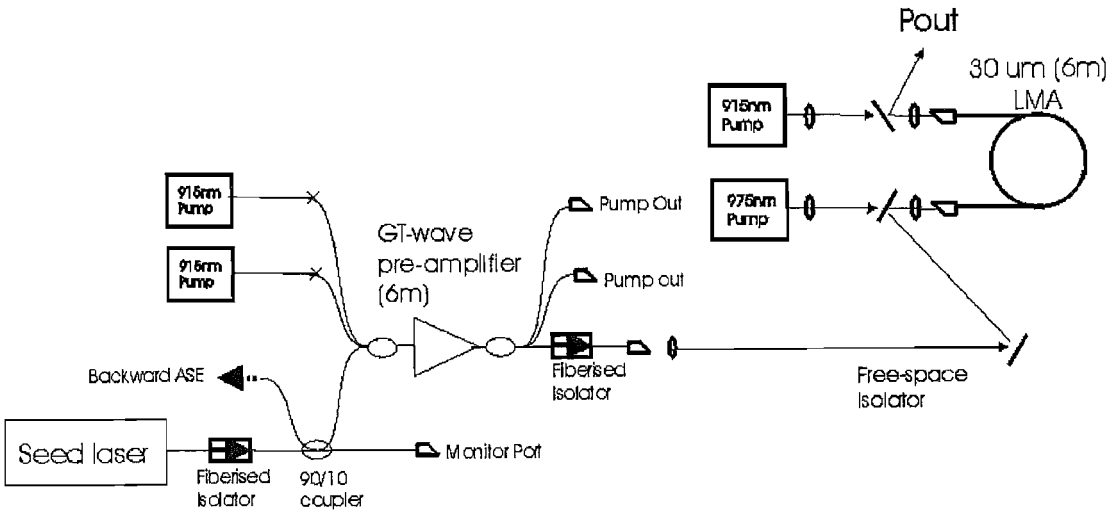

Figure 6.14: Complete schematic of ns pulse amplification cascade

6.6.2 *Performance of amplifier cascade*

A comprehensive characterisation of the amplifier cascade was made using 40 ns input pulses from the GT-Wave amplifier, at different repetition rates. Because it was found that a significant amount of power was transferred to longer wavelengths, due to stimulated Raman scattering (SRS) at high pumping power, especially at the lower repetition rates, performance results are presented in two different ways. The pulse energy in a 10 dB bandwidth, centred at 1070 nm, is presented along with total output pulse energy obtained. If significant wavelength conversion has occurred, this makes it easy to determine the extent to which power has been transferred away from the seed wavelength.

6.6.2.1 Pulse energy, peak power and gain performance.

The output pulse energy and peak powers are shown in figure 6.15 (a) and (b) for the two regimes. Figure 6.15 (a) shows the output pulse energy lying within a 10 dB bandwidth, centred at 1070 nm, that was extracted from the total pulse energy using the output spectrum. The highest 1070 nm signal pulse energy obtained was 0.49 mJ, at 10 kHz repetition rate. The peak intensities of the 1070 nm signal were estimated using temporal pulse shapes just before the onset of Raman scattering. Therefore some margin of error existed (~20%). In a later section, we will describe further the effects of SRS on the temporal pulse shape, using a bulk grating to separate both the Raman pulse and 1070 nm signal pulse for a particular output pulse. All peak intensities shown in figure 6.15 were calculated by multiplying the peak amplitude of the temporal pulse with the ratio of the actual pulse energy and the total calculated area of the temporal pulse (i.e. $P_{peak} = Amplitude_{peak} \times \frac{Total\ \ Pulse\ \ Energy}{Total\ \ Pulse\ \ Area}$). The peak powers achieved with both seed sources were similar, with highest peak powers of 20.2 kW. The high peak intensities of the amplified pulse were due to gain saturation effects, which sharpen the shape of the output pulses (see figure 6.16 (a) and (b)).

For output signal pulses, centred at 1070 nm, shown in figure 6.15 (a), pulse energies obtained were close to but did not reach the 0.5 mJ targets, even at 10 kHz repetition rate. However, when the total output pulse energy was considered, in figure 6.15 (b), we see that the 0.5 mJ target was achieved. At 10 kHz, the total output pulse energy was 0.76 mJ.

Another important result to note was the dramatic increase in peak powers, compared to the peak powers shown in figure 6.15 (a), when seeded with 10 kHz pulses. This sudden increase in peak power was due to gain saturation (i.e. gain shaping). Gain saturation (see section 6.6.3.2) results in the steepening of the output pulses, increasing their peak powers. This increase in peak powers subsequently results in the generation of narrow spike Raman components via SRS. At the output, the Raman pulse is superimposed together with the original 1070 nm pulse (see section 6.6.3.3.1 figure 6.27 (b)). The highest peak power at 10 kHz was 113 kW. Analysing the spectral content of both pulses, the magnitude of the Raman components, within the amplified pulse of the EVLD02 seed, was higher (see figure 6.17 (c) and (d)). The reason for this higher Raman component generation is because the pulse sharpening effect, due to gain saturation experienced by the seed pulses from the EVLD02 board, was greater compared to seed pulses from the in-house board (see figure 6.13 (d)). This

greater pulse sharpening resulted in amplified pulses having higher peak powers, propagating within the amplifier fibre, and thus generating more Raman.

Figure 6.15 (c) compares the output 1070 nm signal pulse energy with pump power. It should be noted that the output performance for both seed driver boards, with respect to pump power, were found to be very similar. At 50 and 100 kHz repetition rates, the linear response of output pulse energy obtained demonstrates that output was mainly limited by the available pump power. Only slight Raman build up (> 15 dB extinction from 1070 nm peak) can be seen at 50 kHz, with the highest pump power. Whereas at 10 kHz repetition rate, SRS generated Raman components build up, preventing us from obtaining higher output pulse energies. At about 10 W of absorbed pump, the Raman components start to build up significantly and this clamps the maximum output pulse energy of the 1070 nm signal, as any increase in power is transferred into the Raman components. We can see this phenomenon occurring by analysing the 10 kHz plot (denoted by circles and solid line). When the absorbed pump power was increased to ~ 11 W, the build up of Raman clamps the output 1070 nm signal pulse energy. A useful observation was made when a sudden jump in output pulse energy (circled in red in figure 6.15 (c)) was obtained by changing the pumping ratio at the two ends of the active fibre. This changes the pump distribution, and hence the gain distribution, within the fibre. This change delays the occurrence of pulse shaping effects, and hence delays the build up of Raman via SRS to higher pump powers. Slope efficiencies of the 1070 nm output signal for both seed source at 10, 50 and 100 kHz were calculated to be 43%, 56% and 64%.

The total output pulse energy with pump power is shown in figure 6.15 (d). Analysis of the results, presented in this plot, is similar to that in figure 6.15 (c). At 50 and 100 kHz repetition rates, higher pumping power would be required to reach the 0.5 mJ pulse energy objective. At 10 kHz, we found that approximately 13 W of absorbed pump was required to obtain 0.5 mJ pulses having < 40 ns FWHM pulse duration.

The 1070 nm signal gain with pump power of the final stage amplifier is shown in Figure 6.15 (e). The 10 kHz pulses achieved the highest gain, while the 50 and 100 kHz pulses had a similar gain profile. We observed that the gain of the 50 and 100 kHz input pulses started to saturate at pump power levels above 15W. The gain seen by the 10, 50 and 100 kHz seed pulses at ~11 W of absorbed pump power were 16.4, 16 and 16.2 dB respectively. The amplitude jitter performance, at the highest pulse energy for all repetition rates is presented in figure 6.15 (f). The resulting amplitude jitters introduced by the final amplifier were 7, 12.5 and 11.1 % respectively. This was probably due to the noise introduce by the final amplifier which

could be due to a noisy pump source, or the peak wavelength of the signal pulse laying near the slope edge of the final amplifier gain profile. The final amplifier was also expected to be slightly noisy as counter pumping was also used. This means that any propagating noise from the input end would see high amplification near the output end.

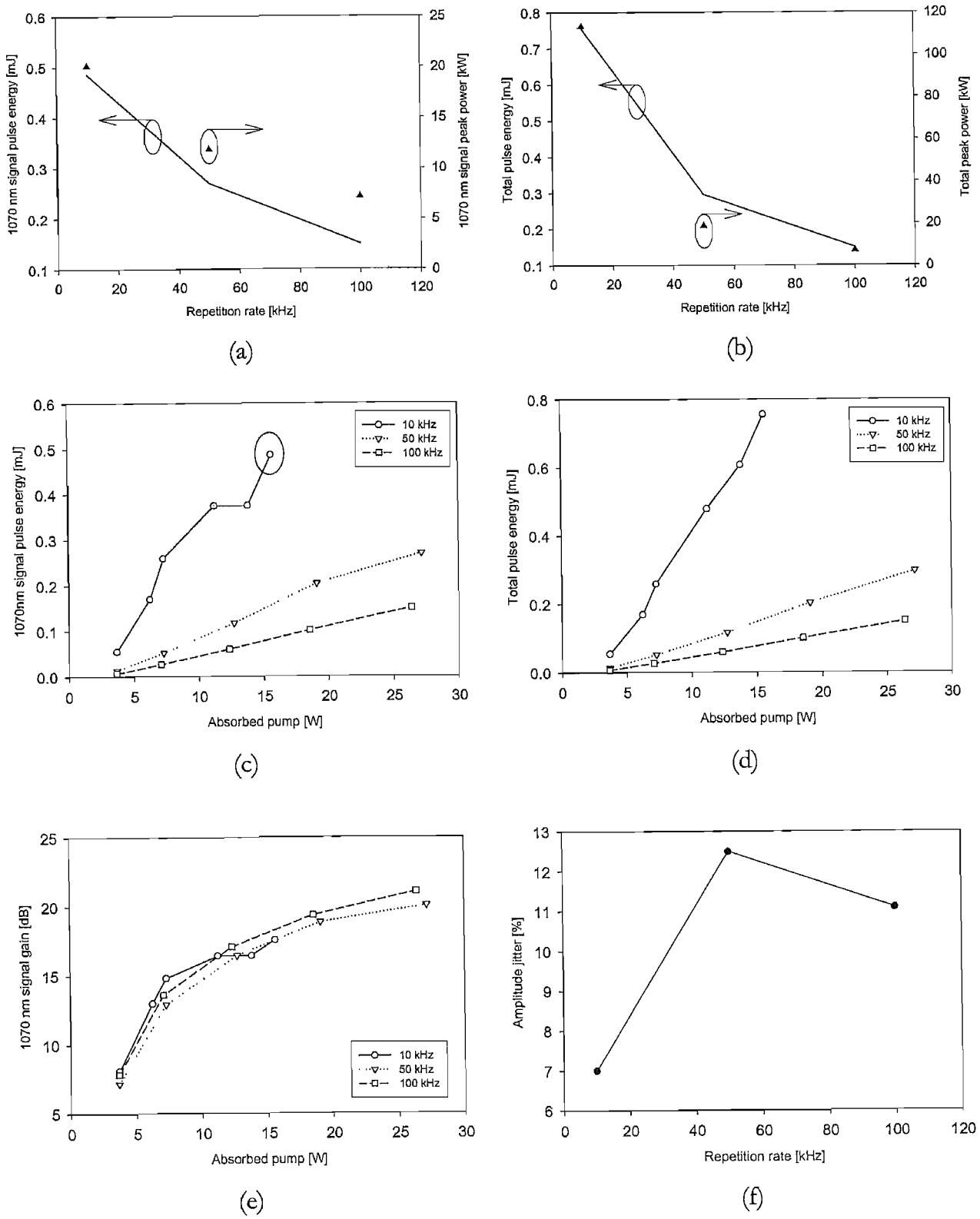

Figure 6.15: Pulse energy, peak power and gain characterisation of amplified 40 ns pulses at 10, 50 and 100 kHz through amplifier cascade for both regimes. Peak power and pulse energy for (a) 1070 nm signal pulse and (b)

total output pulse of entire spectrum. Pulse energy with absorbed pump power (c) 1070 nm signal pulse (10 dB width) and (d) total output pulse of entire spectrum. (e) Gain with absorbed pump power. (f) Amplitude jitter with repetition rate.

6.6.2.2 Output pulse performance

The temporal profile evolution of the output pulses, with total pulse energy (1070 nm + Raman components), from both seed sources from the amplifier cascade, are shown in figure 6.16 (a) and (b). From both figures, we can see that pulse shaping was more evident at the lower repetition rates. Pulse sharpening was starting to occur at ~ 0.2 mJ for all repetition rates. This pulse sharpening effect was again mainly the result of gain saturation.

Figure 6.16 (c) shows how the FWHM pulse width narrows with total output pulse energy for both sources. FWHM pulse widths of the amplified pulses, from the EVLD02 and in-house board, narrowed from 40 ns to ~ 21 ns and ~ 4 ns respectively. Looking at figure 6.16 (a), (b) and (c), we can see that pulse narrowing, due to gain saturation effects, was found to be more apparent with pulses from the EVLD02 board (see figure 6.16 (a)) compared to the in-House board (see figure 6.16 (b)). This can be explained by observing figure 6.13 (d) which shows the input pulses from the GT-Wave pre-amplifier generated by both boards.

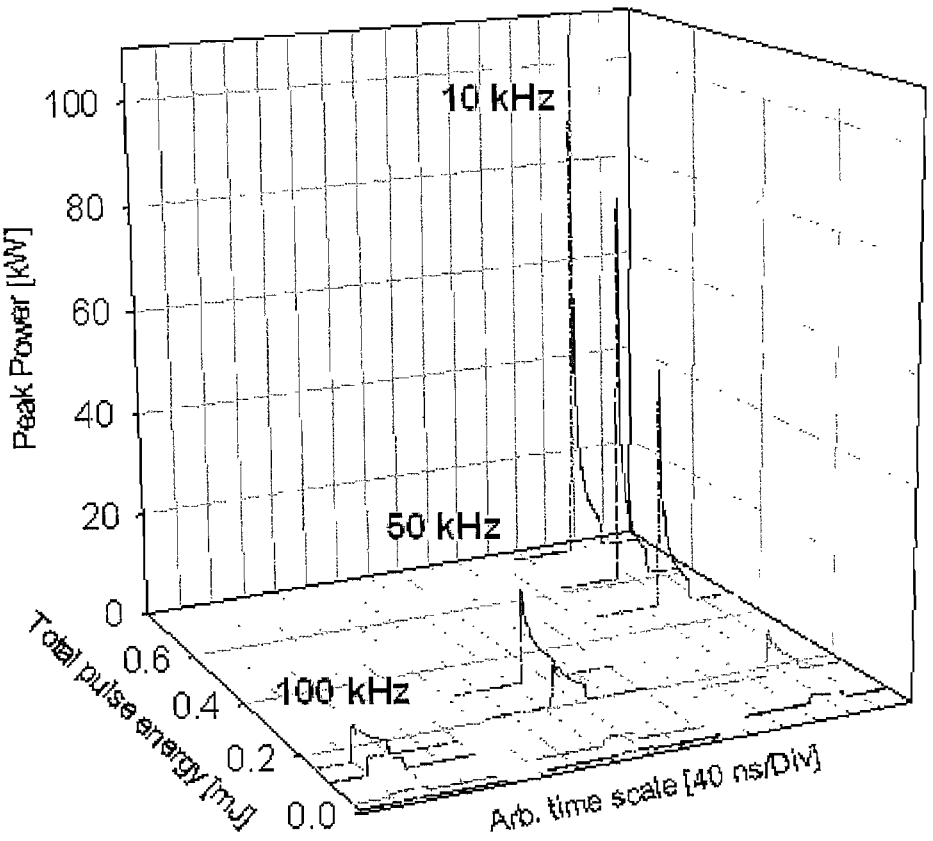
10 kHz
50 kHz
100 kHz
Peak Power [kW]
100
80
60
40
20
0
Total pulse energy [mJ]
0.6
0.4
0.2
0.0
Arb. time scale [40 ns/Div]

(a)

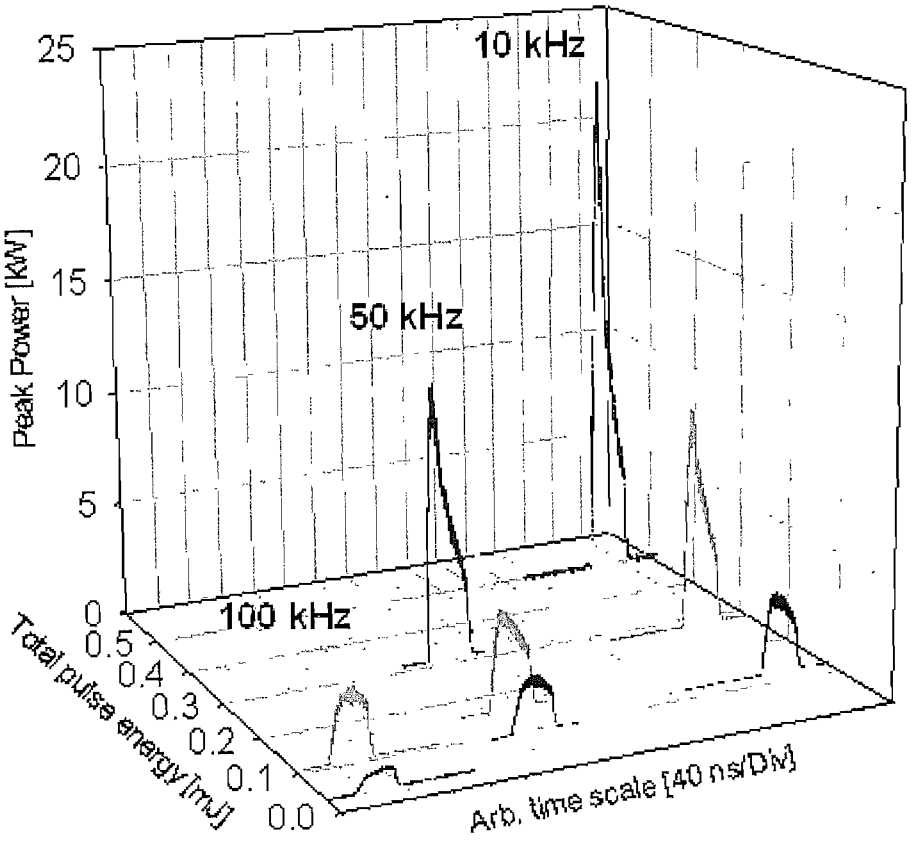
10 kHz
50 kHz
100 kHz
Peak Power [kW]
25
20
15
10
5
0
Total pulse energy [mJ]
0.5
0.4
0.3
0.2
0.1
0.0
Arb. time scale [40 ns/Div]

(b)

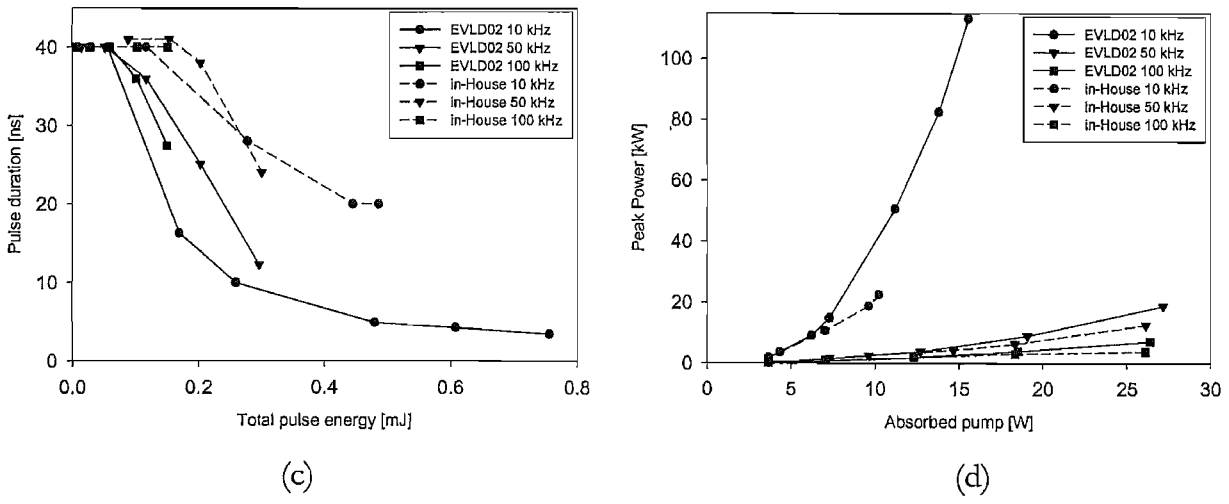

Figure 6.16: Evolution of temporal pulses at 10, 50 and 100 kHz for (a) EVLD02 board, (b) in-house board, (c) FWHM pulse duration with total pulse energy and (d) peak power with absorbed pump.

In a theoretical result, presented by Wang *et al.* [16], it was proposed that pulse distortion due to gain saturation effects could be avoided by shaping the input pulse. Therefore I believe the smaller gain saturation effect for the same output pulse energy, from pulses generated by the in-House board, was because they were less square compared to those generated by the EVLD02 board. The less square pulses from the in-House board resulted in the intensity of the leading edge of the input pulses being lower, hence reducing the amount of gain that was stripped by the leading edge, which enabled the gain to be better distributed across the pulse. Even for the pre-amplified input pulses from the EVLD02 board at the 10 kHz repetition rate, shown in figure 6.13 (d), pulse sharpening effects have already started to occur. The effect of this slight premature pulse sharpening was evident in figure 6.16 (d). At 10 kHz, in figure 6.16 (d), we see that the peak intensity obtained from the EVLD02 seed pulses was approximately twice higher (~ 40 kW) compared to the in-House seed pulses at 11 W absorbed pump power (~ 22 kW).

The output pulse, seen in figure 6.16 (a) with pulse energies > 0.5 mJ, actually consists of both 1070 nm signal pulse and excited pulsed Raman components superimposed on each other. The onset and build up of Raman components can be better observed from the output spectral evolution profile shown in figure 6.17, in the next section.

6.6.2.3 Output spectral performance

The spectral evolution of the amplified output pulses, with their corresponding energy at 10, 50 and 100 kHz repetition rates, are shown in figure 6.17 (a) to (c) respectively. No substantial Raman build up can be seen at both 50 and 100 kHz repetition rates in figures (b) and (c) respectively. However, as observed in figure 6.17 (a), the onset of SRS generated components starts building up, for amplified pulses at 10 kHz, when pulses reach ~ 0.5 mJ. The Raman component continues to rise with increasing pulse energy (i.e pump power) and reached a peak intensity that is ~ 10 dB lower than the 1070 nm signal peak at 0.76 mJ. This dramatic increase in peak powers, (as shown in figure 6.16 (d)) due to gain saturation effects, leads to a considerable increase in Raman components, especially for pulses generated by the EVLD02 board. However with the in-House board, higher pump powers were not tested at that time and, though I believe that the same effects would occur, it was not characterised.

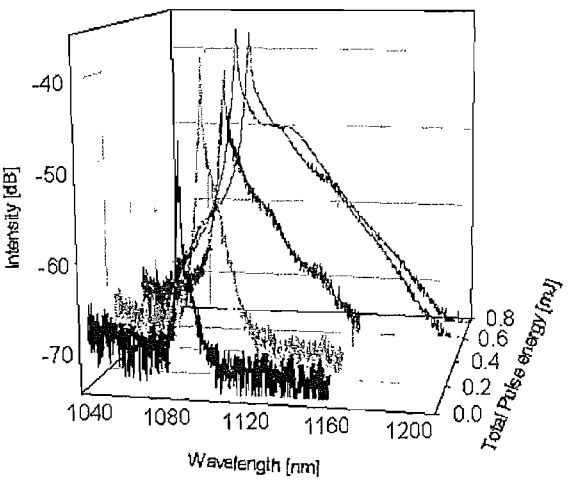

(a)

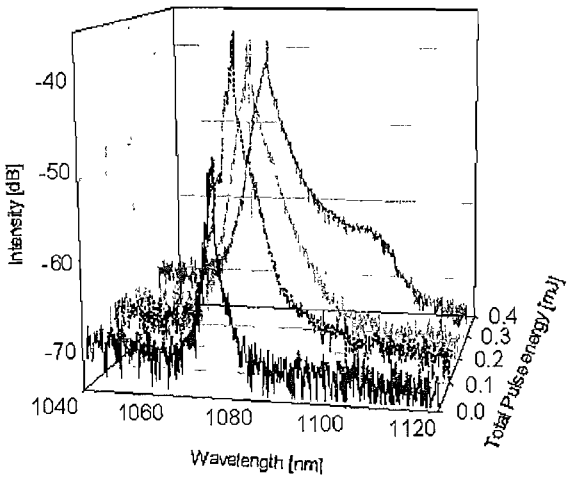

(b)

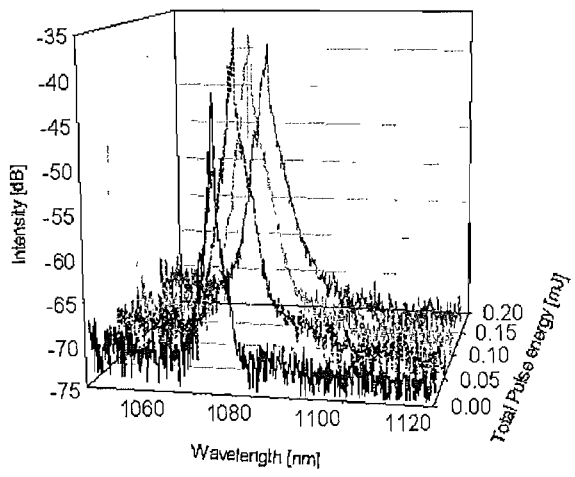

(c)

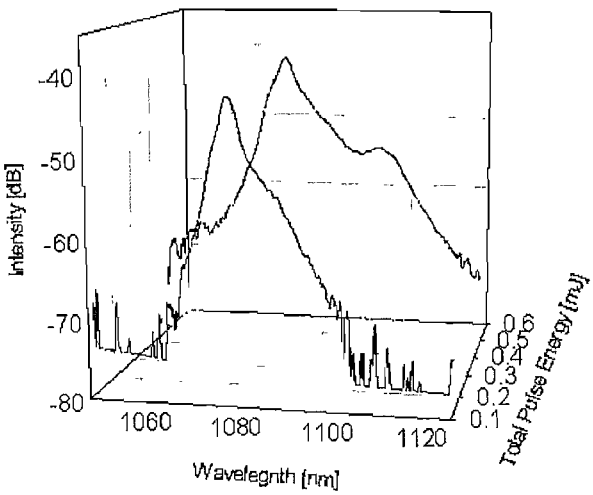

(d)

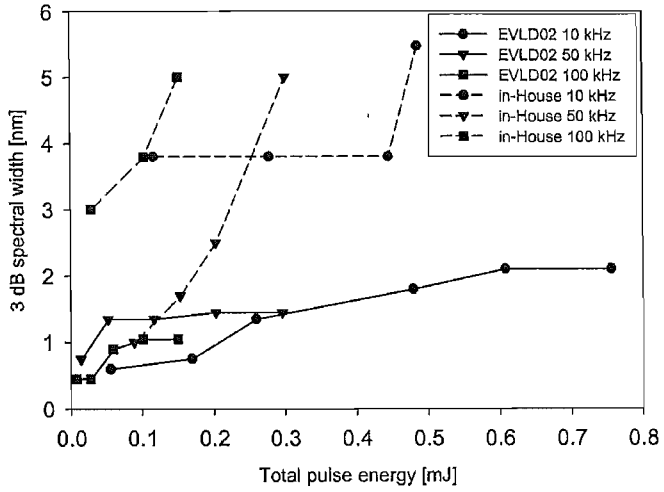

(e)

Figure 6.17: Spectral evolution of amplified 40 ns pulses through amplifier cascade (a) at 10 kHz, (b) 50 kHz and (c) 100 kHz. (d) Spectral evolution at 10 kHz using in-House board and (e) 3 dB FWHM spectral bandwidth with total output pulse energy at various repetition rates for both driver boards.

Figure 6.17 (d) shows the spectral evolution at 10 kHz with increasing total output pulse energy when the in-house driver board was used. Comparing it with figure 6.17 (a), which shows the spectral evolution at 10 kHz when the EVLD02 board was used, the build-up of Raman components occurs at a slower rate with corresponding output energy. The Raman to 1070 nm signal ratio at 0.5 mJ was ~ 2 dB better using the in-House board. Figure 6.17 (e) shows the 3 dB width centred at 1070 nm, with total output pulse energy for the various repetition rates and using both seed sources. The output spectra of the amplified pulses were wider using the in-house board, which was expected since the output seed spectra from the in-House board were originally wider compared to the seed pulses from the EVLD02 board. The widest 3 dB spectral widths were found to be at 10 kHz repetition rate and their widths were 2.1 nm and 5.5 nm for the EVLD02 and in-House board respectively.

6.6.3 *Limitations to achieving mJ pulse energies.*

There were three major limitations we found preventing our objective to attain higher than 0.5 mJ pulses at 10-100 kHz repetition rates. The three limitations are maximum pump power, Stimulated Raman Scattering (SRS) and gain saturation effects. In the next three sub-sections, we will be describing the limitations imposed.

6.6.3.1 *Maximum pump power*

The first limitation was the maximum pump power available while conducting this experiment. Lack of sufficient pump power prevents the achievement of the required average output power to achieve high pulse energies at the highest repetition rates, even where the pulse energies are attainable at lower repetition rates. At the time of these experiments the total available incident pump power was 40.4 W from our 915 and 976 nm pumps. With these, a maximum average power of 15W was obtained, which would correspond, for example, to 0.5mJ pulses being produced at a repetition rate of 30 kHz. However, more powerful (fibreised) diode array pumps do exist, with output powers up to the kW level. Hence maximum pump power is not a critical limitation on the performance of the MOPA system.

6.6.3.2 *Gain Saturation*

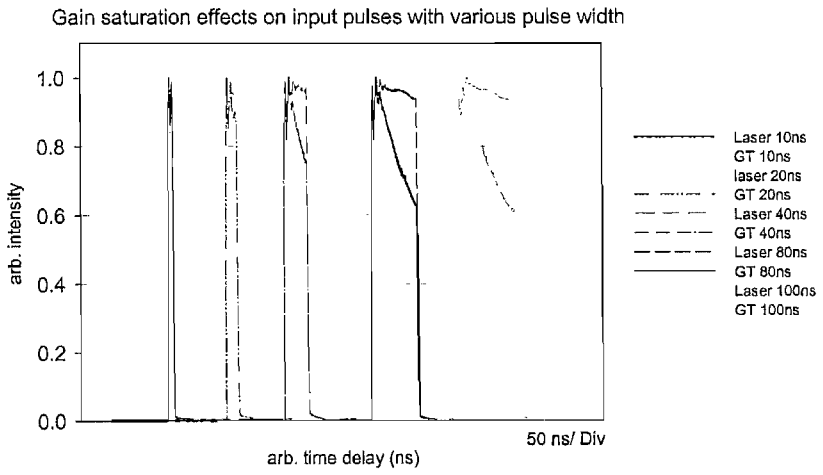

(a)

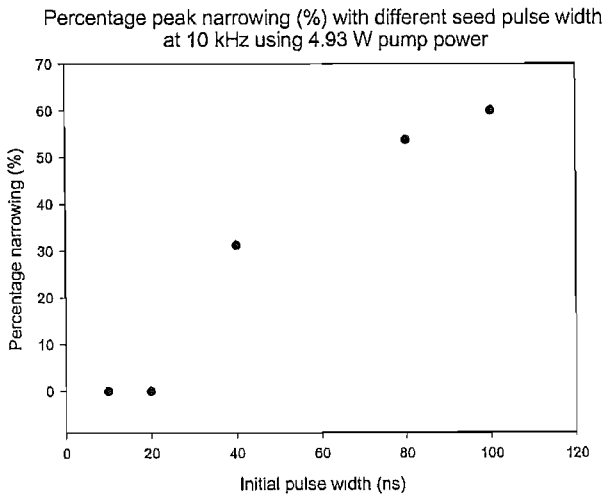

(b)

Figure 6.18: (a) Gain saturation effect on pulses with pulse widths of 10, 20, 40, 80 and 100 ns. (b) Percentage narrowing of pulse peak at the output of GT-wave pre-amplifier, with respect to the input peak width, for various input pulse widths at 10 kHz repetition rate, using 4.93 W of pump power.

The gain saturation effect arises due to the gain of the amplifier being saturated by the leading edge of the input pulse. This distortion to the input super-Gaussian pulse was predicted by theoretical modelling of high power pulse amplification in double-clad fibre amplifiers by Wang *et al.*[16]. As the inversion is depleted by the leading edge, the trailing edge of the pulse experiences lower gain and this results in a triangular pulse shape where the leading edge is higher than the trailing edge. By sharpening the pulse, gain saturation effects can increase the propagating peak intensities thus increasing susceptibility to SRS, and hence reducing the highest achievable output signal (in our case the 1070 nm signal) pulse energies. Using the EVLD02 driver board (because it produces square pulses and so gain saturation was easier to characterise), we shall investigate empirically the gain saturation effects in more detail.

The effect of gain saturation was first observed and characterised at the GT-wave pre-amplification stage with different input pulse widths, at the highest pump power of 4.93 W. Input pulse widths of 10, 20, 40, 80 and 100 ns were launched into the GT-wave amplifier and the results are shown in figure 6.18. It is evident from figure 6.18 (a) that gain saturation distortion increases with increasing pulse widths. If we overlay the GT-Wave amplified pulses together, we find that the gradient and starting point, where gain saturation effects shape the pulse, are identical. Therefore if we cut-off the pulse earlier, then the effects could be less significant. This is illustrated with the 10 ns input pulse, the distortion effects of gain saturation do occur but are minimal with respect to the input pulse (or cut-off prematurely) and do not cause serious distortions to the output pulse shape. However, it becomes more serious at pulse widths above 20 ns. The distortion produces pulses with a triangular shape top.

The amount of narrowing with different input pulse widths is quantified by the percentage change with respect to the input peak width and is shown in figure 6.18 (b). The largest narrowing was seen with a 100 ns input pulse. The FWHM width at the peak of the pulse had narrowed by 60% from the initial width. These sharpening effects [16] on the pulse shape can cause the FWHM of the pulse to decrease below 10 ns at higher output pulse energies.

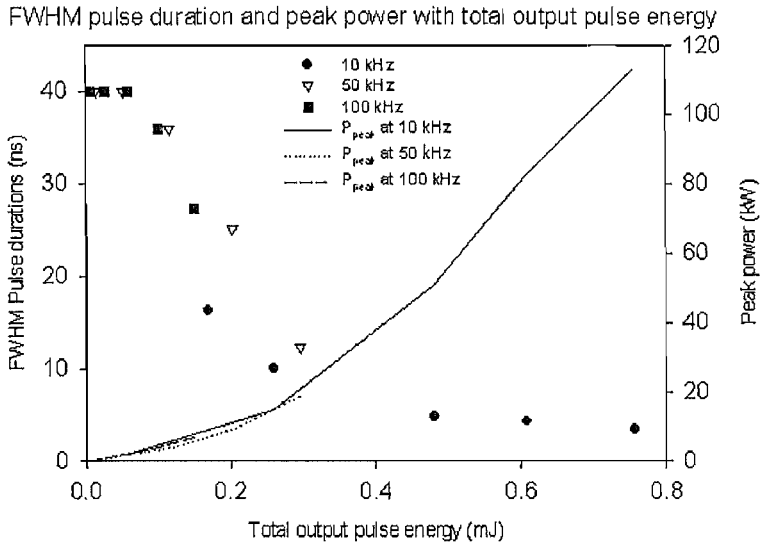

Figure 6.19: FWHM pulse width and peak power with total output pulse energies at different repetition rates utilising seed pulses generated from DEI EVLD02 board.

1070 nm pulses with 40 ns FWHM widths at different repetition rates were injected into the final amplification stage. Figure 6.19 illustrates how the FWHM pulse width and peak power changes with total output pulse energy at different repetition rates. The figure shows the rapid narrowing of the output pulse with increasing pulse energy. We find that the strength of the gain saturation effects is not directly dependent on the pulse repetition rate but on the pulse energy. As a result of this narrowing; very high peak powers are generated and these high peak powers will eventually lead to substantial wavelength conversion via SRS. This is discussed in section 6.6.3.3.1.

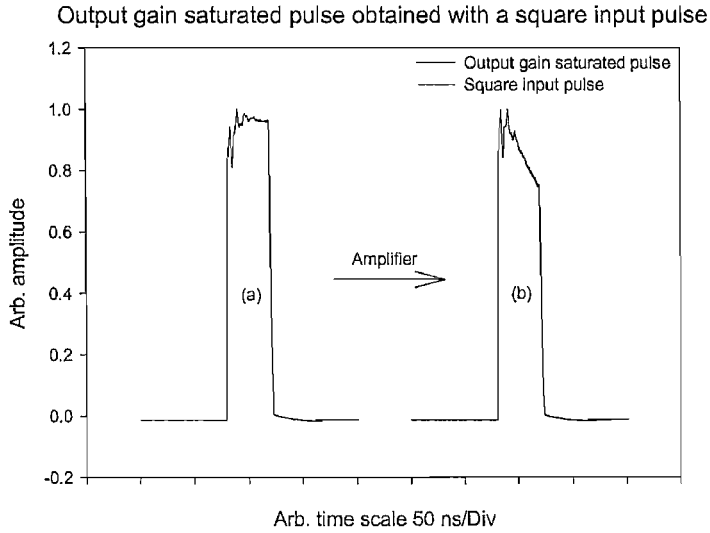

(a)

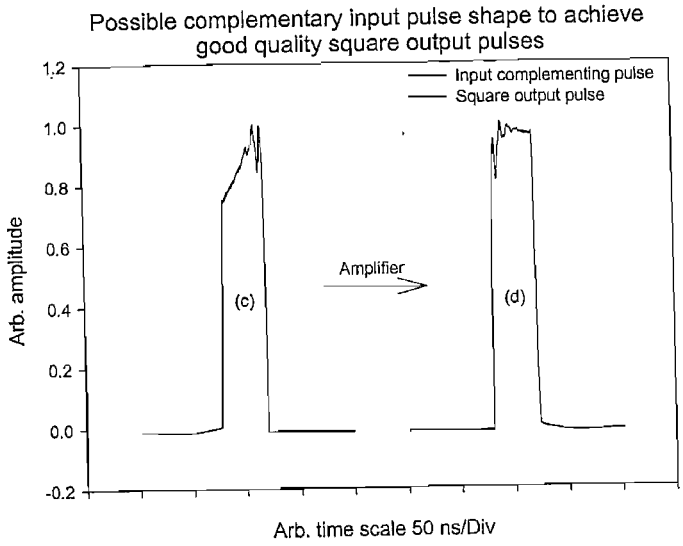

(b)

Figure 6.20: (a) Pulse sharpening effect due to gain saturation and (b) Possible input pulse shaping to obtain good quality square pulses.

Theoretical models utilising amplified two-level rate equations for Ytterbium Doped Double Clad (YDDC) fibre were used by Wang *et al.* [16]. They found theoretically that, under a given pump and signal repetition rate, the distribution of the inverted active ions within the gain medium is mainly determined by the pulse energy rather than the instantaneous power. They found that one way of reducing the effects of gain saturation, to obtain good quality output pulses, is to shape the input pulse. An input pulse shape almost resembling a complement of the output gain saturated pulse shape could be used. This compensates the gain saturation effects caused by the leading edge of the input pulse. This solution is illustrated in figure 6.20.

Figure 6.20 (a) shows the effects of gain saturation on the output pulse after amplification with the current input pulses and figure 6.20 (b) shows the possible complementary input pulse shape that can be used to obtain good quality pulses (after amplification)

Further study of gain saturation effects on arbitrary input pulse shapes were not pursued due to time constraints and availability of equipment to generate arbitrary input pulse shapes. However recently, a group of researchers at Lawrence Livermore Institute investigated output pulse shaping with arbitrary input pulse shapes and the results showed that injecting complementary input pulse shapes to the gain saturated output does compensate the gain saturation effects and produce clean square-shaped pulses (presented at the OSA annual meeting 2004, in Rochester). Though gain saturation limits the maximum pulse energy attainable, this effect could be harnessed to achieve high peak intensities in MOPA systems.

6.6.3.3 Stimulated Raman Scattering (SRS) and Stimulated Brillouin Scattering (SBS)

6.6.3.3.1 Stimulated Raman Scattering (SRS)

SRS effects arise with pulses having high peak intensities propagating in an optical fibre (especially in smaller core fibres with high effective non-linearity). Therefore, Raman effects were expected in the final LMA fibre amplification stage if we were to achieve 10 ns pulses with mJ pulse energies. 10 ns pulses were generated using the in-house driver board and the Raman response of the LMA fibre amplifier was characterised. The Raman threshold for a given fibre with gain is given by equation 6.2 [2] (taken from equation 2.46).

$$P_0^{cr} = \frac{A_{eff}}{g_R . L_{eff}} .16 \qquad (6.2)$$

where P_0^{cr} is the Raman threshold peak power, $g_R = 1 \times 10^{-13}$ m/W is the Raman gain coefficient, A_{eff} is the mode field area of the fundamental mode of the 30 μm core diameter LMA fibre (which is estimated, using Bessel functions with appropriate boundary conditions and refractive index of the perform, to be 351.3 μm^2) and L_{eff} is the effective length given by equation 6.3 for an active fibre

$$L_{eff} = \frac{1}{g}\left[1 - \exp(-gL)\right] \qquad (6.3)$$

where $g = \frac{10}{4.343.L} . \log\left(\frac{Pout}{Pin}\right)$ is the gain per unit length (m) of the fundamental mode of the LMA and L is the total length of the fibre.

Assuming an exponential gain along the LMA fibre and that losses within the LMA fibre are minimal, the empirical gain, measured just before the onset of Raman at different repetition rates, can be used to estimate the actual 1070 nm signal gain of the amplifier for quasi single mode operation. We should also note that Raman threshold is defined as when the Stokes output power is equal to the pump power (in our case, the 1070 nm signal). Hence the

peak power required to observe significant Raman will be lower. Further, taking into account losses due to absorption of the signal into the amplifier, the peak powers that we obtained at the onset of Raman in our experiment are reasonable.

Output pulses	Gain (dB)	Calculated $P_{critical}$ (kW)	Measured Peak power (kW)
13 ns 10 kHz	14.1	31.6	14
9.4 ns 50 kHz	17.3	38.1	11.8
10 ns 100 kHz	19.4	42.2	12.8
20* ns 10 kHz	15.8	35.1	21.3
24* ns 50 kHz	19.4	42.3	12.5
40 ns 100 kHz	19.3	42.1	3.8

* Effective pulse width after pulse shaping from gain saturation effects.

Table 6.3: Shows the calculated critical peak intensity required to reach Raman threshold and experimentally measured output peak intensities at the onset of Raman for different input pulses.

The amplifier gain at different repetition rates, the actual peak powers obtained at the output with no Raman, or just before the onset of Raman, and the corresponding critical peak power required to reach Raman threshold for our 6 m long, 30 μm core diameter, LMA amplifier fibre is shown in table 6.3.

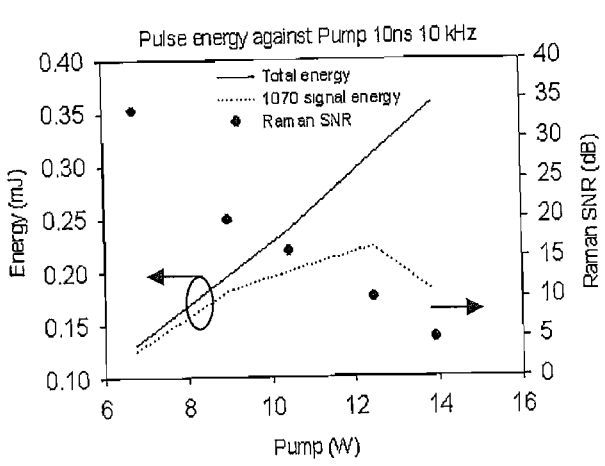

(a)

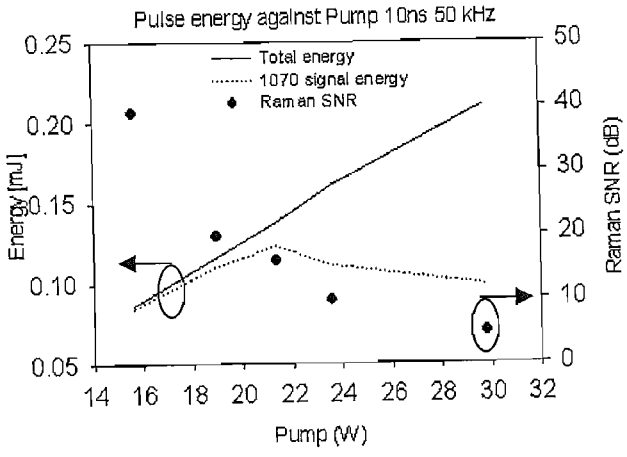

(b)

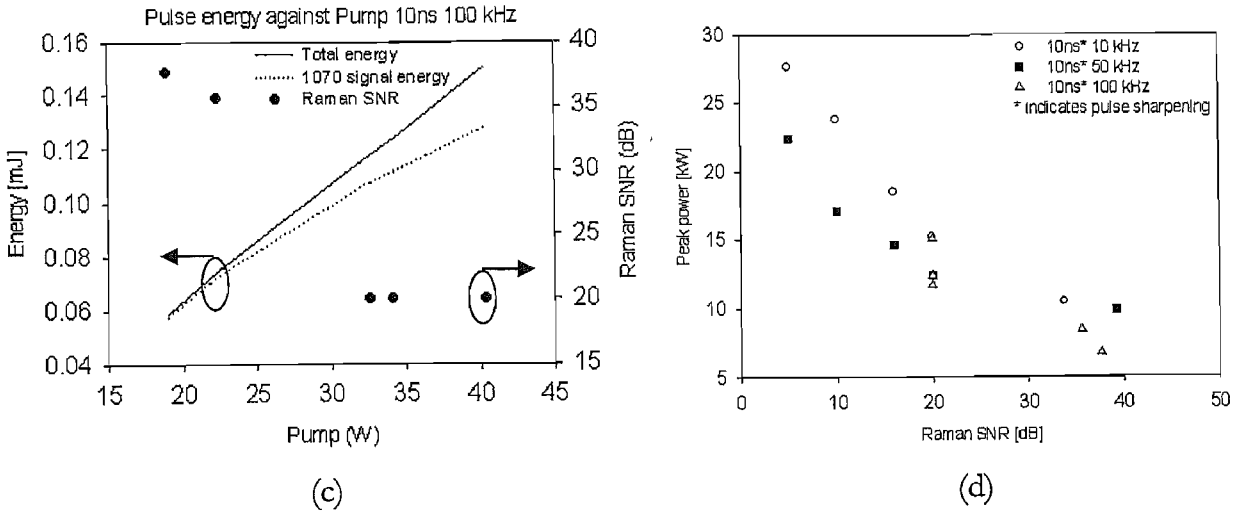

Figure 6.21: Total output and the corresponding signal output power with 10 ns input pulses at (a) 10 kHz, (b) 50 kHz and (c) 100 kHz repetition rates. (d) Illustrates the peak signal intensities and the corresponding signal to Raman component ratio at different repetition rates.

The build up of Raman at the output, with 10 ns input pulses at different repetition rates, was characterised. Figure 6.21 illustrates the increase in the Raman component at the output with increasing pump power.

From the graphs we can see that, at the lower pump powers, the output signal pulse energies centred at 1070 nm increase in parallel with the total output pulse energy measured. The slight difference in energy is due to amplified spontaneous emission (ASE). Upon the onset of Raman (when the peak of the Raman components are ~ 20 dB lower compared to the 1070 nm peak, i.e. Raman SNR ~ 20), the output 1070 nm signal energy starts to level off compared to the total output pulse energy. This is because the 1070 nm signal energy is being transferred to the Raman signal. When the input pump power is further increased, the Raman signal continues to grow and the 1070nm signal shows no increase with pump power and may even decline. Therefore, from graphs (a) – (c), the difference between the total output pulse energy and 1070 nm signal energy would be mainly due to transfer of energy to the Raman components.

The effects of Raman are more evident at the 10 and 50 kHz repetition rates. Graphs 6.21 (a) and (b), show that when the Raman SNR extinction ratio (which we define as as the ratio between the 1070 nm signal peak and the peak of the generated Raman components) reached ~ 10 dB, the 1070 nm signal energy started to decrease slightly with increasing pump power, thus clamping the highest output 1070 nm signal energy at 0.23 mJ and 0.12 mJ for 10 and 50 kHz pulse trains respectively. I observed from the spectra obtained, that the spectral bandwidth of conversion to the longer wavelengths via SRS was very broad (especially at 10

kHz repetition rate). This caused difficulty in separating the actual signal pulse spectra with the generated Raman components and hence created the discrepancies observed between the Raman peak OSNR and the energy differences between the total pulse energy and 1070 nm signal. Using the Raman peak intensity, to estimate the power ratio between the two, is not exact because of the power contained at the adjacent converted wavelengths. But it does gives us an idea of the trend and a rough estimate of the power distribution which was the intention of the figure 6.21. Figure 6.21 (c) shows that at 100 kHz, only minimal SRS occurs at the highest pump power of 32 W. There were no substantial SRS generated components and the output 1070 nm signal pulse energy levels off slightly. At this repetition rate, highest 1070 nm signal output energy was not clamped by SRS but limited by available pump power.

Figure 6.21 (d) shows the corresponding peak powers of the output pulses estimated to have different amounts of SRS generated components. From the graph, we can see that the peak intensity slope increases when the Raman SNR reaches ~ 20 dB. This was consistent with our observation that the Raman pulse components contribute to the steepening of the output temporal pulse profile, hence increasing its effective peak intensity. The highest output peak intensity measured (including the Raman component) was 27.7 kW, at 10 kHz, but the Raman SNR was only 5 dB.

Further characterisation of SRS effects was carried using 40 ns, 10 kHz, pulses generated from the EVLD02 board. A gold coated bulk reflection grating was used to filter-off the converted longer wavelength components to study the temporal evolution of the 1070nm and Stokes-shifted outputs separately.

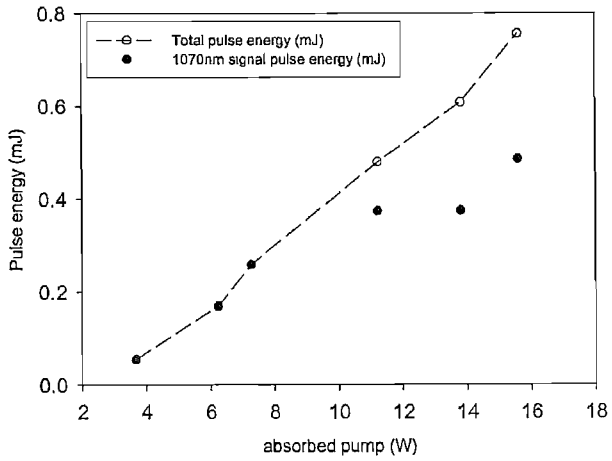

(a)

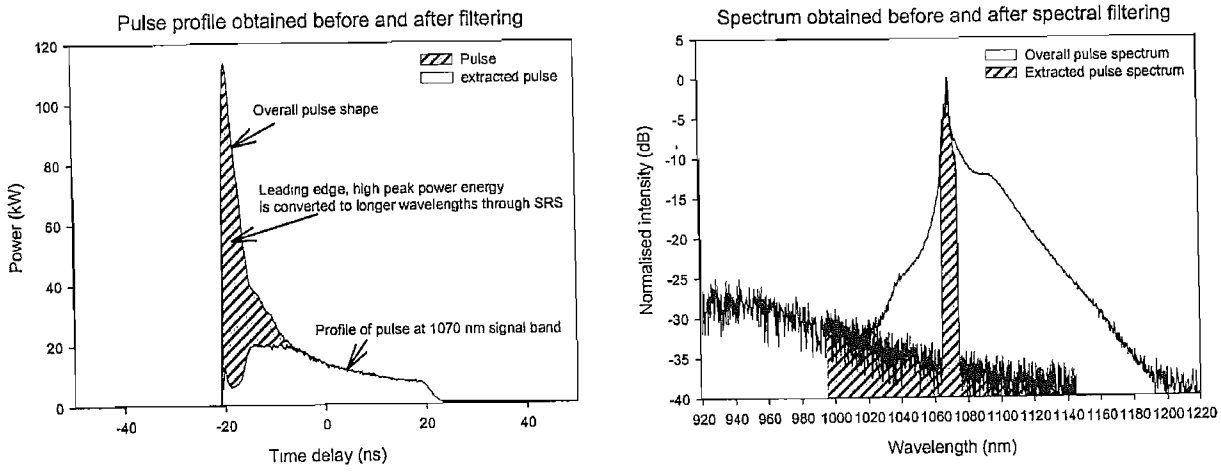

Figure 6.22: (a) Total output pulse energy and energy at signal band with 40 ns 10 kHz pulses, (b) and (c) Temporal and spectral profile of output pulse before and after filtering.

Figure 6.22 (a) compares the total output pulse energy measured (signal energy + SRS wavelength converted energy) with the extracted energy in the signal band obtained through our experiments. We can see that the signal energy is clamped at approximately 0.45 mJ with increasing pump power. A major portion of the difference in energy, between the total and signal energy, would be lost to the converted longer wavelength components via SRS. The clamped signal energy corresponds to ~ 20 kW of peak power obtained from the extracted temporal profile and pulse energy. The distribution of power between the SRS and signal component within the temporal pulse at 0.76 mJ can be seen in figure 6.22 (b). The shaded region depicts the power within the SRS band and the white region depicts the power within the signal. The maximum overall peak power, achieved at the highest pump power, was 113 kW. The small spike at the front of the extracted pulse was probably the initial leading edge spike of the original propagating pulse, before substantial SRS. After which it was stripped of its power to feed the SRS generated components as it propagates further down the amplifier. Figure 6.22 (c) shows that the 1070 nm portion was cleanly filtered to separate the signal and SRS components for analysis. The calculated extracted fraction of the pulse energy in the extracted spectral region was ~ 52%.

6.6.3.3.2 Stimulated Brillouin Scattering (SBS)

The SBS phenomenon is described in more detail in chapter 2 (see section 2.2.3.4). In this section, we present that the backscatter spectrum from the LMA amplifier was characterised and that it indicated no sign of SBS. Since SBS is a backward reflection due to a 'grating' effect,

as a result of the acoustic shock wave that co propagates with the input signal, the coherence of the input signal is critical for SBS generation. However, the linewidth of the directly modulated nanosecond laser is much broader than the narrow linewidth (< 35 MHz for 1070 nm pump signal) required for SBS, and it was expected that no sign of SBS would be detected [17]. As the 'grating' effect is moving at the speed of sound in silica, the wavelength of the Brillouin gain peak is downshifted from the peak signal wavelength at 1070 nm by 11.25 GHz. Hence the Brillouin backscattered signal should peak at ~1070.5nm. This is within the bandwidth of the input signal so will not be spectrally distinguishable from back reflections.

The threshold peak power to generate a SBS Stokes wave is given by equation 6.4 [17] (taken from equation 2.55).

$$P_0^{cr} = \frac{A_{eff}}{g_B . L_{eff}} .21.(1 + \frac{\Delta\nu_p}{\Delta\nu_B}) \qquad (6.4)$$

where $g_B = 5 \times 10^{-11} m/W$ which is the Brillouin peak gain coefficient, $\Delta\nu_p$ is the line width of the signal, $\Delta\nu_B$ = 35 MHz is the Brillouin gain line width for a 1070 nm pump signal, A_{eff} is the effective mode area of the LMA fibre and L_{eff} is the effective length of the LMA fibre which is defined in equation 6.3.

We take the 10 ns, 10 kHz, input pulse as an example; the maximum gain of the LMA fibre is 15 dB which gives a corresponding effective length of 1.69m (assuming exponential gain decay in the LMA fibre) and the effective mode area of the fundamental mode is 351 μm^2. Assuming a 3 dB signal bandwidth of ~ 3 nm at 1070 nm, which corresponds to $\Delta\nu_p$ = 78.45 GHz. The critical peak power to reach the SBS threshold will increase by a factor of $(1 + \frac{\Delta\nu_p}{\Delta\nu_B}) =$ 22419. The calculated critical peak power required for SBS threshold would be 1.96 MW.

Output pulses	Gain (dB)	Calculated $P_{critical}$ (MW)	Measured Peak power (kW)
13 ns 10 kHz	14.1	1.96	14
10 ns 100 kHz	19.4	2.5	12.8
20* ns 10 kHz	15.8	2	21.3
40 ns 100 kHz	19.3	2.5	3.8

* Effective pulse width after pulse shaping from gain saturation effects.

Table 6.4: Shows the calculated critical peak intensity required to reach SBS threshold and the experimentally measured output peak intensities for different input pulses.

Table 6.4 above shows the calculated SBS threshold with the experimentally measured peak intensities of the pulses propagating within the LMA fibre. We calculated that for such a wide bandwidth (FWHM ~ 3 nm) signal, it would require peak intensities in the MW regime for SBS to occur; hence it is unlikely that we would see SBS in our experiment.

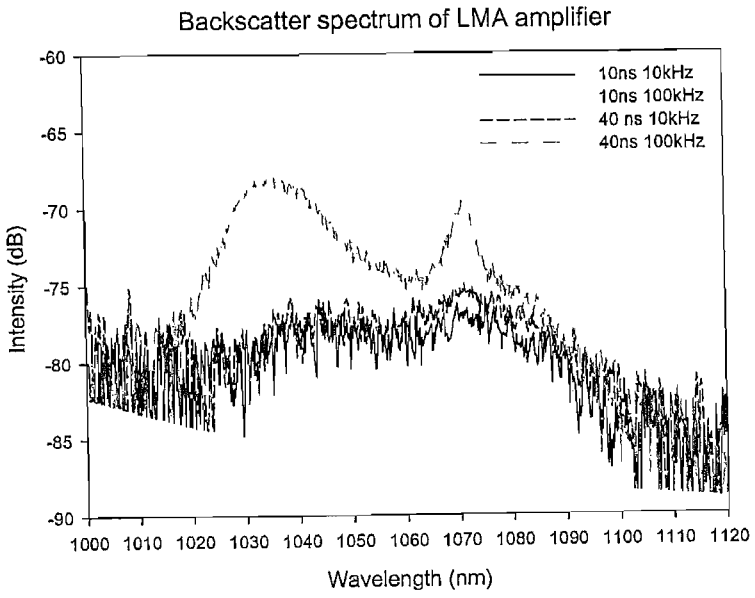

Figure 6.23: Backscatter spectrum of 30μm LMA amplifier at highest output peak power with different input pulses.

Spectra of the backscattered radiation are taken at 10 kHz and 100 kHz repetition rates, for 10 and 40 ns input pulses, using the in-House driver board, the spectra are shown in figure 6.23. From the backscattered spectrum, we see some signal peaking at 1070 nm. However,

from the theoretical calculations we made above, we concluded that this signal was not due to SBS but to backward reflections

6.7 Conclusions

I have demonstrated a nanosecond pulse MOPA system using a directly modulated laser diode operating at ~ 1 μm. The diode produced up to ~400mW peak powers with pulse durations in the range 10-100 ns and 0.4% amplitude jitter. As an example, the above values yield a pulse energy of ~16 nJ for a 40ns duration pulse.

Two different initial amplification stages were tested and characterised. A 4m core-pumped, SM, Yb^{3+} doped fibre amplifier and a 6m cladding pumped, SM, GT-Wave amplifier. Pulse amplification performances of both amplifiers were found to be similar to their c.w. amplification performance which meant that the amplifier parameters and experimental conditions were optimised. Gain for input signal powers between 0.1 – 1 mW, obtained from the GT-wave and core-pumped amplifier, were between 24-36 dB and 16-24 dB respectively. The results show that neither amplifier would give us enough gain to obtain 0.5 mJ pulses hence we estimate that one more amplification stage is required. However the choice of pre-amplifier for the amplifier cascade would be the GT-wave amplifier.

At this pre-amplification stage, we identified that the target pulse energy of 0.5 mJ would be difficult to achieve at repetition rates of 50 kHz and above, if only one more amplification stage was used. This conclusion was based on the assumption that the final LMA amplification stage would only give ~ 20 dB of gain (which was usual). This conclusion was proven to be right as we were only able to achieve the 0.5 mJ target at repetition rates < 30 kHz.

An end-pumped, LMA based, power amplification stage was implemented for the final amplification stage. The 6 m long LMA fibre had core dimensions of 30 μm with a diffraction limited output beam quality. The highest output peak power, total pulse energy (1070 nm signal and Raman components) and 1070 nm signal pulse energy at 10, 50 and 100 kHz, from the final amplifier, are shown in table 6.5. The amplitude stability and 1070 nm signal to Raman peak ratio (Raman SNR) performance of the output were 7% and 13 dB respectively.

The highest output pulse energy at 10 kHz repetition rate, produced output energies of 0.76 mJ and 0.49 mJ for the total pulse energy (includes both 1070 nm signal and Raman components) and the 1070 nm signal pulse energy respectively. The initial FWHM pulse

duration launched into the amplifier was ~40 ns and the corresponding amplified pulse after re-shaping was ~ 10 ns. This resulted in the rapid increase in its peak power to 113 kW.

Repetition Frequency [kHz]	1070 nm Signal Pulse energy (mJ)	Total pulse energy (mJ)	Peak Power (kW)
10	0.49	0.76	113
50	0.27	0.3	19
100	0.15	0.15	7.2

Table 6.5: Output pulse energies and peak power obtained from the final amplifier at 10, 50 and 100 kHz repetition rate using 40 ns input pulses.

The target 0.5 mJ pulse energy (at 1070nm) was only demonstrated at the lowest 10 kHz repetition rate for 40ns input pulses. Limited maximum available pump power prevented us from scaling the 0.5 mJ result to the 100 kHz repetition rate, but this does not present any fundamental limit to performance. I believe that it would be possible to achieve total output pulse energies of 0.5 mJ up to ~ 30 kHz with the available pump power we have, but this was not attempted at the time.

Maximum achievable pulse energy at 1070nm is limited in this system by the onset of SRS, which shifts pulse energy to longer wavelengths. For some applications, where wavelength is not significant (e.g. machining), this may be acceptable, but in many cases the onset of Raman limits the useful pulse energy. SRS is further generated pre-maturely as a consequence of gain saturation effects shaping the amplified pulse. Gain saturation effects, which change the shape of the square input pulses such that the pulse sharpens as it propagates along the amplifier, are also observed. These result in output pulses which are distorted and significantly shorter (measured by FWHM duration) than the input pulses. The resulting increase in peak power of the propagating pulse reduces the threshold for non-linear effects such as SRS.

A possible avenue of further work is to modify the shape of the injected pulses [16] using a lower intensity leading edge to compensate for gain saturation effects, hence producing square output pulses. Modifying the pulse shape would be a relatively straightforward procedure, experimentally, with a directly driven diode. Alternatively, if the fundamental requirement of a system is maximum peak power, rather than maximum pulse energy, gain saturation could be

harnessed to generate very short output pulses with very high peak powers within all-fibre MOPA systems for industrial applications such as machining or ablation.

Several methods could be used to reduce or eliminate SRS. The length of the amplifier fibre could be shortened, larger core dimensions could be used, pulse shaping of the input pulse could reduce the effects of pulse sharpening, and modifying the gain profile within the amplifier fibre could reduce the effective length.

As shown in section 6.6.3.3.1, the SRS generated components lie at the sharp leading edge of the pulse. Hence the Raman pulse is of much shorter duration and higher peak intensity than the 1070nm output pulse. This could be utilised (perhaps in conjunction with amplifying the gain saturation effects) to generate short duration, high peak power, pulses at wavelengths longer than 1070nm.

In conclusion, I demonstrated, characterised and optimised a nanosecond pulse MOPA system which consists of a directly modulated seed laser diode, GT-wave fibre pre-amplifier and a 30 μm core LMA fibre power amplifier. This MOPA system is capable of delivering stable 10 ns, 0.76 mJ (total output pulse energy), pulses at 10 kHz repetition rate with peak powers up to 113 kW. Limitations to achieving higher output pulse energies were studied in detail and possible further work to overcome these limitations was proposed.

REFERENCES

1. Di Teodoro, F., Koplow, J.P., Moore, S.W. and Kliner, D.A.V., *Diffraction-limited, 300-kW peak-power pulses from a coiled multimode fiber amplifier.* Optics Letters, 2002. **27**(7): p. 518-520.
2. Galvanauskas, A., *Mode-scalable fiber-based chirped pulse amplification systems.* IEEE Journal Of Selected Topics In Quantum Electronics, 2001. **7**(4): p. 504-517.
3. Gapontsev, V.P.; Fomin, V.V. and Samartsev, I.E. *25 kW peak power, wide tuneable-repetition-rate and pulse duration eye-safe MOPFA laser.* in *Conference on Lasers and Electro-Optics, CLEO - Technical Digest.* 1996. Pacific Rim. p. 209-210.
4. Goldberg, L., Koplow, J.P. and Kliner, D.A.V., *Highly efficient 4-W Yb-doped fiber amplifier pumped by a broad-stripe laser diode.* Optics Letters, 1999. **24**(10): p. 673-675.
5. Limpert, J., Hoffer, S., Liem, A., Zellmer, H., Tunnermann, A., Knoke, S., Voelckel, H., *100-W average-powerg high-energy nanosecond fiber amplifier.* Applied Physics B-Lasers And Optics, 2002. **75**(4-5): p. 477-479.
6. Limpert, J., Liem, A., Schreiber, T., Zellmer, H., Tunnermann, A., *Power and energy scaling of fiber laser systems based on ytterbium- doped large-mode-area fibers,* in *Proceedings of SPIE: Advances In Fiber Lasers.* 2003. **4974**: p. 135-147.
7. Limpert, J. and Liem, A.Z., H.; Tunnermann, A.;Knoke, S.; Voelckel, H. *High-average-power millijoule fiber amplifier system. Proceedings Conference on Lasers and Electro-Optics, CLEO.* 2002. 1(**1**): p. 591-2.
8. Nilsson, J., Paschotta, R., Caplen, J.E. and Hanna, D.C., *Yb^{3+}-ring-doped fiber for high-energy pulse amplification.* Optics Letters, 1997. **22**(14): p. 1092-1094.
9. Sousa, J.M., Nilsson, J., Renaud, C.C., Alvarez-Chavez, J.A., Grudinin, A. B. Minelly, J. D., *Broad-band diode-pumped ytterbium-doped fiber amplifier with 34-dBm output power.* IEEE Photonics Technology Letters, 1999. **11**(1): p. 39-41.
10. Chen, M.-Y., Chang, Y.-C, Galvanauskas, A., Mamidipudi, P., Changkakoti, R., Gatchell, P., *27-mJ nanosecond pulses in M^2 = 6.5 beam from a coiled highly multimode Yb-doped fiber amplifier. Conference on Lasers and Electro-Optics, CLEO.* 2004. San Francisco, CTuS4. **1**(1): p.3.
11. Lau, K.Y., *Gain Switching of Semiconductor Injection-Lasers.* Applied Physics Letters, 1988. **52**(4): p. 257-259.
12. Yla-Jarkko, K.H., Alam, S.-U., Turner, P.W., Moore, J., Nilsson, J., Selvas, R., Soh, D.B.S., Codemard, C., Sahu, J.K.. *Cladding pumping technology for next generation of fiber amplifiers and lasers. OAA. 6-9 Jul 2003.* 2003. Otaru. *TuC1 (Invited).*
13. Yla-Jarkko, K.H., Codemard, C., Singleton, J., Turner, P.W., Godfrey, I., Alam, S. U., Nilsson, J., Sahu, J. K., Grudinin, A. B., *Low-noise intelligent cladding-pumped L-band EDFA.* IEEE Photonics Technology Letters, 2003. **15**(7): p. 909-911.
14. Nilsson, J., Alam, S.U., Alvarez-Chavez, J.A., Turner, P.W., Clarkson, W. A., Grudinin, A. B., *High-power and tunable operation of erbium-ytterbium co-doped cladding-pumped fiber lasers.* IEEE Journal Of Quantum Electronics, 2003. **39**(8): p. 987-994.
15. Nilsson, J., Sahu, J.K., Jeong, Y., Clarkson, W.A., *et al., High power fiber lasers: New developments,* in *Proceedings of SPIE: Advances in Fiber Lasers.* 2003. **4974**: p. 50-59.
16. Wang, Y. and Po, H., *Dynamic characteristics of double-clad fiber amplifiers for high-power pulse amplification.* Journal Of Lightwave Technology, 2003. **21**(10): p. 2262-2270.
17. Agrawal, G.P., *Nonlinear Fiber Optics.* 3rd Edition ed. 2001, San Diego: Academic Press.

Chapter 7

GAIN SWITCHED LASER DIODE

7.1 Introduction

The availability of a convenient and simple picosecond pulse source in the 1.06μm regime will be very attractive for the development of high power, ultrashort pulse, systems suited for applications which I have already mentioned in chapters 1 and 5.

At the moment, mode-locking is the most common method for generating picosecond pulses in the market. Mode-locked fibre lasers [1-7], harmonically mode-locked fibre lasers [8-11] and external cavity mode-locked semiconductor lasers [12-14] have been widely used to generate ultrashort pulses. In these laser systems, pulses are shaped through non-linear effects such as soliton type propagation and non-linear polarisation evolution via an optical Kerr gate.

High power pulses, with durations ranging between 36 fs to tens of ps, can be produced from mode-locked fibre lasers. Mode-locked fibre lasers are the most commonly used picosecond source due to their simplicity and ease of implementation. However a disadvantage of this approach is that the repetition rate is fixed by the cavity length and therefore not continuously tunable without changing the optical path length.

Higher repetition rates can be achieved through the harmonic mode-locking technique [8-11]. Higher repetition rates are achieved through either passive or active modulation to synchronise the mode-locked cavity to the required repetition rate. Repetition frequencies from the sub GHz to the GHz range with 100 fs to 10 ps pulses can be produced by harmonically mode-locked fibre laser systems. The highest reported repetition frequency range, between 80-200 GHz in an Erbium doped fibre laser, have been achieved with harmonic mode-locking by Yoshida E *et al.* [8]. However, like all mode locking techniques, this is still a resonant technique. Therefore the tunability of the repetition rate is limited to an integer of the fundamental cavity repetition rate and the control of super mode noise can be very difficult. The effect of this super mode noise is the failure of harmonically mode-locked lasers to produce a stable, equal amplitude, pulse train over an extended period of time. Furthermore, like all mode-locking techniques using free space optics, careful alignment of cavity components is required. Another disadvantage is that it requires both complex electronic and RF components.

The external cavity mode-locking scheme uses a semiconductor laser diode that is driven with electrical sinusoidal signals together with an external cavity to achieve mode-locking. The external cavity length, which corresponds to the repetition rate, determines the frequency of the driving electrical sinusoids. Mode-locking is initiated by the back facet of the semiconductor diode which has been changed into a saturable absorber. As with mode-locked fibre lasers, active cavity length control is required to adjust the repetition rate and optimise the timing jitter.

Furthermore, with all mode-locking schemes, they tend to require long lengths of optical fiber to achieve the required nonlinear interactions. This makes them prone to length variations which results in timing jitter. Active cavity length control can be deployed to eradicate these problems and also to manipulate repetition rates, but it requires more complex setups and is susceptible to long term laser mode-locking instability.

Gain switched laser diodes present an attractive solution to most of the problems highlighted above. Like any commercial product, the simplicity, cost, reliability, ergonomics and ease of integration are important factors. Gain switched laser diodes can satisfy these criteria. Furthermore gain switched lasers are not matched to the cavity and it is a non resonant technique, making their repetition rate flexible. The quality of the output train of pulses for gain switched lasers can also be maintained over an extended period of time. It has been demonstrated, through linear and non-linear compression schemes, that sub-picosecond pulses can be produced [15-17] making it attractive for the applications mentioned above.

However as far as we know, gain switching of laser diodes operating at 1.06 μm had never been carried out. The electronics circuitry for driving the laser diode to generate gain switched pulses had to be designed and built. Characterisation of the gain switched pulses had to be made and compression technology, used for gain switch systems in the telecoms market, cannot be implemented because the dispersion properties of silica optical fibers at 1.55 μm and 1.06 μm are different. The amplification cascade has to be designed and constructed to achieve higher output powers.

The development, characterisation and compression of 1.06 μm gain switched pulses from a high speed laser diode were carried out. These gain switched pulses were subsequently used to seed a MOPA system that was constructed to produce high power picosecond pulses at 1.06 μm wavelength.

In this chapter, I will discuss my work on applying gain switching of diodes operating at 1.06 μm and describe amplified systems that I have built using these sources. I believe that these are the first results ever reported for such gain switched systems. I begin this chapter by

discussing some principles and the motivation behind the gain switching of semiconductor laser diodes, to give the reader a better understanding of the technique. I will later describe the design, characteristics and performance of the gain switched system I have developed.

7.2 Background of Gain switching

Demands for bandwidth in communications systems led to the development of high capacity communications systems based on Optical Time Division Multiplexing (OTDM). These systems, operating at Terabit data rates, require picosecond or sub-picosecond pulse sources [18]. Gain switching was a very attractive way to generate ultrashort pulse sources for these communications systems because of its simplicity, convenience and low cost. Therefore, for this reason, and also the availability of high speed diodes, work on the gain-switching of semiconductor laser diodes has been concentrated at the 1.5 μm telecoms wavelength [19-23]. However recently, semiconductor laser diodes operating at the 1 μm wavelength which can be directly modulated at high speeds became available thus raising the possibility of gain-switching semiconductor laser diodes radiating at 1.06 μm.

7.3 Gain Switched Laser Diode

7.3.1 *Principle of gain switching*

The gain-switching of semiconductor laser diodes [24-26] is a simple method to produce picosecond pulses with a continuously tunable repetition rate. This technique was first presented by Ito *et al.* [26]. They showed that, by injecting the semiconductor laser with short electrical pulses, optical pulses much shorter than the electrical pulse durations could be generated.

In gain switching, the laser is biased just below threshold and a modulation current is superimposed on the continuous drive current. The modulation current can be a train of short electrical pulses or a large amplitude sinusoidal electrical signal. The idea is to catch the first spike of a series of optical relaxation oscillations generated upon the onset of the electrical pulse. If the electrical pulse is terminated before the rise of the second peak of the relaxation oscillation, an optical pulse much shorter than the driving electrical pulse can be produced. Figure 7.1 illustrates this principle. The limitation on the duration of the pulses that can be

achieved is imposed by the difficulty in sustaining a large initial inversion before optical emission is caused by gain compression and spontaneous emission.

The manifestation of relaxation oscillation can be explained in this way. At the onset of the electrical pulse, the carrier density inside the active region of the diode rapidly increases. Before reaching lasing threshold, the photon density remains close to zero. At threshold, the photon density rises quickly, via stimulated emission, while rapidly decreasing the carrier density. When the carrier density is depleted, emission also stops. The result of the interaction, between the carrier and photon density, is a photon emission transient response having an initial ringing that will reach a steady state if the drive current is a constant current source above threshold. This initial ringing response is called relaxation oscillation. In gain switching, the drive current is terminated before the onset of the second optical spike. This results in the carrier density dropping to below threshold after the first optical spike and the generated photons are emitted as a short optical pulse.

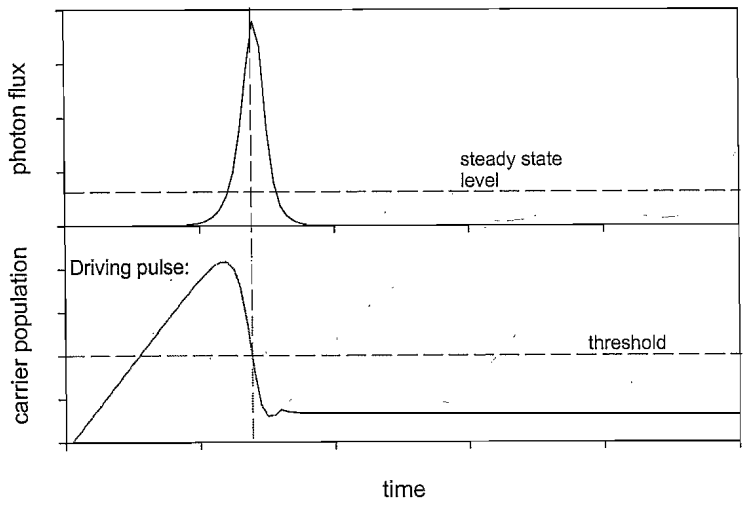

Figure 7.1: Diagram showing the principle of gain-switching.

7.3.2 *Gain-switch setup*

Figure 7.2 (a) shows the gain switched setup that was used for my experiments. The FP semiconductor laser used was a 1047.9nm InGaAsP device, with a threshold current of 34 mA at 1.06 μm, a modulation bandwidth much greater than 1.35 GHz and a longitudinal mode spacing of 0.2 nm. The diode is mounted in a butterfly mount on a home made PCB circuit board. The schematic of the PCB board is shown in the magnified figure in figure 7.2 (a). Two 47 Ω surface mounted resistors are connected in series and 2 pairs are connected in parallel to

make 47 Ω. This configuration is used to reduce the total capacitance and inductance which can cause fluctuations in the drive current and to avoid the current limits of the individual 47 Ω resistors. The total in line impedance, with the diode having a forward resistance of 3 Ω above threshold, is 50 Ω. This provides a matched load to the 50 Ω impedance of the RF cable to ensure maximum power coupling and minimum backward reflection of electrical power into the RF circuitry.

The DC characteristics (provided by the manufacturer) of the laser diode, operating at room temperature, are shown in figure 7.2 (b). The lasing wavelength and threshold of the laser diode, at room temperature, are 1047.9 nm and 20 mA respectively. The spectral output, upon reaching lasing threshold current, is shown in figure 7.2 (c). It can be seen that it lases at a few longitudinal modes and is erratic. This is because the laser diode is not grating stabilised.

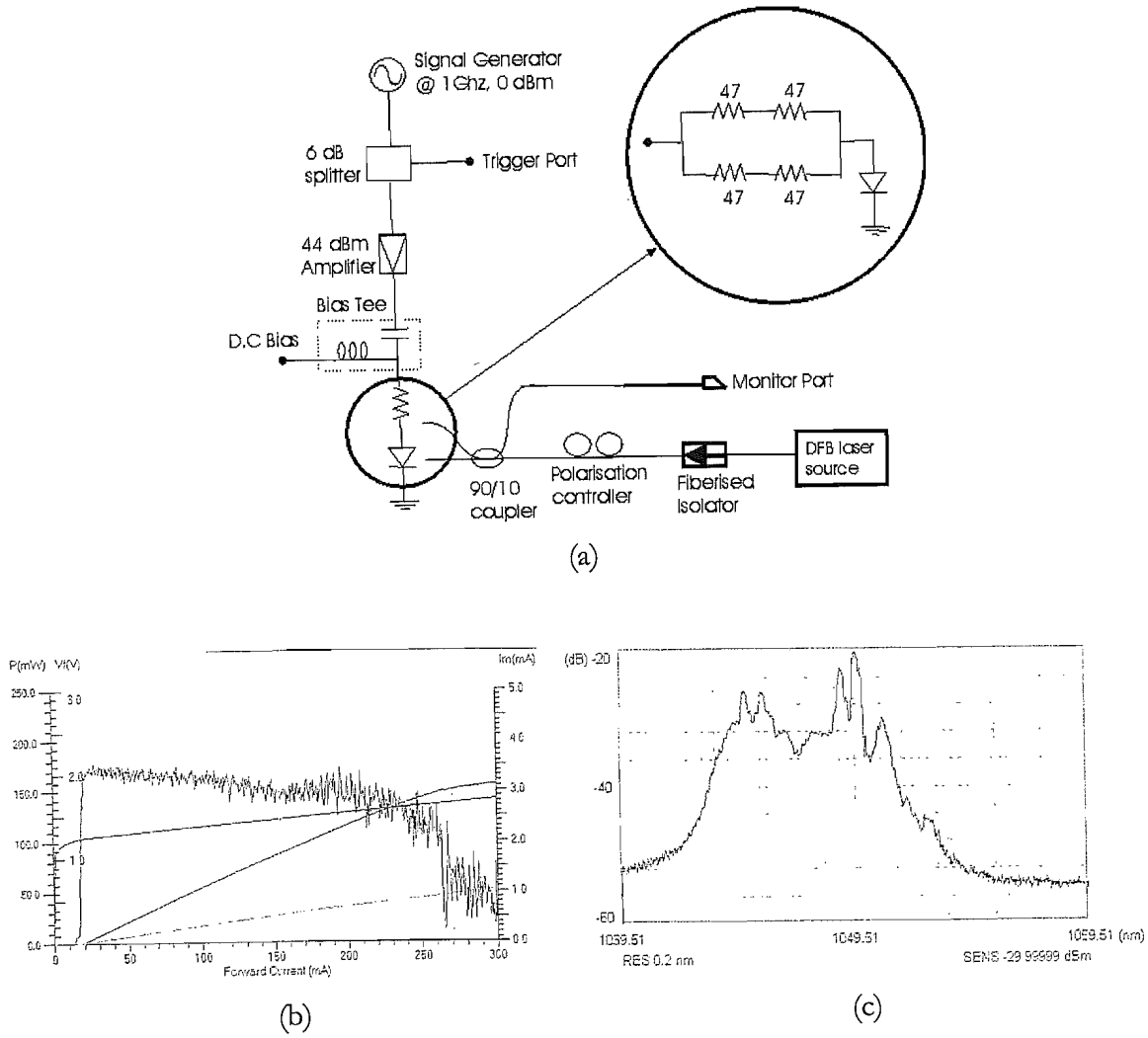

Figure 7.2: (a) Setup of gain-switched laser. (b) DC characteristics and (c) laser spectrum above threshold of laser diode at room temperature

Gain switching was realised by driving the laser with a modulated drive signal superimposed on a DC bias current. The injected modulation signal was a 1 GHz, 35.6 V peak to peak amplitude electrical sinusoid generated by a signal generator (Marconi) and amplified with an RF amplifier. The RF output power from the signal generator was set to 0 dBm. This RF output was then split with a 6 dB splitter, to provide the input to the RF amplifier and to provide a signal to trigger the scope. The -6 dBm input power to the RF amplifier was sufficient to saturate the amplifier so as to clamp the gain and reduce noise introduced from the amplifier. A DC power supply unit was used to bias the laser below lasing threshold, at 8.1 mA, via a bias tee and a DC block. The bias tee and DC block provided isolation with a low frequency cutoff of (<10KHz) between the DC bias source and the RF modulation signal. Therefore, since gain switching is achieved by electrically driving the diode, the output repetition rate does not depend on the cavity length and could easily be adjusted by changing the frequency of the drive signal.

Seeding the gain switched diode (either externally or internally) was essential, not only to improve timing jitter and Side Mode Suppression Ratio (SMSR) but also to lock to a single lasing longitudinal mode (since the laser diode used for gain switching in our experiment was not grating stabilised). As shown in figure 7.2, external injection seeding of the gain-switched laser was provided by a polarisation controlled narrow linewidth (<100 KHz) c.w. distributed feed back (DFB) laser source at 1059.94 nm through a 90/10 fiberised coupler. The polarisation controller tunes the seed polarisation such that the coupling efficiency into the lasing mode is optimised.

The temporal output gain switched pulse, without any seeding, is shown in figure 7.3(a). Here we observed a slightly broader and noisier pulse, compared to the one after seeding was introduced (see figure 7.5 (b)). The timing jitter of an unseeded pulse was measured at 2.8 ps and its FWHM pulse width was ~ 60 ps. The semiconductor laser diode, that was used for gain switching, had a high reflectivity output facet but it did not have any external grating stabilisation. Hence when operated without seeding at c.w. only, or together, with a modulated current, the lasing longitudinal modes were either erratic and random, or numerous modes in the ASE spectra start to lase altogether, as shown in figure 7.3 (b) (ii).

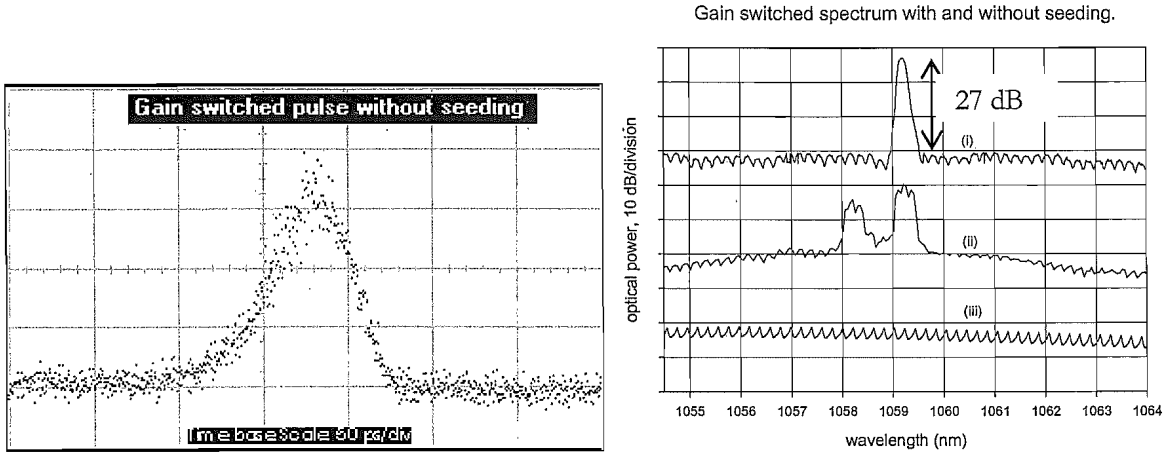

(a) (b)

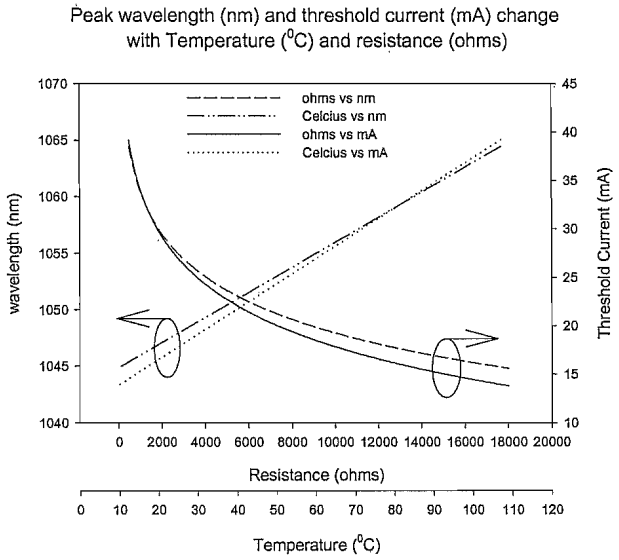

(c)

Figure 7.3(a) Gain switched pulse without external seeding. (b) Spectral plots of the gain switched pulse with and without seeding; (i) seeded with SMSR of ~27 dB and stable lasing mode, (ii) unseeded and unstable lasing mode is seen when laser diode is in c.w. operation above threshold, (iii) unseeded with bias current set near threshold at 32mA and driven with modulation signal at 0dBm. The output is a broad continuum spectrum with numerous lasing longitudinal modes and the SMSR is negligible. (c) Change in operating wavelength and threshold current of gain switched laser diode w.r.t. TEC resistance and operating temperature of diode.

The output spectrum of the gain switched source (when both modulated and DC drive current are injected into laser diode), with and without seed, is shown in figure 7.3 (b). Without seeding, the gain switched output spectra shown in figure 7.3 (b) (iii) was a broad ASE-like continuum with many lasing longitudinal modes and the SMSR was negligible. Even when the

DC drive current was increased to above c.w. lasing threshold, the overall effect was the increase in magnitude of all the longitudinal modes simultaneously without any becoming dominant. Seeding improved the SMSR dramatically and it was measured to be ~ 27 dB. However, further optimisation could be done to improve the SMSR and this will be discussed in later sections.

The output peak wavelength and threshold current of the semiconductor diode were also characterised with temperature. The characterisation result is shown in figure 7.3 (c). In the following sections, we will discuss the effects of seeding on pulse widths, spectral bandwidth, timing jitter and SMSR.

7.4 Characterisation and optimisation of the gain switched diode.

7.4.1 *Improving Side Mode Suppression Ratio (SMSR)*

The characteristics of the gain switched pulses are dependent on many parameters. Trade offs have to be made to produce pulses suitable for different applications. In this section, we report a study on the effects of input bias current, wavelength detuning, and seed power on side mode suppression ratio (SMSR).

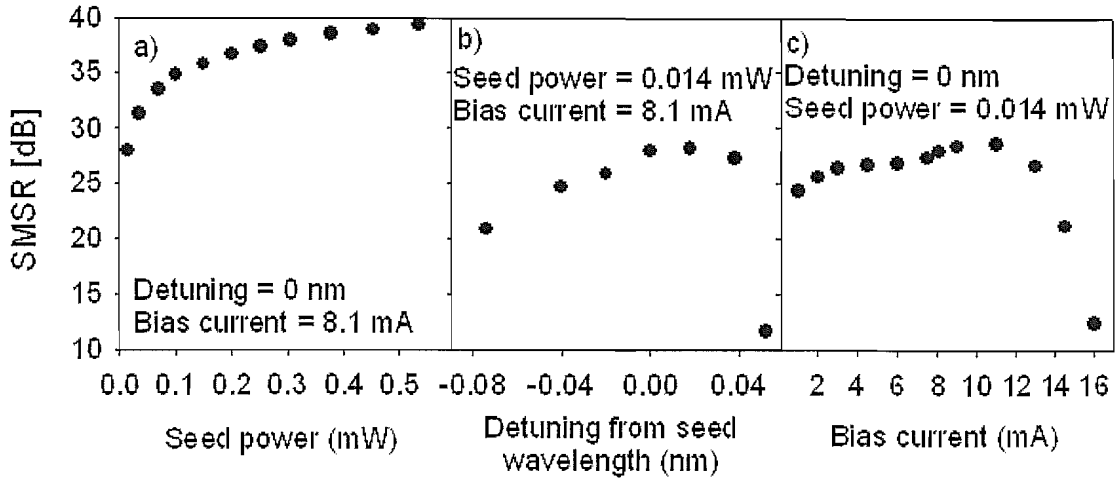

Figure. 7.4: SMSR with (a) seed power, (b) detuning from seed wavelength and (c) bias current.

The DFB laser was used to externally seed the laser diode. Seeding the initial oscillating wavelength provides increased wavelength selectivity before the gain switched pulse is produced. It excites the desired mode causing it to build up faster than the other modes,

thereby preferentially depleting the gain. This suppresses the other cavity modes and improves SMSR. Figure 7.4 (a) shows that the SMSR increases from 28 dB to 40 dB with increasing seed power. However, when the injected seed power was increased > 0.1 mW (-10dBm), additional structure started to develop at the base of the trailing edge of the pulse (see figure 7.9 (a)). We believed that this was due to the residue spontaneous emission from the seed laser. Hence the optimal possible SMSR that could be achieved was around 33.13 dB, by increasing the seed power.

The gain spectrum of the laser diode used in our experiments was peaked at 1047.9 nm at room temperature (r.t.p). It was far from the seed wavelength which was peaked at 1059.94 nm. This resulted in low gain efficiency and an extremely noisy output pulse due to gain fluctuations from competing modes at the gain peak. Since the seed wavelength cannot be changed, we temperature tuned the laser diode to shift the gain peak to be around the seed wavelength. Figure 7.4 (b) demonstrates that detuning the lasing mode about the peak seed wavelength changes the SMSR drastically. Positive values on the horizontal axis indicate that the peak of the excited mode is at a longer wavelength compared to the seed. We found that the method to achieve the best SMSR was to seed the excited mode 0.02nm shorter than the peak wavelength. This slightly better performance, compared to seeding at the peak, was due to the order of the excitation of the different wavelengths with respect to the central wavelength (peak wavelength). It is well known [27] that varying changes in refractive index (due to changes in the carrier density with current) of the active channel of the diode, when driven by a current pulse, results in a intrinsic negatively chirped pulse emitted from a gain-switched diode (the blue shifted light is at the leading edge). Hence, seeding at a slightly shorter wavelength (blue shifted light) coincides with the initial excited wavelength component of the gain-switched pulse thus increasing stability to the initial conditions before the pulse develops.

The initial DC bias of the diode below threshold affects the maximum possible inversion achieved and hence the gain of the gain-switched pulse. Figure 7.4 (c) shows our observation that the SMSR improves gradually, with increasing DC bias, but drops drastically once it reached optimal point. The maximum SMSR was achieved at an input DC bias current of 11 mA.

7.4.2 *Effects of seeding on timing and amplitude jitter*

The amplitude jitter was obtained directly from the HP 83480A digital communications analyser. Using the built-in histogram function, together with high resolution windowing, the

standard deviation of the peak amplitude and the mean values were measured. The amplitude jitter improved from 8.8 % without the seed to less than 1% with increasing seed power. The results are shown in figure 7.5 (c).

Timing jitter of the gain switched pulse can be classified into two categories: correlated and uncorrelated jitters [28]. Correlated jitter is attributed to the noise that is introduced through the drive circuit. Uncorrelated jitter, often called the "turn-on-delay timing jitter", arises due to the randomness between the onset of the electrical pulse and laser radiation. At the onset of the electrical pulse, the carrier density starts to grow. However, before it reaches threshold, random intra cavity spontaneous emissions cause fluctuations in the photon density [29] which results in timing jitter.

Introducing an external seed will improve the timing jitter [22] by improving modal selectivity and control to initial lasing conditions. The injected seed reduces the randomness in photon density at threshold by exciting the desired mode so that it is above the spontaneous emission level. The magnitude of timing jitter of the output pulse can be estimated easily in real time, from an oscilloscope, by using a high-speed photodiode. Figure 7.5 (a) and (b) shows the real time, temporal gain switched pulse, captured on our scope without and with 0.014 mW injected seed power bias at 8.1 mA. The spread on the leading and trailing edges of the pulse indicates the magnitude of the timing jitter. Comparing the spread on the leading edges of both pulses, we can see that the magnitude of the timing jitter is greater without seed. The estimated jitters were measured at 5 ps and 2.5 ps respectively.

However because the oscilloscope, that was used to measure the jitter, had an intrinsic scope jitter of ~ 2ps, our measurements were limited to a resolution of 2 ps. To obtain a more accurate measurement of the timing jitter, for a periodic pulse train, frequency domain measurements are needed [28, 30, 31].

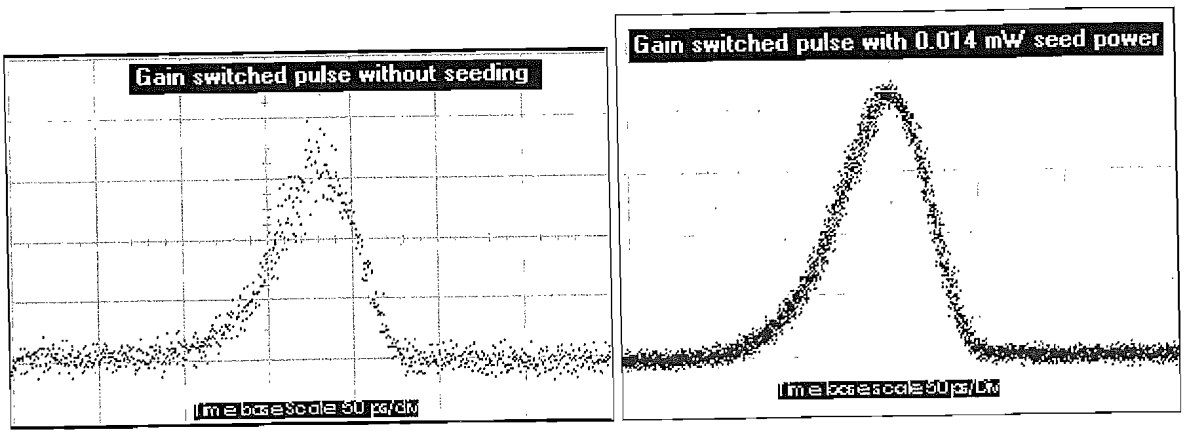

(a) (b)

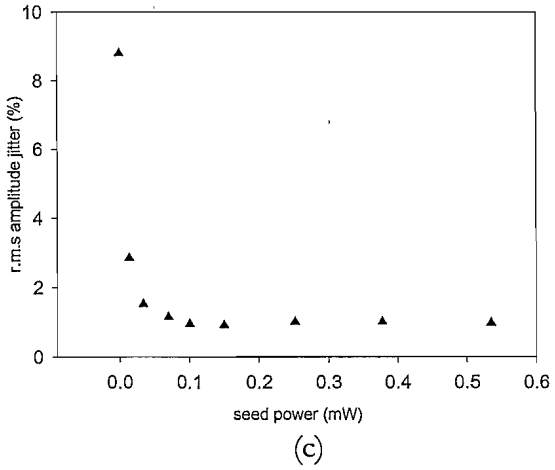

(c)

Figure 7.5: shows the (a) temporal output pulse without seeding and (b) with 0.034mW injected seed power. (c) r.m.s amplitude jitter obtained from the HP digital communications analyser with histogram function.

Von der Linde [31] used a frequency domain technique to measure timing jitter in mode-locked lasers, but since uncorrelated timing jitter is not found in mode-locked lasers, Von der Linde did not account for it in his paper. However, Leep *et al.* [30] found that at the low noise limit and with sufficient frequency range at high sensitivity, this technique could still be applied to the gain switch case to obtain the magnitude of both the correlated and uncorrelated timing jitter. The method for calculating both types of jitter is described in appendix A1.

An 8 GHz low noise photodetector and a 33 GHz Tektronix RF spectrum analyser were used to measure the power spectra of the output light. However as the photodetector's wavelength sensitivity was optimised at 1.3 μm, operating it at 1.06 μm would result in a reduced sensitivity. This reduction in sensitivity, together with the low output power from the diode, reduces the frequency cutoff of the detector to 5 GHz instead of 8 GHz. Depending on the frequency span and the resolution bandwidth of the power spectra taken on the spectrum analyser, different frequency components of the correlated jitter can be measured.

For the high resolution and low frequency span, the low frequency jitter contribution is measured and vice versa. The high frequency correlated jitter components were measured, with a frequency span of 100 kHz, at a resolution bandwidth of 300 Hz, and the timing jitters were found to be negligible ~ 0.15 ps for all seed powers. Figure 7.5 (b) below shows a scan of the 5^{th} harmonic, taken with a narrow frequency span of 5 kHz and fine resolution bandwidth of 30 Hz. At this resolution, additional structure due to lower frequency noise components was observed. The origin of the two adjacent side spikes (~ 1 kHz away from central peak) was not the gain switch diode. The origin was found to be the inherent noise (due to, I suspect the mechanical vibrations or electronic components) of the Marconi RF signal source when we

were characterising the signal source. The corresponding low frequency timing jitter was found to be ~ 1.8 ps with 0.014 mW seed power. Therefore we can see that the correlated jitter of the gain switch laser is mainly contributed by the low frequency jitters.

Figure 7.6 (a) shows the five appended scans each taken with a wide frequency span of 1 GHz and resolution bandwidth of 1 MHz. From the figure, we can see two dominant noise components, one noise band that is fairly uniform across all the harmonics, indicating mainly uncorrelated noise, and some form of repetitive structures in-between each harmonic. We believe this is due to mode beating of the adjacent modes but we had not identified this noise before this thesis was written. The turn-on-delay jitter was calculated from equation 7.1 [28] to be 1.57 and 1.47 ps with 0.014 mW and 0.07 mW seed power respectively,

$$\sigma_\tau = \frac{1}{2.\pi.\sqrt{\mu^2 + \frac{1}{12}}.f}.\sqrt{\frac{P_n}{P_c}.\frac{f}{\Delta f_{res}}} \qquad (7.1)$$

where σ_τ is the r.m.s. uncorrelated timing jitter, μ is the μ^{th} order harmonic, f is the repetition frequency, Δf_{res} is the resolution bandwidth, P_n is the peak power of the noise band and P_c is the peak power of the carrier.

The corresponding correlated and uncorrelated timing jitters, at different seed powers, are plotted in figure 7.6 (c). Adding both contributions, by assuming a Gaussian noise distribution, the total r.m.s. timing jitter for the gain switched laser is obtained and plotted in figure 7.6 (c). The correlated timing jitter from the Marconi RF signal generator is also characterised, and plotted in this figure, and is indicated by the red dotted line. We found that the timing jitter improved from 2.8 -> 2.24 ps when the seed power was increased to 0.07mW. Investigations on the effects of external seeding on gain-switched FP laser diodes, at 1550 nm, by Seo *et al.*, found that minimum timing jitter coincides at maximum SMSR [32]. Comparing figure 7.4 (a) and 7.6 (c), we found that this agrees with their findings, as the SMSR starts to level off between 0.07 mW and 0.1 mW seed power. We believe that the uncorrelated timing jitter started to rise dramatically at 0.25 mW seed power as a result of the injected spontaneous emission from the excess seed power.

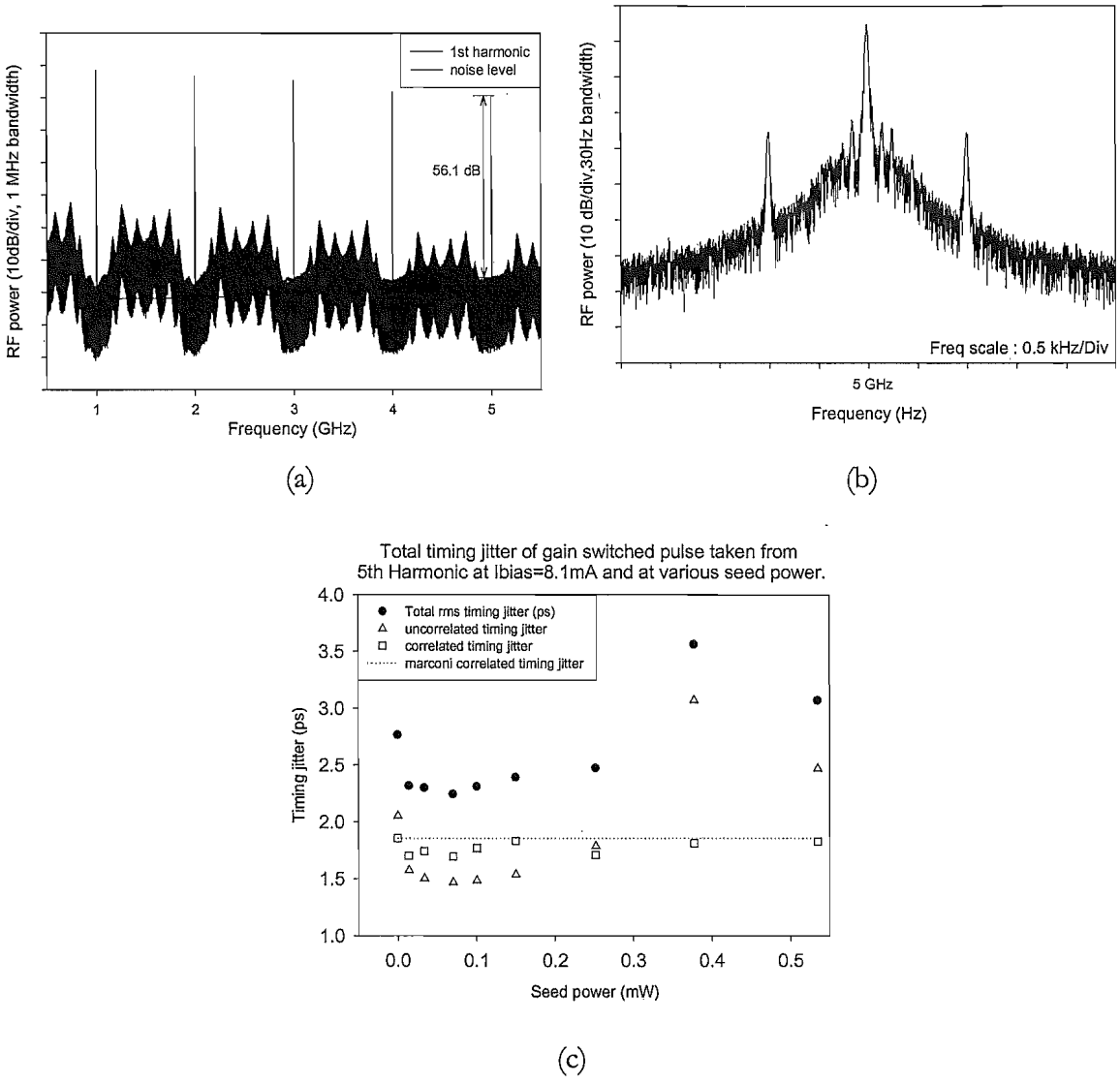

Figure 7.6: (a) Power spectra for the uncorrelated noise band at 0.014 mW seed power. (b) Power spectrum for a narrow noise band at the 5th harmonic (5 GHz). (c) Uncorrelated, correlated and the total r.m.s iming jitter as a function of seed power.

7.5 Pulse compression

It has been found that the optical output pulses generated from modulated semiconductor lasers have an intrinsic negative frequency chirp across the pulse. Although this could be detrimental for high bit rate long-haul transmission systems, we can harness this property to generate shorter duration pulses through pulse compression techniques.

This frequency deviation across the pulse is due to the changes to the refractive index of the active channel of the semiconductor laser diode with the varying input drive current. Upon

the sudden jump in drive current, at the leading edge of the modulated signal, the carrier density in the active region increases momentarily as the increased current is not immediately converted into output light. This temporary jump in carrier density reduces the refractive index of the diode cavity which shortens the optical path length of the cavity. This results in a brief blue shift in wavelength, followed by a momentary shift to the red as the carrier density decreases below equilibrium when the drive current rapidly falls back down [27, 33].

Previously we have identified two categories of compression scheme that several authors, in the past, have demonstrated using fiber based compressors, non-linear [15, 17] and linear compression [16, 20]. Recently, pulse compression down to 5ps durations has been achieved in a Chirped Fibre Bragg Grating (CFBG) by Roelens M.A.F *et al.* [18]. Khawaja A.A *et al.* have carried out both linear and non-linear fiber pulse compression with gain switched pulses.

Pulses were linearly compressed, via dispersion shifted fibers (DSF), to 3.6 ps durations and subsequently a soliton type compression technique was used to non-linearly compress the pulses down to 185 fs. However, up to the time that this thesis was written, only experimental work on linear compression had been carried out.

7.5.1 *Linear pulse compression*

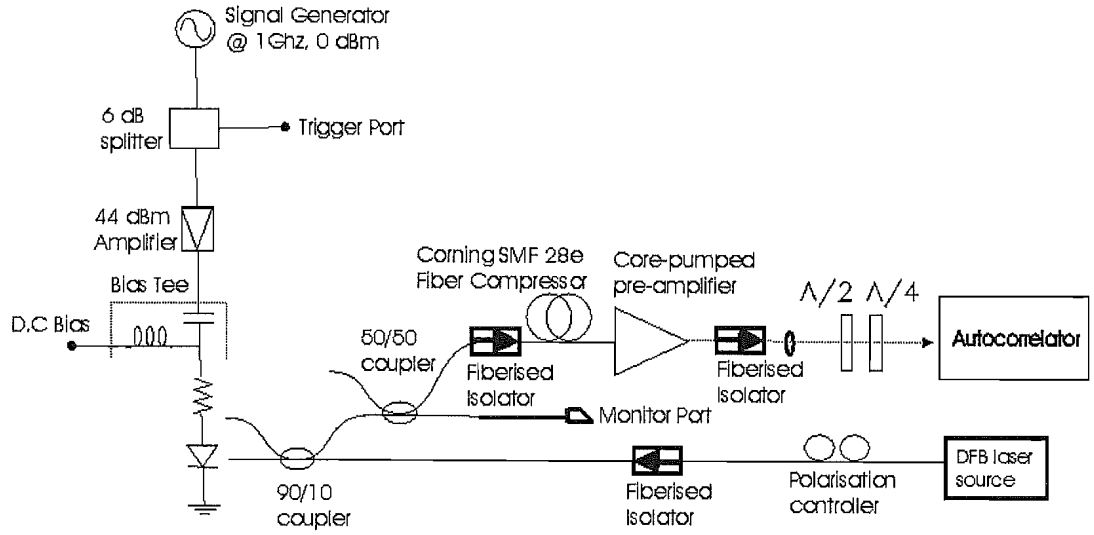

Figure 7.7: shows the setup used for linear pulse compression

The inherent negative frequency chirp, that is produced in a gain switched optical pulse, is usually almost linear [34]. Therefore with an appropriate linear compressor, the gain switched pulses can be efficiently compressed. Many different methods [18, 34] have been used to accurately calculate the required compression strength needed to optimally compress the gain

switched pulses. Dudley *et al.* [34] characterised the chirp of the pulses using a method that combines second harmonic generation (SHG) with frequency resolved optical gating (FROG). And recently, Roelens *et al.* [35], from our group, characterised the phase and intensity profiles of a gain switched laser diode with a frequency resolved optical gating technique which uses an electro-absorption modulator (EAM) to sample the pulse.

Liu and Ahmed *et al.* both estimated the strength of the linear compressor, using a Gaussian pulse propagation approximation, by equation 7.2 [19, 20]. However, this method becomes inaccurate when a highly modulated drive signal is used. Investigations, made by Chusseau *et al.* [16], found that the compression figure obtained can deviate from the optimum value by a factor of 2. This is because the Gaussian approximation model cannot account for the increase in pulse asymmetry and non-linear chirp due to the stronger modulation. They developed simple rate equations, which include gain compression, to estimate such gain switched pulses and found close agreement.

However, we found that in our experiment, the simple Gaussian approximation was sufficient to estimate the required compression strength.

$$-\frac{2.\pi.c}{\lambda^2}.\beta_2.L = \frac{\Delta T}{\Delta \lambda} \qquad (7.2)$$

where β_2 is the dispersion parameter, ΔT is the pulse width of the chirped pulse, $\Delta\lambda$ is the spectral width of the chirp pulse and L is length of the compressor.

Figure 7.7 illustrates the setup that was used for linear pulse compression. A fiberised 3 dB coupler was used to separate the output from the gain switched laser, to allow monitoring of the pulses from the diode and to provide an input source to the pulse compressor. With an external injection seed power of 0.14mW, the negatively chirped gain switched pulses were compressed with a length of 1.55 μm single mode fiber (SMF 28e) which is normally dispersive at 1.06 μm. This fiber was used because we did not have the required length of 1.06 μm SM fibers during the time of the experiment. Though using the SMF 28e fiber compressor could result in multimode transverse output, this did not pose a problem as the higher order modes were stripped out, by the following fiberised isolator and amplifier chain, before the output pulse was autocorrelated.

The initial linear chirp was compressed and the shortest pulse duration of 18.6 ps (assuming a Gaussian pulse shape) was achieved using 15.7 km of SMF 28e fiber. The pulse

width, with compressor length, is shown in figure 7.8 (d). Figure 7.8 (a), (b) and (c) shows the temporal and spectral characteristics of the initial and compressed pulse. The time-bandwidth ($\Delta\tau.\nu$) product of the compressed pulse is 0.79 which is nearly twice the time bandwidth product of a Gaussian, transform limited, pulse. This indicates that there was some initial non-linear chirp which could not be fully compensated for. A dispersive CFBG can be used to compress the gain switched pulses. This has the advantage of eliminating the long compression fiber lengths (km) required to compress the pulses. However at the time of the experiment, the required CFBG was not available, although suitable gratings have now been made to my specifications and await testing.

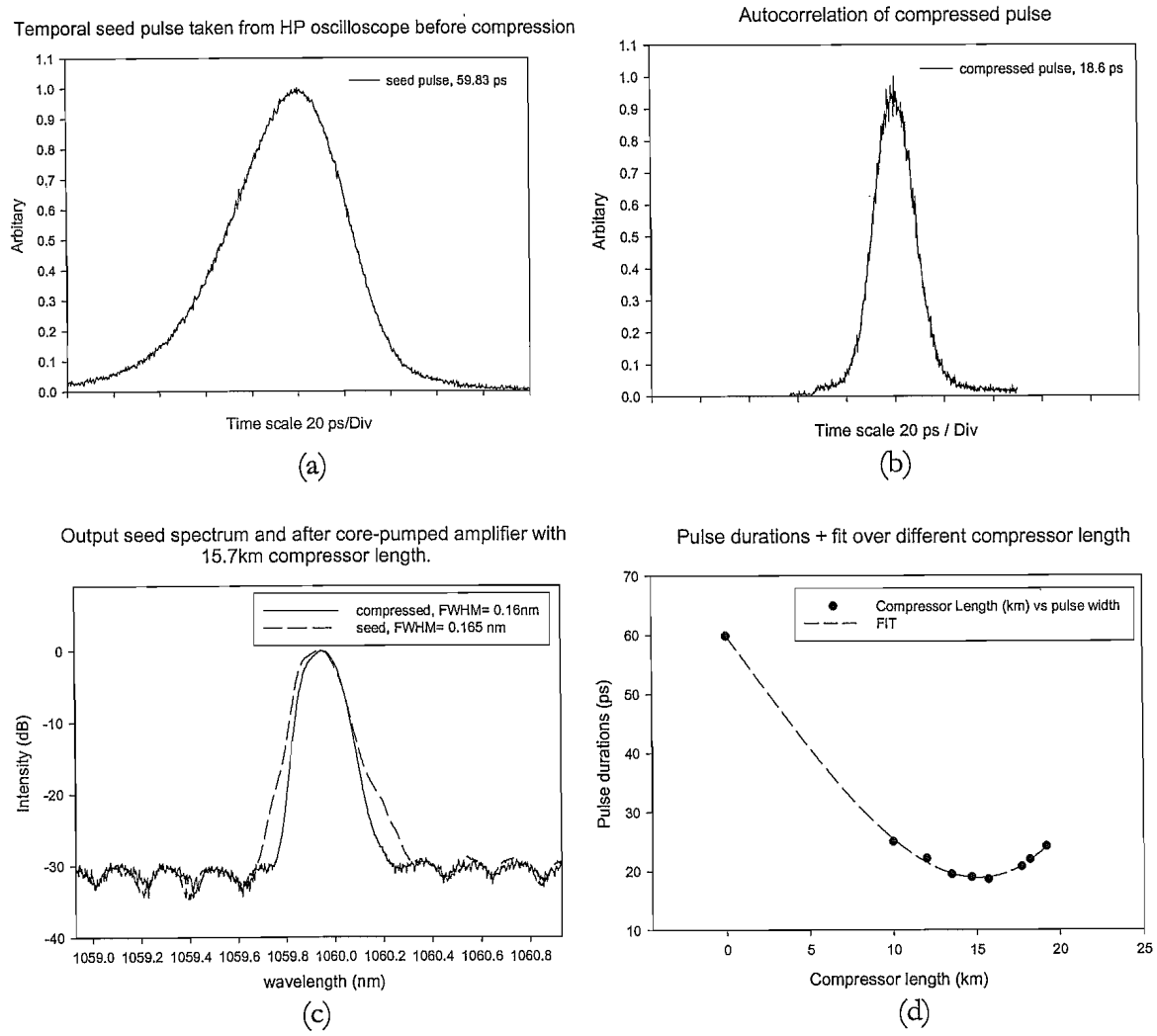

Figure 7.8: (a) ,(b) and (c) shows the temporal and spectral characteristics of the initial and compressed pulse, (d) Pulse compression with fiber length using an injected seed power of 0.14 mW.

The injection seed power also reduces the peak inversion level attained by the lasing mode. Therefore the higher the injection power, the lower the gain the mode sees. This reduces the degree of chirp the gain switched pulse obtains [21, 23, 32, 36] and hence a longer compressor length is required.

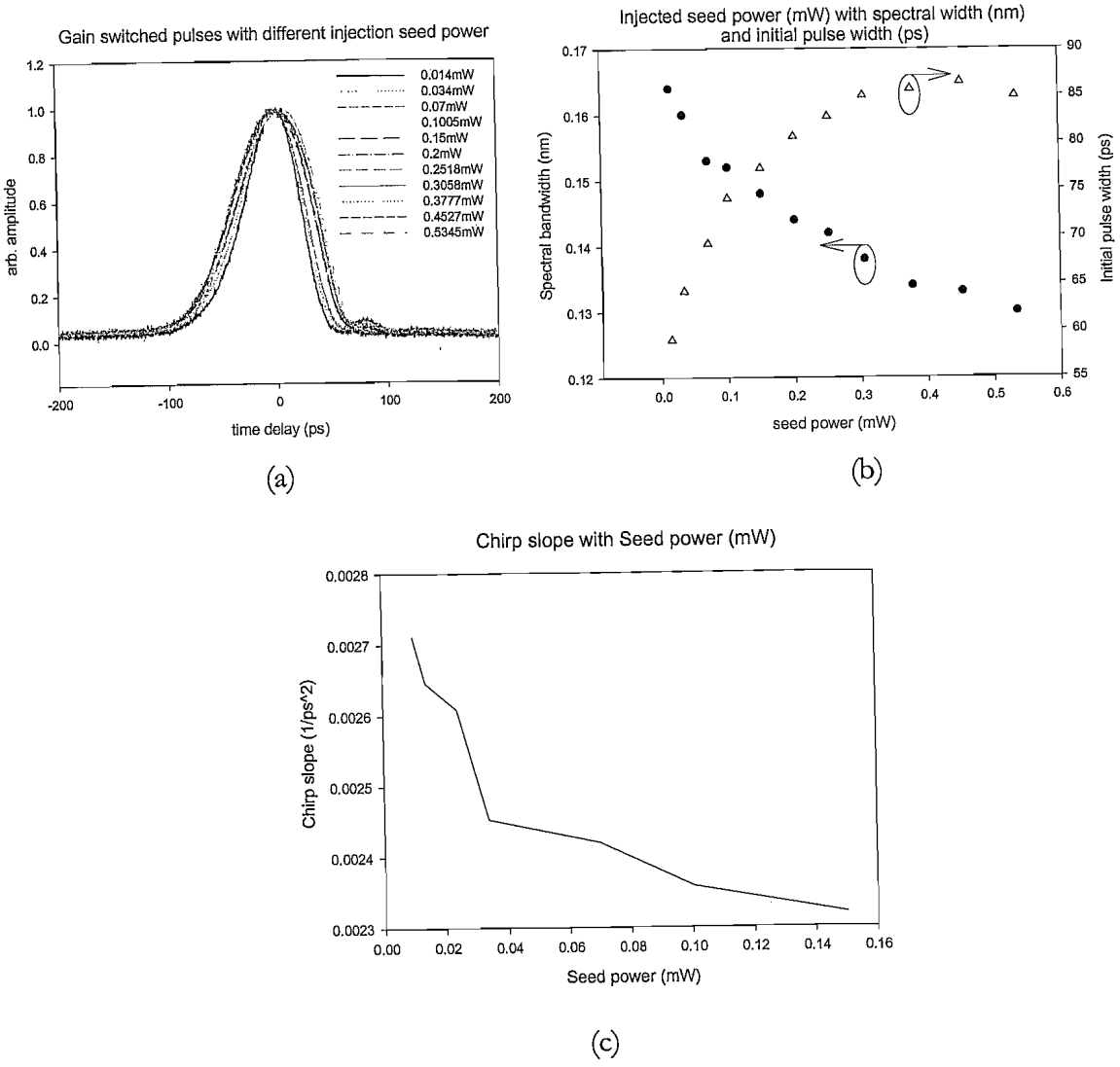

Figure. 7.9: (a) Temporal gain switched pulse shape with seed power (additional structure can be seen when injected seed power > 0.1 mW. This is either due to spontaneous emission from the excess seed power or the adjacent longitudinal mode reaching threshold, with the added gain from the excess seed power), (b) FWHM spectral bandwidth and temporal pulse width of the gain switched pulses, with a bias current of 8.1mA and detuning of 0.2 nm, (c) Chirp slope of a gain-switched pulse with injected seed power, with a bias current of 8.1mA and without detuning.

The temporal pulse shapes of the gain switched pulses, with different seed powers, are shown in figure 7.9 (a). We can see that the gain switched pulses start to broaden with increasing seed power (indicating a lower chirp) and, at injection levels > 0.1 mW, additional structure starts to form at the trailing edge of the pulse. Results of the spectral and temporal

FWHM bandwidth of the initial pulse with increasing seed power were recorded, and are presented in Figure 7.9 (b). We observed that the spectral and temporal width of the initial pulse decreases and increases respectively with increased seeding, demonstrating that the pulse chirp decreases with seed power. Our initial observation was confirmed when the pulse chirp was determined from the compressor performance and this is shown in figure 7.9 (c). The results show that the frequency chirping of the gain switched pulses reduces with increasing seed power. Together, figure 7.9 (b) and (c) show the correlation between the frequency chirp, seeding power and spectral bandwidth of the gain switched pulses which relates to the minimum pulse width achievable through linear compression (assuming the right compressor is used).

7.6 Pulse amplification

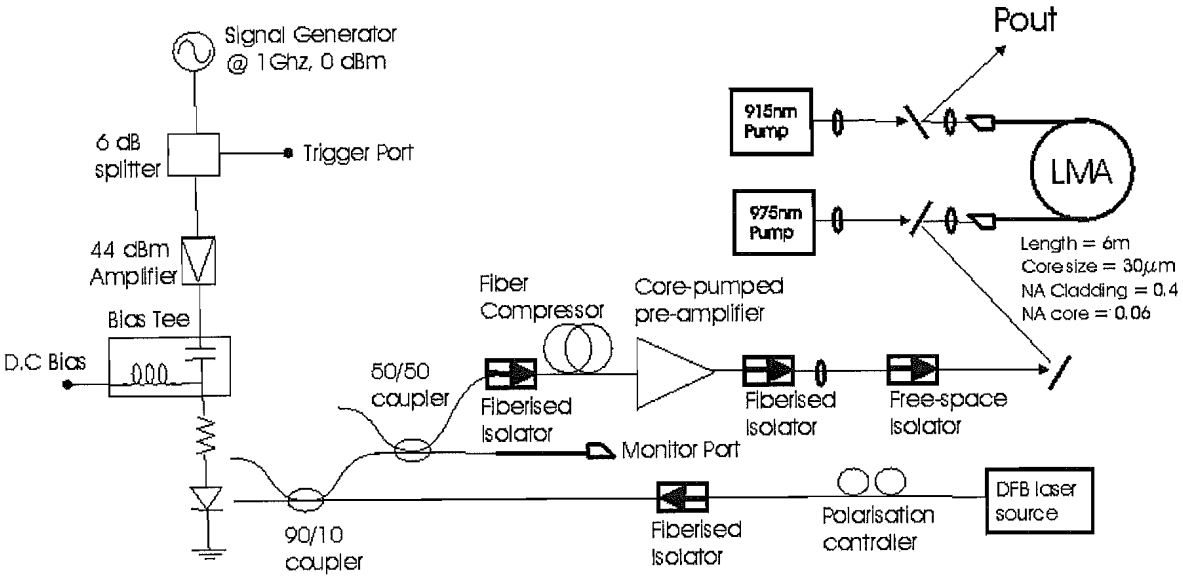

Figure 7.10: Schematic of the complete system with pulse compression and amplifier cascade

Many of the applications mentioned in the introduction of this chapter rely on the excitation of the non-linear effects induced by the peak powers of the gain switched pulses. To make the gain switched pulses more applicable, amplification of the pulses to obtain higher peak powers is necessary. Gain switched pulses from semiconductors have been amplified previously at 1.55 μm with an Er^{3+}/Yb^{3+} fiber amplifier [23, 37]. In this section, we will present some results obtained from the amplification of the gain switched source characterised in section 7.4.

Figure 7.10 illustrates the schematic of the complete system, with pulse compression and the amplifier cascade. The compressed pulses pass through an amplifier chain which consists of a 4m length of core-pumped, SM, Yb^{3+} doped (2300 ppm) fiber (N.A 0.21; cutoff ~940 nm) and an end-pumped 6m long, Yb-doped (8000 ppm) silica, Large Mode Area (LMA) fiber with a 30 μm core and 300 μm cladding diameter, havin a flat index profile and NA~0.06. During operation, we obtained single transverse mode output from the LMA fiber.

Before amplifying the gain switched pulse, the injection seed power and bias current were increased slightly to 0.34 mW and 11 mA respectively. As mentioned in the previous section, increasing the injection seed power will result in a decrease in spectral width and a subsequent increase in compressed pulse width. However, this would lead to an improvement in SMSR and increased spectral symmetry [23]. Therefore some compromises in pulse width for higher SMSR and spectral symmetry were made. The SMSR was improved by 4 dB to 38 dB and the spectral width decreased by 0.04 nm to 0.11 nm which corresponds to a $\Delta\tau.\nu$ of 0.58 (which was close to transform limited but was not obtained due to uncompressed higher order dispersion within the pulse).

Comparing the pulse spectrum obtained after the core-pumped amplifier, displayed in figure 7.8 (c) and 7.11 (c), it can be seen that the spectral symmetry was enhanced. The gain switched pulses were amplified with two stages. The core-pumped amplifier provided ~18 dB of gain and the LMA power amplifier provided ~ 30 dB of gain at full pump power. The 915 and 975 nm pump diodes, used in this experiment, have been described in chapter 6, section 6.6.1. The maximum output pump power possible from the 915 and 975 nm pumps were 30 W and 25 W respectively. However, at the time of this experiment, the total available incident pump power was only 40.4 W, due to the degradation of the diode performance from both pumps. The pump launch efficiency was ~ 70%, of which ~ 26 W was absorbed. The highest output power obtained was 11.1W, with a pulse width of 20 ps, at 1 GHz repetition rate, thereby achieving a peak power of 0.56 kW.

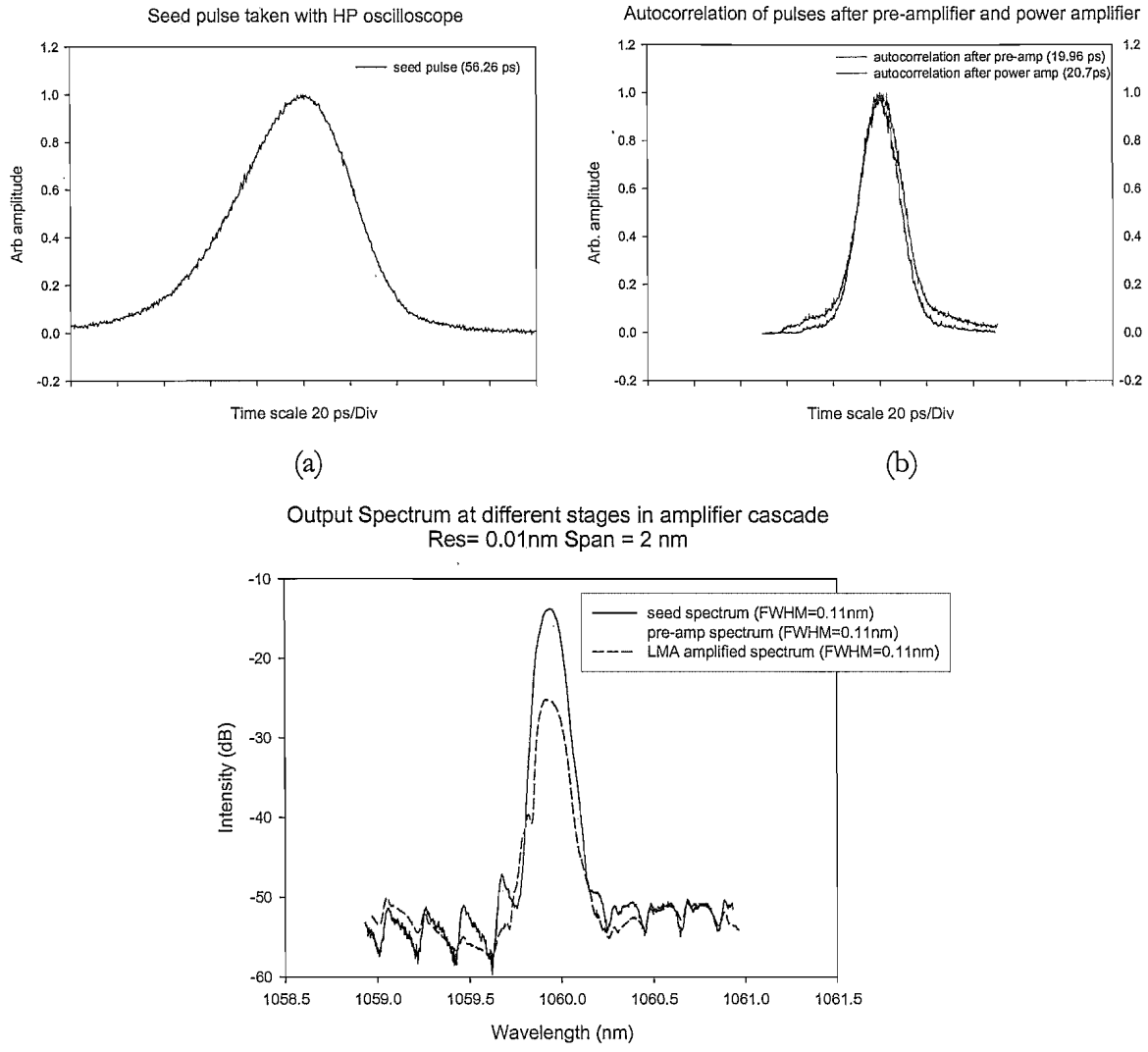

Figure 7.11: (a) Seed pulse obtained using the HP 83480A scope, (b) Autocorrelation of output pulses obtained at different stages of the amplifier chain, (c) Output pulse spectrum at different stages in the amplifier chain. Pulse shape and spectrum at the final amplification stage was taken at the highest output power of 11.1 W.

Figure 7.11 shows the temporal and spectral characteristics of the output pulse at different stages of the amplification chain. The pulse characteristics, shown in figure 7.11 (b) for the final amplifier, were taken at the highest output power. We can see that there was negligible temporal and spectral pulse broadening after the LMA amplifier. However, some degradation in the SMSR (28.5 dB) and spectral filtering can be observed.

7.7 Conclusion

We believe that this is the first time that gain switched pulses have been generated using 1.06 μm semiconductor laser diodes. We experimentally determined the dependence of SMSR on the injected seed power, wavelength and bias conditions. Pulse chirp was studied and it was found that the initial chirp decreased with increasing seed power. This is in accordance with much of the previous work that has been done on 1.55 μm semiconductor laser diodes. The negatively chirped gain switched pulse was linearly compressed with a fiber compressor to achieve 18.6 ps, near transform limited, pulses. We believe that full compression was not obtained due to the uncompressed non-linear chirp. The compressed pulse was amplified in two amplification stages to obtain pulses with peak powers up to 0.56 kW. The pulses were 20 ps long, with an average output power of 11.1 W at 1 GHz. The maximum output power achievable was limited by the pump power available at the time of the experiment. However it has been calculated, from previous experiments (see chapter 6 section 6.6.3.3.1), that the threshold peak power for SRS for this 6 m long, 30 μm, LMA fiber was ~ 30 kW (depending on the gain required from the amplifier fiber). This will ultimately limit the maximum output power achievable with this final amplifier.

Since then, more work has been done to improve the system. CFBGs, specially written for the gain switched laser developed, have been implemented to provide linear compression of the gain switched pulses. 16.4 ps compressed pulses were obtained and, subsequently, these compressed pulses were amplified in a MOPA chain (using high powered diode-laser-stack-based pump sources [38, 39]) to 321 W, at 1 GHz repetition rate. Papers based on these experiments have been accepted for oral presentations in CLEO Europe 2005, in Munich and OFC 2005 (postdeadline) respectively. The CLEO Europe and OFC submissions are attached in appendix A3 and A4 in this thesis respectively.

Further optimisation and characterisation of the gain switched system is possible. With a suitable signal generator and RF amplifier, better amplitude and timing jitter performance can be obtained. Besides using these high output power, high repetition rate, ps systems for laser display applications, the repetition frequency of the gain switched pulses could be stepped down to achieve higher peak powers which could be used in applications requiring higher peak power such as sources for higher harmonic generation.

BIBLIOGRAPHY

1. Fermann, M.E., Hofer, M., Haberl, F., Schmidt, A.J., Turi, L., *Additive-Pulse-Compression Mode-Locking of a Neodymium Fiber Laser.* Optics Letters, 1991. **16**(4): p. 244-246.
2. Hofer, M., Fermann, M.E., Haberl, F., Ober, M.H., Schmidt, A. J., *Mode-Locking with Cross-Phase and Self-Phase Modulation.* Optics Letters, 1991. **16**(7): p. 502-504.
3. Tamura, K., Jacobson, J., Ippen, E.P., Haus, H.A., Fujimoto, J. G., *Unidirectional Ring Resonators for Self-Starting Passively Mode-Locked Lasers.* Optics Letters, 1993. **18**(3): p. 220-222.
4. Zirngibl, M., Stulz, L.W., Stone, J., Hugi, J., Digiovanni, D., Hansen, P. B., *1.2ps Pulses from Passively Mode-Locked Laser Diode Pumped Er- Doped Fiber Ring Laser.* Electronics Letters, 1991. **27**(19): p. 1734-1735.
5. Desouza, E.A., Soccolich, C.E., Pleibel, W., Stolen, R.H., Simpson, J. R., Digiovanni, D. J., *Saturable Absorber Modelocked Polarization-Maintaining Erbium- Doped Fiber Laser.* Electronics Letters, 1993. **29**(5): p. 447-449.
6. Ilday, F.O., Buckley, J., Kuznetsova, L. and Wise, F.W., *Generation of 36-femtosecond pulses from a ytterbium fiber laser.* Optics Express, 2003. **11**(26): p. 3550-3554.
7. Ilday, F.O., Buckley, J. R., Lim, H., Wise, F. W., Clark, W. G., *Generation of 50-fs, 5-nJ pulses at 1.03 μm from a wave- breaking-free fiber laser.* Optics Letters, 2003. **28**(15): p. 1365-1367.
8. Yoshida, E. and Nakazawa, M., *80 similar to 200GHz erbium doped fibre laser using a rational harmonic mode-locking technique.* Electronics Letters, 1996. **32**(15): p. 1370-1372.
9. Deng, Y., Koch, M. W., Lu, F., Wicks, G. W. and Knox, W.H., *Colliding-pulse passive harmonic mode-locking in a femtosecond Yb-doped fiber laser with a semiconductor saturable absorber.* Optics Express, 2004. **12**(16): p. 3872-3877.
10. Roth, J.M., Ulmer, T.G., Spellmeyer, N.W., Constantine, S., Grein, M. E., *Wavelength-tunable 40-GHz picosecond harmonically mode-locked fiber laser source.* IEEE Photonics Technology Letters, 2004. **16**(9): p. 2009-2011.
11. Ortac, B., Hideur, A. and Brunel, M., *Passive harmonic mode locking with a high-power ytterbium-doped double-clad fiber laser.* Optics Letters, 2004. **29**(17): p. 1995-1997.
12. Derickson, D.J., Helkey, R. J.,Mar, A.,Karin, J. R.,Wasserbauer, J. G. and Bowers, J.E., *Short Pulse Generation Using Multisegment Mode-Locked Semiconductor-Lasers.* IEEE Journal of Quantum Electronics, 1992. **28**(10): p. 2186-2202.
13. Ludwig, R., Diez, S., Ehrhardt, A., Kuller, L., Pieper, W., Weber, H. G., *A tunable femtosecond mode-locked semiconductor laser for applications in OTDM-systems.* IEICE Transactions on Electronics, 1998. **E81C**(2): p. 140-145.
14. Yvind, K., Skovgaard, P.M.W., Mork, J., Hanberg, J., Kroh, M., Performance of external cavity mode-locked semiconductor lasers employing reverse biased saturable absorbers. Physica Scripta, 2002. **T101**: p. 129-132.
15. Ahmed, K.A., Chan, K.C. and Liu, H.F., *Femtosecond Pulse Generation from Semiconductor-Lasers Using the Soliton-Effect Compression Technique.* IEEE Journal of Selected Topics in Quantum Electronics, 1995. **1**(2): p. 592-600.
16. Chusseau, L. and Kazmierski, C., *Optimum Linear Pulse-Compression of a Gain-Switched 1.5 μm DFB Laser.* IEEE Photonics Technology Letters, 1994. **6**(1): p. 24-26.
17. Mollenauer, L.F., Stolen, R.H. and Gordon, J.P., *Experimental-Observation of Picosecond Pulse Narrowing and Solitons in Optical Fibers.* IEEE Journal of Quantum Electronics, 1981. **17**(12): p. 24-24.

18. Roelens, M.A.F., Thomsen, B.C., Richardson, D.J., *High quality 5ps pulse generation at 10 Gbit/s using a fibre Bragg grating compensated gain-switched laser diode.* in *Tech. Dig. OECC 2004.* 2004. Kanagawa. 16D1-4. p. 836.
19. Liu, H.F., Ogawa, Y. and Oshiba, S., *Generation of an Extremely Short Single-Mode Pulse (Approximately 2 ps) by Fiber Compression of a Gain-Switched Pulse from a 1.3 μm Distributed-Feedback Laser Diode.* Applied Physics Letters, 1991. **59**(11): p. 1284-1286.
20. Ahmed, K.A., Liu, H. F.,Onodera, N.,Lee, P.,Tucker, R. S. and Ogawa, Y., *Nearly Transform-Limited Pulse (3.6 ps) Generation from Gain- Switched 1.55 μm Distributed-Feedback Laser by Using Fiber Compression Technique.* Electronics Letters, 1993. **29**(1): p. 54-56.
21. Matsui, Y., Kutsuzawa, S., Arahira, S. and Ogawa, Y., *Generation of wavelength tunable gain-switched pulses from FP MQW lasers with external injection seeding.* IEEE Photonics Technology Letters, 1997. **9**(8): p. 1087-1089.
22. Barry, L.P., Debeau, J. and Boittin, R., *Simple Technique to Improve the Spectral Quality of Gain- Switched Pulses from a DFB Laser.* Electronics Letters, 1994. **30**(25): p. 2143-2145.
23. Barry, L.P., Thomsen, B. C.,Dudley, J. M. and Harvey, J.D., *Characterization of 1.55-μm pulses from a self-seeded gain- switched Fabry-Perot laser diode using frequency-resolved optical gating.* IEEE Photonics Technology Letters, 1998. **10**(7): p. 935-937.
24. Liu, P.L., Lin, C., Kaminow, I.P. and Hsieh, J.J., *Picosecond Pulse Generation from InGaAsP Lasers at 1.25 and 1.3 μm by Electrical Pulse Pumping.* IEEE Journal of Quantum Electronics, 1981. **17**(5): p. 671-674.
25. Lau, K.Y., *Gain Switching of Semiconductor Injection-Lasers.* Applied Physics Letters, 1988. **52**(4): p. 257-259.
26. H. Ito, Yokoyama, H., Murata, S., Inaba, H., *Picosecond optical pulse generation from an RF modulated AlGaAs diode laser.* Electronics Letters, 1979. **15**: p. 738-740.
27. Linke, R.A., *Modulation Induced Transient Chirping in Single Frequency Lasers.* IEEE Journal of Quantum Electronics, 1985. **21**(6): p. 593-597.
28. Jinno, M., *Correlated and Uncorrelated Timing Jitter in Gain-Switched Laser-Diodes.* IEEE Photonics Technology Letters, 1993. **5**(10): p. 1140-1143.
29. Weber, A.G., Ronghan, W., Bottcher, E.H., Schell, M., Bimberg, D., *Measurement and Simulation of the Turn-on Delay Time Jitter in Gain-Switched Semiconductor-Lasers.* IEEE Journal of Quantum Electronics, 1992. **28**(2): p. 441-446.
30. Leep, D.A. and Holm, D.A., *Spectral Measurement of Timing Jitter in Gain-Switched Semiconductor-Lasers.* Applied Physics Letters, 1992. **60**(20): p. 2451-2453.
31. Von der Linde, D., *Characterization of the Noise in Continuously Operating Mode- Locked Lasers.* Applied Physics B-Photophysics and Laser Chemistry, 1986. **39**(4): p. 201-217.
32. Seo, D.S., Liu, H.F., Kim, D.Y. and Sampson, D.D., *Injection Power and Wavelength Dependence of an External-Seeded Gain-Switched Fabry-Perot Laser.* Applied Physics Letters, 1995. **67**(11): p. 1503-1505.
33. Tucker, R.S., *High-Speed Modulation of Semiconductor-Lasers.* Journal of Lightwave Technology, 1985. **3**(6): p. 1180-1192.
34. Dudley, J.M., Barry, L. P., Harvey, J. D., Thomson, M. D., Thomsen, B. C., Bollond, P. G. and Leonhardt, R., *Complete characterization of ultrashort pulse sources at 1550 nm.* IEEE Journal of Quantum Electronics, 1999. **35**(4): p. 441-450.
35. Roelens, M.A.F., Thomsen, B.C., Richardson, D.J., *Multi-wavelength EAM based optical sampling for performance monitoring in high Bit-rate systems.* in *Tech. Dig. ECOC 2004.* 2004. Stockholm. We4 P116. p. 700.
36. Lee, Y.C. and Shu, C., *Wavelength-tunable nearly transform-limited pulses generated by self-injection seeding of a laser diode at an arbitrary repetition rate.* IEEE Photonics Technology Letters, 1997. **9**(5): p. 590-592.

37. Thomsen, B.C., Jeong, Y., Codemard, C., Roelens, M.A.F., Dupriez, P., Sahu, J.K., Nilsson, J., Richardson, D.J., *60W 10GHz 4.5ps pulse source at 1.5 μm. CLEO/IQEC 2004 16-21 May 2004.* San Francisco. *CMAA.* **1**(1): p.2.
38. Jeong, Y., Sahu, J.K., Payne, D.N. and Nilsson, J., *Ytterbium-doped large-core fibre laser with 1 kW of continuous- wave output power.* Electronics Letters, 2004. **40**(8): p. 470-472.
39. Jeong, Y., Nilsson, J., Sahu, J.K., Soh, D.B.S., Alegria, C., Dupriez, P., Codemard, C.A., Payne, D.N., Horley, R., Hickey, L.M.B., Wanzcyk, L., Chryssou, C.E., Alvarez-Chavez, J., Turner, P.W., *Single-frequency polarized ytterbium-doped fiber MOPA source with 264W output power.* Optics Letters, 2005. **30**(5): p.459-461.

Chapter 8

CONCLUSIONS

8.1 Introduction

As I have outlined in chapter 1, the work presented in this thesis lies in three distinct research areas; to generate high average power/energy pulses in the femtosecond, picosecond and nanosecond regimes using Yb-doped fiber based systems. In chapters 3 and 4 [1], I have described the development of an Yb-fiber based CPA system and a direct amplification system (based on a parabolic pulse amplification technique) to produce high average power/energy femtosecond pulses. Next in chapters 5 and 6, I described the development of a Q-switched system (chapter 5) and a directly modulated laser diode amplification system (chapter 6) to produce high energy nanosecond pulses. Finally, in chapter 7, I have described work carried out to develop a gain switched laser diode (operating at 1 μm wavelength) to produce picosecond pulses and thereafter applications using it as a seed source in an amplifier cascade to achieve high output powers. Each topic is briefly summarised and suggestions for improvements and potential future research are considered in this chapter.

8.2 Femtosecond pulse laser systems

8.2.1 Yb-doped fiber oscillator

The development of a modified version of the oscillator, previously built by Dr Jonathan Price from our group [1], was completed. Further detailed empirical studies were carried out to better understand the limitations of its performance and thereafter improvements were made to the cavity. The result was the demonstration of an oscillator which produces shorter pulse durations and environmentally more stable pulses than the original. The addition of a short length of Hi-Bi fiber, changing the SESAM (to one with a wider and flatter reflectivity spectrum) and reducing the cavity fiber length (to reduce the TOD contribution from both the fiber and the diffraction grating), allowed us to achieve output pulses with durations as short as 106 fs and a FWHM bandwidth of 22 nm compared to previous durations of 141 fs and a FWHM bandwidth of 18nm.

The oscillator was also made environmentally more stable by adding Faraday rotators (FR) at both ends of the fiber gain section. The FRs cause the polarisation of the pulses travelling in

the cavity to be rotated by 90 degrees when traveling in opposite directions along the fiber. This averages to zero any linear polarisation changes within the cavity, over a round trip, thereby maintaining the modelocking stability while the fiber is disturbed and also over a wide temperature range. This modified oscillator, with improved overall reliability (i.e. self starting, environmental and noise) and output pulse performance (shorter duration and broader bandwidth), was later used as a seed source for many experiments carried out (see chapter 5) in our group.

Further modifications could be made to the oscillator cavity to improve its performance. For example, in order to achieve ultrashort optical pulses, we need to minimise the phase distortions within the cavity. Treacy, Christov and Tomov [2, 3] pointed out that the pulse compression of a large bandwidth signal, using bulk gratings, is limited by uncompensated cubic phase distortion i.e. TOD. Thus by using prism sequences to provide the required anomalous dispersion compensation, the TOD could also be simultaneously compensated, as the prisms provide TOD with an opposite sign to the cavity fiber. This prism sequence was demonstrated by Vincent Cautaerts [4] when he was in the ORC. He implemented this prism sequence to provide anomalous dispersion compensation in a stretched pulse Yb^{3+} ring cavity laser, achieving pulse durations as short as 65 fs, with a spectral bandwidth of 32 nm. His results provided evidence that shorter pulses were possible to achieve using prisms.

The frequency shifted feedback (FSF) technique could be implemented to ensure robust self-starting without any limitation on the wavelength of operation. This FSF technique has been demonstrated by J. Porta *et al.* [5] to develop an environmentally stable, picosecond, Yb^{3+} fiber laser and by L. Lefort *et al.* [6] within a similar cavity design as ours. He managed to achieve a highly stable stretched pulse 68 fs Yb^{3+} fiber laser using this technique.

We would also like to move towards an all fiber cavity by replacing the bulk grating pair with a length of anomalously dispersive HF [7, 8] and by replacing the PBS with a fiber polarizer.

8.2.2 Chirped Pulse Amplification

In this thesis, I have described the development of a commercially sponsored, all Yb^{3+} fiber, CPA system incorporating a CFBG pulse stretcher and bulk grating compressor with both 2^{nd} and 3^{rd} order dispersion compensation. The CPA system produced clean and stable 500 fs pulses with spectral FWHM bandwidth of ~ 5 nm and having 10 μJ pulse energy. We had hoped to achieve up to 50 μJ but were limited by the onset of SRS.

Another limitation was imposed by the bulk grating compressor that was used. We would encounter ~ 3 dB loss due to the efficiency throughput at the optimum compressor settings. Therefore to reach the 50 μJ target, meant that we have to obtain ~ 100 μJ pulses after the final amplification stage. This limitation may be resolved by using a more efficient compressor grating with a reflective dielectric coating (e.g. >95% efficiency) or by using silica transmission gratings that have been designed to handle >100W average power from a CPA system [9], these however are not currently commercially available.

Another group [10] have demonstrated Yb-fiber CPA systems producing 1.2 mJ pulses (repetition rate 1.7 kHz) with 380 fs duration, and M^2=1.16, using a 50 μm core (length = 2.6 m) fiber for the final amplifier. However this system utilised a bulky, free-space, pulse stretcher and a complex seed source which makes it less practical commercially. The maximum pulse energy was again limited by the onset of SRS, so obtaining higher energy pulses will require use of larger core fiber. Therefore we intend to use fiber amplifiers with larger core-dimensions (to increase the effective mode area, as described in section 2.2.3.3) in the final amplification stage. Since then, we have fabricated LMA amplifier fibers with larger core diameters. Two examples of these fibers are 30 and 40 μm core diameter, LMA fibers. Using a 6 m length for both, and with the requirement to obtain 20 dB of gain, the SRS threshold for both fibers was calculated to be ~ 70 μJ and ~ 125 μJ respectively, which would be sufficient to achieve 50 μJ pulses. This increase in effective core area also increases the maximum energy storage possible in the power amplifier. Extracting from figure 2.9, the maximum energy storage in a 30 μm and 40 μm core diameter fiber are 3.8 mJ and 6.7 mJ compared to 1 mJ for a 16.5 μm diameter core. However, the trade-off for significant further increases in pulse energy, by using fiber amplifiers with larger core dimensions may be the loss of output beam quality. Previously, we have used both 915 and 976 nm pump diodes for the final amplification stage. Since the pump absorption length of the 915 diode was ~ three times longer than the 976, by using only 976 nm diode pumps, we would be able to use shorter fiber lengths and hence increase the SRS threshold.

Dr Ibsen of the ORC has recently obtained a phase mask which could fabricate CFBGs with larger spectral windows, and optimised 2nd and 3rd order dispersion values could also be implemented to achieve higher pulse energies and shorter compressed pulse durations. But this improvement must be preceded by increasing the gain bandwidths of the pre-amplifier stages at the operating wavelength so that spectrally broader pulses could be amplified. Increasing the gain bandwidth will also proportionately increase the duration of the stretched pulses for a fixed chirp rate, which will also raise the SRS threshold.

By focussing diffraction limited, moderate energy, femtosecond pulses (i.e. ~100 μJ, <200 fs) to achieve extreme fields, applications for fiber pumped ultrashort pulses would be possible in areas such as femtosecond high harmonic generation extending into the UV and x-ray spectral regions.

8.2.3 Direct amplification

Yb^{3+} fiber direct amplification systems obtaining parabolic pulses have previously been demonstrated with average powers up to 17 W (pulse energy ~ 230 nJ) using a bulk glass seed laser [9] and up to 13 W (pulse energy ~ 260 nJ) with a fiber based seed laser [11]. However both of these systems utilised only a single amplification stage which limits the gain to ~ 30-40 dB hence restricting the number of possible applications and suitable seed sources. Much higher total gain should therefore be possible by using a cascade of amplifiers compared to the single stage amplifier systems.

In chapter 5 of this thesis, I have demonstrated a robust, diode pumped, cascaded, all Yb^{3+} fiber, direct amplification system (both seed and amplifier) based on parabolic pulse amplification, capable of producing high quality single moded ~ 400 nJ pulses with recompressed pulse durations of 110 fs at average powers in excess of 25 W. With further engineering work, this system could have a compact form to provide a simple and practical fibre based solution for a wide range of high average power femtosecond pulsed laser applications.

Maximum pulse energies were limited (before the onset of pulse distortions) by the gain bandwidth of the final amplifier. Therefore it would be useful to investigate the possibility of exploiting the potential Yb-bandwidth (>50 nm) to achieve amplifiers with wider gain bandwidths, hence enabling clean higher energy pulses to be obtained. However I believe the ultimate limitation on output pulse energies would be SRS. Therefore to achieve a significant increment in output pulse energy, increasing the SRS threshold would be necessary. The initial practical approach would be to increase the effective core area of the fibre amplifier. Using this approach would also delay the amplified pulse from experiencing the parabolic phenomenon till reaching higher energies, thereby relaxing the earlier constraint imposed by the amplifier's gain bandwidth at lower pulse energies. Another practical limitation that we found, whilst running this experiment, was damage to the LMA fibre end facet. However this issue could be easily solved by using end caps (see section 5.3.2.4).

A robust high-repetition rate fibre-based source of high peak power pulses could be envisaged for supercontinuum generation which could be used for metrology, high speed micro and nano-scale material processing which would enable dramatic improvements in processing times and precision for industrial processing applications, frequency doubling/quadrupling of the pulses into the visible/UV would be interesting for laser displays and biological studies and finally, it can be used in LIDAR range finding systems.

8.3 High power nanosecond pulsed fibre laser system

8.3.1 Q-switch fibre laser

The motivation behind the work in this chapter is produce a low cost, compact, Q-switched fibre laser system that can provide pulse energies compatible with application requirements and comparable to their solid state counterparts. Traditionally, and still currently, solid state systems have been used to provide high energy and peak power laser systems to the industry [12]. However compared to these solid state systems, fibre laser systems provide better quality (the tighter beam confinement within their smaller core provides better output modal quality) pulses at much higher repetition rates, higher wall-plug efficiency and excellent heat dissipation. Besides these benefits, they have a smaller footprint, and lower production and ownership costs make them even more commercially attractive.

In chapter 5, I have completed the development of a compact and cheap Q-switched fibre laser system that meets the requirements specified by our commercial sponsors. The work presented in chapter 5 was unique, compared to other Q-switched systems previously developed. Previous authors have demonstrated Q-switched fibre laser systems which provide pulse energies up to 7.7 mJ but the beam was highly multimode, with an M^2 of 7, and the pulse duration was long [13]. 0.6 mJ pulses energy at a very high repetition rate of 200 kHz have been achieved within a medium size 30 μm core, LMA, Yb^{3+} doped fibre ($M^2 > 2$) [14] and 4.2 ns output pulses with relatively high 1.57 mJ pulse energies through a stimulated Brillouin scattering Q-switched technique (however this is generally an unstable process) [15]. Though these systems each have their attractive attributes, the output pulses were either too long, unstable and/or multi transverse moded to be used by the industry (for example, material processing applications). Most recently, 27 mJ, 50 ns long, pulses (M^2 of 6.5) were achieved from a master oscillator power amplifier (MOPA) chain at repetition rates of a few Hz.

Though high output pulse energies were achieved, the output beam quality was poor and the production cost also increases with a cascaded system.

Hence, our group was contracted by our commercial sponsor to develop a cheap and compact (single stage), reliable, high repetition rate (to increase processing speeds in a production line), high output energy (~ 1mJ), short pulse duration (< 40 ns) good beam quality (M^2 < 2) system. In chapter 5, a single stage single mode (M^2=1.1) beam quality Q-switched system providing output pulses with 1.21 mJ pulse energy and duration of 37 ns, operating at a 10 kHz repetition rate, was achieved and its performance characterised in detail.

8.3.2 Direct modulated laser diode MOPA.

In Chapter 5, I highlighted that although a single stage oscillator reduces manufacturing cost and size, it does not offer the flexibility to allow the real time adjustments to output pulse parameters, such as pulse durations and peak powers, that MOPA systems can give. Several nanosecond MOPA systems, based on fibre amplifiers, have been developed and commercialised over the years [11, 16-19]. However, none of the pulse seed sources used in these MOPA systems gives us enough flexibility and control over the output pulse parameters. This is because these systems utilise Q-switching techniques for their seed source which do not readily allow real time control to their output pulse parameters as the output pulse width depends on the cavity lifetime, hence limiting the available freedom of operation.

In chapter 6, I have described the development of a fibre MOPA system utilising a directly modulated laser diode seed source, where control over its output pulse characteristics is possible in real time. This project is a collaboration between Southampton Photonics Inc. (SPI) and our group. The objectives were to develop a MOPA system that delivers 0.5 mJ pulses, with durations between 10 -100 ns and at repetition rates of 10 – 200 kHz. These goals were partially met with the development of a MOPA system capable of delivering stable 10 ns, 0.76 mJ (of which 0.5 mJ pulse enrgy is centred at 1070 nm), pulses at 10 kHz repetition rate, with peak intensities up to 113 kW. This development is described in chapter 6.

There were various limitations preventing us from achieving all our objectives. Firstly, maximum available pump power prevented us from scaling the 0.5mJ result to the 100 kHz repetition rate, but this did not present any fundamental limit to performance. The main issue limiting the maximum pulse energy achievable arises from the onset of SRS. Furthermore, the onset of SRS is created prematurely, as a consequence of gain saturation effects shaping the

amplified pulse. This gain shaping effects change the shape of the square input pulses, such that the pulse sharpens as it propagates along the amplifier, resulting in output pulses which are distorted and significantly shorter (measured by FWHM duration) than the input pulses. This results in an increase in the peak intensity of the propagating pulse hence reducing the threshold for non-linear effects such as SRS.

A possible avenue of further work is to modify the shape of the injected pulses [20], using a lower intensity leading edge to compensate for gain saturation effects, hence producing square output pulses. Modifying the pulse shape would be a relatively straightforward procedure experimentally with a directly driven diode. Alternatively, if the fundamental requirement of a system is maximum peak power, rather than maximum pulse energy, gain saturation could be harnessed to generate very short output pulses with very high peak powers within all-fibre MOPA systems for industrial applications such as machining or ablation.

Several methods could be used to reduce or eliminate SRS. The length of the amplifier fibre could be shortened, larger core dimensions could be used, pulse shaping of the input pulse could reduce the effects of pulse sharpening, and modifying the gain profile within the amplifier fibre could reduce the effective length.

As shown in section 6.6.3.3.1, the SRS generated components lie at the sharp leading edge of the pulse. Hence the Raman pulse is of much shorter duration and higher peak intensity than the 1070nm output pulse. This could be utilised (perhaps in conjunction with amplifying the gain saturation effects) to generate short duration, high peak power pulses at wavelengths longer than 1070nm.

In conclusion, high power nanosecond pulse fibre laser systems have the potential to become very attractive for the industry as they provide a cheaper, more compact, more efficient and better output beam quality, alternative to their solid state counterparts. These high power, nanosecond pulse, fibre laser systems are used in today's industries for laser marking/engraving, welding, machining and material processing. Furthermore these systems could also be envisaged in the near future for frequency conversion, laser spectroscopy and sensing (i.e. LIDAR) applications.

8.4 Gain switched laser diode

In chapter 7, I have described the development and completion of a gain switched laser diode source producing ps pulses operating at ~ 1 μm wavelength. We believe that this is the first time that gain switched pulses have been generated using 1.06 μm semi-conductor laser diodes. In this chapter, I have also described a two stage amplifier cascade used to amplify the compressed seed pulses generated by the gain switched laser diode developed. Negatively chirped, 57 ps, gain switched pulses, at 1 GHz repetition rate, were compressed using a long length (~15.7 km) of telecoms grade, SMF 28e, fibre to 20 ps. These pulses were subsequently amplified to average powers of 11.1W, which corresponds to output pulses having peak powers of 0.6 kW. The amplified pulses had FWHM spectral width = 0.11 nm and a $\Delta\tau.\Delta\nu$ = 0.58. The maximum output power achievable was limited by the pump power available at the time of the experiment.

Further work (though not presented in this chapter) was subsequently carried out using this gain switched seed source. Additional work was carried out to use chirped fibre bragg gratings (CFBG) developed in house by Dr Ibsen. He made the CFBGs using dispersion parameters that were obtained when the length of SMF 28e fibre compressor was used. In this experiment, 57 ps gain switched pulses were compressed down to 16.4 ps and subsequently amplified to provide 3 W of average output power at 1 GHz repetition rate. The amplified pulses had FWHM spectral width = 0.16 nm and a $\Delta\tau.\nu$ = 0.692. The results were presented in Conference on Lasers and Electro Optics (CLEO) Europe (Munich) 2005 (see appendix A3). Together with another colleague, Pascal Dupriez, we later integrated this system, presented in CLEO Europe 2005, into another amplifier chain and the 16.4 ps pulses were amplified to produce an output with average power in excess of 320 W, at a repetition rate of 1 GHz, at 1060 nm, which we believe was the record. This corresponds to output pulses with peak powers of 16 kW. This work was presented in Optical Fibre Communications (OFC) 2005 in Anaheim as a post deadline paper. A copy of the submission can be found in appendix A4.

These high average power laser sources with picosecond pulse durations, in the 1 μm wavelength range, would be attractive for applications such as micro-machining [21] and laser projection systems [22]. Furthermore, by reducing the output repetition rate of the gain switched laser diode (which is a trivial process compared to mode-locked oscillators, and could be done in real time), higher output peak powers can be achieved. Applications such as frequency doubling/quadrupling of the pulses into the visible/UV could be envisaged by

achieving higher output peak powers. This would be interesting for ultrafast chemical and biological studies.

BIBLIOGRAPHY

1. Lefort, L., Price, J.H.V., Richardson, D.J., Spuhler, G.J., Paschotta, R., Keller, U., Fry, A. R., Weston, J., *Practical low-noise stretched-pulse Yb^{3+}-doped fiber laser.* Optics Letters, 2002. **27**(5): p. 291-293.
2. Christov, I.P. and Tomov, I.V., *Large bandwidth pulse compression with diffraction gratings.* Optical Communications, 1986. **58**(5): p. 338-342.
3. Treacy, E.B., *Optical pulse compression with diffraction gratings.* IEEE Journal of Quantum Electronics, 1969. **5**(9): p. 454-458.
4. Cautaerts, V., Richardson, D.J., Paschotta, R. and Hanna, D.C., *Stretched pulse Yb3+:silica fiber laser.* Optics Letters, 1997. **22**(5): p. 316-318.
5. Porta, J., Grudinin, A.B., Chen, Z.J., Minelly, J.D., Traynor, N. J., *Environmentally stable picosecond ytterbium fiber laser with a broad tuning range.* Optics Letters, 1998. **23**(8): p. 615-617.
6. Lefort, L., Albert, A., Couderc, V. and Barthelemy, A., *Highly stable 68-fs pulse generation from a stretched-pulse Yb3+-doped fiber laser with frequency shifted feedback.* IEEE Photonics Technology Letters, 2002. **14**(12): p. 1674-1676.
7. Lim, H., Ilday, F.O. and Wise, F.W., *Generation of 2-nJ pulses from a femtosecond ytterbium fiber laser.* Optics Letters, 2003. **28**(8): p. 660-662.
8. Avdokhin, A.V., Popov, S.V. and Taylor, J.R., *Totally fiber integrated, figure-of-eight, femtosecond source at 1065 nm.* Optics Express, 2003. **11**(3): p. 265-269.
9. Limpert, J., Schreiber, T., Clausnitzer, T., Zollner, K., Fuchs, H. J., Kley, E. B., Zellmer, H., Tünnermann, A., *High-power femtosecond Yb-doped fiber amplifier.* Optics Express, 2002. **10**(14): p. 628-638.
10. Galvanauskas, A., Sartania, Z. and Bischoff, M. *Millijoule femtosecond all-fiber system.* in *Tech. Dig. Conference Lasers Electro-Optics, CLEO.* 6-11 May. 2001.CMA1. p. 1-2.
11. Galvanauskas, A., *Mode-scalable fiber-based chirped pulse amplification systems.* IEEE Journal Of Selected Topics In Quantum Electronics, 2001. **7**(4): p. 504-517.
12. StPierre, R.J., Holleman, G.W., Valley, M., Injeyan, H., Berg, J. G., Harpole, G. M., Hilyard, R. C., Mitchell, M., Weber, M. E., Zamel, J., Engler, T., Hall, D., Tinti, R. Machan, J., *Active tracker laser (ATLAS).* IEEE Journal Of Selected Topics In Quantum Electronics, 1997. **3**(1): p. 64-70.
13. Renaud, C.C., Alvarez-Chavez, J.A., Sahu, J.K., Nilsson, J., Richardson, D. J., Clarkson, W. A., *7.7mJ pulses from a large core Yb-doped cladding pumped Q-switched fibre laser.* in *Tech. Dig. Conference on Lasers and Electro-Optics, CLEO.* 2001. Baltimore, CTuQ5. p.219.
14. Jeong, Y., Sahu, J.K., Laroche, M., Clarkson, W.A., Furusawa, K., Richardson, D. J. Nilsson, J., *120-W Q-switched cladding-pumped Yb-doped fibre laser. CLEO/Europe-EQEC.* 2003. Munich, CL5-4-FRI.
15. Fan, Y.X., Lu, F.Y., Hu, S.L., Lu, K.C., Wang, H. J., Dong, X. Y., Zhang, G. Y., *105-kW peak-power double-clad fiber laser.* IEEE Photonics Technology Letters, 2003. **15**(5): p. 652-654.
16. Di Teodoro, F., Koplow, J.P., Moore, S.W. and Kliner, D.A.V., *Diffraction-limited, 300-kW peak-power pulses from a coiled multimode fiber amplifier.* Optics Letters, 2002. **27**(7): p. 518-520.
17. Limpert, J., Hoffer, S., Liem, A., Zellmer, H., Tunnermann, A., Knoke, S., Voelckel, H., *100-W average-powerg high-energy nanosecond fiber amplifier.* Applied Physics B-Lasers And Optics, 2002. **75**(4-5): p. 477-479.

18. Limpert, J., Liem, A., Zellimer, H., Tunnermann, A., Knoke, S., Voelckel, H., *High-average-power millijoule fiber amplifier system.* in *Tech. Dig. Conference Lasers Electro-Optics, CLEO.* 2002. **1**(1): p.591-2.
19. Chen, M.-Y., Chang, Y.-C, Galvanauskas, A., Mamidipudi, P., *et al., 27-mJ nanosecond pulses in M^2 = 6.5 beam from a coiled highly multimode Yb-doped fiber amplifier.* in *Conference on Lasers and Electro-Optics, CLEO.* 2004. San Francisco, CTuS4. **1**(1): p.3.
20. Wang, Y. and Po, H., *Dynamic characteristics of double-clad fiber amplifiers for high-power pulse amplification.* Journal of Lightwave Technology, 2003. **21**(10): p. 2262-2270.
21. Chichkov, B.N., Momma, C., Nolte, S., Alvensleben, F.V., Tünnermann, A., *Femtosecond, picosecond and nanosecond laser ablation of solids.* Applied Physics A, 1996. **63**: p. 109-115.
22. Brunner, F., Innerhofer, E., Marchese, S.V., Südmeyer, T., Paschotta, R., Usami, T., Ito, H., Kurimura, S., Kitamura, K., Arisholm, G., Keller, U., , *Powerful red-green-blue laser source pumped with a mode-locked thin disk laser.* Optics Letters, 2004. **29**: p. 1921-1923.

Appendix A1

TIMING JITTER MEASUREMENTS

In this appendix, I describe the technique used to characterise the amplitude and timing jitter of a laser generating a periodic train of pulses. The power spectral density approach to quantify the amount of noise in our system is mainly extracted from these three publications [1-3].

I start by assuming some possible causes of noise in our system. In the gain switched system, the two possible sources are i) Drive circuit and ii) Turn-on transients at the onset of the driving electrical pulse (see section 8.4.2). The frequency of the noise from the drive circuit should be in the range of 1 kHz to 1 MHz. It is important to note that the phase information is lost when the power spectrum is measured. Though the equations presented from the Von der Linde paper [1] are derived for the c.w. mode-locked laser case, the principle behind it can be generic for all systems producing a periodic train of pulses, i.e. gain switched system, since it does not take into account any phase deviations but only the pulse to pulse intensity and timing variations. However we must note that the output from the gain switched system consists of other noise components that are not found in CW mode-locked lasers and we will discuss these later.

A1.1 Correlated Jitters

Von der Linde describe the output intensity of a perfectly mode-locked laser as

$$F_o(t) = \sum_{\mu} f(t + \mu T) \qquad \text{(A1.1)}$$

where f(t) = temporal intensity profile of the individual pulse, T is the repetition period and integer μ runs from negative to positive infinity.

A noisy mode-locked oscillator with fluctuations is then describe by,

$$F(t) = F_o(t) + \delta F(t) \qquad \text{(A1.2)}$$

I assume that the output fluctuations vary slowly relative to the pulse intensity f(t) and that the pulse shape can be considered constant and is still Fourier transform limited. Thus the noisy train of pulses can be described as,

$$F(t) = F_o(t) + F_o(t)A(t) + \dot{F}_o(t).T.J(t) \qquad \text{(A1.3)}$$

The second term on the R.H.S denotes the amplitude jitter where A(t) gives the random deviations from the mean. The third term represents the timing jitter or change in repetition time ($f(t_\mu + \Delta t_\mu) = f(t_\mu) + \dot{f}(t_\mu).\Delta t_\mu$ when Δt_μ is small, such that $\Delta t_\mu = T.J(t)$). $\dot{F}_o(t)$ is the time derivative of the pulse intensity in the absence of noise and J(t) represents the time deviation from the repetition time. Because the fluctuation components in F(t) are uncorrelated, the RF power spectrum of the laser intensity can be derived from the Fourier transform of the autocorrelation function F(t) (real values) which is expressed as,

$$P_F(\omega) = (\Delta\omega)^2 \left|\tilde{f}(\omega)\right| \sum [\delta(\omega_\mu) + P_A(\omega_\mu) + (2.\pi.\mu)^2 P_J(\omega_\mu) \qquad \text{(A1.4)}$$

The sum represents a series of frequency bands centred around ω_μ with spacing $\Delta\omega = \frac{2.\pi}{T}$. Each band consists of the δ-component which represents the noise free pulse train, $P_A(\omega_\mu)$ is the power spectrum of amplitude noise A(t) and $P_J(\omega_\mu)$ is the power spectra of the timing jitter J(t). $f(\omega)$ is the Fourier transform of the pulse intensity which was assume earlier to be slow-varying and treated as a constant. Definition of μ is an integer running from minus infinity to plus infinity. From equation (A1.4), we can see that the timing jitter term increases in proportion to μ^2, this contribution increases for higher harmonics. This allows us to distinguish between the amplitude and timing jitter contributions of the total noise power spectrum.

Figure A1.1 shows a sketch of the different noise contributions. P_c = peak of the δ-function contribution, P_A = peak of amplitude jitter contribution and P_J = peak of the timing jitter contribution.

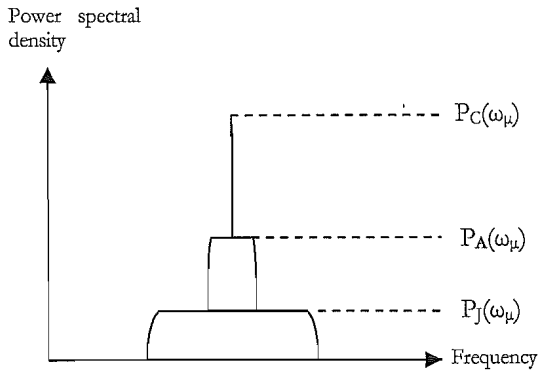

Figure A1.1: Power spectral density (PSD) sketch of various contributions of components to fluctuations.

The r.m.s. intensity deviation (ΔE of pulse energy E) and temporal deviation (Δt from pulse repetition period T) can be directly obtained from the area of the respective noise spectrum [1] as,

$$(\frac{\Delta E}{E})^2 = \int_{-\infty}^{+\infty} P_A(\omega)d\omega \qquad \text{(A1.5)}$$

$$(\frac{\Delta t}{T})^2 = \int_{-\infty}^{+\infty} P_J(\omega)d\omega \qquad \text{(A1.6)}$$

Depending on the frequency span and resolution bandwidth used on the RF spectrum analyser, noise contributions at different noise bands can be obtained. For example,

i) High resolution allows the low frequency components to be resolved.

ii) Low resolution allows the high frequency noise components to be determined.

To quantify the noise contributions, it is useful to consider the following,

i) extinction ratio between P_C and the peak of the various bands (P_A or P_J)

ii) FWHM bandwidth of the various noise bands (which allow discrimation between the different timing jitter contributions).

The integrals (A1.5) and (A1.6) can be approximated by the product of the FWHM bandwidth of the noise component and its peak power density which gives,

$$\int_{-\infty}^{+\infty} P(\omega)d\omega \approx 2.\pi.\Delta f.P(\omega_\mu) \qquad \text{(A1.7)}$$

From equation (5) we obtained the equation to calculate r.m.s amplitude jitter (Δf_{res} = selected resolution bandwidth of spectrum analyser),

$$\frac{\Delta E}{E} = \sqrt{\frac{\Delta f_C}{\Delta f_{res}} . (\frac{P_A}{P_C})_{\mu=0}} \qquad \text{(A1.8)}$$

However in the evaluation of the gain switch diode, we did not use this method to calculate amplitude jitter (this equation is mention for completeness) as we have obtained it directly from the HP 83480A digital communication analyser using the histogram function. The amplitude jitter was found to be < 1% with seeding (see section 7.4.2).

For r.m.s timing jitter, we ignore the amplitude jitter terms if we obtain measurements to a sufficient order of the harmonic such that the two contributions de-couple (i.e. $(2.\pi.\mu)^2 P'_J(0_\mu) >> P_A(0)$. We obtain,

$$\frac{\Delta t}{T} = \frac{1}{2.\pi.\mu} \sqrt{(\frac{\Delta f_J}{\Delta f_{res}}) . (\frac{P_J}{P_C})_\mu} \qquad \text{(A1.9)}$$

where μ is the μth harmonic. From the pedestal on the 5th harmonic (see figure 7.6 (b) in section 7.4.2), we estimate Δf_J =2.8 KHz (FWHM of pedestal i.e. 2.8 kHz noise component) and $(\frac{P_J}{P_C})_5$ =-49.3dB=$10^{-4.93}$, using a frequency span of 50 KHz and a resolution bandwidth of $\Delta f_{res} = 300Hz$, we obtained a correlated 2.8 kHz noise component Δt of ≈ 0.33 ps with 0.07 mW of seed power.

A1.2 Uncorrelated Jitters

Several authors have presented measurements of the r.m.s. correlation timing jitter and amplitude jitter using the power spectrum. The theory method described in [1], can be used to consider jitter with any degree of pulse to pulse correlation (correlated jitter), however it is inadequate for gain switched systems. This is because in gain switched systems, additional uncorrelated timing noise is introduced as a result of the random intra-cavity spontaneous emission at the onset of each pulse (i.e. randomness between the onset of the electrical pulse

and laser radiation). In this section, we will be describing the method we used to obtain the uncorrelated noise jitter. The theory presented here is mainly extracted from [2, 3].

Leep *et al.* modelled the gain switched laser as a comb of output pulses having random intensity variations and turn-on-delays. The temporal intensity of the pulse train, assuming that the pulses are periodic with period T and having finite duration Δ, is modelled as,

$$F(t) = \sum_{\mu=-N}^{N} x_\mu f(t - \mu T - \tau_\mu) \qquad \text{(A1.10)}$$

where Δ = (2N+1)T, f(t) = pulse shape and x_μ and τ_μ are the amplitude and time delay of the nth pulse. Since x_μ and τ_μ are independent random variables, they can be described by the probability density functions $p_\mu(x)$ and $p_\mu(t)$ that are the same for all values of μ.

After evaluating the Fourier transform of $|F_\Delta(\omega)|^2$ (which is describe in [2]), the power spectrum function in the limit iof N → ∞ of the train of pulses can be described by,

$$P_F(\omega) = \frac{\langle x \rangle^2 |F(\omega)|^2}{T} \cdot \left[\sigma^2{}_r + (1 - |P_\tau(\omega)|^2) + \omega_1 |P_\tau(\omega)|^2 \sum_{\mu=-\infty}^{\infty} \delta(\omega - \omega_\mu) \right] \qquad \text{(A1.11)}$$

where $F(\omega)$ is the Fourier transform of the pulse profile f(t), $\langle x \rangle^2$ is the mean-square x_μ, T is the pulse to pulse period, $\sigma^2{}_r$ is the relative variance $= \dfrac{\sigma^2{}_x}{\langle x \rangle^2}$ (where $\sigma^2{}_x$ is the variance of intensities $= \langle x^2 \rangle - \langle x \rangle^2$), $P_\tau(\omega)$ is the Fourier transform of the probability density $p_\mu(t)$, $\omega_1 = \dfrac{2\pi}{T}$ is the pulse repetition frequency and $\omega_\mu = \mu\omega_1$ is the μth harmonic.

Let us evaluate equation (A1.11):

If it is a noiseless system, the first two terms in (A1.11) disappear because $p_\mu(x)$ and $p_\mu(t)$ become delta functions giving $\sigma^2{}_r = 0$ and $|P_\tau| = 1$. Thus leaving the third term where we now have a spectrum that represents a perfect pulse train having intensity proportional to $|F(\omega)|^2$ and period ω_1.

If the intensity noise is now introduced, the first term contributes a component proportional to $\sigma^2{}_r$ at each harmonic which is spectrally uniform (other than the factor $|F(\omega)|^2$). The mean squared intensity caused by the noise is proportional to the energy in this continuum.

The second term contributes a ω dependent continuum caused by the timing jitter. The energy is generated as a consequence of a loss of the discrete lines but there is also a roll off at the higher frequencies due to the attenuation factor $|P_\tau(\omega)|^2$. The different contributions to the power spectrum of the gain switched laser are represented independently in Equation (A1.11). Therefore the equation is valid for uncorrelated noise of any magnitude.

The frequency dependence component $P_\tau(\omega)$ of equation (A1.11) can be expanded in a Maclaurin series in the low noise limit. $P_\tau(\omega)$ is expressed as,

$$P_\tau(\omega) = 1 - i\langle\tau\rangle\omega - \frac{1}{2}\langle\tau\rangle^2\omega^2 + \ldots \qquad \text{(A1.12)}$$

using the Fourier transform derivative theorem. Therefore,

$$|P_\tau(\omega)|^2 = 1 - \sigma_\tau^2\omega^2 + O(\omega^4) \qquad \text{(A1.13)}$$

Approximating to the lowest order in $\sigma_\tau\omega$, the spectrum in equation (A1.11) is then,

$$P_F(\omega) = \frac{\langle x\rangle^2|F(\omega)|}{T}\left[\sigma^2{}_r + \sigma_\tau^2\omega^2 + \omega_1\sum_{\mu=-\infty}^{\infty}\delta(\omega-\omega_\mu)\right] \qquad \text{(A1.14)}$$

We should note that as in equation (A1.4) earlier, the ω^2 factor in the timing jitter term helps us to discriminate between the intensity and timing jitter quantities if a high enough order of harmonic the power spectra is obtained from experiment. We then take the ratio M(ω) of the continuous part of the spectral density derived in equation (A1.14) to the envelope of the discrete lines, we get $\omega_1 M(\omega) = \sigma^2{}_r + \sigma_\tau^2\omega^2$. The area B_μ under the continuum M(ω) over the spectral range $\omega_\mu \pm \frac{1}{2}\omega_1$ is then,

$$B_\mu = \sigma^2{}_r + (\mu^2 + \frac{1}{12})\sigma_\tau^2\omega_1^2 \qquad \text{(A1.15)}$$

Figure A1.2 shows an example power spectral density (PSD) plot of a train of pulses from a gain switched laser showing the discrete components at each harmonic and the continuous

part of the PSD consequence of uncorrelated jitter. Though this model is not complete for gain switched systems, as they consist of noise due to pulse shape fluctuations, and these contributions to M are only considered as ω^4 or higher. If you compare equation (A1.4) and A1.14), they are comparable except that the amplitude and timing jitter are modelled as continuous time variables A(t) and J(t) with power spectra $P_A(\omega_\mu)$ and $P_J(\omega_\mu)$ respectively (see figure A1.1). Whereas, in the uncorrelated case, the intensity jitter has no ω dependence and timing jitter contributes as an energy loss component of the discrete lines (see figure A1.2).

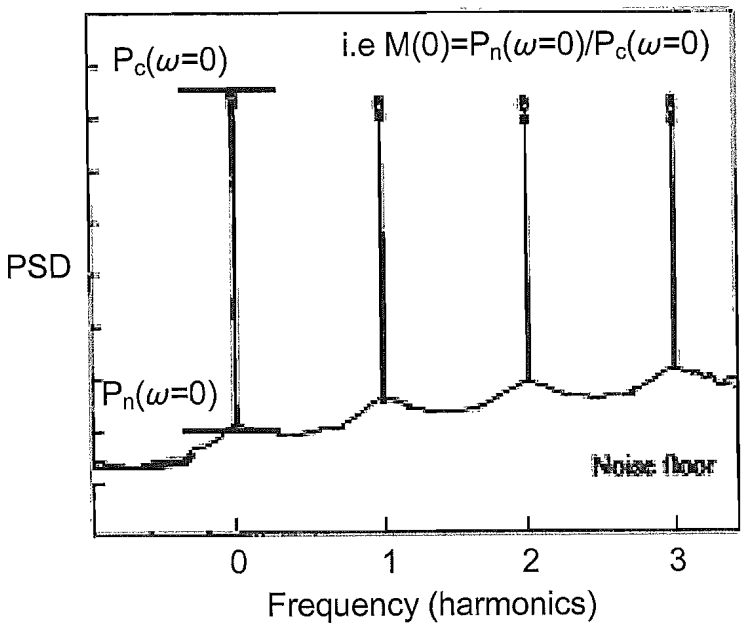

Figure A1.2: An example of a power spectral density (PSD) plot for a gain switched pulse train showing the envelope of the discrete lines at each harmonic and the continuous part of the PSD consequence of uncorrelated jitter between pulses.

From equation A1.15, we can estimate the separate contribution of the uncorrelated amplitude and timing jitters by obtaining experimental measurements of B_μ for a number of values of μ. Approximating equation (A1.15) by the product of the FWHM bandwidth of the noise component and the peak power of the μ^{th} harmonic (see figure A1.2), B_μ can written as,

$$B_\mu = \frac{\omega_1 . P_n}{2.\pi.\Delta f_{res} P_c} = \frac{f_1 . P_n}{\Delta f_{res} P_c} \qquad \text{(A1.16)}$$

where f_1 is the repetition frequency, P_n is the power density of the uniform noise between harmonics and P_C is the integral of power density of the discrete components taken at the respective resolution bandwidth Δf_{res}.

Hence from equation (A1.15) and (A1.16) we obtained [3] the r.m.s. uncorrelated timing jitter,

$$\sigma_\tau = \frac{1}{2.\pi.\sqrt{\mu^2 + \frac{1}{12}}.f_1} \sqrt{\frac{P_n}{P_c}.\frac{f_1}{\Delta f_{res}}} \qquad \text{(A1.17)}$$

here we assume that the intensity term σ_r^2 term is negligible ≈ 0 compared to the timing jitter term if we can measure the power spectra at a harmonic much higher than the fundamental. How high a harmonic depends on the magnitude of the σ_r^2 term and frequency cut-off for the jitter term due to $P_\tau(\omega)$ in equation (11). $\sigma^2 r$ can be obtained directly from equation (A1.15) once σ_τ is found.

In terms of uncorrelated jitter for our system (see section 7.4.2), from the uniform noise power between $\omega_5 \pm \frac{1}{2}\omega_1$ at the 5th harmonic, we estimate $(\frac{P_n}{P_c})_5$ =-56.1dB=$10^{-5.61}$, using a frequency span of 1 GHz and a resolution bandwidth of $\Delta f_{res} = 1MHz$, we obtained the r.m.s. timing jitter $\sigma_\tau \approx$ 1.57 ps at 0.014 mW seed power (see figure 7.6(c)).

Substituting estimated values from experiment of P_n= -79.8 and P_C=-10.5 at the fundamental harmonic $((\frac{P_n}{P_c})_1 = -69.3dB = 10^{-6.93})$ and σ_τ into equation (A1.15), we get the r.m.s. intensity jitter.

$$\sigma_r = \sqrt{B_1 - (1^2 + \frac{1}{12})\sigma_\tau^2 \omega_1^2} = \sqrt{\frac{f_1.P_n}{\Delta f_{res} P_c} - (1^2 + \frac{1}{12})\sigma_\tau^2 (2.\pi.f_1)^2} = 0.5\%$$

REFERENCES

1. Von der Linde, D., *Characterization of the Noise in Continuously Operating Mode- Locked Lasers.* Applied Physics B-Photophysics and Laser Chemistry, 1986. **39**(4): p. 201-217.
2. Leep, D.A. and Holm, D.A., *Spectral Measurement of Timing Jitter in Gain-Switched Semiconductor-Lasers.* Applied Physics Letters, 1992. **60**(20): p. 2451-2453.
3. Jinno, M., *Correlated and Uncorrelated Timing Jitter in Gain-Switched Laser-Diodes.* IEEE Photonics Technology Letters, 1993. **5**(10): p. 1140-1143.

Appendix A2

DIRECTLY MODULATED DIODE SOURCES.

A2.1 Electronic Drive Circuit

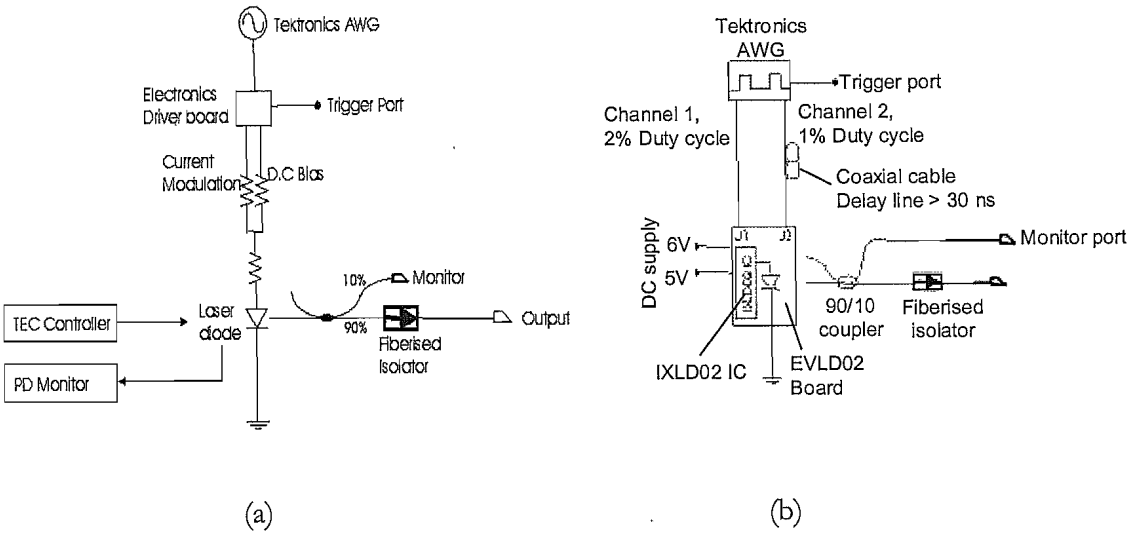

Figure A2.1: Setup of direct laser diode module (a) In-house (b) Commercial EVLD02 board.

The setup for the directly modulated diode laser is shown in figure A2.1. Two different high speed laser diode driver circuits were used in our experiments. The first driver was developed in house and the other was a commercial EVLD02 board from Directed Energy Inc. (DEI). A Tektronics 2021 arbitrary waveform generator (AWG) was used to control both drivers. However, unlike the in-house built driver board, which requires the AWG to determine the output pulse duration, the EVLD02 board has on-board control over the output pulse duration. Impedance matching resistors and a butterfly mount were used to interface the laser diode to the driver boards.

The schematic of the in-house driver board can be found in figure A2.2 (a). The circuit on the PCB board in (a) is separated into 3 main sections, the laser diode, the iC-HK 155MHz laser switch chip and the bypass circuitry. Demands on the power supply, to function at frequency rates of up to MHz, with sub-nanoseconds or nanoseconds rise and fall times, can increase the effective impedance (due to the inductive reactance of any inductive conductors

(i.e. printed circuit trace, wire) between the power rail and the active device) by up to hundreds of ohms. This increase in impedance can result in perturbations in the power supply rail generating oscillations or instability in the whole circuit which can result in circuit failure. The solution is to use a set of 8 capacitors (C13 to C20) in parallel, to act as a bypass between the VCC power supply rail and ground before each device (i.e. the laser diode and iC-HK chip). This bypass circuit is critical to maintain the integrity of the power distribution to the various devices, i.e., to maintain the low impedance of the true voltage source, to counteract the inductance of the finite length of the conductors that distribute the power to the circuits.

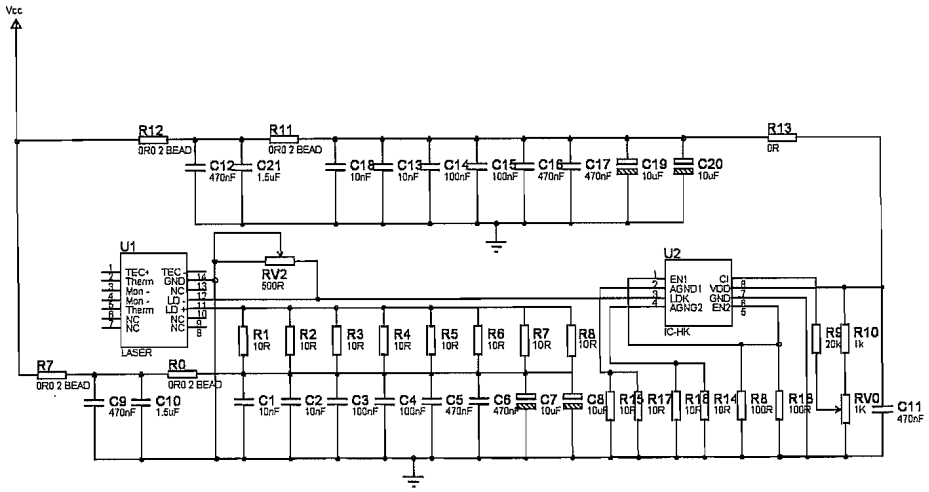

(a)

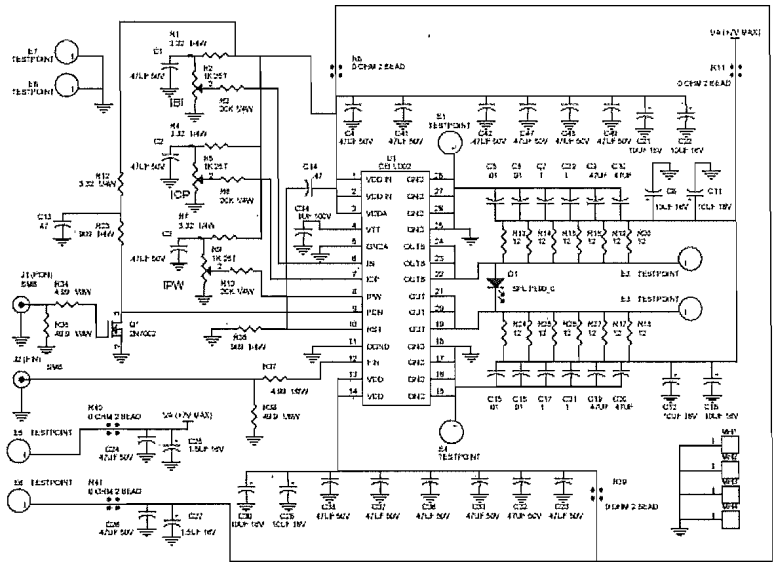

(b)

Figure A2.2: Schematic diagram of (a) In-house and (b) DEI EVLD02 fast laser diode drivers.

The iC-HK chip from iC-Haus is a laser switch for driving laser diodes from c.w. to 155 MHz. It provides spike-free switching of the laser current into the diode. The operating voltage range of 1 – 6V (maximum power supply voltage) that can be applied into the chip corresponds to a lower level peak current of 20 mA and maximum peak current limit of 1700 mA (limited by power supply and parallel resistors R1 to R8) during pulse operation. Schematic of the iC-HK chip can be found in the iC-Haus website [1].

A set of 8 resistors (R1 – 8) and capacitors (C1 - 8) in parallel, were used at the drive input into the laser diode to provide efficient current transfer and reduce circuit inductance. With this driver, the AWG directly controls the pulse duration, repetition rate and the peak magnitude of the modulated current driving the diode. Therefore changing the parameters of the output pulse requires changing the waveform settings on the AWG. Variable resistor RV2 sets the bias input to the laser diode and RV0 controls the magnitude of the modulated current injected into the laser diode. The set of eight 10 Ω resistors in parallel, before the laser diode LD+ port, is to reduce the effective impedance and inductance to allow high speed drive current operation.

The schematic of the commercial EVLD02 board can be found in figure A2.2 (a). The output pulse parameters are not set by the AWG when the EVLD02 driver board is used. The

AWG was used to provide pulse input only to turn the IXLD02SI chip on the board on and off, thereby controlling the repetition rate of the output. The EVLD02 evaluation board consists of DEI's IXLD02 laser diode driver Integrated Chip (IC) and the electronic circuitry required to operate the IXLD02 chip. The IXLD02 chip can generate pulses having pulse widths of < 1.5ns and rise times of approximately 600 ps at operating frequencies up to 17 MHz. The output pulse width, current and bias can be set at real-time by variable resistors labelled IPW, IOP and IBI respectively in figure A2.2 (b). A detailed specification and functional description of the EVLD02 driver board can be found in the DEI website [2].

A bypass circuit was implemented by connecting a row of capacitors to the VDD of the IXLD02SI chip. A similar configuration, having parallel sets of resistors and capacitors connected to the laser diode, was used. A comparison of the output performance of the diode using different boards will be discussed in the next section.

A2.2 Comparison of diode output between the two boards

Using the in-house driver board, 10 ns pulses at 100 kHz were generated from the laser diode. The output peak powers of these pulses were obtained over a range of wavelengths. The results are shown in figure A2.3 below. The highest peak power obtained is 402 mW, at a wavelength of 1054.8 nm, however it was found that the peak powers vary by only 4% over a 17 nm range. With the EVLD02 driver board, a peak power of 215 mW was obtained over the same range of wavelengths.

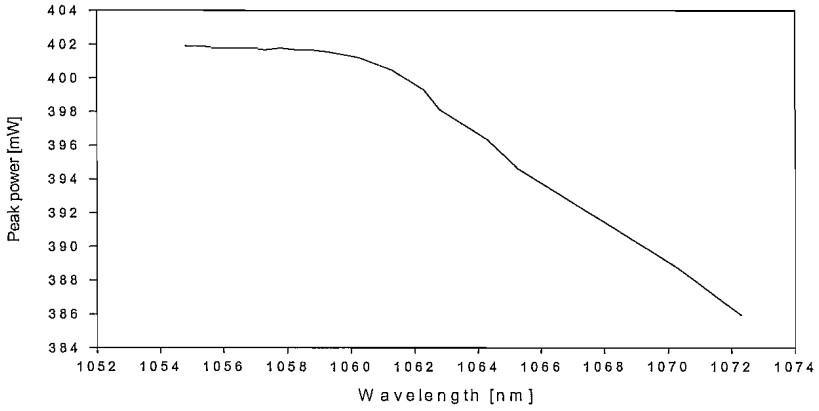

Figure A2.3: Diode peak power of 10 ns pulses at 100 kHz with lasing wavelength using in-house driver board.

Subsequently, 40 ns output pulses at 10, 50 and 100 kHz repetition rates were characterised for both driver boards. Figure A2.4 (a) shows the peak powers obtained from the two driver boards over the range of repetition rates. Amplitude jitter was also characterised for both driver boards, and results are presented in figure A2.4 (b).

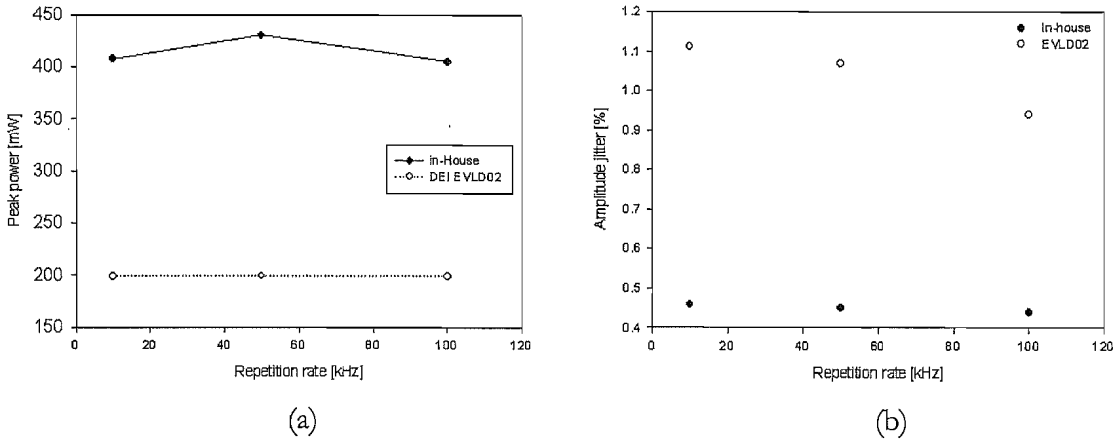

Figure A2.4: 40 ns pulses from laser diode using both drivers (a) Peak power (b) Amplitude jitter at 10, 50 and 100 kHz repetition rates.

Using the in-House driver board, we produced 40 ns pulses from the laser diode with peak powers between 405 – 430 mW over the above repetition frequency range. These were twice the peak power obtained using the EVLD02 board which produced only 200 mW peak-power output pulses. This I believe was because the maximum magnitude of the drive current injected into the laser diode using the in-house board was higher than the EVLD02 board. The amplitude jitter performance from the laser was better (0.44%) using the in-house driver board compared to the EVLD02 commercial board (0.94%).

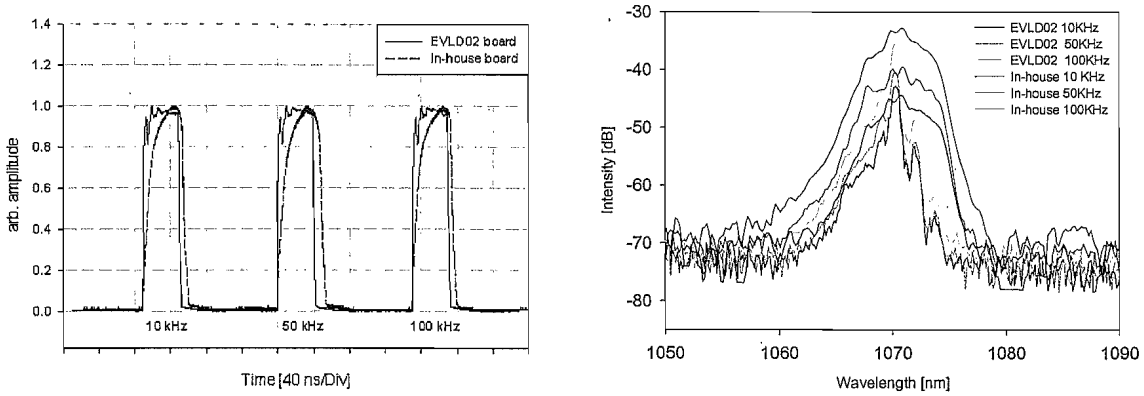

(a) (b)

Figure A2.5: Output 40 ns pulses from the directly modulated laser diode at different repetition rate. (a) Output temporal pulse and (b) spectra from laser diode with different driver boards.

The temporal and spectral outputs using the different driver boards, generating 40 ns pulses at 10, 50 and 100 kHz repetition rates, are shown in figure A2.5 (a) and (b) respectively. Output temporal pulse shapes from both driver boards, measured with a HP 83480A digital communications analyser, were compared. The difference in output pulse shape between the two boards I believe was due to the difference in transient response of the drive signal provided by the EVLD02 and in-house board. The transient response of the drive signal using the EVLD02 board was faster, generating squarer output pulses than the in-house driver board. This is because of the longer rise time delay caused by the electronic components on the in-house board.

Driver Board	**Peak power (mW)**	**Spectral FWHM (nm)**	**Amplitude noise (%)**	**Pulse energy [nJ]**
In-house	405	3.4	0.4	16.3
EVLD02	200	0.7	0.94	8

Table A2.1: Comparing performance of 40 ns pulses at 100 kHz between the, in-house developed, and commercially produced DEI EVLD02 ultra fast laser diode driver.

The spectra obtained from the in-house board have ~ 3-5 dB better optical signal to noise ratio (OSNR) compared to the EVLD02 board and have a slightly broader 3 dB bandwidth.

This is not surprising as the magnitude of the modulated signal injected into the diode is higher. Table A2.1 compares the performance between the two driver boards at 100 kHz repetition rate.

REFERENCES

1. iC-Haus, I.C. 2002: http://www.ichaus.de/.
2. Directed Energy, I., *EVLD02 evaluation board.* 2003: http://www.directedenergy.com/.

Appendix A3

A compact 1 GHz, 16ps pulse source operating at 1.06μm incorporating high power gain switched semiconductor laser and a fiber grating based pulse compressor

A. Piper, P.Dupriez, M.Ibsen, A.Malinowski, J.H.V. Price, B.C.Thomsen, D.J.Richardson
Optoelectronic Research Centre, University of Southampton, Southampton SO17 1BJ, UK
Tel: +44 23 8059 4527, Fax: +44 23 8059 3142, email: djr@orc.soton.ac.uk
L. M. B. Hickey, M. N. Zervas
SPI (Southampton Photonics, Inc.), 3 Wellington Park, Tollbar Way, Hedge End, Southampton SO30 2QU, UK
Tel: +44 (0)1489 779696 Fax: +44 (0)1489 779698

Abstract: 15.6 ps pulses at 1 GHz repetition rate were obtained from an amplified gain-switched 1.06 μm semiconductor diode laser utilising a Chirped Fiber Bragg Grating for pulse compression.

Gain-switching of semiconductor laser diodes provides a practical and potentially low cost means of generating picosecond optical pulses. To date the majority of work in the area has focused on the development of gain-switched DFB lasers operating at 1.55μm for telecommunication. However, there is emerging interest in the use of gain-switched systems as seed lasers for high power fiber based pulse MOPA systems – particularly for use with the highly efficient Yb-based systems operating at 1.06μm. Work in this direction was hindered for a long while by the lack of suitable gain-switched sources operating at wavelengths around 1.06μm. Suitable FP laser diodes have recently become available and the first results in this direction have now been reported [2]. Gain switching results in the generation of chirped pulses at the diode output and in order to realise the shortest possible pulses external pulse compression is required. In these first experiments we compressed 1 GHz, 57ps pulses down to 20ps by passing them through ~15km of normally dispersive SMF28 fiber. Although this allowed us to demonstrate the principle of the approach, the need for such a long length of compression fiber renders the technique impractical, dictating the need for a more compact compression approach. In this paper we describe the use of a chirped fiber Bragg grating to perform the required pulse compression. Pulse compression from 57ps down to 16.4ps is demonstrated in a very compact and stable system.

A fiber-coupled FP laser diode was gain-switched at 1 GHz with a modulated drive signal superimposed on a DC bias current. Average output power was 7mW (peak power 123mW). External CW seeding of 0.02mW was provided by a narrow linewidth (<100 KHz) CW laser at 1059.94 nm in order to achieve single longitudinal mode operation. The spectral FWHM of the diode was 0.165nm. Uncompressed output pulse duration was 57ps. Previous work determined that chirp was in the region of ~0.0025 ps^2, with some tuning possible by varying the seed laser power. We produced a Chirped Fiber Bragg Grating (CFBG) with a D*Length of -671 ps/nm, 3 dB bandwidth of ~0.48 nm and reflectivity at the centre wavelength of 1059.91 nm of 78% (insert to fig. 1), which we connected to the diode via a 3dB fiber coupler. The overall insertion loss (including double pass through the coupler) is ~ 7.07 dB. A compressed pulse width of 16.4ps was obtained (TBW=0.72). In addition to chirp compensation, the CFBG also provides spectral filtering to reduce unwanted longitudinal modes and ASE. The compressed pulse was amplified in a chain of 3 Yb-doped fiber amplifers, achieving 3 W average power without pulse distortion. The entire system is fiber-coupled. We acknowledge the 1.06μm laser diodes supplied under an SPI-Bookham joint development program.

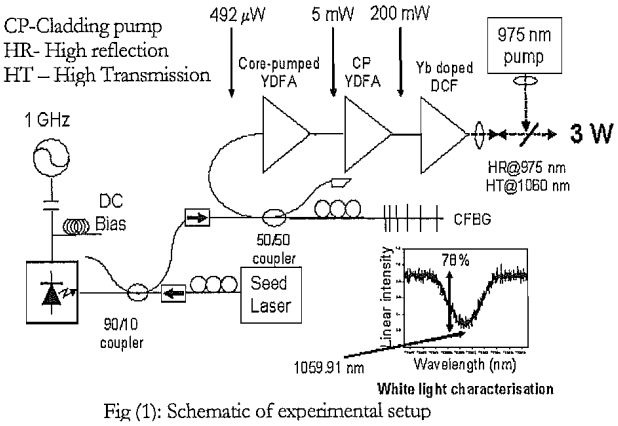

Fig (1): Schematic of experimental setup

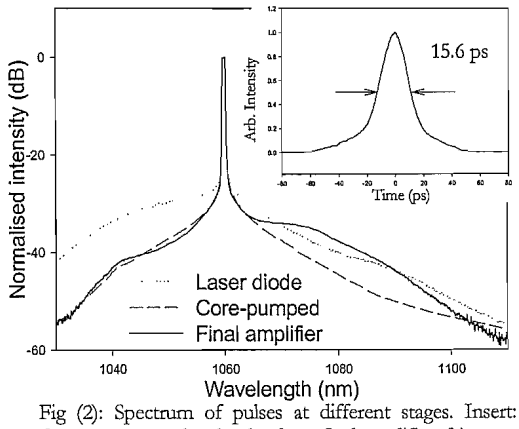

Fig (2): Spectrum of pulses at different stages. Insert: Output autocorrelated pulse from final amplifier. (b)

[1] B.C.Thomsen, Y.Jeong, C.Codemard, M.A.F.Roelens, P.Dupriez, J.K.Sahu, J.Nilsson, D.J.Richardson, "60W 10GHz 4.5ps pulse source at 1.5microns", CLEO/IQEC 2004 San Francisco 16-21 May 2004 CMAA.

[2] A.Piper, A.Malinowski, B.C.Thomsen, D.J.Richardson, L.M.B.Hickey, M.N.Zervas, "11.1W average power 20ps pulses at 1 GHz repetition rate from a fiber-amplified gain-switched 1.06 micron Fabry-Perot laser diode ",*CLEO/QELS 2005* Baltimore 23-26 May 2005 CTuCC3.

Appendix A4

321 W average power picosecond fiber MOPA source at 1060 nm

P. Dupriez, A. Piper, A. Malinowski, J. K. Sahu*, B. C. Thomsen, Y. Jeong, J. Nilsson*, D. J. Richardson*

Optoelectronic Research Centre, University of Southampton, Southampton SO17 1BJ, UK
**also with Southampton Photonics, Inc., 3 Wellington Park, Hedge End, SO30 2QU, United Kingdom.*
Tel: +44 23 8059 4527, Fax: +44 23 8059 3142, email: pad@orc.soton.ac.uk

Abstract: Picosecond pulses generated by a gain-switched laser diode were amplified in a fiber MOPA system to produce in excess of 320 W of average power at a repetition rate of 1 GHz at 1060 nm.

OCIS codes: (060.2320) Fiber optics amplifiers and oscillators; (140.2020) Diode lasers.

1. Introduction

High average power laser sources with picoseconds pulse durations in the 1 μm wavelength range are useful for applications such as micro-machining [1] and laser projection systems [2]. Gain switching of laser diodes has proved to be a convenient and practical method to generate picosecond pulses. Gain-switched distributed feedback (DFB) and Fabry-Pérot (FP) lasers were primarily developed for telecommunications applications [3-5] and have also been utilized as seed laser for high-power cladding pumped erbium:ytterbium doped fiber master-oscillator power amplifier (MOPA) source emitting at 1.55 μm [6]. The development of gain-switched FP laser diodes emitting around 1-1.1 μm has only recently allowed the extension of this approach to realize efficient ytterbium doped fiber MOPA systems. Cladding-pumped ytterbium doped fiber sources are capable of producing kilowatt levels output power with high efficiency and excellent beam quality [7,8]. The combination of fiber-based laser and amplifier systems with the telecommunication grade low power gain-switched laser diode constitute an attractive technology for versatile, robust and compact short pulse sources. We demonstrate here a 20 ps pulsed ytterbium doped fiber master-oscillator power amplifier (MOPA) source with 321 W of average output power seeded by a gain-switched laser diode emitting at 1060 nm.

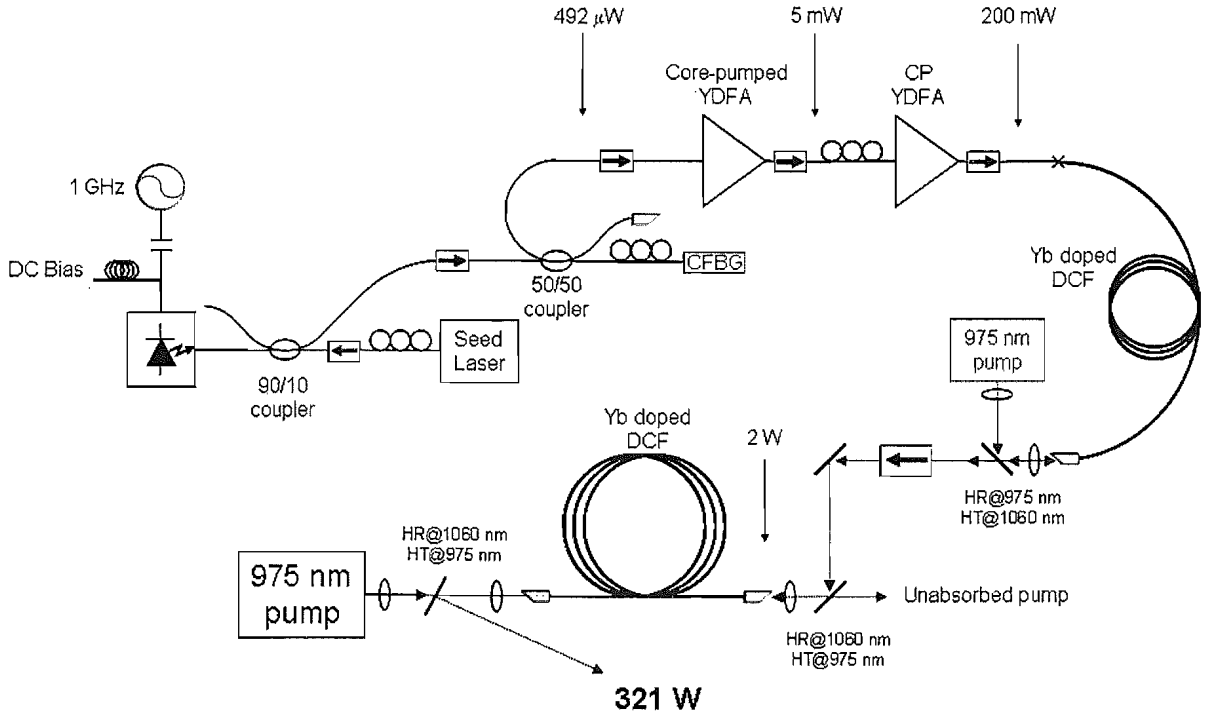

Fig. 1. Experimental set-up. CFBG: chirped fiber Bragg grating, YDFA: ytterbium doped fiber amplifier, DCF: double-clad fiber, HR: high reflectivity, HT: high transmission.

2. Experiment and results

The fiber MOPA system is depicted in Fig. 1. A 1060 nm FP laser diode in a high-speed fiber pigtailed package is gain-switched by driving it with a 1 GHz sinusoid with a DC bias current. The FP diode is seeded with CW DFB fiber laser source emitting at 1059.94 nm through a 90/10 coupler. A chirped fiber Bragg grating (CFBG) designed to compensate the chirp of the pulses was coupled with a 3 dB coupler. The resulting pulses were compressed to a duration of 20 ps with a corresponding average power of 492 μW. The gain-switched laser diode system constitutes the master-oscillator of the MOPA which comprised four cascaded ytterbium doped fiber amplifiers (YDFA). The compressed pulses were first amplified by a core-pumped 4 m long YDFA and by a cladding-pumped YDFA with a fiber length of 6 m and core diameter of 10 μm, pumped by two 915 nm diodes. The double-clad fiber is then spliced to an 8 m, 13 μm core in diameter, double-clad Yb doped fiber pumped by a 975 nm diode that amplified the signal up to 3 W of average power. After transmission through a high-power free-space isolator with 1.5 dB of insertion loss, the signal was free-space launched into the final high-power fiber amplifier stage which was pumped in a counter propagating scheme by a diode stack at 975 nm. The fiber of the power amplifier had a 43 μm diameter ytterbium doped core with a numerical aperture (NA) of 0.09. The D-shaped inner cladding had a 650/600 μm diameter for the longer/shorter axis and was coated with a low index polymer coating providing a nominal NA of 0.48. The pump absorption rate in the inner cladding was ~3 dB/m at the pump wavelength. The fiber length used in the final stage of amplification was 8 m.

The power amplifier was seeded with 2 W of average power and could produce pulses with average powers up to 321 W. The slope efficiency of the power amplifier was 78% with respect to launched pump power (79% with against absorbed pump power) as shown in Fig. 2(a). The beam quality (M^2) at the output of the amplifier was measured to be 2.4. Autocorrelation traces were measured at various levels of amplification to verify the pulse shape and duration. The initial 20 ps pulse shape is maintained after high-power amplification as presented in Fig. 2(b). At 1 GHz repetition rate, the corresponding maximum peak power was 16 kW.

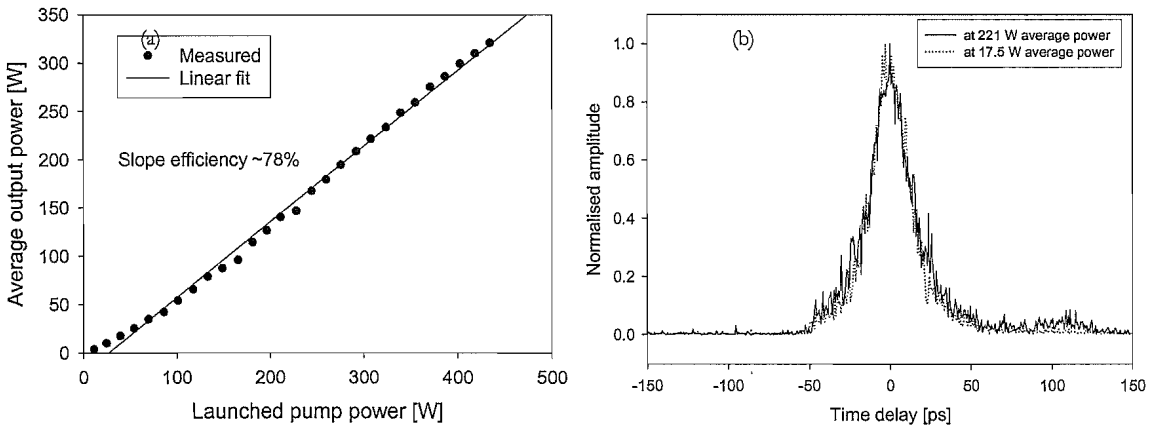

Fig. 2. (a) High average power amplifier efficiency. (b) Autocorrelation traces of the pulses measured at 17.5 W and 321 W of average output power.

Fig. 3(a) shows the optical spectra at the seed and output of the MOPA measured over a broad wavelength range. At 321 W of average output power the 1060 nm signal peak is 20 dB above the peak of the background amplified spontaneous emission (ASE). Although the level of ASE increases significantly at maximum power, it was estimated from spectrum that the signal power represents 82% of the total average output power leading to an actual peak power of 13 kW. Mid-stage spectral filtering would significantly improve the spectral quality. Stimulated Raman Scattering (SRS) was not observed at maximum power.

A detailed view of the spectrum presented in linear scale in Fig 3(b) reveals spectral broadening caused by self-phase modulation obtained along the high-power fiber amplifier. As a result the 0.12 nm linewidth of the seed source, preserved at the input of the power amplifier, was broadened to 0.49 nm at 321 W average power. The laser linewidth at FWHM was kept below 0.5 nm due to the large core area of the ytterbium doped fiber. As most of the pump power is absorbed by the doped fiber, a reduction of fiber length would decrease the spectral broadening while not affecting the output power.

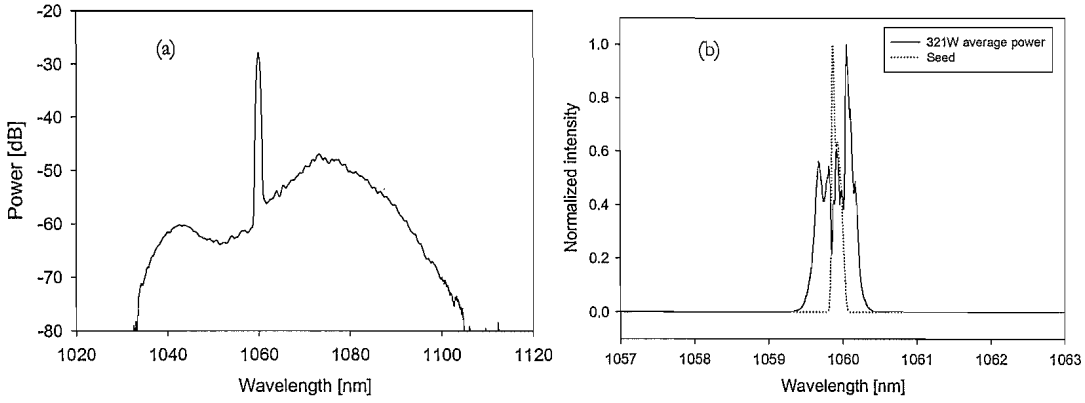

Fig. 3. (a) Optical spectrum at seed and at various average powers (resolution: 0.5 nm). (b) Detailed view of the optical spectrum showing spectral broadening due to self-phase modulation (resolution: 0.01 nm).

3. Conclusion

We have demonstrated a 321 W, 20 ps pulse source with 1 GHz repetition rate based on an ytterbium fiber amplifier chain seeded by a gain-switched laser diode at 1060 nm. The high repetition rate regime enables the generation of high average powers while maintaining a reasonable peak power leading to moderate impact of nonlinearities such as self-phase modulation and stimulated Raman scattering in the fiber amplifier. In addition, the low power electrically driven high-speed diode inherited from the telecom technology offers high flexibility as various repetition rates can be conveniently achieved to obtain the peak power suited for the application. Such a high average power, high repetition rate source is an attractive technology for the generation of high average powers in the visible via nonlinear frequency conversion.

We acknowledge the seed source has been supplied under an SPI-Bookham joint development program.

4. References

[1] B.N. Chichkov, C. Momma, S. Nolte, F. von Alvensleben, and A. Tünnermann, "Femtosecond, picosecond and nanosecond laser ablation of solids," Appl. Phys. A **63**, 109-115 (1996)

[2] F. Brunner, E. Innerhofer, S. V. Marchese, T. Südmeyer, R Paschotta, T. Usami, H. Ito, S. Kurimura, K. Kitamura, G. Arisholm, and U. Keller, "Powerful red-green-blue laser source pumped with a mode-locked thin disk laser," Opt. Lett. **29**, 1921-1923, (2004).

[3] P.-L. Liu; C. Lin; I. Kaminow; and J. Hsieh, "Picosecond Pulse Generation from InGaAsP Lasers at 1.25 and 1.3 μm by Electrical Pulse Pumping," IEEE J. Quantum Electron. **17**, 671-674, (1981).

[4] H.F. Liu, Y. Ogawa, and S. Oshiba, "Generation of an Extremely Short Single-Mode Pulse (Approximately-2 ps) by Compression of a Gain-Switched Pulse from a 1.3μm Distributed-Feedback Laser Diode," Appl. Phys. Lett. **59**, 1284-1286, (1991).

[5] Y. Matsui, S. Kutsuzawa, S. Arahira, and Y. Ogawa, "Generation of wavelength tunable gain-switched pulses from FP MQW lasers with external injection seeding," IEEE Photon. Technol. Lett. **9**, 1087-1089 (1997).

[6] B.C.Thomsen, Y.Jeong, C.Codemard, M.A.F.Roelens, P.Dupriez, J.K.Sahu, J.Nilsson, and D.J.Richardson, "60W 10GHz 4.5ps pulse source at 1.5microns," CLEO/IQEC 2004, paper CMAA (2004).

[7] Y. Jeong, J. K. Sahu, D. N. Payne, and J. Nilsson, "Ytterbium-doped large-core fiber laser with 1.36 kW continuous-wave output power," Opt. Express **12**, 6088-6092 (2004).

[8] A. Liem, J. Limpert, H. Zellmer, A. Tünnermann, V. Reichel, K. Mörl, S. Jetschke, S. Unger, H.-R. Müller, J. Kirchhoff, T. Sandrock, and A. Harschak "1.3 kW Yb-doped fiber laser with excellent beam quality," CLEO/IQEC 2004, postdeadline paper (2004).

Appendix A5

LIST OF PUBLICATIONS

Journal publications

1. Price, J. H. V., Belardi, W., Monro, T. M., Malinowski, A., Piper, A. and Richardson, D. J., "Soliton transmission and supercontinuum generation in holey fiber, using a diode pumped Ytterbium fiber source," Optics Express **10**, p. 382-387 (2002).
2. Malinowski, A., Piper, A., Price, J.H.V., Furusawa, K., Jeong, Y., Nilsson, J., Richardson, D.J., "Ultrashort-pulse Yb^{3+}-fiber-based laser and amplifier system producing >25-W average power." Optics Letters **29**(17) p.2073-5 (2004)
3. Piper, A., Malinowski, A., Furusawa, K., Richardson, D.J., "High-power high-brightness mJ Q-switched ytterbium-doped fibre laser." Electronics Letters **40**(15) p.928-9 (2004).

Conference publications

4. Belardi, W., Monro, T.M., Lee, J.H., Yusoff, Z., Price, J.H.V., Malinowski, A., Piper, A., Richardson, D.J., "Silica holey fibres: fabrication and nonlinear effects" Photon 2002 Cardiff 2-5 Sep (2002).
5. Piper, A., Malinowski, A., Furusawa, K., Richardson, D.J., "1.2 mJ, 37 ns single-moded pulses at 10 kHz repetition rate from a Q-switched ytterbium fiber laser." CLEO/IQEC 2004 San Francisco 16-21 May (2004).
6. Malinowski, A., Piper, A., Price, J.H.V.P., Furusawa, K., Jeong, Y., Nilsson, J. Richardson, D.J., "Ultra-short pulse Yb^{3+} fiber based laser and amplifier system producing >25W average power". CLEO/IQEC 2004 San Francisco 16-21 May (2004).
7. **INVITED** Richardson, D.J., Jeong, Y., Alegria, C., Sahu, J.K., Williams, R.B., Malinowski, A., Piper, A., Price, J.H.V., Nilsson, J., Payne, D.N., "Recent developments in high power fibre laser technology." MicroTech 2004 (IMAPS) Cambridge 3-4 Mar (2004).
8. **INVITED** Richardson, D.J., Jeong, Y., Alegria, C., Sahu, J.K., Williams, R.B., Malinowski, A., Piper, A., Price, J.H.V., Furusawa, K., Nilsson, J., Payne, D.N., "The rising power of fibre laser technology." EPS-QEOD Europhoton Conference Lausanne 29 Aug - 3 Sep 2004 TuB1 Plenary Talk (2004).
9. **INVITED** Malinowski, A., Piper, A., Price, J.H.V., He, F., Ibsen, M., Nilsson, J., Richardson, D.J., "Short pulse high power fiber laser systems." CLEO/QELS 2005 Baltimore 23-26 May (2005).
10. **INVITED** Price, J.H.V., Malinowski, A., Piper, A., He, F., Belardi, W., Monro, T.M., Ibsen, M., Thomsen, B.C., Jeong, Y., Codemard, C., Roelens, M.A.F., Dupriez, P., Sahu, J.K., Nilsson, J., Richardson, D.J., "Advances in high power short pulse fiber laser systems and technology." Photonics West 2005 San Jose 22-27 Jan 2005 p. 5709-30 (2005)

11. **INVITED** Nilsson, J., Sahu, J.K., Jeong, Y., Philippov, V.N., Soh, D.B.S., Codemard, C., Dupriez, P., Kim, J., Richardson, D.J., Malinowski, A., Piper, A.N., Price, J.H.V., Furusawa, K., Clarkson, W.A., Payne, D.N., "High power fiber lasers." OFC 2005 Anaheim 6-11 Mar (2005).

12. **POSTDEADLINE** Dupriez, P., Piper, A., Malinowski, A., Sahu, J.K., Ibsen, M., Jeong, Y., Hickey, L.M.B., Zervas, M.N., Nilsson, J., Richardson, D.J., "321 W average power 1 GHz 20 ps 1060nm pulsed fiber MOPA source." OFC 2005 Anaheim 6-11 Mar (2005).

13. Dupriez, P., Piper, A., Farrell, C., Malinowski, A., Sahu, J.K., Y.Jeong, Thomsen, B.C., Nilsson, J., Richardson, D.J., Hickey, L.M.B., Zervas, M.N., "High average power picosecond pulses from a fiber amplified diode laser at 1060nm." CLEO/Europe-EQEC 2005 Munich 12-17 Jun 2005 CJ3-1-MON (2005).

14. Piper, A., Malinowski, A., Thomsen, B.C., Richardson, D.J., Hickey, L.M.B., Zervas, M.N., "11.1W average power 20ps pulses at 1 GHz repetition rate from a fiber-amplified gain-switched 1.06 μm Fabry-Perot laser diode." *CLEO/QELS 2005* Baltimore 23-26 May 2005 CTuCC3 (2005).

15. **INVITED** Dupriez, P., Nilsson, J., Jeong, Y., Sahu, J.K., Codemard, C., Soh, D.B.S., Farrell, C., Kim, J., Piper, A., Malinowski, A., Richardson, D.J., "Current progress in high-power fiber lasers and amplifiers." Optical Amplifiers and their Applications (OAA) Budapest 7-10 Aug (2005).